

*Metallic Nanoparticles
and Thin Films for
Optical Sensors on Glass Substrates*

Dissertation

(kumulativ)

zur Erlangung des akademischen Grades doctor rerum naturalium

(Dr. rer. nat.)

vorgelegt dem Rat der Chemisch-Geowissenschaftlichen Fakultät der
Friedrich-Schiller-Universität Jena

von Dipl.-Ing. Michael Kracker

geboren am 14.04.1984 in Sonneberg

Gutachter:

1. Prof. Dr. Dr. Christian Rüssel
(Otto-Schott-Institut, Friedrich-Schiller-Universität Jena)
2. PD Dr. Wolfgang Seeber
(LEG, Landesentwicklungsgesellschaft Thüringen)

Tag der Verteidigung: 15.Oktober 2014

Die experimentelle Arbeit für diese Promotion wurde im Zeitraum zwischen Januar 2011 und Juni 2014 am Otto-Schott-Institut der Friedrich-Schiller-Universität Jena unter der Betreuung von Prof. Dr. C. Rüssel durchgeführt.

Contents

1. Preface	1
2. Introduction	3
2.1 Preparation.....	3
2.2 Optical properties of small metal nanoparticles	10
3. Articles	15
3.1 C. Worsch, M. Kracker, W. Wisniewski, C. Rüssel; <i>Optical properties of self assembled oriented island evolution of ultra-thin gold layer.</i> Thin Solid Films, 520 (2012) 4941–4946	15
3.2 C. Worsch, W. Wisniewski, M. Kracker, C. Rüssel; <i>Gold nano-particles fixed on glass.</i> Applied Surface Science, 258 (2012) 8506–8513	22
3.3 M. Kracker, C. Worsch, C. Bocker, C. Rüssel; <i>Optical properties of dewetted thin silver/gold multilayer films on glass substrates.</i> Thin Solid Films, 539 (2013) 47–54	31
3.4 M. Kracker, C. Worsch, C. Rüssel; <i>Optical properties of palladium nanoparticles under exposure of hydrogen and inert gas prepared by dewetting synthesis of thin-sputtered layers.</i> Journal of Nanoparticle Research, 15 (2013) 1594	40
3.5 M. Kracker, C. Worsch, C. Rüssel; <i>The effect of thermal annealing and hydrogen on the morphology and the optical properties of thin palladium layers.</i> Materials Letters 110 (2013) 114–116	51
3.6 M. Kracker, C. Worsch, W. Seeber, C. Rüssel; <i>Optical hydrogen sensing with modified Pd-layers: A kinetic study of roughened layers and dewetted nanoparticle films.</i> Sensors and Actuators B: Chemical, 197 (2014) 95–103	55
3.7 C. Worsch, M. Kracker, J. Edelmann, A. Schubert, C. Rüssel; <i>Microfluidic plasmon sensors prepared by dewetting of metal films during hot embossing of glass.</i> Sensors and Actuators B: Chemical 202 (2014) 365–372.....	65
3.8 M. Kracker, W. Wisniewski, C. Rüssel; <i>Textures of Au, Pt and Pd/PdO Nano Particles Thermally Dewetted from Thin Metal Layers on Fused Silica.</i> Manuscript Submitted To Small, (2014)	74

4.	Discussion	104
4.1	Particle preparation.....	104
4.2	Optical characterization.....	110
4.3	Sensor application	116
4.4	Theoretical consideration (Simulation).....	118
4.5	Crystallographic, morphological and analytic.....	121
5.	Conclusion.....	125
6.	Abstract	127
7.	Zusammenfassung.....	129
8.	References	131
9.	Figures	142
10.	Poster.....	143
11.	Presentations.....	144
12.	Danksagung.....	145
13.	Lebenslauf / Curriculum Vitae	146
14.	Appendix A: Corrigendum to Chapter 3.6 “Optical hydrogen sensing with modified Pd-layers: A kinetic study of roughened layers and dewetted nanoparticle films”	149
15.	Appendix B: Finally published version of Chapter 3.8 “Textures of Au, Pt and Pd/PdO Nanoparticles Thermally Dewetted from Thin Metal Layers on Fused Silica” RSC Advances, 4 (2014) 48135 – 48143	151

1. Preface

Two worlds. The research on very small structures restarted 40 years ago caused by a steady development of new or already existing characterization methods. Expressed in scientific periods of time, it is more probably a young branch of science. Nevertheless, nanotechnology combines two worlds of “history”. Today, the new “Nano”-Science has only just begun to understand how such systems behave, but they are empirically used for several thousand years. From Bronze Age (more than 3000 years ago) [1] the Roman period (1600 years ago), the modern Egyptian history (1000 years ago) [2], the middle age (more than 500 years ago) and finally up (more than ever) to the present time. The nanotechnology has already arrived in our everyday life with things such as sun cream, toothpaste and the well-known lotus effect on textiles and coatings.

However for science, the nanotechnology is of much greater significance because, nanoparticles are not only a continuous connection within time; rather they connect two widely different physical “worlds”. “The single isolated nanoparticle is certainly the ideal subject to study the transition between the molecular state and the bulk solid or liquid state.”[3]. Especially, this transition between the worlds is the subject of modern research, because it promises interesting and spectacular phenomena as well as a unique insight into the “heart” of matter.

To grant such an insight into the nature of (nano) materials, it requires not only the knowledge for preparation of nano-technological products, but rather the continuous development of nano-technological characterization methods is a major contribution and nanoparticles also form a link between production and analysis.

This work is focused on the optical properties of metallic nanoparticles and thin films on glass. There, starting with the production and modification of nanoparticles by a self-organized process, on the characterization and simulation right through to the application as a sensor system. The main subject of this work, the optical properties is caused by the plasmon resonance. That means a collective electron oscillation in a metallic material respectively a metal particle excited by an external electric field. The mathematical explanation of the resulting optical properties was already done more than 100 years ago by Gustav Mie, although without the exact knowledge of the existence of an electron oscillation. Nevertheless, Mie’s contribution allows up to the present time (or even at the present time), predictions about the optical behavior of metallic nanoparticles. A very important prediction is in fact (in addition to the effect of particle size) the sensitivity to a variation in the optical properties of the surrounding medium. Especially metallic particles of the type prepared in this work are applicable as a sensitive element on the basis of this knowledge.

The peculiarity of optical properties of small metal nanoparticles is that they are often easy to measure. But on the other hand, the behavior of such “plasmonic” effects is fairly hard to describe and to predict. A large number of papers on plasmonic properties of gold or (and) silver nanoparticles have been published. This is due to the fact that the plasmonic effects of these metals (also copper) can be found in the visible range of light. However, the number of publications is significantly lower away from these “model” systems.

Two different metallic systems were particularly investigated. The first is focus on gold nanoparticles; they are compared to the existing research and specifically described with respect to tailoring of the optical properties. The second system describes the preparation of stabilizing-agent free palladium nanoparticles for hydrogen sensing based on the change of the plasmon resonance properties. In all systems, this work is dedicated to the presentation of problems and their solutions that may (or will) result in affecting the formation and analysis of metallic nanoparticles.

2. Introduction

In the following, a method is described which enables the preparation of nano particle containing layers on glass substrates. For this purpose, a thin sputtered metal layer is thermally treated at temperatures usually below those of the respective melting points. This results in dewetting of the layer and in the formation of nano particles with sizes in the 20 to 200 nm range.

The application of metal particles, especially on glass surfaces, has disclosed some unresolved issues. Glass surfaces are well suited to generate optically active metal nanoparticles. The use of glass allows a simple access to the optical properties of metallic nanoparticles. Glass can be thermally stable up to 1100 °C which enables a thermal preparation procedure as well as investigations up to or even above the melting point of some metals, e.g. gold. Large area coating systems offer the possibility to produce supported particles in an industrial scale. Hence the question arises how far a particle layer can be tailored, protected and applied in technological settings. Here the optical and the dewetting behavior within a metallic and dielectric layer stack must be considered. The optical properties in dependence on environmental circumstances e.g. atmosphere and embedding medium have to be determined. Furthermore, a shift in the absorption maximum which depends on the refractive index of the surrounding medium may also be utilized to draw conclusions on the nanoparticle systems. Additionally, the dewetting of non-inert metals showing phase transitions during annealing has yet to be analyzed in detail as well as an influence of the annealing temperature and heating/cooling rates applied during dewetting.

2.1 Preparation

The preparation of nanoparticles can be achieved by numerous methods and is described by an almost unmanageable amount of publications. For this reason it is nearly impossible to give a complete overview on the existing techniques what is ultimately due to the enormous research activity in this field. A suitable classification of manufacturing methods is available by differentiation to chemical and physical approaches [4,5].

Chemical methods are frequently used to prepare metallic nanoparticles for example from a solution [6–10]. The most common method was presented as early as in 1951 by Turkevich et al. [11] and is known as salt reduction methods. However, if the particles are mobile *e.g.* in a solution, they need to be stabilized, in order to avoid agglomeration and coalescence of the particles [4,5,12,13]. Most of the

stabilization procedures are realized by chemical modifications of the particle surface. Schmid et al. [4] described the possibilities to embed the nanoparticles into a substrate as well as in micelles. They reported on the electrostatic repulsion, the steric hindrance and embedding in nano capsules. Electrostatic stabilization is realized by ions at the metal surface which results in repulsion forces (due to their electric charges) between the particles [6,14].

Sterically stabilized nanoparticles are surrounded by a barrier of *e.g.* polymers or surfactants. Thus the a direct contact between the particles is prevented. In addition, the particles are held in such a distance that they are not exposed to mutual attraction forces [6,15–17]. Capek identified also the possibility to combine both type of stabilizing mechanisms using cationic polyelectrolytes [18]. Another strategy to prevent aggregation is the subsequent incorporation of the particles in a matrix for example by a sol gel process [19,20] or their preparation inside a matrix [21–23].

With respect to chemical preparation methods it can be concluded, the (wet) chemical route is most suitable way, to achieve particles highly controllable in size, shape, composition as well as functionalization [24,25]. In this regard, Bönemann and Richards summarizes: “The use of metal vapor techniques is, however, limited because the operation of the apparatus is demanding and it is difficult to obtain narrow particle size distributions.” Furthermore, they conclude: “The chemical reduction of transition metal salts in the presence of stabilizing agents ... become one of the most common and power-full synthetic methods in this field.” [26] However, this interpretation is not generally valid.

Thus, additional chemicals at the particle surface such as polymers or charged ions are undesirable for some applications. Hence the optical properties of the metallic particles depend on the direct surrounding media as well as on the possible access of reaction educts, such as hydrogen in contact to palladium. Additionally, the optical properties of some metals *e.g.* palladium (where the plasmon resonance is to be expected in the UV-range [27]) may be covered by the cut off wavelength of the stabilizing chemistry as described in Ref. [3,12,28,29]. In order to obtain stable and manageable nanoparticles, they should be deposited and fixed on a substrate. However, the generation of a layer composed by metallic nanoparticles *e.g.* on glasses, is not always simple. It possibly requires a previous modification of the glass surface. Shipway et al. present in an overview article a suitable and commonly used pretreatment procedure to achieve a particle monolayer prepared from a solution [30].

In order to achieve particles without additional chemicals, the surface can be used even as a support. If it is possible to form particles directly on the surface, the surface can even serve as a stabilizer. **Physical preparation** methods are also commonly used and suitable to provide particles, by nucleation on surfaces or inside a vapor. Physical preparation methods include (among others),

sputtering [31–37], thermal and electron beam evaporation [38,38–43] as well as laser ablation [44–48].

It further provides the possibility to produce particles in the vapor by a subsequent deposition onto a surface [49]. Special experimental conditions also enable the particle formation directly at the surface [50–53]. In this thesis a route for the nanoparticle preparation is chosen which only shows formal similarities to the vapor deposition techniques described above. It uses a **sputter deposition technique** during which by contrast to the procedure described above, a metal layer is prepared. During subsequent thermal annealing, dewetting occurs which leads to the formation of metallic nanoparticles on the surface. The particles are in a well-defined distance and also in a certain orientation correlation to each other. The formation of such structures will be explained in the following sections.

At first, sputter deposition is well known in thin film technologies as well as for coating of glass surfaces. Argon ions, provided by a glow discharge, are accelerated to the cathode (target) and their kinetic energy leads to the ejection of target atoms [54]. Due to the impulse, the ejected atoms move away from the cathode towards the substrate, are deposited on the surface and form a film. The atoms are relative fast, but the velocity is rapidly decreased by collisions with other gas atoms. Hence the process pressure and the target to substrate distance are critical to the resulting layer properties. The used DC sputtering system is applicable for sputtering of metals and semiconductors. A conductive anode is required, but the substrate need not necessarily be conductive [55]. Further literature, which deals with the exact process of sputtering can *e.g.* be found in [56,57] and especially in [58]. As already mentioned, in addition to the distance, the gas pressure as well as the temperature is decisive for the resulting structures. Thornton proposed a structure model which describes the effect of argon pressure and substrate temperature [59,60]. This model is based on the final mobility of the deposited atoms on the substrate surface in dependence on the direction of incidence and incoming atoms per time as well as the thermal energy (in comparison to the bulk melting point of the deposited material). Additionally, Thornton described the mechanism which leads to a crystallographic orientation inside a sputtered metallic layer [61,62]. This orientation may also result in the formation of oriented particles during subsequent dewetting as shown in **article 3.1**. However the preferred orientation of a 111 direction perpendicular to surface is also found if other physical deposition methods are applied [63].

As already mentioned, it is thus possible to form nanoparticles already during sputtering [64]. By contrast, the particles prepared in the experiments concerning this thesis are based on a dewetting process. Hence, closed layers will be formed at the surface first. According to the structural zone model of Thornton [59], the layer deposited with the experimental parameters used in this work, provides the structural properties of zone 1. Zone 1 structures are indicated by voids between columns

and hence the point of origin is not a perfectly dense layer [39,58]. Hence, the **articles 3.1, 3.2, 3.3** as well as **3.5** and **3.7** illustrate the described appearance of the freshly sputtered layers on glass.

If thin metal layers are exposed to elevated temperatures [65,66], laser [67–69], ion [70,71] or electron beam radiation [72] they tend to form particles by a rupture process, called **dewetting**. From a mechanical point of view, it corresponds to the formation of water droplets on a sheet of glass, as it is drawn out from a water vessel. Generally, dewetting is a result of the energy minimization in the system substrate/layer/atmosphere [73]. The effect and the theoretical fundamentals are described extensively for thin liquid films and polymers on various substrates [74–77].

Bischof et al. identified the fundamental mechanism, which describes the dewetting of a metastable film [78]. First the nucleation of holes occurs and then, spinodal dewetting takes place caused by thermally activated surface waves. Michalak et al. expanded the definition of the nucleation of holes to thermal grooving (at grain boundaries), heterogeneous nucleation caused by defects or impurities and the thermal nucleation of holes caused by temperature fluctuations [79]. Furthermore, he proposed the basic classification according to nucleation-dominated mechanisms and thermodynamic system instabilities (spinodal dewetting). In this respect, liquid polymer films, heated up to the glass transition temperature [80] as well as liquid crystal and metal films [81], exhibit a spinodal dewetting behavior. The film disrupts spontaneously due to periodic film thickness fluctuations and a subsequent formation of a characteristic wavelength of the surface modulation [75,82]. On the other hand, the nucleation of holes which is reported to be not related to spinodal dewetting is found in [41]. However this clear and unique separability and their conclusion on a sole function of the dewetting mode is doubt by several authors [78,83]. Bischof et al. consider in his regard: “Often the basics of dewetting have been studied on liquid films because heterogeneous influences, i.e., from grain boundaries or stresses, associated with solid films are not as prominent or must not be considered.” [78].

Furthermore, the applied films are not ideally smooth, and contain irregularities. As already mentioned, this can very well be recognized in the case of thin layers sputtered at room temperature. Layers attributed to the zone 1 morphology in the Thornton model, contain irregularly shaped areas, divided by voids [59].

After the initial nucleation state, the **holes grow** and the former layer material accumulates at the hole perimeter which leads to an elevated rim around the them. This behavior was found for polymers [74–77,81] and metal layers [38,67–69]. A rim of material is comparable with a nano wire. Such a thin an elongated structure tends to disintegrate into particles by the Rayleigh instability [74,84,85]. A combination of both mechanisms is described in [75,76,86,87] and gives a detailed illustration of the hole growth process during which simultaneously particles are formed. If a rim disintegrates into particles, exactly at this point, a new hole starts to grow and a new rim is formed. However, if the rims

are not destroyed by Rayleigh instabilities, a network of material threads (webs) is formed. An ongoing energy input will disintegrate these webs subsequently, so that the original arrangement of the network is properly maintained [74–76]. This phenomenon is not limited to liquid or polymer films [67–69].

After the film rupture is finished, the formed separated islands shows an irregular shape. This is well recognized in [41]. From now, the mechanisms of **further energy minimizations** are changed and will occur in morphological transformations of the particle by means of surface or volume diffusion as well as particle migration.

The irregular structure of the particles disappears and obtains a smooth shape. This does not mean that the particles are round. There are particles with energetically unfavorable shape *e.g.* elongated or branched structures. The same process which destabilized the rims of the holes is responsible for the breakdown of the elongated particles. The **Rayleigh instability** leads to more and smaller uniformly shaped particles [84,85,88]. Such a process is indicated by constrictions of the particles, such as observed in Ref. [65,79].

At the same time, the interfacial energy can further decrease by a **ripening process** as well as particles merge to larger ones. The driving force is again the tendency to reduce the surface to volume ratio. In this regard, the particle should increase in size and decrease in number [89] which however requires a material transport between the particles. In principle, this leads to a coarsening of the particle arrangement and in this regard, two different mechanisms are discussed [89,90]. First the transport is carried out by diffusion. The smaller particles shrink, while the large particles further grow while the particles are not in contact. This effect is called **Ostwald ripening** [39,90–92]. Datye et al. demonstrated also the influence on the particle size distribution. The effective number of particles is decreased. Hence, the particle becomes so small that they vanish [3]. The arising question is now, whether the diffusion takes place in the glassy phase, on the surface or, however, in the gas phase. In the year 2002 Bowker designate the mechanism of mass transport, as the surface diffusion and not through the gas phase, for a particle supported by a surface [89].

The second possible type of mass transport is the movement of the whole particle itself, followed by a **merging of the particles** [88,89,93–95]. The driving force is the same, *i.e.* the minimization of the surface energy. Coalescence occurs usually in high density particle system [90]. The movement seems to be affected by size of the particles and the distance in between. Datye et al. analyzed the sintering behavior of metallic Pd and Pt in detail [96]. They found a narrow log normal size distribution shifted towards larger particle sizes. They conclude the occurrence of diffusion controlled particle transport for Pd caused by a high vapor pressure. For Pt, they found, strongly depend on the atmosphere, the particle migration process (reducing conditions) and on the other hand Ostwald ripening controlled

growth mechanisms during annealing in air occur. In contrast to the oxidation affected ripening mechanisms in air, Geissler et al. determined the mass transport of small Ni particles on oxidized Si wafers, by particle migration. Furthermore, they observed a strict dependence on the hydrogen partial pressure. Thus, the magnitude and type of mass transport is depending on atmosphere, substrate, temperature and particle size. Hence, the accurate determination of the relevant contribution and a comparison of the results with each other are complicated.

Further annealing will finally transfer the particles into the **equilibrium shape**. However, this is not a sphere. Therefore, faceting represents a further minimization of the particle energy and the equilibrium shape of small single crystals is based on Wulff construction (**Figure 1**). This fact is also indicated by the large number of papers (including **article 3.1** and **3.8**) reporting on faceted metal nanoparticles [6,39–41,97–99]. Here, the surface energies of the individual facet surfaces plays an important role. The size and specific surface energy of each facet determine the minimum energy of small (single crystalline) mostly particles [100]. The most studies were performed with small particles with sizes of few to some ten nano meters. However, the work of Heyraud and Metois proved the validity at different temperatures for particle sizes of some microns [101]. Marks noted in this regard, that the Wulff construction provides the expected equilibrium shape and is indeed (theoretically) size independent, but the influence of edges and corners becomes more prominent with smaller particle sizes. Based on thermodynamically calculations, Barnard and Curtiss found that an effect of edged and corners significantly occurs below 3 nm in diameter [102,103].

The applicability of the Wulff construction is limited to free floating particles inside a matrix. The theory is in principle not valid for particles deposited on surfaces. Winterbottom described and completed the **Wulff construction to the effect of flat homogeneous (rigid) substrates**. He introduced a component for the free energy of adhesion to modify the free energy at the surface in contact with the substrate [100,104] (**Figure 2**). Marks and Ajayan [105] extended the theory to non-rigid surfaces, but also showed the possibility of transformed morphology [100]. Another crystallographic phenomenon is twinning. Twinning is well known in small metal single crystals (see **article 3.1** and **3.8**) and also corresponds to Wulff shape. Marks proposed a modified Wulff construction for twinned particles [106–108]. Thus, he showed that a twinned particle also represents an energetically favorable equilibrium shape.

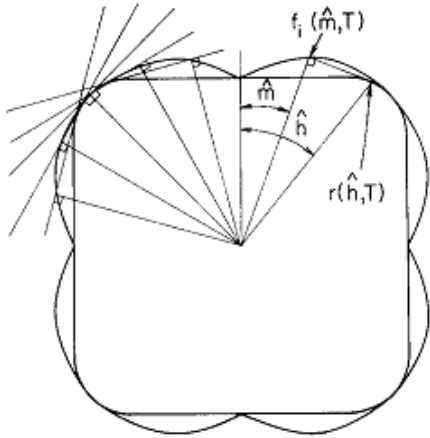


Figure 1 Wulff – construction, to determine the equilibrium shape of small single crystal [109]

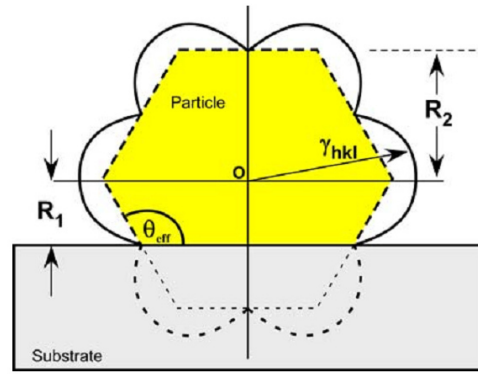


Figure 2 Modified Wulff – construction for supported nanoparticles [110]

2.2 Optical properties of small metal nanoparticles

As already mentioned, the optical properties of small particles are directly affected by the size. In comparison with the (visible) wavelength of the light, the dimension of a bulk material can be assumed to be infinite. Hence classical conceptions of optics are applicable. However, small particles are in size below the range of the light wavelengths, the size is not to be assumed as infinite and size depend optical behaviors can occur. These interpretations are so far independent of the nature of the particle material. However in contrast to dielectric materials, the (in a first approximation) free conductive electrons in metals interact with an electromagnetic wave and specify the optical properties of small metal nanoparticles (Drude metal).

The insights described below, are published in a very detailed manner in [3,111–114]. In order to describe and illustrate the special behavior of small metal structures, it should introduce first a simple electrostatic interaction model for spherical particles called **quasistatic approximation** or quasistatic regime [114]. The simplification of this system is restriction to the size of spherical particle is much smaller than the wave length of the incident light (for visible light $\sim d = 50 \text{ nm}$ [112]). Thus it can be assumed that the applied electric field is (spatially relative to the particles) constant and the interaction is dominated by electrostatic rules instead of electrodynamics. If an electric field is applied to the particle, the conductive electron cloud is displaced by force in dependence of the field direction (**Figure 3**). The displacement is done in relation to the remaining ion cores of the metal lattice. The electrons accumulate at the surface in the opposite direction of the electromagnetic field and induce a negative charge at the surface. At the opposite a positive charge is performed by the remaining metal ions (**Figure 4**). In this manner, a dipole is created and the metal sphere is polarized. The polarizability of a metal sphere is given in **eq. 1** and the influence of the surrounding medium ϵ_m becomes obvious. Further, the polarizability is maximum if the denominator in **eq. 1** becomes small and thus a **resonance condition** can be specified and is given in **eq. 1a** and **1b**. Metals show a complex dielectric function and the dielectric constant ϵ in **eq. 1** have to be replaced with $\epsilon(\omega) = \epsilon_1(\omega) + \epsilon_2(\omega)$ (where denotes $\epsilon_1(\omega) = \text{real part}$, $\epsilon_2(\omega) = \text{the imaginary part}$) and the resonance condition therefore is given by **eq. 1c**.

If the direction of the incident field is changed according to the nature of wave, the polarity of the resulting dipole reverses. Thus, the induce movement of the electrons relative to nuclei leads to oscillatory system. However, the resulting restoring forces caused by electron-ion Coulomb attraction, as well as the rejection of the inflowing electrons by the induced negative pole (a new dipole is induced by accumulated electrons itself [112]). Hence, the oscillating system comes into a destructive resonant state, if the electron cannot longer follow the stimulating wave. Kelly et al. designate four factors influencing the frequency: the density of electrons, the effective electron mass, and the shape

and size of the charge distribution [113]. The latter is depending on the type and size of the particle geometry, thus different or more than one Eigenfrequency can occur [114]. Such a destructive resonance exhibits a narrow-band light absorption, with the shape of a resonance curve [115]. Garcia compares the nanoparticle as a result of damping factors with a linear oscillator inside an alternating external force field [112]. He concludes that the amplitude and the phase are depending on the force and the oscillator properties. The frequency is identical with that of the external force, but the amplitude is strongly increased at the resonance frequency. Furthermore, he described the increased absorbance in the optical spectra with the increased energy requirement (due the resonance) of the dipole and as a result of the energy conservation, the required energy is derived from the external field.

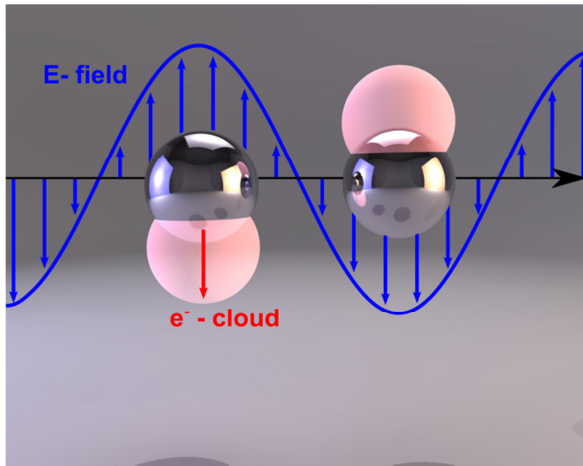


Figure 3 Illustration of small metal particle by light irradiation induced electron movement (plasmon oscillation)

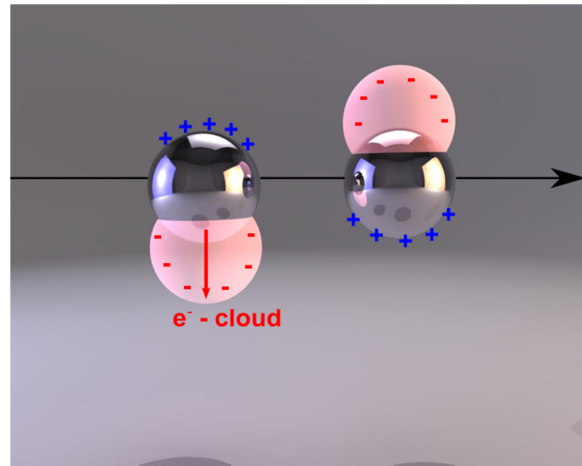


Figure 4 Resulting polarization of the metal particle by accumulation of electrons (negative pole) and the remaining lattice of ionic cores (positive pole)

This enhanced interpretation is described in the dipolar approximation, [112] or simplified Mie theory [114] (certain simplifications can transform the Mie theory in this approximation) and is given in **eq. 2**. In contrast to the electrostatic description, the solution of the equation results in an extinction cross section (area as a unit) and corresponds to the interaction strength of particle and light. The cross section area may be larger than the real geometric size, caused by the induce field and its interaction with the external irradiation field [111]. However, the maximum of the cross section is also only dependent on the relation between the real part of the complex dielectric function and the surrounding media. This results from the resonance condition in **eq. 2a**.

In the following, an overview of quasistatic models (electrostatic) and the simplified electrodynamic Mie theory in the quasistatic regime taken from [114] is given:

$$\alpha = 4\pi\varepsilon_0 R^3 \frac{\varepsilon - \varepsilon_m}{\varepsilon + 2\varepsilon_m} \quad (1)$$

$$|\varepsilon + 2\varepsilon_m| = \text{Minimum} \quad (1a)$$

$$\varepsilon = -2\varepsilon_m \quad (1b)$$

$$\varepsilon_1(\omega) = -2\varepsilon_m \quad (1c)$$

$$\sigma_{ext} = 9 \frac{\omega}{c} \varepsilon_m^{3/2} V_0 \frac{\varepsilon_2(\omega)}{[\varepsilon_1(\omega) + 2\varepsilon_m]^2 + \varepsilon_2(\omega)^2} \quad (2)$$

$$\varepsilon_1(\omega) = -2\varepsilon_m \quad (2a)$$

Where α is the polarizability of a small sphere, ε_0 the vacuum permeability, R radius of a sphere, ε dielectric constant of a material, ε_m dielectric constant of the surrounding matrix, σ_{ext} extinction cross section, ω angular frequency, c light speed in vacuum, V_0 volume of a sphere, $\varepsilon_1(\omega)$ real part and $\varepsilon_2(\omega)$ the imaginary part of the sphere materials complex dielectric function.

Such a simplified model provides general statements about the behavior nanoparticle systems: First, the basic dependence of the plasmon resonance to the particle material. The real part dielectric function defines the position of the plasmon resonance, governed the resonance condition given in **equations 2a**. Additionally, the slope of the dielectric function exactly at the resonance generates the width of the plasmon resonance. Thus, metals can also exhibit multiple or warped resonances, caused by a discontinuous profile of $\varepsilon_1(\omega)$ exactly at the corresponding wavelength. From the **equations 1c** and **2a**, the resonance condition leads to an independence of the imaginary part $\varepsilon_2(\omega)$ of the dielectric function. This may lead to incorrect positions and resonance strengths. Strictly spoken, a simple resonance condition based on the conductive electrons and thus the plasma frequency, is only valid for alkali metals (Drude metals) [114] Noble metals such as Ag, Au or even Cu cannot be regarded as Drude metal. They exhibit interband transition from 5 d to the hybridized 6 sp for example of gold.

Hence, it is necessary to use the measured dielectric functions. Especially the imaginary part $\varepsilon_2(\omega)$, which contains stands for effects such as the contribution of the interband transitions in noble metals are required. The second dependency is given by the effect of the surrounding media. Here, the polarizability of a spherical particle is defined by the combination of the particle material and embedding media. However, in both equations, the size of the particle has not any influence on the position of the resonance band. Together with the limitations of the resonance conditions, the model is

too simple (neglect of the imaginary part of the dielectric function), and does not take into account the effect of size and size distribution. A more accurate model had to be used. One possibility is the usage of the complete Mie theory, the exact electrodynamic calculation, which includes both parts of the dielectric function.

In the early 20th century, Gustav Mie developed a mathematical approach to explain the ruby color of suspensions containing gold nanoparticles, the “**Mie theory**” [116]. He solved the Maxwell equation of a spherical particle inside a homogenous medium by using spherical coordinates for the boundary conditions. The boundary condition corresponds to a sharp transition between the matrix material and the dielectric complex function of the nanoparticle. He performed a multipole expansion by taking into consideration an electric and a magnetic field [111,114]. Mie summed up the contribution of each multipole component (dipole, quadrupole, octupole ...)[112]. He also took into account the electrical and magnetic mode respectively. The latter is based on eddy currents, consequently no magnetic material properties but rather electrical [114,117]. Thus Mie obtained extinction and scattering cross-sections in dependence of the wavelength, the type of material the particles are composed of (including the imaginary part), the type of the embedding matrix as well as size. In this regard, the model is taking into account the most important parameters and hence is a good approximation.

$$\sigma_{ext} = \frac{2\pi}{k_M^2} \sum_{n=1}^{\infty} (2n+1) \text{Re}(a_n + b_n) \quad (3)$$

$$\sigma_{sca} = \frac{2\pi}{k_M^2} \sum_{n=1}^{\infty} (2n+1) (|a_n|^2 + |b_n|^2) \quad (4)$$

$$\sigma_{ext} = \sigma_{sca} + \sigma_{abs} \quad (5)$$

$$Q_{ext} = \frac{\sigma_{ext}}{\pi R^2} \quad (6)$$

Where σ_{ext} the extinction cross section, σ_{sca} the scattering cross section, σ_{abs} the absorption cross section, k wave vector, n order of partial waves (not the refractive index), a_n and b_n scattering coefficients as well as Q_{ext} the extinction efficiency. Calculations using the Mie theory also result in cross sections. However two cross sections are obtained. These are an extinction cross section **eq. 3** and scattering cross section **eq. 4**. The sum of these two is the absorption cross (see **eq. 5**). The dependence on particle size and surrounding medium is introduced into Mie theory by the scattering coefficients a_n and b_n . These include Riccati-Bessel, Riccati-Neumann and Riccati-Hankel functions. Furthermore, the particle size, the refractive index of the matrix and of the sphere are input parameters.

Thus, two different cross sections are calculated. It also shows that the extinction spectrum consists of two spectra caused by different interaction mechanisms. In comparison to the electrostatic regime, the cross section area may also be larger than the real geometric size. Hence an efficiency Q_{ext} can be defined **eq. 6**

The explanation of a “sloshing” electron gas was developed 60 years later by Kreibig and Zacharias [118]. Mie did not have knowledge on the underlying principles. A combination of the analytical Mie theory and collective plasma oscillation is evident in the following statements: Kelly et al. [113] concludes that the dipole is a radiating dipole, which is followed by the Maxwell equation. The radiative dipole contributes to the extinction and the Rayleigh scattering of the sphere. Thus he confirmed the statements of Mie, who proposed two different interaction cross sections (the third cross section, “absorption” is calculated from extinction and scattering). Furthermore, Aussenegg and Ditzbacher [115] refer to an energy transfer by scattering into the far field and thus visible with the eye (see **article 3.1**). This corresponds to a loss of energy caused by radiation damping. The notation follows Quintin [3] but similar expressions are published in [111,114] or [119].

Generally, it should be noted that the applicability of **the Mie theory is limited**. Today, the use of a sharp discontinuity as boundary conditions is discussed critical. Hence, the dielectric function of a material cannot readily apply for nanoparticles because at the border of a nanoparticle a continuous transition of the dielectric function occurs. Furthermore, the dielectric function depend on the size of the particle [114,117]. Additionally Mie theory does not consider multiple excitations by coupling of individual particles. In analogy, the transfer of electrons between the matrix and the particle cannot be included in the Mie theory [120]. The Mie theory is primarily limited by the exclusive validity on spheres.

The following will be presented briefly, a third option, which is suitable to avoid the shape limitations of the Mie theory, the **discrete dipole approximation (DDA)**. Hereby, the particle in interaction with light is represented by finite cloud of dipoles. Each dipole has a polarizability given by the particle dielectric function. Furthermore, the dipoles are arranged in a cubic grid spaced by a lattice parameter and the shape of the particle is defined by the coordinates of each dipole. An applied electric field induces a dipole moment and the resulting field is in interaction with another dipole (all other dipoles) [3]. In this way, wave propagation is possibly corresponding to a dispersion relation of the bulk material [119].

3.1

C. Worsch, M. Kracker, W. Wisniewski, C. Rüssel

***Optical properties of self assembled oriented island evolution
of ultra-thin gold layers***

Thin Solid Films, 520 (2012) 4941–4946

DOI: <http://dx.doi.org/10.1016/j.tsf.2012.03.016>

Optical properties of self assembled oriented island evolution of ultra-thin gold layers				
Beteiligt an				
	Dr. Christian Worsch	Michael Kracker	Dr. Wolfgang Wisniewski	Prof. Christian Rüssel
Konzeption des Forschungsansatzes	X	X		X
Planung der Untersuchung	X			
Datenerhebung		X	X	
Datenanalyse und Interpretation	X	X	X	
Schreiben des Manuskripts	X	X	X	X
Vorschlag Anrechnung Publikationsäquivalente		0,75		
<p>Erklärung</p> <p>Teile der publizierten Ergebnisse wurden bereits in der Diplomarbeit <u>„Temperaturinduzierte Entnetzung dünner Goldschichten zur Herstellung nanoskaliger Partikel“</u> (erstellt am Otto-Schott-Institut, eingereicht bei der Physikalisch-Astronomischen Fakultät) erhoben. Es handelt sich um optische Untersuchungen, Abbildung der erzeugten Farben und deren Entstehung sowie UV-Vis-NIR Spektroskopie. Weiterhin sind die rasterelektronenmikroskopischen Aufnahmen sowie die daraus extrahierten Partikelgrößenverteilung Teil dieser Diplomarbeit. Strukturelle Untersuchungen wie Textur, Orientierung, und Kristallographie sind nicht Teil der eigentlichen Diplomarbeit. Die Publikation wurde erst während der Promotion erstellt und veröffentlicht.</p> <p>Diese Ergebnisse der restlichen Publikationen sind nur im Zusammenhang mit dieser Arbeit zu diskutieren.</p> <p>Michael Kracker</p>				



Optical properties of self assembled oriented island evolution of ultra-thin gold layers

Christian Worsch, Michael Kracker, Wolfgang Wisniewski*, Christian Rüssel

Otto-Schott-Institut, Jena University, Fraunhoferstr. 6, 07743 Jena, Germany

ARTICLE INFO

Article history:

Received 19 September 2011

Received in revised form 23 February 2012

Accepted 7 March 2012

Available online 14 March 2012

Keywords:

Gold

Nanoparticles

Sputtering

Dewetting

Color

Electron backscatter diffraction

X-ray diffraction

Scanning electron microscopy

ABSTRACT

Gold layers with a thickness of only 8 to 21 nm were sputtered on soda-lime-silica glasses. Subsequent annealing at 300 and 400 °C for 1 and 24 h resulted in the formation of separated round gold particles with diameters from 8 to 200 nm. Crystal orientations were described using X-ray diffraction and electron backscatter diffraction. The gold particles are oriented with their (111) planes perpendicular to the surface. Most gold nano particles are single crystalline, some particles are twinned. Thermal annealing of sputtered gold layers resulted in purple samples with a coloration comparable to that of gold ruby glasses. The color can be controlled by the thickness of the sputtered gold layer and the annealing conditions. The simple method of gold film preparation and the annealing temperature dependent properties of the layers make them appropriate for practical applications.

© 2012 Elsevier B.V. All rights reserved.

1. Introduction

Materials containing nanoscale particles of gold have been produced for centuries. The oldest applications are the so called “gold ruby glasses” and corresponding glazes, where gold nano particles (GNP) with a size of a few nm are crystallized from a glassy matrix. This results in a red to purple coloration of the glass. The primary fundamental investigations of colloidal GNP and thin metallic films were performed over a century ago by Faraday [1] and Mie [2]. Subsequently, applications and optical properties of metal nano particles were widely studied in the past decade [3–9]. Today many optical effects associated with nanosized metal particles are well understood: the scattering of light and the optical absorption of GNP result from a collective oscillation of surface electrons, known as surface plasmons, which are excited by the incident electromagnetic radiation. For GNP with sizes from 5 to 100 nm, the resonance frequency of the surface plasmons corresponds to the visible and near infrared range of the electromagnetic spectrum [10], leading to an enhanced absorption and scattering at these wavelengths. There are many factors that affect the plasmon resonance frequency and the attributed absorption spectrum. Here, especially the size and shape of the GNP, the type of the supporting substrate and/or the surrounding material of the particles are to be mentioned. The distance between the particles is also relevant if it is small enough to enable electromagnetic coupling [11–15].

To summarize, the optical properties of GNP strongly depend on the structure and vary notably. This enables a large variety of different applications, such as catalysts [16], chemical [17] and plasmonic sensors [18], surface enhanced Raman scattering [19] and non-linear optics [20,21]. In addition, optical recordings [22] and plasmonic photovoltaic applications [23] are conceivable. For biological applications such as diagnosis and even destruction of microorganisms the GNP can be engineered to possess chemical and biological functionalities [24].

An easy way to utilize GNP is the application as thin layers on a substrate. GNP films are usually prepared by chemical precipitation [20,25,26], thermal evaporation [27,28] or sputtering [27,29]. Thermal annealing of thin metal films can lead to a disaggregation of the more or less dense film into particles [30], a process driven by the minimization of surface energy [31] and denoted as solid state dewetting. The dewetting starts at infinity or small surface fluctuations and results in the growth of holes. Surface fluctuations can be voids, thermal grooving at grain or twin boundaries, nucleation of vacancies at the film–substrate–interface or in areas of high local stress. It is assumed that the growth of a hole removes material from the edge of the hole via surface diffusion [32–34]. The varying distribution and agglomeration of holes result in irregular growth [35]. The growth of holes initially leads to a network structure as a neck of the film material is formed between adjacent holes [32]. The Rayleigh instability leads to a progressive thinning of these necks and results in the formation of discrete and isolated particles [36,37].

The crystallographic orientation of thin noble metal coatings and of nano particles of noble metals deposited on various, usually crystalline, substrate materials has been investigated but does not show consistent results [31,38–43].

* Corresponding author at: Fraunhoferstr. 6, 07743 Jena, Otto-Schott-Institut, Jena University, Germany. Tel.: +49 3641 948501; fax: +49 3641 948515.

E-mail address: wolfgang.w@uni-jena.de (W. Wisniewski).

The optical properties of GNP and small metal particles in general have already been the topic of a large number of publications. However, a technology to use layers containing GNP for decorative coatings is rarely described. A contribution to a possible “embedded” coating step, e.g. in an industrial float glass production line, seems to be possible.

This paper reports a simple and highly reproducible method for the fabrication of transparent materials with red coloration and adjustable light transmission. In the work presented here, float glasses served as substrates, providing a smooth, transparent, chemically inert, and inexpensive platform for a wide range of applications. Thin gold films with a thickness of only 8 to 21 nm were deposited. It is shown that the gold layers show a preferred crystallographic orientation. In a subsequent low-temperature annealing process these thin gold layers form well separated GNP. The resulting optical properties as well as the morphology and crystal orientation of the GNP are studied. A discrete texture is described using X-ray diffraction (XRD) and electron backscatter diffraction (EBSD). Twinning is also observed.

2. Experimental section

Substrates of soda–lime–silica glass sheets with a diameter of 7 mm and a thickness of 1 mm were used. The substrates were cleaned in a liquid composed of 58.1 vol.% distilled water, 29.2 vol.% isopropanol, 11.7 vol.%, 25 vol.% ammonia solution and 1 vol.% of a 15% aqueous tenside for 10 min at 65 °C in an ultrasonic bath. Subsequently they were rinsed with distilled water and placed in the ultrasonic bath for another 15 min after which the samples were dried at 110 °C for 1 h.

Gold layers were sputtered using a planar magnetron with a 50 mm gold target. The following parameters were kept constant during the coating procedure: the target–substrate–distance (55 mm), the prevacuum (<1 mPa), the current (100 mA), the resulting voltage (250 V) and the argon pressure (2.13 Pa). The ratio between the substrate temperature and the melting point of gold (T/T_m) was 0.22. A deposition time of 5 to 15 s was used.

Annealing was carried out in a muffle furnace at 300 and 400 °C. The unheated samples were transferred into the furnace preheated to the desired temperature and annealed for 1 and 24 h.

The samples were studied using a scanning electron microscope (SEM) Jeol JSM-7001F FEG-SEM equipped with a TSL Digiview 1913 EBSD-Camera and the software TSL OIM Data Collection 5.31 and TSL OIM Analysis 5. A thin coat of carbon was applied at about 10^{-3} Pa to enhance the surface conductivity for EBSD-analysis which was performed using an accelerating voltage of 20 kV, 1.6 nA emission current and a EBSD-pattern resolution of 234×234 pixels (binning 4×4). A short introduction on EBSD and relevant tools of describing EBSD-results such as the Confidence Index (CI) and the Inverse Pole Figure (IPF) was previously published [44].

The particle size and Feret-ratio of the GNP were determined from SEM-micrographs. The Feret-ratio describes for ellipsoidal particles the ratio semi-minor to semi-major of a particle (a ratio of 1 equates a sphere). X-ray diffraction was performed in a Siemens D5000 using $\text{CuK}\alpha$ -radiation in a Bragg–Brentano $2\theta/\theta$ setup. UV–vis–NIR spectra of wavelengths from 400 to 1000 nm were recorded (UV–vis–NIR spectrometer, TRIAX 320, ISA Jobin Yvon Spex Instruments S.A.). A scanner (CanoScan 8800f, Canon) was used to visualize the color of the gold layers. To illustrate the color of the transmitted light, the samples were scanned with the transmitted light function of the scanner while the color of the backscattered light was visualized by scanning with a black background (backscattered light). The samples were scanned with a white background to illustrate the visual color (visual). The latter is composed of the double transmitted and the backscattered light.

3. Results and discussion

Sputtering gold onto the glass substrates leads to the formation of gold layers, the layer thickness varies with the deposition time. Fig. 1 presents SEM micrographs of layers with thickness of 8, 16 and 21 nm showing a typical percolating structure with voids and flaws. The structure coarsens with increasing layer thickness. Although the freshly sputtered gold layers show numerous cracks, the layers are continuous and the structure is above the percolation threshold, i.e. continuous metallic paths over the surface occur [45].

After annealing for 1 h at 400 °C the gold layers have dewetted and transformed into well separated particles with sizes of 17 ± 8 ,

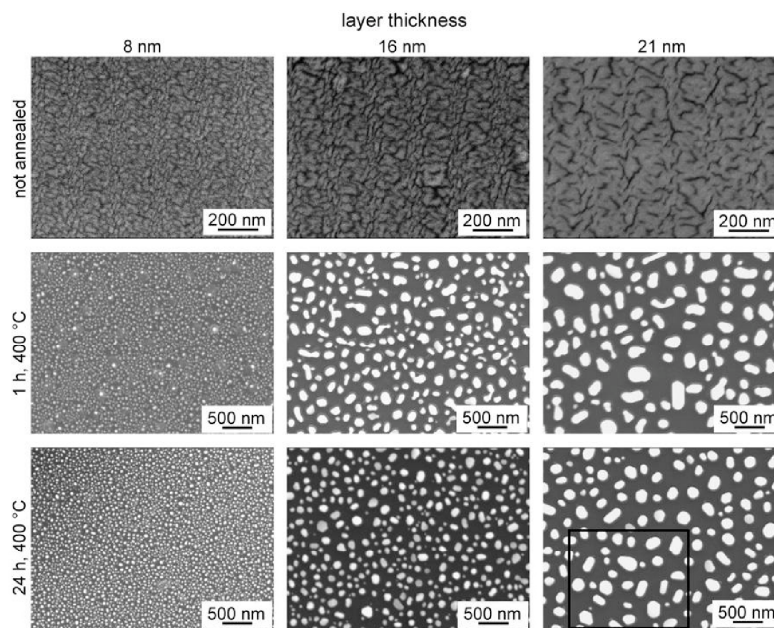


Fig. 1. SEM-micrographs of freshly sputtered and annealed gold layers. The black frame outlines the area presented in Fig. 2.

Table 1
Particle size and Feret ratio of the GNP from gold layers with a thickness of 8 to 21 nm after dewetting using different annealing times and temperatures.

Annealing time	Annealing temperature Layer thickness	300 °C			400 °C		
		8 nm	16 nm	21 nm	8 nm	16 nm	21 nm
1 h	Particle size	28 nm ± 16 nm	112 nm ± 55 nm	133 nm ± 56 nm	17 nm ± 8 nm	124 nm ± 39 nm	189 nm ± 55 nm
	Feret ratio	0.74 ± 0.1	0.72 ± 0.1	0.74 ± 0.1	0.75 ± 0.1	0.71 ± 0.1	0.69 ± 0.1
24 h	Particle size	33 nm ± 13 nm	80 nm ± 38 nm	241 nm ± 76 nm	36 nm ± 13 nm	88 nm ± 36 nm	167 nm ± 47 nm
	Feret ratio	0.8 ± 0.1	0.75 ± 0.1	0.71 ± 0.2	0.8 ± 0.1	0.8 ± 0.1	0.78 ± 0.1

124 ± 39 and 189 ± 55 nm respectively. Table 1 summarizes the average particle size and corresponding Feret ratio depending on the thickness of the former gold layer and the annealing time at 300 and 400 °C. The given errors are standard deviations. Increasing layer thickness results in an increased GNP-size after annealing. The size and number of the particles in layers annealed for 24 h at 400 °C are approximately the same as in layers annealed for 1 h at the same temperature, indicating the annealing time is of minor importance to the particle size. The Feret ratio of the particles ranges from 0.69 to 0.80. Annealing at higher temperatures and/or annealing times seems to result in larger Feret ratios in most cases. This indicates the shape of the GNP approaches a circle in a 2-D-view, which is a result of the decay of prolate particles and the effect that particles of irregular shape become increasingly spherical due to surface minimization [36,37]. In contrast, the particles tend to form facets at larger annealing times instead of becoming increasingly spherical, leading to the straight edges outlined in Fig. 2. Similar structures were also observed in GNP presented in Ref. [25].

In agreement to the literature [31], annealing the gold coated glass samples resulted in the dewetting of the gold layers and the formation of well separated gold particles. During the process, the fraction of glass/gold interface decreases, while the fraction of glass/atmosphere interface is increased. The amount of gold/atmosphere interface should decrease during annealing, thus, decreasing the total interface energy, which is the driving force for the formation of discrete clusters [25]. Reducing the thickness of the sputtered gold layer reduces the critical size of the structural fluctuations necessary to initiate the dewetting process [46]. Hence, thin layers contain a larger number of stable starting points for the growth of voids, leading to a larger number of small particles. By contrast, the dewetting starts at fewer and larger available voids in thicker layers, resulting in a longer growth phase and increasing the void size before the formed holes meet and coalesce, separating the layer into discrete particles [46].

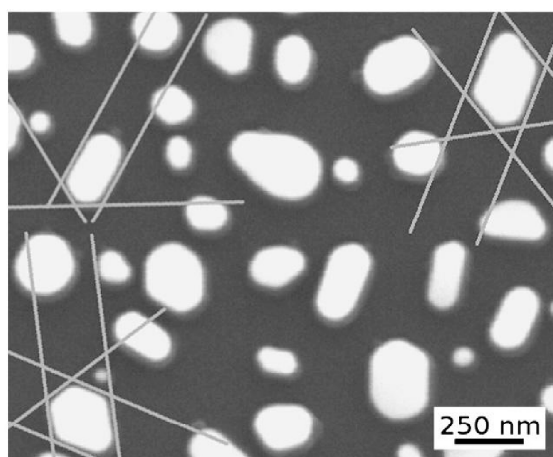


Fig. 2. SEM-micrograph of the area marked by the black frame in Fig. 1: a gold layer annealed at 400 °C for 24 h (higher magnification). Faceting of GNP is indicated by the superimposed lines.

Thus the particles as well as their interspaces are larger. Higher temperatures promote surface diffusion, accelerating the dewetting process.

The vis-NIR-spectra of freshly sputtered as well as annealed gold layers with a thickness of 8 to 21 nm are shown in Fig. 3. A decrease in the transmission is observed with increasing thickness of the gold layers. The sputtered 8 nm gold layer showed a transmission maximum at 500 nm and a transmission minimum at 700 nm. Both values are shifted to larger wavelengths with increasing layer thickness. The spectra of gold layers annealed for 24 h at 400 °C show a higher transmission at wavelengths larger than 700 nm compared to the freshly sputtered layers. The spectrum obtained from the annealed 8 nm gold layer shows a minimum of the transmitted light at a wavelength of 545 nm. This is caused by a plasmon resonance [47]. Increasing the thickness of the initial gold layer leads to a shift of this minimum to larger wavelengths and a broadening of the peak.

The visual color of the freshly sputtered gold layers is shown in Fig. 4 a–c. It is green and increases in intensity with an increasing layer thickness. The transmitted light is turquoise and becomes darker with an increasing layer thickness (Fig. 4 d–f). The optical properties of the freshly sputtered gold layers are governed by the dielectric function of gold [48]. A low absorption at a wavelength of about 500 nm results in the green color of the layers presented in Fig. 4 a–c. Diffuse scattering does not occur at the continuous gold layers, leaving the images of the backscattered light black in Fig. 4 g–i.

Fig. 4 k–n shows the colors of the gold layers after annealing them for 1 h at 400 °C. The annealed 8 nm gold layer is purple to the naked eye in Fig. 4 k. The transmitted light is also purple, but less intense (Fig. 4 o) while the image of the backscattered light is black in Fig. 4 r, indicating the small particles (<40 nm) do not lead to significant light scattering [2].

To the naked eye, the annealed 16 and 21 nm layers are purple-violet in Fig. 4 m and n, whereas the transmitted light in Fig. 4 p and q is blue with a touch of purple in Fig. 4 p. For particles larger than 80 nm, the red-shift of the absorbance peak results in a higher

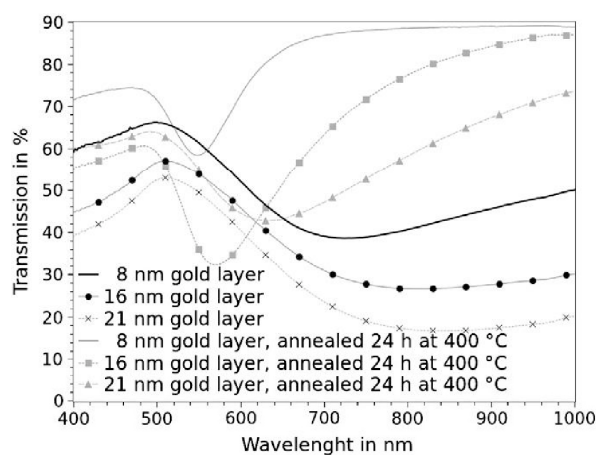


Fig. 3. Vis-NIR spectra of freshly sputtered and subsequently annealed gold layers.

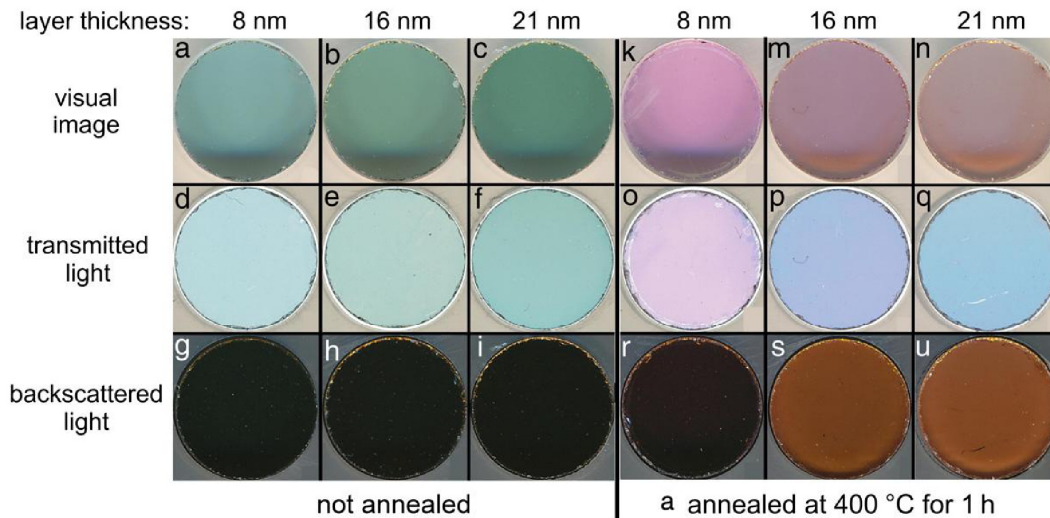


Fig. 4. Images obtained with a flatbed scanner of freshly sputtered and annealed (for 1 h at 400 °C) samples: visual image (a–c for freshly sputtered films and k–n for annealed films), transmitted light (d–f and o–q) and the color of the backscattered light (g–i and r–u).

transmission at wavelengths <550 nm, while the light scattering increases at wavelengths >600 nm. The scattered light of both samples in Fig. 4 s and u is orange-red. An increase in the NIR absorption and a red shift of the absorption maximum is observed with an increasing particle diameter [2] (also see Fig. 3). Because the visual color of the layers is caused by the superposition of the double transmitted light and the backscattered light, the visual color of the annealed 8 nm sample is more intense, as scattering does not occur significantly (see Fig. 4 r) due to the small particles. The layers where scattering does occur are purple-violet, which is a superposition of the blue transmitted light (Fig. 4 p and q) and the orange backscattered light (Fig. 4 s and u).

Using a flat bed scanner is a simple method to illustrate the color of the GNP layers. This method provides the color of the transmitted and the reflected light as well as their superposition. In comparison to other techniques [8], the terms of exposure are very constant and show a high color reproduction. This allows an accurate description of the visual optical effects of GNP layers, which is important for the coloring of surfaces. The color perception of the human eye is only a slightly effected by the annealing time. The change of color at the applied annealing temperature of 400 °C is completed within 1 h.

Other parameters besides the particle size significantly affect the optical properties of the GNP. The shape of the particles (parallel or perpendicular to the substrate surface), their distance and the dielectric properties of the phases they are in contact with, must be mentioned here [49].

The XRD-patterns obtained from a fresh 21 nm gold layer and after annealing for 24 h at 400 °C are presented in Fig. 5 along with the theoretical pattern of gold for comparison. Only a single, low intensity peak attributable to the 111-peak of gold is observed in the pattern of the freshly sputtered gold layer. The peak is notably broadened due to small crystallites. Using the Scherrer equation [50], the mean crystallite size calculated from XRD-line broadening is 13 nm. As gold is the only crystalline phase in the system and the 111-peak is the only observed peak, it can be concluded that the gold particles are preferably oriented with their crystallographic [111]-direction perpendicular to the surface. This has already been reported for sputtered layers of gold and other metals with cubic face centered structures on crystalline substrates [6]. It should be noted that according to Ref. [51] gold layers sputtered at a temperature of around $0.22 T_m$ (melting temperature) exhibit twin boundaries.

After annealing, only the 111- and 222-reflexes of gold appear in the XRD-pattern in Fig. 5, indicating the preferred orientation is still present. The thermally annealed GNP were also analyzed by EBSD. Fig. 5 shows an SEM-micrograph of the surface superimposed by the approximate frame of the EBSD-scan performed with a step size of 40 nm covering an area of $6.45 \mu\text{m}^2$. Reducing the step size below 40 nm under the applied parameters led to the destruction of the substrate material, thus limiting the spatial resolution for EBSD-scans of these samples. The distortion of the frame is a result of the geometrical setup in the SEM. The glass substrate and unreliably indexed patterns were excluded; only points with a minimum CI-value of 0.100 were evaluated. The resulting IPF-map of the scan is also presented in Fig. 6 where blue colors (see colored online document) indicate a 111-orientation is predominant. The frames 1 and 2 in Fig. 6 mark areas where the gold particles are not mono crystalline, i. e. different sectors of a gold particle show different orientations which fulfill the conditions of a first-order twin boundary ($\Sigma 3$, rotation around 111-direction by 60°). The occurrence of $\Sigma 3$ twin boundaries has been previously described for GNP dewetted on Si-wafers using EBSD [52].

Twinning usually serves the purpose of stress relaxation [53] and its existence indicates some type of stress occurring either during

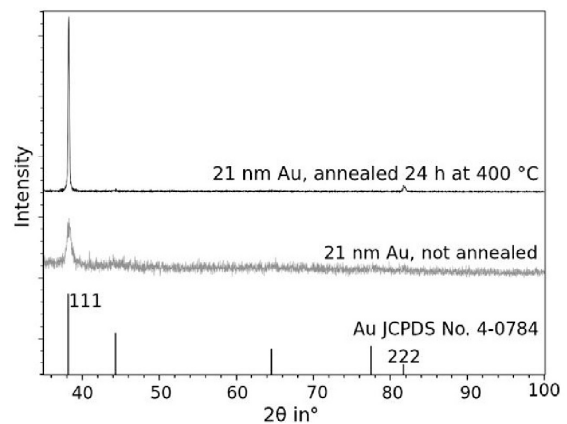


Fig. 5. XRD-pattern of a freshly sputtered, 21 nm thick gold layer and of the same sample after annealing for 24 h at 400 °C.

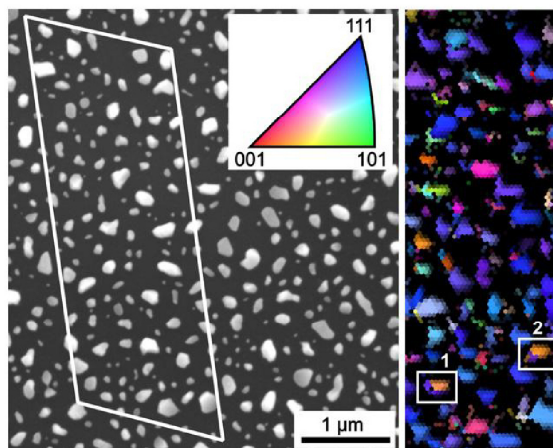


Fig. 6. SEM-micrograph of the annealed surface superimposed by a frame indicating where an EBSD-scan was performed. The IPF-map of the scan performed with a step size of 40 nm is presented. The GNP 1 and 2 show twinning.

dewetting or, in principle, also during the cooling of the sample. The latter might occur due to the mismatch in the thermal expansion coefficients of gold and the substrate. The XRD-data presented here indicate that the texture of the initial layers increases during the dewetting process, which is in agreement to previous studies of gold layers on single crystals [31,41,43].

Fig. 7 a shows the equal area 111-pole figure of the scan featured in Fig. 6 confirming the impression of a preferred orientation gained from the IPF-map of the scan and the XRD-data presented in Fig. 5. If larger areas with more particles are scanned, the texture appears more homogenous (see Fig. 7 b which is the equal area 111-pole figure of a scan covering 248.19 μm² scanned with a step size of 50 nm). This image indicates, that most grains of gold show an orientation with the [111]-direction perpendicular to the substrate (or the (111)-plane parallel to the substrate) with a deviation up to ±5° from the substrate normal. The homogeneous ring observed at an angle of 70° results from the other (111)-planes, since the (111) lattice planes enclose an angle of 70.5° in a cubic symmetry and indicates that the rotation around the [111]-direction perpendicular to the surface is random. This corresponds to previous measurements where the homogeneity of the ring also increased with a growing number of analyzed GNP [52].

The [111]-orientation of the GNP has already been described via XRD and EBSD-measurements of dewetted gold layers formed on

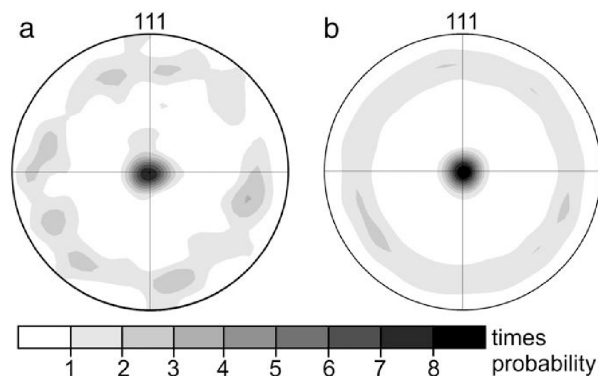


Fig. 7. Equal area 111-pole figures of a) the scan featured in Fig. 6 covering 6.45 μm² and b) of a scan covering 248.19 μm².

silicon wafers [31]. It must be noted that the structures featured in this publication are significantly smaller and grown from thinner layers of gold. Except for the rarely occurring twin boundaries, grain boundaries are not observed in the gold layers; the gold particles are single crystals. Epitaxial growth can be excluded as the reason for the observed texture because an amorphous substrate was used in the present studies. The crystallographical texture of the gold particles on an amorphous substrate is observed. The gold particles are formed during a self assembling process where the driving force is the minimization of the total interfacial energies. In Ref. [54] sputtered and subsequently annealed gold layers were studied on glasses using X-ray diffraction and electrical measurements, however, the optical transmission as well as electron microscopy was not reported.

Thermal evaporation and wet chemical deposition are commonly preferred techniques for the deposition of gold and GNP. Sputtering, however, is a coating technology commonly used in an industrial scale, e.g. for float glasses. This paper provides the description of the process of thermal dewetting applied to thin sputtered gold films on glass substrates. The respective optical properties and crystallographic orientations of the sputtered layers, as well as the GNP resulting from the dewetting process, are described and discussed. The process of producing GNP layers is quite flexible and could principally be applied off-line or at the end of an existing float glass production line.

4. Conclusion

A simple, inexpensive, and highly reproducible method to fabricate GNP layers of various colors is presented. Gold layers with a thickness of 8, 16 and 21 nm were sputtered on soda-lime-silica glass and annealed at 300 and 400 °C. This resulted in dewetting of the gold layers and subsequently in the formation of well separated gold nano particles with an average diameter from 17 to 200 nm. Thicker gold layers led to larger particles. Higher annealing temperatures resulted in a faster dewetting process and a tendency of the GNP to facet. Increasing the annealing time from 1 to 24 h did not significantly affect the structure of the annealed samples. Layers composed of GNP with sizes smaller than 40 nm show a maximum light absorption at 550 nm caused by plasmon resonance and do not show light scattering. These samples have a purple coloration. GNP with a size of >80 nm show light scattering at wavelengths >600 nm while the plasmon resonance peak is broader and shifted toward larger wavelengths. This results in a blue color in transmission, an orange-red color of the scattered light and subsequently to a purple-violet color in their superposition. The color of the layers can be adjusted by the layer thickness and the annealing temperature. XRD and EBSD were used to prove a crystallographic texture of the GNP with the [111]-direction perpendicular to the surface. Most GNP are single crystals but twinning was observed as well. The described process allows the production of GNP layers with tailored optical properties for transmission and reflection of light and enables the easy production of materials with tunable colors and reflectivity on standard float glasses.

References

- [1] M. Faraday, *Philos. Trans. R. Soc. London* 147 (1857) 145.
- [2] G. Mie, *Ann. Phys. (Berlin)* 25 (1908) 377.
- [3] J.Z. Euler, *J. Phys.* 137 (1954) 318.
- [4] U. Kreibitz, *J. Phys. F: Met. Phys.* 4 (1974) 999.
- [5] S. Norrman, T. Andersson, C.G. Granqvist, *Phys. Rev. B* 18 (1978) 674.
- [6] J.A. Thornton, *J. Vac. Sci. Technol. A* 4 (1986) 3059.
- [7] J.A. Creighton, D.G. Eadon, *J. Chem. Soc. Faraday Trans.* 87 (1991) 3881.
- [8] T. Ung, L.M. Liz-Marzán, P. Mulvaney, *Colloids Surf. A* 202 (2002) 119.
- [9] T. Karakouz, D. Holder, M. Gomanovsky, A. Vaskevich, I. Rubinstein, *Chem. Mater.* 21 (2009) 5875.
- [10] R. Gupta, M.J. Dyer, W.A. Weimer, *J. Appl. Phys.* 92 (2002) 5264.
- [11] G. De, S. Bhattacharya, *J. Mater. Chem.* 18 (2008) 2816.
- [12] K.L. Kelly, E. Coronado, L.L. Zhao, G.C. Schatz, *J. Phys. Chem.* 107 (2003) 668.

- [13] G. Gupta, D. Tanaka, Y. Ito, D. Shibata, M. Shimojo, K. Furuya, K. Mitsui, K. Kajikawa, *Nanotechnology* 20 (2009) 025703.
- [14] E. Hutter, J.H. Fendler, *Adv. Mater.* 16 (2004) 1685.
- [15] M.A. Garcia, S. Paje, J. Llopis, *Chem. Phys. Lett.* 315 (1999) 313.
- [16] M.S. Chen, D.W. Goodman, *Acc. Chem. Res.* 39 (2006) 739.
- [17] A.M. Ruiz, A. Cornet, K. Shimanoe, J.R. Morante, N. Yamazoe, *Sens. Actuators B* 109 (2005) 7.
- [18] C. de Julián Fernández, M.G. Manera, J. Spadavecchia, G. Maggioni, *Sens. Actuators B* 111 (2005) 225.
- [19] C. Hrelescu, F.K. San, A.F. Rogach, F. Jackel, J. Feldmann, *J. Appl. Phys. Lett.* 94 (2009) 153113.
- [20] N. Venkatram, R.S.S. Kumar, D.N. Rao, S.K. Medda, S. De, G. De, J. *Nanosci. Nanotechnol.* 6 (2006) 1990.
- [21] Y. Hosaya, T. Suga, T. Yanagawa, Y. Kurokawa, *J. Appl. Phys.* 81 (1997) 1475.
- [22] P. Zijlstra, J.W.M. Chon, M. Gu, *Nature* 459 (2009) 410.
- [23] S. Pillai, K.R. Catchpole, T. Trupke, M.A. Green, *J. Appl. Phys.* 101 (2007) 093105.
- [24] D. Pissuwan, C.H. Cortie, S.M. Valenzuela, M.B. Cortie, *Trends Biotechnol.* 28 (2010) 207.
- [25] I.U. Vakarelski, R. Maenosono, J.W. Kwek, K. Higashitani, *Colloids Surf. A* 340 (2009) 193.
- [26] C.S. Kealley, M.B. Cortie, A.I. Maarouf, X. Xu, *Phys. Chem. Chem. Phys.* 11 (2009) 5897.
- [27] C.G. Granqvist, O. Hunderi, *Phys. Rev. B* 16 (1977) 3513.
- [28] D. Porath, J.I. Gersten, O. Millo, *J. Vac. Sci. Technol.* 14 (1996) 30.
- [29] F. Parmigiani, S. Samoggia, G.P. Ferrais, *J. Appl. Phys.* 57 (1985) 2524.
- [30] C. Schrank, C. Eisenmenger-Sittner, E. Neubauer, H. Bangert, A. Bergauer, *Thin Solid Films* 459 (2004) 276.
- [31] C.M. Müller, R. Spolenak, *Acta Mater.* 58 (2010) 6035.
- [32] R. Brandon, F. Bradshaw, Technical Report No. 66095, 1966.
- [33] A.E.B. Presland, G.L. Price, D.L. Trimm, *Surf. Sci.* 3 (1972) 63.
- [34] A.E.B. Presland, G.L. Price, D.L. Trimm, *Surf. Sci.* 29 (1972) 435.
- [35] E. Jiran, C.V. Thompson, *J. Electron. Mater.* 19 (1990) 1153.
- [36] M.S.R. Khan, *Bull. Mater. Sci.* 9 (1987) 5.
- [37] M.E.T. Molaes, A.G. Balogh, T.W. Cornelius, *Appl. Phys. Lett.* 85 (2004) 5337.
- [38] J.R. White, *Thin Solid Films* 22 (1974) 23.
- [39] K. Lee, J.T. Lue, *Appl. Opt.* 27 (1988) 1210.
- [40] K.C. Lee, N.H. Kim, B.-H. O, H.W. Kim, *Mater. Sci. Forum* 475 (2005) 3923.
- [41] X. Hu, T. Wang, S. Dong, *J. Colloid Interface Sci.* 316 (2007) 947.
- [42] P. Sangpour, O. Akhavan, A.Z. Moshfegh, M. Roozbeh, *Appl. Surf. Sci.* 254 (2007) 286.
- [43] A. Proszynski, D. Chocyk, G. Gladyszewski, *Opt. Appl.* 4 (2009) 705.
- [44] W. Wisniewski, R. Harizanova, G. Völksch, C. Rüssel, *CrystEngComm* 13 (2011) 4025.
- [45] M. Hövel, B. Gompf, M. Dressel, *Phys. Rev. B* 81 (2010) 035402.
- [46] M. Lanxner, C.L. Bauer, R. Scholz, *Thin Solid Films* 150 (1987) 323.
- [47] U. Kreibig, M. Vollmer, *Optical Properties of Metal Clusters*, Springer Series in Material Science, New York, Berlin, Heidelberg, 1995.
- [48] C.G. Olson, *CRC Handbook of Chemistry and Physics*, 91nd. ed. CRC Press, Boca Raton, London, New York, 2010.
- [49] U. Kreibig, L. Genzel, *Surf. Sci.* 156 (1985) 678.
- [50] H.P. Klug, L.E. Alexander, *X-ray Diffraction Procedures for Polycrystalline and Amorphous Materials*, Wiley, New York, 1954.
- [51] J.A. Thornton, *J. Vac. Sci. Technol.* 12 (1975) 830.
- [52] M. Bechelany, X. Maeder, J. Riesterer, J. Hankache, D. Lerosé, S. Christiansen, J.I. Michler, L. Philippe, *Cryst. Growth Des.* 10 (2010) 587.
- [53] G. Gottstein, *Physikalische Grundlagen der Materialkunde*, 3rd ed., Springer-Verlag, Berlin, Heidelberg, New York, 2007.
- [54] V. Švorčík, J. Siegel, P. Šutta, J. Mistrík, P. Janíček, P. Worsch, Z. Kolská, *Appl. Phys. A* 102 (2011) 605.

3.2

C. Worsch, W. Wisniewski, M. Kracker, C. Rüssel

Gold nano-particles fixed on glass

Applied Surface Science, 258 (2012) 8506–8513

DOI: <http://dx.doi.org/10.1016/j.apsusc.2012.05.010>

Gold nano-particles fixed on glass				
Beteiligt an				
	Dr. Christian Worsch	Dr. Wolfgang Wisniewski	Michael Kracker	Prof. Christian Rüssel
Konzeption des Forschungsansatzes	X			X
Planung der Untersuchung	X			
Datenerhebung	X	X	X	
Datenanalyse und Interpretation	X	X	X	
Schreiben des Manuskripts	X	X	X	X
Vorschlag Anrechnung Publikationsäquivalente			0,75	



Gold nano-particles fixed on glass

Christian Worsch, Wolfgang Wisniewski*, Michael Kracker, Christian Rüssel

Otto-Schott-Institut, Universität Jena, Fraunhoferstr. 6, 07743 Jena, Germany

ARTICLE INFO

Article history:

Received 19 October 2011
Received in revised form 25 April 2012
Accepted 1 May 2012
Available online 9 May 2012

Keywords:

Gold–ruby coatings
Sputtering
CCVD
Wear resistant
EBSD

ABSTRACT

A simple process for producing wear resistant gold nano-particle coatings on transparent substrates is proposed. Soda–lime–silica glasses were sputtered with gold and subsequently coated with SiO₂ using a combustion chemical vapor deposition technique. Some samples were first coated with silica, sputtered with gold and then coated with a second layer of silica. The samples were annealed for 20 min at either 550 or 600 °C. This resulted in the formation of round, well separated gold nano-particles with sizes from 15 to 200 nm. The color of the coated glass was equivalent to that of gold–ruby glasses. Silica/gold/silica coatings annealed at 600 °C for 20 min were strongly adherent and scratch resistant. X-ray diffraction and electron backscatter diffraction (EBSD) were used to describe the crystal orientations of the embedded particles. The gold particles are preferably oriented with their (1 1 1) planes perpendicular to the surface.

© 2012 Elsevier B.V. All rights reserved.

1. Introduction

Gold nano-particles (GNP) are currently used for a large variety of purposes. Among these are applications as catalysts [1], chemical [2] and plasmonic sensors [3], as well as Surface Enhanced Raman Scattering (SERS) [4] and non-linear optics [5,6]. Furthermore, biological applications such as diagnosis and even destruction of microorganisms should be mentioned [7]. Although GNP are a priori biologically inert, they can be engineered to possess chemical and biological functionality.

GNP exhibit a plasmon resonance (PR), which occurs at wavelengths from 510 to 580 nm [8] leading to enhanced absorption and scattering in this part of the spectrum. The PR is affected by the size and shape of the GNP, the type of the supporting substrate (mainly its refractive index) and/or the surrounding material of the particles. The distance between the particles is also relevant if it is small enough to enable electromagnetic coupling [9–11].

Layers of GNP are usually prepared by precipitation from aqueous solutions [6,12,13] on various materials, e.g. on etched glass surfaces [13–15]. Thermal annealing of thin gold films produced by thermal evaporation [16,17] or sputtering [11,16] can also lead to a disaggregation into particles [18].

The formation of GNP from continuous gold layers is driven by the minimization of surface energy and is denoted as solid state dewetting [19]. All the described methods suffer from the poor adhesion of GNP to the substrate surface.

GNP crystallized inside a glassy matrix may lead to a red to purple coloration (gold–ruby glasses) and have been produced for centuries. Gold–ruby coatings on glasses prepared by the sol–gel method result in the formation of a layer, e.g. consisting of an Al₂O₃ [9] or SiO₂–matrix [20–22] surrounding the GNP.

This paper reports on a new route where float glass substrates are sputtered with gold layers and covered or embedded in silica layers using the combustion chemical vapor deposition (CCVD) of SiO₂. Finally, these layer systems are thermally annealed to produce wear resistant, discretely textured GNP embedded in an amorphous matrix. This method for the fabrication of transparent materials with gold–ruby coloration and adjustable light transmission could be interesting for (nonlinear) optical and sensoric applications.

2. Experimental procedure

Samples of soda–lime–silica glass with a diameter of 7 mm and 1 mm thick were used as substrates. The substrates were cleaned in a liquid composed of 58.1 vol% distilled water, 29.2 vol% isopropanol, 11.7 vol% ammonia solution (25%) and 1 vol% aqueous tenside (15%) for 10 min at 65 °C in an ultrasonic bath. Afterwards, the substrates were rinsed with distilled water, placed in the ultrasonic bath for another 15 min and subsequently dried at 100 °C for 1 h.

The silica coatings were deposited via CCVD using a commercial flame coating device (Pyrosil® Flame coating device GVE, SURA Instruments GmbH, Jena, Germany). The device contains a burner and a base unit holding two gas cartridges to enable a continuous operation. The burner was mounted on a linear motion unit (Jenaer Antriebstechnik GmbH, Jena, Germany) to improve the

* Corresponding author. Tel.: +49 03641 948501; fax: +49 03641 948515.
E-mail address: wolfgang.w@uni-jena.de (W. Wisniewski).

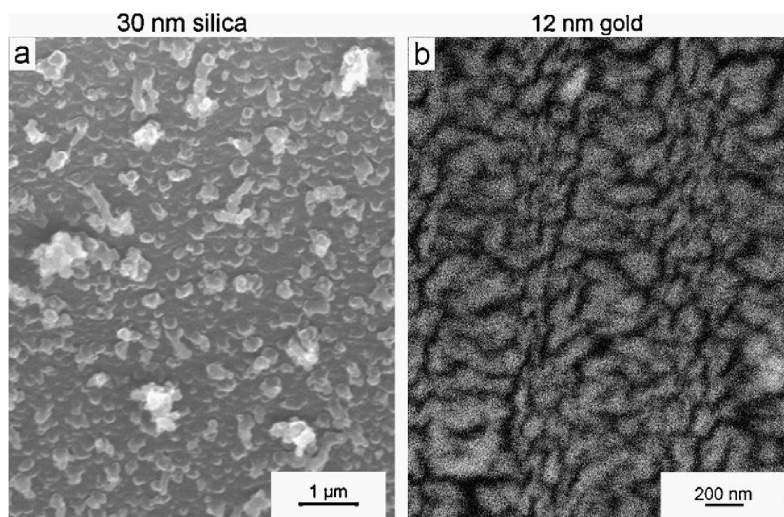


Fig. 1. SEM-micrograph of (a) a 30 nm thick silica layer deposited with CCVD and (b) a freshly sputtered gold layer with a thickness of 12 nm.

reproducibility and moved across the substrate. During the experiments, all parameters such as gas pressure, distance burner/substrate and burner velocity were kept constant. In the applied process, propane was used as carrier gas (100 kPa pressure) with a constant concentration of tetramethylsilane. The distance burner/substrate was 7 mm. The temperature of the flame was about 1300 °C and the burner velocity was 100 mm/s. Five passes of the burner were applied for each silica layer. A detailed description of the experimental procedure is given in Ref. [23].

A planar magnetron with a 50 mm gold target was used to sputter gold with the following constant parameters: target–substrate–distance (55 mm), prevacuum (<1 mPa), current (100 mA), voltage (250 V), the argon pressure for coating (2.13 Pa) and the deposition time (10 s). Two types of coating systems were applied: a two-layer gold/silica and a three-layer silica/gold/silica system where the respective layers are 12 nm (gold) and 30 nm (silica) thick. Both layer systems were also performed with slightly thicker gold coatings (17 nm) in order to facilitate EBSD analysis.

The samples were annealed in a muffle furnace at temperatures of 550 and 600 °C. The temperature was increased linearly from room temperature to the annealing temperatures within 45 min and the temperature was held for 20 min.

The samples were investigated using scanning electron microscopy (Jeol JSM-7001 F FEG-SEM). All micrographs were obtained with an Everhart-Thornley detector and an accelerating voltage of 15 kV. EBSD-patterns were recorded using a TSL Digiview 1913 EBSD-Camera and an accelerating voltage of 20 kV. Individual patterns were obtained with a binning of 2×2 (e.g. a camera resolution of 468×468 pixels) using a current of 4.55 nA and an exposure time of 0.45 s. Scans were performed with a binning of 4×4 (e.g. a camera resolution of 234×234 pixels) using a current of 1.7 nA and an exposure time of 0.23 s.

UV–vis–NIR spectra were recorded for wavelengths from 400 to 1000 nm (UV–vis–NIR spectrometer, TRIAX 320, ISA Jobin Yvon Spex Instruments S.A.).

3. Results

Fig. 1a shows the SEM micrograph of a silica layer deposited on a glass substrate via CCVD containing particles of about 40 nm and agglomerations with sizes up to 500 nm. To the naked eye, the

sample is fully transparent and no obvious difference to an uncoated substrate is observed. The surface of a glass substrate sputtered with gold is shown in Fig. 1b which shows a typical percolated gold layer with voids and flaws [25].

Fig. 2a–f present micrographs obtained from the respective layer systems after applying the stated annealing conditions. The gold/silica layer system is shown in Fig. 2a, which shows a particle-like structure of the silica-layer superimposed by the percolated structure of the gold layer. A similar structure is observed in the silica/gold/silica layer system (see Fig. 2b). The silica layers are barely visible and only larger particles appear. Micrographs of the gold/silica layers annealed for 20 min at 550° are shown in Fig. 2c containing bright, unshaped or branched structures with sizes from 200 to 600 nm. Fig. 2d shows a micrograph of the silica/gold/silica system annealed at a temperature of 550 °C for 20 min. Here, bright particles with a size of 200–500 nm are visible. In comparison to Fig. 2c bright, unshaped or branched structures exist, but in a finer form. In both Fig. 2c and d some darker, agglomerated, particle-like structures with sizes of approximately 50 nm are visible. Fig. 2e and f show the surfaces after annealing the layer systems for 20 min at 600 °C. Particles of bright appearance with sizes from 30 to 300 nm occur in the gold/silica coated sample. The silica/gold/silica coated sample shows smaller particles with sizes from 15 to 200 nm. Furthermore, some darker, agglomerated, particle-like structures similar to those in Fig. 2c and d are observed in both figures. All the annealed layer systems have an excellent adhesion to the glass substrate and the samples annealed at 600 °C display an enhanced scratch resistance.

Fig. 3a and b shows the framed areas in Fig. 2 with a higher magnification. In addition to the bright, branched structures observed in Fig. 2c, a darker, agglomerated, particle-like structure with particle sizes around 50 nm is visible in Fig. 3a. This structure also occurs in the bright areas, where the edges are clearly of enhanced contrast. Fig. 3b shows a similar particle-like structure comparable to that shown in Fig. 3a, especially within the bright areas.

To the naked eye, the gold/silica layer annealed for 20 min at 550 °C shows a slight blue–turquoise color in transmission, while the scattered light is orange–red. After annealing at 600 °C, the sample is slightly bluish–purple. The silica/gold/silica layer annealed at 550 °C is green while the sample annealed at 600 °C is purple and

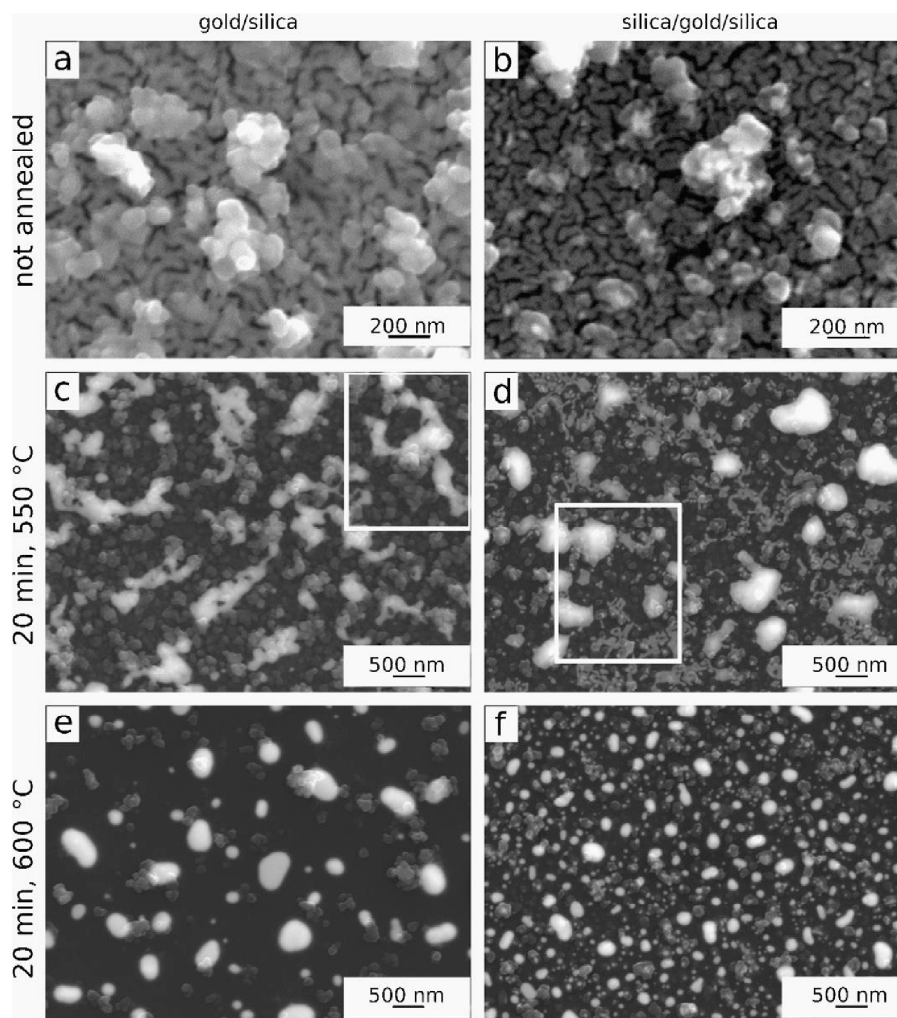


Fig. 2. SEM-micrographs of (a) the gold/silica and (b) the silica/gold/silica layer system without annealing. The surfaces of layer systems annealed for 20 min at 550 (c and d) and 600 °C (e and f) are also presented. The white frames in (c and d) outline the areas presented in Fig. 3.

blue–purple in transmission. To the naked eye the scattered light is slightly red.

Fig. 4 presents UV–vis–NIR spectra of the respective samples. The gold/silica layer shows a transmission maximum at 515 nm and a transmission minimum at 850 nm. Annealing the layer for 20 min at 550 °C increased the transmission, notably at wavelengths >550 nm. The maximum transmission is shifted towards smaller wavelengths by increasing the annealing temperature. The spectra of the silica/gold/silica layers show a maximum transmission at 500 nm and a minimum transmission at 755 nm. In comparison, annealing for 20 min at 550 °C results in an increase of light transmission and the spectrum shows a second minimum at about 540 nm. The silica/gold/silica layer shows a minimum transmission at 570 nm after annealing for 20 min at 600 °C and a high NIR transmission. As before, the maximum of the transmission is also shifted towards smaller wavelengths by increasing the annealing temperature.

The XRD-patterns obtained from a freshly sputtered 12 nm gold layer and a silica/gold/silica layer system annealed for 20 min at 600 °C are presented in Fig. 5 along with the theoretical

XRD-pattern of gold for comparison (JCPDS no. 4-0784). Both the freshly sputtered gold layer and the annealed layer system only show a single, broadened peak attributable to the 1 1 1-peak of gold, justifying the conclusion that it is of increased intensity. Using the Scherrer equation, the mean crystallite size calculated from XRD-line broadening is 100 ± 8 nm.

During EBSD-analysis, the samples were destroyed if the energy input of a scan (ratio between step size, current and exposure time) was chosen too high. Fig. 6 presents the surface of a GNP covered substrate after such a scan had been performed. Fig. 7 presents an overview of EBSD-patterns acquired from GNP in the respective layer systems. All patterns were acquired with a binning of 2×2 for better quality although this binning was not suitable for scanning as it always lead to sample destruction at any reasonable step size. The weak EBSD-pattern in Fig. 7a was the best pattern of only a few patterns that could be obtained from GNP dewetted from a 12 nm gold layer in the gold/silica layer system. It proves that it is possible to obtain EBSD-patterns from the described system, although the pattern quality was not sufficient to enable reliable scans with a binning of 4×4 .

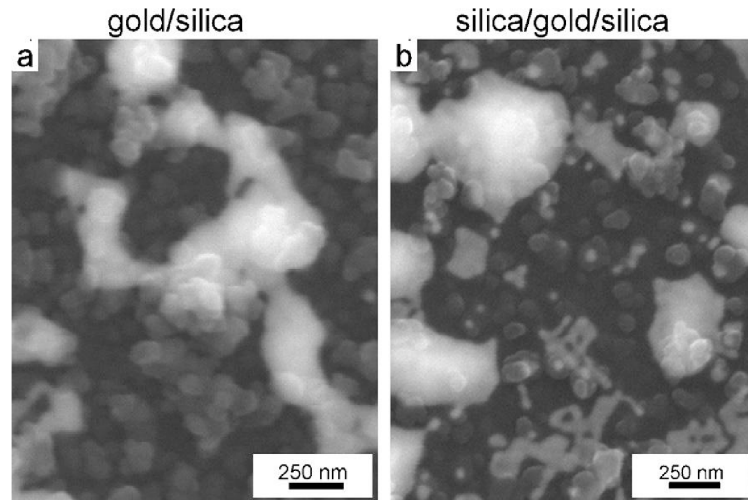


Fig. 3. SEM-micrographs of the areas framed in Fig. 2(c and d): layer systems annealed for 20 min at 550 °C (higher magnification).

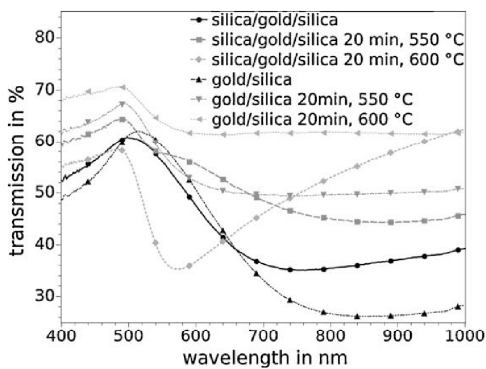


Fig. 4. Vis-NIR spectra of not annealed and annealed layer systems.

Under the assumption that the crystallographic orientation of the GNP dewetted from slightly thicker gold layers is comparable to that of GNP dewetted from 12 nm gold layers, the layer thickness was increased. GNP prepared by annealing 17 nm thick gold layers under otherwise identical conditions resulted in significantly better EBSD-patterns. Fig. 7 shows representative examples of the average

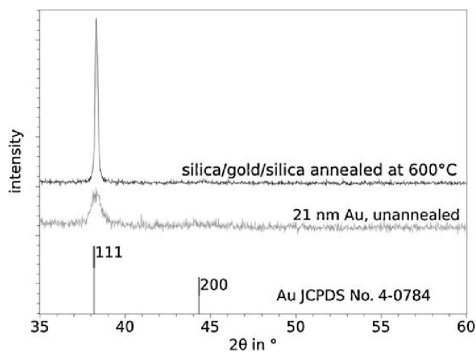


Fig. 5. XRD-pattern of a fresh, 12 nm thick, sputtered gold layer and of a silica/gold/silica layer system annealed for 20 min at 600 °C.

pattern quality b and d and the best pattern c and e obtained from samples of the respective systems.

The average quality of patterns in the silica/gold/silica system was too low to enable scans with a binning of 4×4 . Hence it was only possible to perform reliable EBSD-scans of GNP grown from 17 nm thick gold layers in the gold/silica system. A step size of 40 nm was used in the scans as this was the smallest step size applicable without destroying the sample.

Fig. 8 presents three maps indicating the data points (white) contributing to the respective equal area 1 1 1-pole figures (PF) of such a scan based on differently filtered datasets: Fig. 8a is based on all the data points in the scan with a confidence index $CI > 0.1$, which means an orientation solution has a probability of $\geq 96\%$ to be correct [24]. This PF is quite confusing which is why the image quality-parameter (IQ) was added to the data filter and the CI-threshold was raised to 0.2 to increase the reliability of the data points contributing to Fig. 8b and c. Fig. 8b is based on all data points with a $CI > 0.2$ and an IQ-value of more than 20% of the maximum value of the scan while Fig. 8c is based on all data points with a $CI > 0.2$ and an IQ-value of less than 20%.

4. Discussion

As the difference of the atomic numbers of the elements in the silica layer and the glass substrate is low, the contrast in the

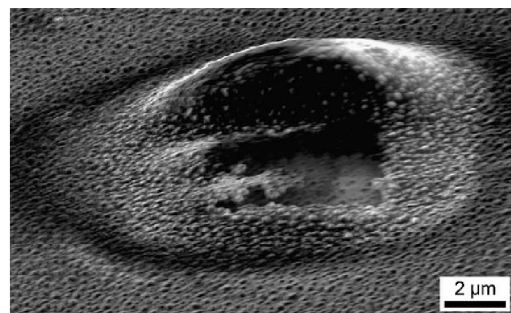


Fig. 6. SEM-micrograph obtained from a GNP-covered surface (tilted by 70°) after an EBSD-scan was performed with a binning of 4×4 and a step size of 20 nm. The substrate was overheated during the scan, rendering the scan useless.

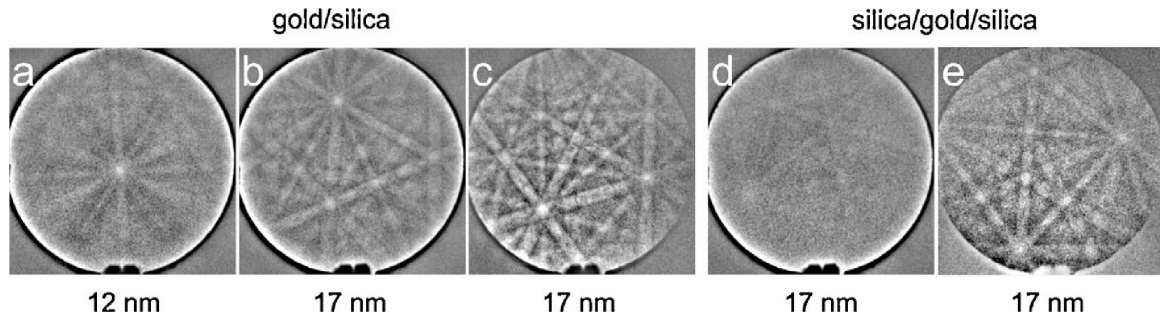


Fig. 7. EBSD-patterns obtained from GNP annealed from sputtered gold layers of 12 and 17 nm thickness in the respective layer systems.

SEM-micrographs of the silica layers should primarily be caused by the topography. Gold has a significantly higher atomic number and thus produces a strong material contrast in the SEM. The information depth of the micrographs depends on the accelerating voltage and the atomic number as well as the quantity of the respective elements in the information volume of an SEM-spot. In both the gold/silica and silica/gold/silica system, the gold below the silica-layer is still visible due to the material contrast, whereas the surface topography of the sample is widely caused by the silica layer (see Fig. 2a and b). The bright areas in Fig. 2c–f result from the high material contrast of gold. The darker, particle-like structure (see also Fig. 3) is the result of the silica layer topography. This structure shows brighter edges within the bright areas attributed to gold, suggesting that the silica layer occurs above the gold. Increasing the annealing temperature leads to a smaller number of particles in the silica layer while the contrast of the residual silica particles is decreased. This can be caused by a smoother surface, e.g. less topography contrast. Fig. 2d shows fine, unshaped or branched

structures, which are not agglomerated and probably thin residues of the sputtered gold film.

Thermal annealing of the silica/gold/silica layer system leads to the agglomeration of gold and the formation of separated gold particles embedded in a silica matrix.

It is known, that thermal annealing of thin noble metal films leads to a disaggregation of the film and to the formation of well separated gold particles [16,26,27]. This process is driven by the minimization of the surface energy, and is reported to occur via surface diffusion and depends on the film material, the film thickness and the annealing temperature [19,28,29]. However, it is well-known, that sputtered gold films exhibit a poor adhesion to glass substrates.

The dewetting observed in the silica/gold/silica layer system cannot be caused by surface diffusion but must occur via volume diffusion. This requires a higher activation energy than surface diffusion and hence requires higher annealing temperatures. Verifiable volume diffusion in glasses begins at the glass transition

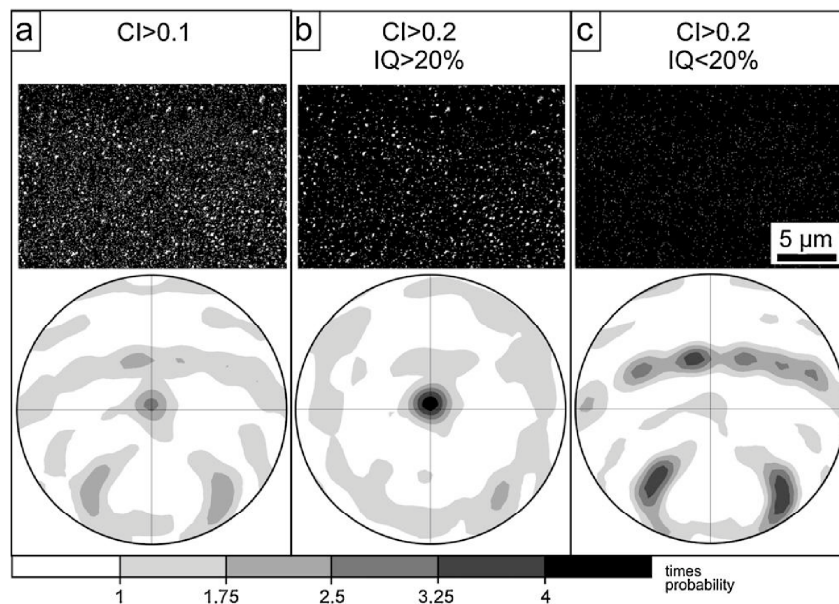


Fig. 8. IQ-maps and equal area 111-pole figures calculated from an EBSD-scan performed on a sample of the gold/silica system annealed from a 17 nm thick gold layer and filtered as stated in the figure.

temperature T_g and Ref. [12] demonstrates that gold nano-particles can be embedded in a glass surface by annealing at temperatures slightly above T_g .

Silica layers deposited by the CCVD process are composed of amorphous SiO_2 with a porosity of approximately 13% [23]. The T_g of fused silica (1130 °C) is notably higher than the applied annealing temperatures of 550 and 600 °C. By comparison, the T_g of the glass substrate is 525 °C meaning diffusion will mainly occur in the substrate.

Hence it is plausible that annealing the coated samples above T_g led to a diffusion of the network modifier ions (NMI) of the glass substrate bottom-up into the silica layer, decreasing the viscosity of the silica layer. The particle-like structure of the silica layers means locally varying layer thickness and hence different amounts of material available for diffusion. This results in locally different concentration gradients, diffusion profiles and subsequently in different local viscosities of the glass. At the same time, this material transport enables the diffusion of gold and thus the possibility for gold agglomeration, leading to the formation of gold particles. However, the diffusion of gold is enhanced by low glass viscosities.

In the gold/silica system the gold film is directly sputtered onto the substrate. Initially this enables a homogeneous dewetting of the gold film. Due to the gradually dewetting gold film, the NMI can diffuse into the covering silica layer as the layers are no longer separated by gold. The local variation in the glass viscosity changes the local mobility of gold, leading to the formation of the unshaped or branched structures as seen in Fig. 2c. Similar structures, but without the covering silica layer and annealed at 250 °C, were reported in Ref. [12].

By comparison, the bottom layer in the silica/gold/silica system immediately leads to locally different glass viscosities during annealing at temperatures above T_g . Accordingly, areas with a high and a low mobility of the gold must exist. The second silica layer covering the gold film increases these local differences in diffusion. Hence, not only the small, unshaped or branched structures, but also particles of varying sizes exist at the same time (see Fig. 2d). Generally, the formation of particles seems to be incomplete after annealing for only 20 min at 550 °C. Higher temperatures accelerate the diffusion, however, the mean free path length of the gold atoms decreases, resulting in smaller structures. Consequently, gold completely exists in the form of small particles after annealing for 20 min at 600 °C and the unshaped or branched structures have disappeared. Due to the higher concentration of silica, and hence a generally higher glass viscosity, the gold particles in the silica/gold/silica system are smaller than those observed in the gold/silica system.

The optical properties of both layer systems before annealing are comparable to those of gold films with a thickness around the percolation threshold [29], i.e. 15 nm [30]. Generally, the transmission of light at wavelengths >600 nm increases with decreasing coalescence of gold [30]. The rough, particle-like structure of the silica layer leads to a less coalescent structure of gold after sputtering in the silica/gold/silica system. Before annealing, the silica/gold/silica system shows a higher transmission at wavelengths >650 nm in comparison to the gold/silica system. At wavelengths <700 nm, the UV-vis-NIR spectrum of the gold/silica layer annealed for 20 min at 550 °C is similar to very thin gold films far below the percolation threshold [30], probably due to a similar structure of the layer. However, the gold in the gold/silica system annealed at 20 min at 550 °C is thicker than the gold films with thicknesses far below the percolation threshold, resulting in a stronger reflection and hence a lower transmission at wavelengths >700 nm (see Fig. 4) as well as the orange-red color of the scattered visible light. Light transmission is increased by increasing the annealing temperature. In comparison to the gold/silica system annealed

for 20 min at 550 °C, the layers annealed for 20 min at 600 °C do not show significant light scattering, leading to a notably higher transmission at wavelengths >600 nm. The spectrum of the silica/gold/silica system annealed for 20 min at 550 °C is similar to that of gold films with a thickness below the percolation threshold [30]. The small absorption peak at approximately 540 nm is caused by the PR of small gold particles, which are formed during annealing. The UV-vis-NIR spectrum of a silica/gold/silica system shows a minimum of the transmitted light at 570 nm caused by PR [31]. The typical PR peak of GNP occurs at around 520–550 nm [32].

An increasing particle diameter, increased dielectric constant of the particle environment (e.g. silica in comparison to air) and/or the non-spherical shape of the GNP leads to an increase in the NIR extinction and to a red shift of the absorption maximum. This runs parallel to a larger full width at half maximum of the PR-peak [31]. Consequently the peak of the silica/gold/silica system annealed for 20 min at 600 °C is broadened and a red shift occurs (Fig. 4).

Gold is the only crystalline phase in the system. The only peak observed in the XRD-patterns is the 1 1 1-peak, other peaks are not detected although the JCPDS-file includes further peaks. This indicates a preferred orientation of gold with its crystallographic [1 1 1]-direction perpendicular to the surface. The latter has already been reported for gold and other face centered cubic structures [25]. After annealing, the 1 1 1-peak is still the only peak while its intensity is significantly increased, indicating that the homogeneity of the crystal orientation has increased. The calculated mean crystal size of 100 nm equates the mean crystal size observed via SEM. This indicates a symmetrical particle size distribution.

The 1 1 1-orientation of the GNP is confirmed by the EBSD-measurements in Fig. 7b.

Analyzing the crystal orientation of the GNP on a glass substrate with EBSD is problematic due to the following three factors: (i) the size of the GNP, (ii) the thermally sensitive substrate with a low thermal conductivity and (iii) the silica layer covering the sputtered gold layer before annealing. The small size of the GNP limits the applicable step size of an EBSD-scan as it is preferable to obtain more than one pattern from each GNP to judge the reliability of the acquired data. A small step size leads to a high energy impact as the area in which electrons heat the sample is more comparable to the information volume of EDX-analysis which is larger than $1 \mu\text{m}^3$ under the given settings, remembering that the substrate area between the GNP is also scanned. Hence the thermal footprints of the patterns acquired during a scan overlap and lead to a local heating in the sample due to its low thermal conductivity. If, i.e. T_g of the substrate is reached, the surface is destroyed during the scan. This is shown in Fig. 6 where a part of the substrate has clearly flowed down the 70° slope of the tilted sample.

The small size of the GNP limits the probability of hitting a GNP with the fixed grid of a scan and increases the grain/grain-boundary ratio. The small information volume of EBSD [33–35] and a possible layer of silica covering the GNP may both significantly reduce the quality of EBSD-patterns as they reduce the amount of crystal lattice for diffraction in the information volume. It is not trivial that EBSD-patterns can be acquired from crystals covered by a thin layer of glass, but recent application of EBSD to surface crystallized glass ceramics has shown it is possible if the glass layer is thin enough [36–38].

The high quality of the patterns in Fig. 7c and e indicates that the GNP were not covered by a glass layer. Hence it is plausible that the silica layer becomes porous to a certain degree during the annealing process and some GNP are exposed to the atmosphere. The low quality of the majority of patterns might be caused by a thin glass layer and/or the small size of the GNP. If only part of the

information volume of an EBSD-pattern is composed of crystalline gold, the resulting pattern quality is reduced.

The map of Fig. 8b shows that the data points contributing to the texture showing the 111-fiber texture originate from the larger GNP. This was previously also observed in GNP grown on glass substrates without the covering silica layer [39] and on oxidized silicon wafers [19,40]. The map in Fig. 8c shows that the data points contributing to the corresponding PF are single points and not part of a cluster of points. This is generally problematic in EBSD, reducing the reliability of this PF despite the high level of CI-values of the contributing data. Because very small GNP exist in the surface, it is not impossible that these data points represent acceptable EBSD-data from very small GNP. If this data are reliable the small GNP would show different or more diverse crystal orientations than the larger GNP.

It must be noted, that the curious PF in Fig. 8a, which is clearly a superposition of the PF's in Fig. 8b and c, was based on data filtered in the same way as the data was filtered in Ref. [39] where the resulting PF showed a clear 111-orientation of the particles including the single point data in the scan. Hence it can be speculated, that the small particles annealed from a silica covered gold layer behave differently from those annealed from an uncovered gold layer.

It is also possible, that the large GNP are all exposed during the annealing process [41] and that this contact to the atmosphere initiates the formation of the texture. If a pore is formed in the silica layer during annealing, this might ease the formation of a large GNP which would be oriented comparably to the GNP on oxidized wafers [19,40] or glass [39] as similar surface energies would interact due to the contact to air.

On the other hand it is also possible that the large GNP simply keep the texture already present in the sputtered layer (see Fig. 5 and Ref. [25]), if diffusion is the only occurring mechanism of transport. Since the melting point of very small particles is much smaller than that of larger particles [42], it is not sure that the annealing temperature is still below the melting point. Fig. 6 shows that the GNP keep their morphology even when heated above T_g of the substrate (525 °C). Assuming the data in Fig. 8c is reliable, it would appear possible that very small particles liquefy during annealing and hence do not share the orientational preference of the larger GNP. In other studies GNP embedded in glassy silica films were prepared by a sol-gel-process and subsequent annealing for 1 h at 700 °C. They also showed a 111-orientation [43]. The nucleation and growth of gold also occurred in the solid state, concurrently with the densification of the SiO₂ films. However, the growth mechanism was not discussed.

This simple and inexpensive process enables the production of chemically stable and wear resistant GNP layers. The effect, that some of the GNP in the layer systems are apparently not covered by silica may be interesting for application as local plasmon sensors [44], substrates for SERS applications [45] and for improving photovoltaic efficiency [46]. The described method for producing wear resistant nano-particles layers can easily be adopted for other noble metals. This enhances the repertory of available decorative colors (e.g. yellow with silver) and enables further possibilities for functionalizing, e.g. antibacterial coatings (silver) or for catalytic applications (platinum).

5. Conclusions

We presented a simple two-step coating approach for producing wear resistant gold-ruby coatings where GNP are preferably oriented in the (111) plane parallel to the surface. Two separate layer systems were performed on soda-lime glass: first a

sputtered 12 nm gold layer was covered by a 30 nm silica layer, which was applied via a CCVD process and secondly a 12 nm gold layer was embedded between two 30 nm silica layers. The coated samples were annealed for 20 min at 550 °C and 600 °C. This led to a dewetting of the gold layer caused by volume diffusion within the glass substrate and the silica layer, leading to the formation of GNP with sizes from 200 to 600 nm. The gold layers show an excellent adhesion to the substrate after annealing at 550 °C. Increasing the annealing temperature from 550 to 600 °C results in smaller particles with sizes of 15–200 nm and an increased wear resistance. The silica gold silica system annealed at 600 °C shows a PR absorption peak at 550 nm and a purple coloration. The crystallographic texture was proved via XRD and EBSD. It was shown, that EBSD-patterns can be acquired from gold crystals covered by a thin layer of glass and that some of the particles are not covered by glass.

References

- [1] M. Chen, D.W. Goodman, *Accounts of Chemical Research* 39 (2006) 739–746.
- [2] A.M. Ruiz, A. Cornet, K. Shimanoe, I.R. Morante, N. Yamazoe, *Sensors and Actuators B* 93 (2003) 509–518.
- [3] C. de Julian Fernandez, M.G. Manera, J. Spadarechia, G. Maggioni, *Sensors and Actuators B* 111 (2005) 225–229.
- [4] C. Hrelescu, F.K. San, A.L. Rogach, F. Jäckel, J. Feldmann, *Applied Physics Letters* (2009) 153113.
- [5] N. Venkatram, R.S.S. Kumar, D.N. Rao, S.K. Medda, S. De, G. De, *Journal for Nanoscience and Nanotechnology* 6 (2006) 1990–1994.
- [6] Y. Hosoya, T. Suga, T. Yanagawa, Y. Kurokawa, *Journal of Applied Physics* 81 (1997) 1475–1480.
- [7] D. Pissuwan, C.H. Cortie, S.M. Valenzuela, M.B. Cortie, *Trends in Biotechnology* 28 (2010) 207–213.
- [8] R. Gupta, M.J. Dyer, W.A. Weimer, *Journal of Applied Physics* 92 (2002) 5264–5271.
- [9] G. De, S. Bhattacharya, *Journal of Materials Chemistry* 18 (2008) 2816–2824.
- [10] E. Hutter, J.H. Fendler, *Advanced Materials* 16 (2004) 1685–1706.
- [11] F. Paramigiani, *Journal of Applied Physics* 57 (1985) 2524–2528.
- [12] I.U. Vakarelski, D.Y.C. Chan, T. Nonoguchi, H. Shinto, Ko. Higashitani, *Physical Review Letters* 105 (2009) 058303.
- [13] C.S. Kealley, M.B. Cortie, A.I. Maaruf, X. Xu, *Physical Chemistry Chemical Physics* 11 (2009) 5897–5902.
- [14] X. Xu, M. Stevens, M.B. Cortie, *Chemistry of Materials* 16 (2004) 2259–2266.
- [15] X. Xu, M.B. Cortie, M. Stevens, *Materials Chemistry and Physics* 94 (2005) 266–274.
- [16] C. Schrank, C. Eisenmenger-Sittner, E. Neubauer, H. Bangert, A. Bergauer, *Thin Solid Films* 459 (2004) 276–281.
- [17] C.G. Granqvist, O. Hunderi, *Physical Reviews B* 16 (1976) 3513–3534.
- [18] D. Porath, O. Millo, *Journal of Vacuum Science & Technology* 14 (1996) 30–37.
- [19] C.M. Müller, E. Spolenak, *Acta Materialia* 58 (2010) 6035–6045.
- [20] L.M. Liz-Marzan, M. Giersig, P. Mulvaney, *Langmuir* 12 (1996) 4329–4335.
- [21] T. Ung, L.M. Liz-Marzan, P. Mulvaney, *Journal of Physical Chemistry B* 10 (2001) 3441–3452.
- [22] Y. Hu, R.C. Fleming, R.A. Drezek, *Optics Express* 16 (2008) 19579–19591.
- [23] C. Worsch, C. Rüssel, *Thin Solid Films* 518 (2010) 4798–4803.
- [24] J.A. Thornton, *Journal of Vacuum Science and Technology A* 4 (1986) 3059–3065.
- [25] A.J. Schwartz, M. Kumar, B.L. Adams, D.P. Field, *Electron Backscatter Diffraction in Materials Science*, 2nd ed., Springer, Berlin, Heidelberg, New York, 2009, <http://dx.doi.org/10.1007/978-0-387-88136-2>.
- [26] A. Proszynski, D. Chocyk, G. Gladyszewski, *Optica Applicata* 4 (2009) 705–710.
- [27] R. Brandon, F. Bradshaw, J. Royal Aircraft Establishment, Technical Report No. 66095, (1966).
- [28] A.E.B. Presland, G.L. Price, D.L. Trimm, *Surface Science* 3 (1972) 63–96.
- [29] P. Gadenne, *Thin Solid Films* 57 (1979) 77–81.
- [30] Doron-Mor, Z. Barkay, N. Filip-Granit, A. Vaskevich, I. Rubinstein, *Chemistry of Materials* 16 (2004) 3476–3483.
- [31] U. Kreibitz, M. Vollmer, *Optical Properties of Metal Clusters*, vol. 25, Springer Series in Material Science, New York, Berlin, Heidelberg, 1995, Chapter 2, 23 pp.
- [32] G. Mie, *Annalen der Physik-Berlin* 25 (1908) 377–445.
- [33] D. Dingley, *Journal of Microscopy* 213 (2004) 214–224.
- [34] K.Z. Baba-Kishi, *Journal of Materials Science* 37 (2002) 1715–1746.
- [35] A. Bhattacharyya, J. Eades, *Scanning* 31 (2009) 114–121.
- [36] W. Wisniewski, T. Zschechel, G. Völksch, C. Rüssel, *CrystEngComm* 12 (2010) 3105–3111.
- [37] W. Wisniewski, C.A. Baptista, G. Völksch, C. Rüssel, *Crystal Growth & Design* 11 (2011) 4660–4666.
- [38] W. Wisniewski, G. Völksch, C. Rüssel, *Ultramicroscopy* 111 (2011) 1712–1719.
- [39] C. Worsch, M. Kracker, W. Wisniewski, C. Rüssel, *Thin Solid Films*, DOI:10.1016/j.tsf.2012.03.016.

- [40] M. Bechelany, X. Maeder, J. Riesterer, J. Hankache, D. Lerose, S. Christiansen, J.I. Michler, L. Philippe, *Crystal Growth & Design* 10 (2010) 587–596.
- [41] P. Sangpour, O. Akhavan, A.Z. Moshfegh, M. Roozbehi, *Applied Surface Science* 254 (2007) 286–290.
- [42] P. Buffat, J.-P. Borel, *Physical Reviews A* 13 (1976) 2287–2298.
- [43] G. De, C.N.R. Rao, *Journal of Physical Chemistry B* 107 (2003) 13597–13600.
- [44] T. Okamoto, I. Yamaguchi, *Optics Letters* 25 (2000) 372–374.
- [45] Z. Pan, A. Zavalin, A. Ueda, M. Guo, M. Groza, A. Burger, R. Mu, S.H. Morgan, *Applied Spectroscopy* 59 (2005) 782–786.
- [46] H.A. Atwater, A. Polman, *Nature Materials* 9 (2010) 205–213.

3.3

M. Kracker, C. Worsch, C. Bocker, C. Rüssel

***Optical properties of dewetted thin silver/gold multilayer films
on glass substrates***

Thin Solid Films, 539 (2013) 47–54

DOI: <http://dx.doi.org/10.1016/j.tsf.2013.04.153>

Optical properties of dewetted thin silver/gold multilayer films on glass substrates				
Beteiligt an				
	Michael Kracker	Dr. Christian Worsch	Dr. Christian Bocker	Prof. Christian Rüssel
Konzeption des Forschungsansatzes	X			X
Planung der Untersuchung	X			
Datenerhebung	X		X	
Datenanalyse und Interpretation	X	X	X	
Schreiben des Manuskripts	X	X	X	X
Vorschlag Anrechnung Publikationsäquivalente	1,0			



Optical properties of dewetted thin silver/gold multilayer films on glass substrates

Michael Kracker^{*}, Christian Worsch, Christian Bocker, Christian Rüssel

Otto-Schott-Institut, Jena University, Fraunhoferstr. 6, 07743 Jena, Germany

ARTICLE INFO

Article history:

Received 21 August 2012

Received in revised form 7 December 2012

Accepted 28 April 2013

Available online 18 May 2013

Keywords:

Nanoparticles

Alloy

Sputtering

Silver

Gold

Multilayer

ABSTRACT

Layer systems composed of gold and silver with a maximum total thickness in 15 nm were consecutively sputtered on soda-lime-silica flat glasses. Subsequently, the coated glasses were annealed at a temperature of 400 °C for 1 h in air. This resulted in the formation of tiny, well separated alloyed metal particles on the glass surface. The attributed optical transmission spectra showed a single plasmon resonance peak for alloyed particles. The wavelength of the plasmon resonance is reported in dependence of the thickness of the respective layers of gold and silver. A direct dependence of the stacking sequence, with respect to the contact with the furnace atmosphere was detected. If the upper layer consisted of silver, oxidation occurred and an alloy was not formed.

© 2013 Elsevier B.V. All rights reserved.

1. Introduction

If metallic particles possess sizes, d , in the range much smaller than the wavelength of visible light, λ , the optical properties are dramatically changed in comparison to the bulk material [1]. This results in special optical properties, e.g. sharp absorption bands which depend on size and shape of the particles as well as on the distance between the particles, the dielectric properties of the surrounding medium and in particular on the type of metal. The optical effects associated with nano-sized metallic particles were widely studied and are well understood [2]. Especially systems of gold and silver are extensively studied [3–12]. Metallic gold and silver nanoparticles show single absorption peaks at 520 and 400 nm, respectively. However, nanoparticles consisting of an alloy of Au and Ag result in tunable optical properties depending on the composition. The resulting absorbance is then located between the single plasmonic resonances of gold and silver.

The optical properties can, for the case of a quasistatic limitation ($d \ll \lambda$), be explained by the simplified Mie-theory combined with the real part of the complex dielectric function of the respective metals. The dielectric function of the alloy in a first approximation is the result of a weighted linear combination between the dielectric functions of the pure metals [6,13]. Additionally, the resulting optical behavior in general is affected by many parameters; among these are dielectric properties of the surrounding medium (such as the

refractive index), the particle size, the size-distribution as well as the shape of the particles [2,14–23].

Metallic nanoparticles have been prepared by various approaches including for example sputtering, pulse laser deposition and wet chemical deposition. Nanoparticles of metallic alloys are also in focus of research. The most frequently used way to synthesize nanoparticle alloys is the wet chemical precipitation. This method exhibits a very good reproducibility and results in a high homogeneity of the particles. Some studies described the possibility of producing alloyed nanoparticles by sputtering. More recently, such a procedure was introduced, which also used a sequential coating procedure [24,25]. Usually, the metal alloy layers or particles were prepared by sputtering using targets, which consist of the respective alloy or a mixture of several metals in the aimed atom ratio. However, the latter only allows the preparation of alloyed particles with a fixed composition.

A well-known property of thin layers can also be used to produce nanoparticles as well. First, a substrate is coated by vapor deposition, sputtering or electron beam evaporation, then as a second process step the sample is thermally annealed which results in a dewetting of the layers and the formation of nanoparticles. The dewetting is a process driven by the minimization of the total surface energy (substrate/metal, substrate/air and metal/air) as well as by stress relaxation within the layers [23,26–30]. Depending on film thickness, particles with diameters in the range of a few nm up to several hundred nm can thus be produced. Due to Rayleigh and Kelvin instabilities as well as sintering and phase separation effects, the size and shape of the nanoparticles can be varied [31,32]. Due to the large number of experimental parameters (e.g. annealing temperature,

^{*} Corresponding author. Tel.: +49 3641 948522; fax: +49 3641 948502.
E-mail address: Michael.Kracker@uni-jena.de (M. Kracker).

layer thickness, material, atmosphere) this process is very complex, but in principle well understood.

This paper reports on the optical features of multilayer systems prepared by thin sputtered and subsequently annealed gold and silver layers. In addition, the change in the optical properties running parallel to the alloying process was studied. Furthermore, the effect of the atmosphere as well as of the stack-sequence of the metal layers is reported.

2. Experimental procedure

Soda-lime silica glass samples with a thickness of 1 mm and a diameter of 8 mm were used for gold/silver coatings. The substrates were cleaned using a solution composed of 58.2 vol.% deionised water, 29.1 vol.% isopropanol, 11.7 vol.% ammonia solution (25 vol.%) and 1 vol.% of an aqueous tenside (15%) for 10 min at 65 °C in an ultrasonic bath. Afterwards the substrates were rinsed with deionised water and treated twice again in deionised water with ultrasonic assistance. Finally the glass substrates were dried at 110 °C for 1 h in air and stored in vacuum until the layers were sputtered.

Gold and silver layers were sputtered using a DC-sputter-system (Edwards Auto 306 with high vacuum system). The target diameters were 50 mm; the target purity of gold was 99.99% and 99.95% for silver. The coating processes were carried out while the following parameters were kept constant: substrate-temperature (21 °C), target-substrate-distance (130 mm), the pressure in the vacuum-chamber (<10 mPa), the voltage (4 kV), the argon pressure (10 Pa) and the resulting current (35 mA).

Different sets of multi-layers were deposited on soda-lime glass. The layer sequence as well as the ratio silver/gold was varied. To control the thickness of the sputtered layer, a variable deposition time was used. The preparation procedure of different sets is schematically illustrated in Fig. 1d–f and in Table 1 the coating time with the corresponding layer thicknesses can be seen. The layer thickness was obtained using an atomic force microscope (Zeiss Ultraobjektiv, SIS, Germany).

Annealing was carried out in a muffle furnace at a temperature of 400 °C in air. The samples were transferred into the furnace and heated using a rate of 10 K/min. The desired temperature was kept for 1 h. Subsequently, the furnace was cooled down to room temperature supplying a cooling rate <1 K/min; then the samples were removed.

UV–vis–NIR spectra were recorded in the wavelength range from 190 to 1200 nm using an UV–vis–NIR spectrometer (Shimadzu 3201). The electron micrographs were obtained using a scanning electron microscope (SEM JEOL 7001F). For that purpose, most samples had to be coated with a thin carbon layer in order to avoid charging of the scanned sample surface.

Table 1

Deposition time and corresponding layer thickness.

Material	Deposition time in s	Determined film thickness in nm
Gold	60	8 ± 1
	45	6 ± 1
	30	5 ± 1
	15	2 ± 0.5
Silver	60	7 ± 1
	45	6 ± 1
	30	3 ± 1
	15	2 ± 0.5

3. Results and discussion

This paper presents a route for the preparation of alloyed nanoparticles by sequential sputtering of different thin metal layers and subsequent annealing at low temperatures in air. Thin metallic layers consisting of silver and gold with thickness of few nm were deposited on soda-lime-glass substrates.

Fig. 1a and b shows schematic illustrations of the possible dewetting behavior. After annealing a single layer leads to the formation of small particles. In the case of multilayers, the influence of the stacking sequence on the particles is unknown. In Fig. 1c, potential morphologies after dewetting of two layers are presented. In the left part, a nanoparticle surrounded by a layer i.e. a core shell structure is shown, in the middle a nanoparticle composed of two different metals and in the right of Fig. 1c a solid solution is shown. Fig. 1d–f presents different applied ways to stack gold and silver in order to investigate the dewetting and alloying behavior and to control the optical properties.

The quantities of gold and silver were varied by controlling the deposition times. Fig. 2a to c show UV–vis–NIR transmission spectra of freshly sputtered sandwich layers with different compositions and coating sequences. In Fig. 2a a sandwich system composed by a silver layer with a thickness of 7 nm (deposition time 60 s) and a gold layer deposited on top of the silver layer with different thickness (2, 5, 6 and 8 nm) is shown. The thickness of the respective layer increases with longer gold deposition times. This leads to a decrease of the optical transmittance. If only a silver layer was deposited, a transmission maximum occurs at 350 nm and a transmission minimum at 800 nm. The transmission maximum is shifted to longer wavelengths with increasing thickness of the gold layer.

Fig. 2b shows optical transmission spectra of a freshly sputtered sandwich system. First a gold layer of 8 nm (deposition time 60 s) and subsequently a silver layer with a thickness of 2, 3, 6 and 7 nm (deposition times 15, 30, 45 and 60 s) were sputtered. The thickness

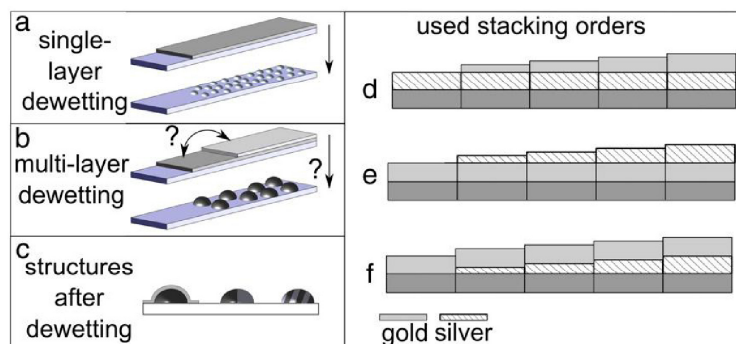


Fig. 1. Schematic illustration of layer dewetting. a) Dewetting of a single-layer-system; b) dewetting of a multi-layer-system; c) possible morphologies after dewetting of multi-layer-system, left: nanoparticle core-shell-structure, middle: nanostructure of two non-miscible components, right: alloyed nanoparticles (solid solution, indicated by the hatching). Used stacking orders d) silver/gold (varied) e) gold/silver (varied) f) silver (varied)/gold.

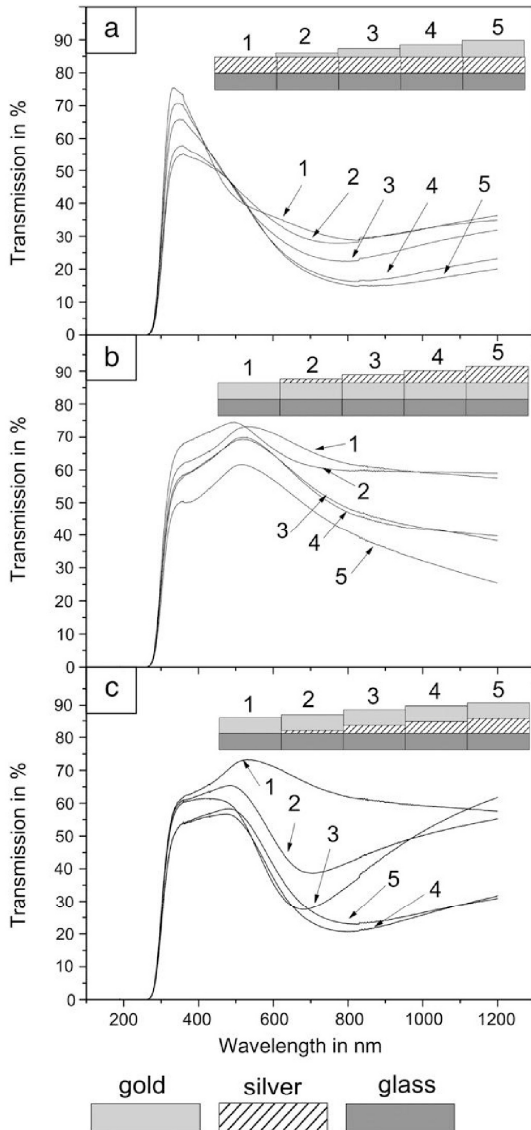


Fig. 2. UV-vis-NIR transmission spectra of freshly sputtered multilayer systems, a) layer thickness for silver 7 nm + gold 0 nm (No. 1), +2 nm Au (No. 2), +5 nm (No. 3), +6 nm Au (No. 4), +8 nm Au (No. 5); b) Layer thickness for gold 8 nm + silver 0 nm (No. 1), +2 nm (No. 2), +3 nm (No. 3), +6 nm (No. 4), +7 nm (No. 5); c) Layer thickness for silver 0 nm (No. 1), 2 nm (No. 2), 3 nm (No. 3), 6 nm (No. 4), 7 nm (No. 5) +8 nm of gold.

of the respective layers increases with longer silver deposition times, which results in a decrease of the transmission. If only a gold layer was freshly sputtered, a transmission maximum at 535 nm is observed. A subsequently deposited 2 nm silver layer leads to a shift of the maximum to 495 nm. With an increase of the respective layer thickness, the maximum shifts to 520 nm.

Fig. 2c shows optical transmission spectra of freshly sputtered sandwich systems composed by silver layers of 2, 3, 6 and 7 nm (using various deposition times of 15, 30, 45 and 60 s) subsequently covered by a gold layer with a thickness of 8 nm. With increasing the thickness of the first layer (silver), the shapes of the spectra clearly change. For a layer thickness of 2 nm silver, a new transmission

minimum occurs at around 695 nm. A further increase in the silver layer thickness to 3 nm (spectrum no. 3) results in a shift of the transmission minimum from 695 to 680 nm, which runs parallel to a strong increase in the transmission at wavelengths >1000 nm. For 6 and 7 nm thick silver layers the transmission minimum shifts to 800 nm.

In Fig. 3a and b SEM micrographs of freshly sputtered sandwich layers are presented. They show a typical percolating structure of thin metal layers (deposited at room temperature) with cracks and voids. Fig. 3a presents a respective layer composed of 7 nm silver covered by 8 nm of gold (compare with spectrum no. 5 in Fig. 2a). Fig. 3b shows a freshly sputtered layer composed of 8 nm gold and 2 nm silver on the top (compare with spectrum no. 2 in Fig. 2b).

Fig. 4 shows UV-vis-NIR transmission spectra of freshly sputtered sandwich layers (open symbols) composed of a silver layer with a thickness of 7 nm and a gold layer deposited on top of the silver layer using 2 to 8 nm thick layers.

After annealing the sample at 400 °C for 1 h, all gold containing layers show a characteristic transmission minimum, the so-called plasmon resonance (PR). When gold was sputtered for 15 s (2 nm), the spectra showed a transmission minimum at 488 nm. The value of the minimum is shifted to larger wavelengths and the transmission gets smaller with increasing sputtering time, i.e. thicker gold layers. For a layer thickness of 8 nm of gold, the minimum occurs at a wavelength of 520 nm. A layer solely composed of silver, does not at all show a transmission minimum if annealed at 400 °C. This is further illustrated in Fig. 5 where the wavelength of the characteristic transmission minima for silver/gold layers annealed at 400 °C for 1 h (compare with Fig. 1d) is plotted as a function of the gold layer thickness. With increasing thickness of the gold layer, which is deposited on top of a silver layer, the wavelength attributed to the transmission minima increases continuously. After annealing, the wavelength of the transmission minimum for a layer sputtered for 15 s (2 nm) is 488 nm. While increasing the gold layer thickness to 5 nm, the minimum is shifted to 486 nm. A further increase in the gold layer thickness to 6 and 8 nm led to minima at 510 and 520 nm, respectively. Silver layers which were not covered by gold layer did not show a transmission minimum also if an annealing temperature of only 350 °C was supplied (not shown).

In the following (see Fig. 6) another stacking order was used which is different from the experimental setup described in Fig. 5: The substrate was first coated with a gold layer of constant thickness, (8 nm), then a silver layer was deposited with a thickness of 2, 3, 6 or 7 nm using deposition times of 15, 30, 45, and 60 s, respectively (compare Fig. 1e). The wavelength of the characteristic transmission minima of layered samples after annealing at 400 °C is shown in Fig. 6 as a function of the silver layer thickness. After annealing a continuous increase of the plasmon resonance wavelength is observed for increasing thickness of the silver layer. The transmission minimum is shifted from 528 nm for pure gold to 562 nm if prepared from gold with an additional silver layer of 7 nm.

Fig. 7 presents UV-vis-NIR transmission spectra of silver layers with different thickness (2, 3, 6 and 7 nm) covered by a gold layer with a constant thickness of 8 nm which was deposited for 60 s (the stacking order is shown in Fig. 1f). The layers are annealed at 400 °C for 1 h. The transmission is in the range from 75 to 80% at wavelengths below 400 nm, passes through a minimum and increases to around 90% for wavelengths larger than 650 nm. With increasing layer thickness, the minimum is shifted to smaller wavelengths and the attributed transmission slightly decreases. This is further illustrated in Fig. 8 which presents the wavelengths of the transmission minima as a function of the silver layer thickness (compare to Fig. 1f). The silver layers were all covered with a gold layer with a constant thickness of 8 nm. Subsequently the samples were annealed at 400 °C for 1 h. After annealing, the transmission decreases while increasing the thickness of the silver layer. The position

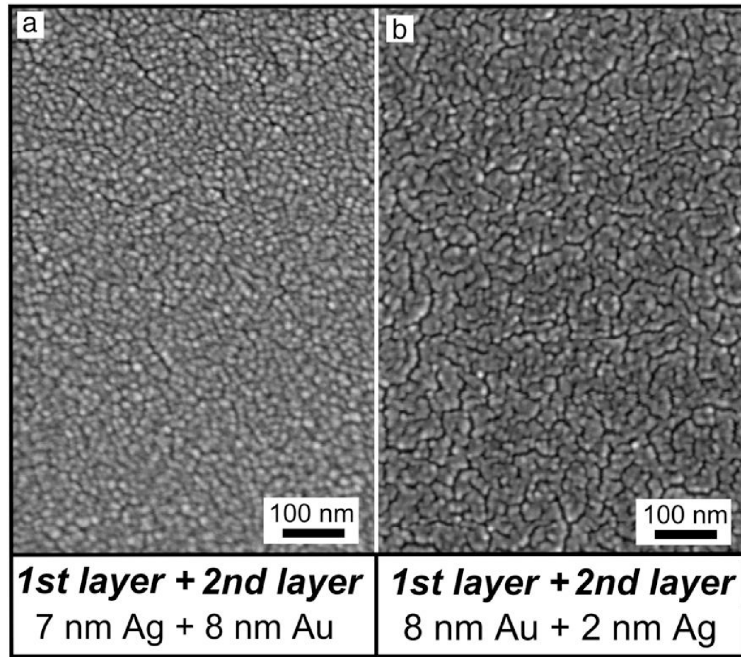


Fig. 3. SEM-micrographs of layer systems composed of silver and gold layers with different stacking sequences and layer thickness, a) silver 7 nm and gold 8 nm, b) gold 8 nm and silver 2 nm.

of the transmission minima shifts to smaller wavelength with increasing silver deposition time.

At the sample with a silver layer thickness of 2 nm, the transmission minimum occurs at 524 nm after annealing at 400 °C. A silver layer thickness of 3 nm results in a transmission minimum of 512 nm and layer thickness for silver of 7 nm and gold of 8 nm result in a transmission minimum of 510 nm.

In Fig. 9 SEM micrographs of a single gold layer with a thickness of 8 nm after annealing at 400 °C is presented. The SEM are equipped with two different detectors for the secondary electrons (SE), an in-lens detector (IL) and a common Everhart–Thornley (ET) detector; both were used for recording the micrographs at the same place and

at the same time. The micrographs show bright particles which are attributed to gold particles with sizes in the range from 36 to 110 nm providing a high materials contrast with the glass substrate which appears dark. The in-lens detector reveals some structures with diameters in the range from 150 to 500 nm that are placed in between the gold particles. These structures are visible if the in-lens detector is used because of the detector's high sensitivity to topographical contrast. Furthermore, the detection of secondary electrons (SE) arises directly from the primary electron beam having a high energy and emerging from a very thin layer (few nm) of the surface. By contrast, the Everhart–Thornley detector which also detects SE with lower

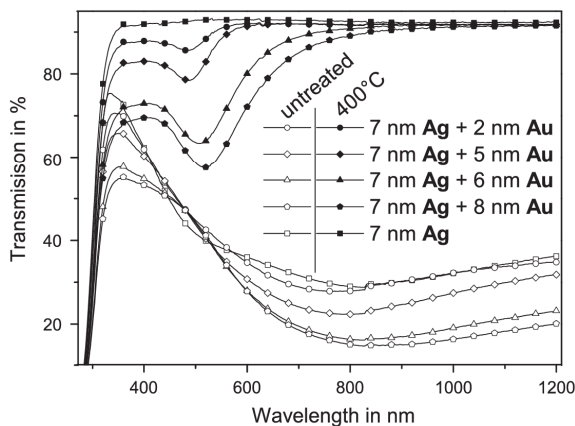


Fig. 4. Optical transmission spectra of silver/gold layers with different; a) freshly sputtered (open symbols) and b) layers after annealing at 400 °C for 1 h using a heating rate of 10 K/min (filled symbols).

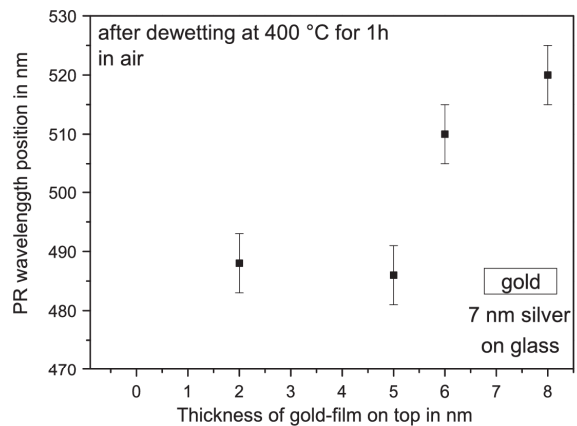


Fig. 5. Wavelengths of the transmission minima (plasmon resonance peak) of silver layers of constant thickness (7 nm) as a function of the covering gold layer thickness after annealing at 400 °C for 1 h using a heating rate of 10 K/min. The box indicates the position of the varied part of the layer system.

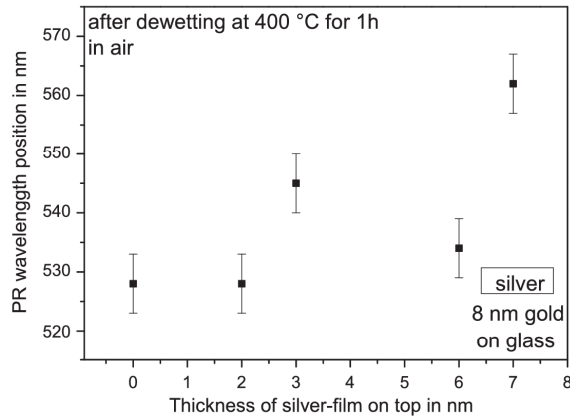


Fig. 6. Wavelengths of the transmission minima (plasmon resonance peak) of gold layers of constant thickness (8 nm) as a function of the covering silver layer thickness after annealing at 400 °C for 1 h using a heating rate of 10 K/min. The box indicates the position of the varied part of the layer system.

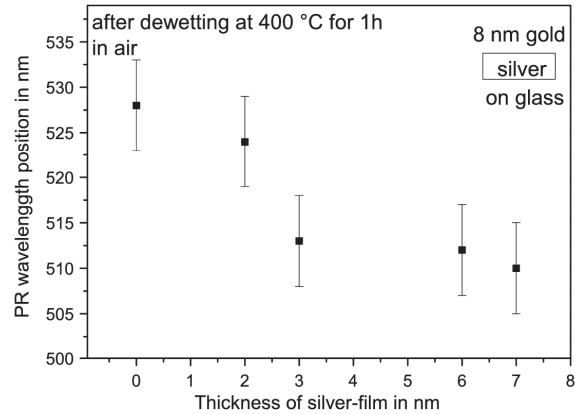


Fig. 8. Wavelengths of the transmission minima (plasmon resonance peak) of gold covered silver layer as a function of the silver layer thickness after annealing at 400 °C for 1 h using a heating of 10 K/min. The thickness of the gold layer is constant at 8 nm. The box indicates the position of the varied part of the layer system.

energy (but larger yield) from deeper regions (<10 nm) and also SE generated by back scattered electrons (also from the chamber walls) leading to a more pronounced background signal [33].

This leads to a second effect that can be observed if the micrographs of the two detectors are compared: At a first glance the particles in the micrograph recorded by the in-lens detector seem to be larger than those recorded by the Everhart–Thornley detector. However, when the contrast and brightness is adjusted (i.e. the background signal suppressed), the particles are equal in size in both micrographs as can be seen in Fig. 9c and d.

Fig. 10 shows SEM-micrographs of different layer systems annealed at 400 °C for 1 h. In analogy to Fig. 9, the micrographs were recorded using both detectors at the same place and at the same time. Fig. 10a and b) present SEM micrographs of a silver layer of 7 nm and covered with gold using a deposition time of 30 s (5 nm). In Fig. 10c and d) the same system is shown, but using a deposition time of 60 s (8 nm) for gold. Increasing deposition times of the covering gold film results in larger particles size and a more irregular shape of the particles after annealing.

In Fig. 10 and f, an annealed layer composed of silver with a layer thickness of 3 nm covered by a gold layer of 8 nm (deposition time 60 s) is shown. In the IL images (Fig. 10e), a layer, composed of

particles with sizes in the range from 100 to 300 nm is observed. Furthermore, smaller particles with sizes in range from 35 to 50 nm can be seen.

From the SEM micrographs, it is evident that sputtering of gold and silver layers onto a glass surface and subsequent annealing at 400 °C, results in the formation of small metallic nanoparticles. This conclusion facilitates to explain the UV–vis–NIR spectra.

The UV–vis–NIR spectra shown in Fig. 2a and b describe a layer system consisting of two different metals. However, the transmission is apparently defined by only one layer, in the following denoted as “dominant”. In Fig. 2a a typical spectrum of a thin silver layer [34] and in Fig. 2b of a thin gold layer [23,26] is shown. The shape of the spectrum is not significantly affected by the additionally sputtered metal. It can be concluded that the layer, which “dominates” the optical properties of the layer system, is located in the middle of the system (between substrate and top layer). This behavior can also be found in Fig. 2c. Here, the layer thickness of the dominant layer is increased. The optical behavior of the layer system is changing from a spectrum of a thin gold layer into the spectrum of a thin silver layer (Fig. 2c, No. 1 and No. 5). Here also combinations are possible, which show a significant transmission minimum, which is strongly reminiscent to a plasmon resonance.

Fig. 3 presents the structure of the deposited layer systems. These layers show a structure which according to the theory of Thornton [35,36] are in agreement with those deposited far below the melting point of the deposited metal (gold $T/T_m = 0,22$ and silver $T/T_m = 0,24$). This is evident in the numerous cracks and voids.

In the following, the samples sputtered with silver and then with gold will be discussed first. As shown in Figs. 4 and 5 an increase in the thickness of the gold layer results in a more pronounced transmission minimum to larger wavelengths. A thicker layer system shows larger nanoparticles after dewetting. This runs parallel to a shift of the plasmon resonance peak to larger wavelengths [26]. In analogy, alloying silver with gold should also result in a shift of the plasmon resonance peak to larger wavelengths as reported in Refs. [37–39]. This can easily be explained by the formation of a gold/silver alloy and the change in the internal electronic structure (to be exact the metals dielectric function) of the nanoparticles [40]. Thus, increasing gold concentration in the nanoparticles leads to a shift of the plasmon resonance to increasing wavelength, and thus, gold dominates the plasmon resonance of the nanoparticles. According to the literature, the characteristic transmission minima are located at around 420 nm for silver nanoparticles and 550 nm for gold nanoparticles. The shift in the absorption minima is also seen in Figs. 4 and 5. The

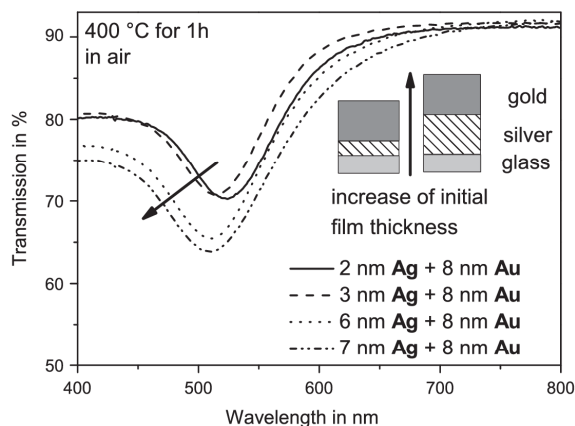


Fig. 7. UV–vis–NIR transmission spectra of silver/gold layers with different deposition times and corresponding layer thickness annealed at 400 °C for 1 h using a heating rate of 10 K/min.

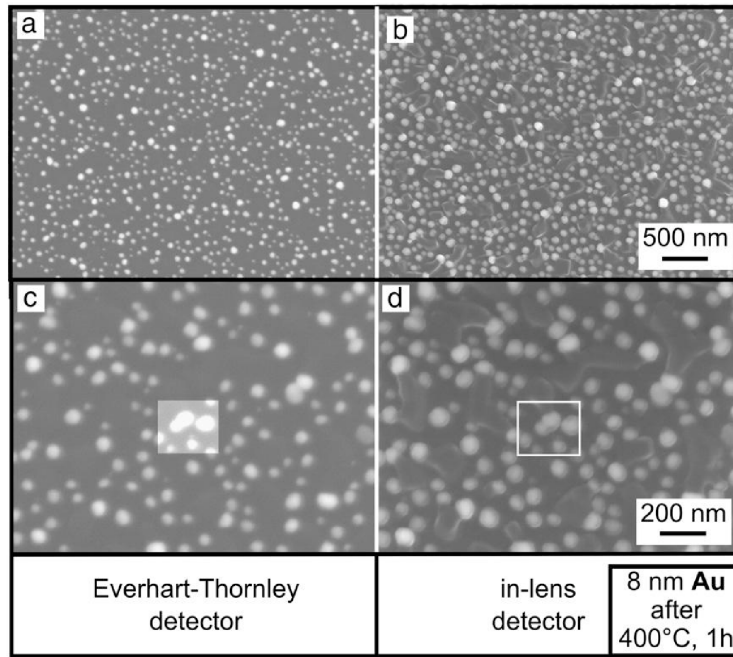


Fig. 9. SEM-micrographs of an annealed gold layer after annealing at 400 °C for 1 h and using a heating rate of 10 K/min. Two different electron detectors (IL = In-Lens detector and ET = Everhart–Thornley detector) for the recording of the images were simultaneously used.

minimum plasmon resonance for very small gold nanoparticles, calculated from the dielectric functions using Mie's Eq. as well as the experimentally determined value is in the range from 510 and 520 nm [15,37,38]. Here, the effect of particle shape of a high refractive indexed environment as well as the interaction between the particles is not yet taken into account [6].

A plasmon resonance initiated by pure silver was not observed since thin silver layers or nanoparticles are not stable against air at elevated temperatures of 400 °C (this behavior will be discussed later). However a gold layer of 2 nm prepared using a deposition time of 15 s, covered by a silver layer of 7 nm prepared by using a deposition time of 60 s results in a small resonance peak located at

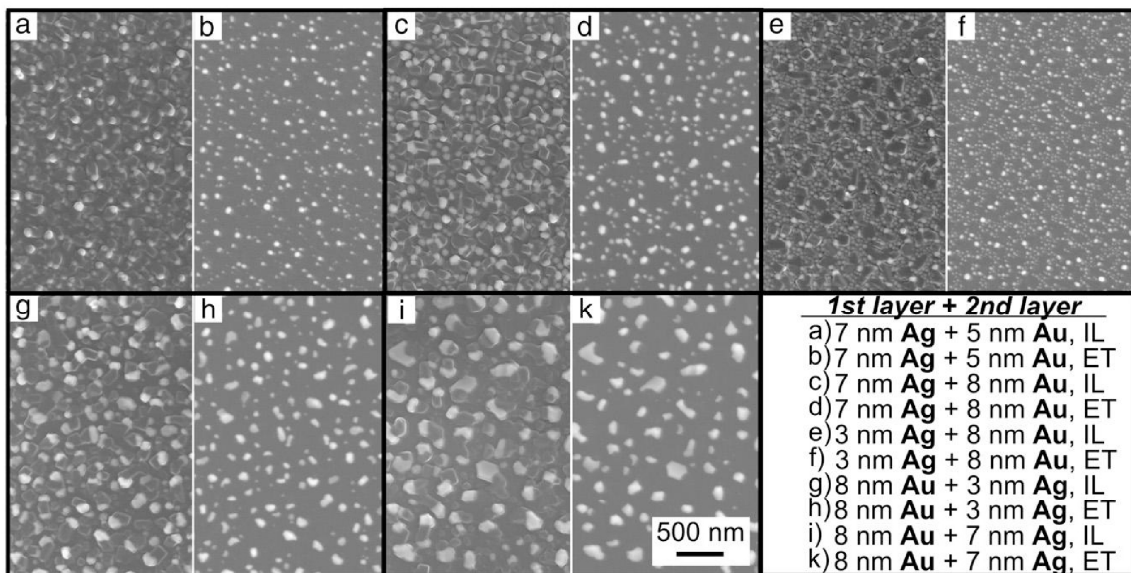


Fig. 10. SEM-micrographs of layer systems composed of silver and gold layers with different stacking sequences after annealing at 400 °C for 1 h (compare Fig. 1d–f). Two different electron detectors (IL = In-Lens detector and ET = Everhart–Thornley detector) were simultaneously used for recording the images. The sequence the deposition steps were performed and the used deposition times are given in the upper right corner of the illustration.

495 nm. This peak is shifted significantly in comparison to the silver resonance, but the resulting resonance is located at lower wavelengths than for the pure gold.

In Fig. 1f, a schematic of an experiment is shown in which silver is sputtered directly on the substrate and subsequently a gold layer of 8 nm is sputtered using a deposition time of 60 s. In contrast to Figs. 4 and 5, the thickness of the silver layer was kept constant while that of the gold layer was varied. Fig. 8 shows the UV–vis–NIR spectra of a sample after annealing at 400 °C for 1 h. The wavelength attributed to the minima of the plasmon resonance decreased with increasing quantity of silver [4,8]. The shift of plasmon resonances to smaller wavelengths is also in contrast to the increase in the total layer thickness. The latter also leads to larger particles (compare Fig. 10b and d) [1,15,26,39]. Furthermore the plasmon resonances occur at wavelengths smaller than those observed for pure gold. Silver/gold alloys should, however, show the opposite effect, i.e. an increase in the wavelength attributed to the minimum of the plasmonic resonance.

In order to confirm this effect, the thickness of the gold layer was kept constant and the thickness of a subsequently sputtered silver layer was increased. Certainly the experiment schematically shown in Fig. 1e and described in Fig. 6 shows the same effect as described in the last paragraph, i.e. a shift of the plasmon resonance peak to larger wavelengths.

Thermal annealing was carried out under ambient conditions. During the annealing procedure, silver is in contact with the furnace atmosphere, therefore the experimental procedure (illustrated in Fig. 6) implies that silver (although with different thickness) is always on top of the layer system. It should be noted that silver layers only few nm thick and especially small particles are very reactive and in contrast to the silver bulk materials also react with oxygen at the temperature supplied during annealing [41–44].

If metallic silver reacts with oxygen to an oxide such as Ag₂O or AgO, free electrons will no longer occur and hence, the plasmon resonance will no longer be visible in the spectrum. Then the optical behavior changes to that of a “non-metal” dielectric material with a high refractive index.

If silver reacts to a silver compound inside a gold silver layer system (Fig. 6), then the following should be taken into account: first the formation of an alloy by solid diffusion does not take place, but silver oxide with a high refractive index is formed near the gold nanoparticles. Such a structure leads to significant changes in the optical properties of the adjacencies of the gold nanoparticles. A shift of plasmon resonance to longer wavelengths by the damping of the electron gas oscillation would be expected, if the refractive index near the nanoparticles increases [37,38]. With respect to the effective medium theory, the effect of a shell or a part of a shell with high refractive index increases with increasing shell thickness. Hence, the plasmon resonance peaks attributable to silver nanoparticles observed in Figs. 4 and 5 are no longer detected. In analogy to the gold/silver layers this can be explained by an oxidation of the silver and the loss of metallic properties.

It is hence concluded that the formed silver oxide or another silver compound (e.g. highly silver doped glass) which possess a much higher refractive-index than the glass used as substrate and is located near the gold particles is responsible for the shift in the wavelengths attributed to the plasmonic resonance [40,45].

Silver also has a strong tendency to adsorb oxygen on its surface. An addition of oxygen was observed in the literature as well [46]. In the case of such chemisorptions, the density of free electrons of the metal is reduced by a charge transfer from the particles to the adsorbents. This will also result in a shift of the resonance to longer wavelengths [22].

In addition to the properties of the surrounding medium, it is shown in Fig. 10h and k, that with increasing silver layer thickness, the gold particles get larger and have a more complex shape. This

also leads to a shift of the resonance to longer wavelengths [14,47–49].

In summary, annealing of substrates coated first with gold and subsequently with silver leads to particles with optical properties different from that of an (inverted) multilayer film coated first with silver and afterwards with gold. It is assumed that in the stacking order gold/silver, the silver layer is in direct contact with the ambient atmosphere, which enables its oxidation. It can further be concluded that the oxidation is energetically preferred in comparison to alloying.

Here, the small particles play an important part and possibly also the diffusion of Ag⁺ into the glass which both may shift the redox equilibrium to the oxidized species [50].

4. Conclusion

A simple method to fabricate alloyed nanoparticle layers is presented. Gold and silver layers are sputtered on a soda lime silicate glass. The thickness and the stacking order of silver and gold were varied. The coated samples were subsequently annealed at 400 °C for 1 h at ambient conditions. This resulted in the formation of nanoparticles. The formation of alloyed nanoparticles can be observed, if the silver layer is subsequently covered by a gold layer. This is indicated by a shift of the plasmon resonance to lower wavelengths while the particle diameter is increased. However if the upper layer consists of silver during annealing, the plasmon resonance peak (contrary to expectations) is shifted to higher wavelengths. This can be explained by an increasing particle diameter and the oxidation of silver which leads to the formation of high dielectric adjacencies around the resulting particles.

Acknowledgments

This work is supported by the DFG “Deutsche Forschungsgemeinschaft” under grant nos.: Se 698/10-1 and Se 698/10-2.

References

- [1] G. Mie, *Ann. Phys. (Berlin)* 330 (1908) 377.
- [2] C. Granqvist, O. Hunderi, *Phys. Rev. B* 16 (1977) 3513.
- [3] D. Barreca, A. Gasparotto, C. Maragno, E. Tondello, S. Gialanella, *J. Nanosci. Nanotechnol.* 7 (2007) 2480.
- [4] V.I. Belotelov, G. Carotenuto, L. Nicolais, A. Longo, G.P. Pepe, P. Perlo, A.K. Zvezdin, *J. Appl. Phys.* 99 (2006) 044304.
- [5] L.L. Henry, Q. Yang, W.C. Chiang, P. Holody, R. Loloee, W.P. Pratt, J. Bass, *Phys. Rev. B* 54 (1996) 12336.
- [6] K.J. Major, C. De, S.O. Obare, *Plasmonics* 4 (2009) 61.
- [7] K.-i. Okazaki, T. Kiyama, K. Hirahara, N. Tanaka, S. Kuwabata, T. Torimoto, *Chem. Commun.* (2008) 691.
- [8] R.K. Roy, S.K. Mandal, A.K. Pal, *Eur. Phys. J. B* 33 (2003) 109.
- [9] P. Sangpour, O. Akhavan, A.Z. Moshfegh, *J. Alloys Compd.* 486 (2009) 22.
- [10] Q.Q. Wang, B.F. Yang, D.C. Tian, G.G. Xiong, Z.G. Zhou, *Surf. Coat. Technol.* 131 (2000) 408.
- [11] J. Wilcoxon, *J. Phys. Chem. B* 113 (2009) 2647.
- [12] D.H. Chen, C.J. Chen, *J. Mater. Chem.* 12 (2002) 1557.
- [13] L.M. Liz-Marzan, A.P. Philpse, *J. Phys. Chem.* 99 (1995) 15120.
- [14] K.L. Kelly, E. Coronado, L.L. Zhao, G.C. Schatz, *J. Phys. Chem. B* 107 (2003) 668.
- [15] X.D. Xu, M. Stevens, M.B. Cortie, *Chem. Mater.* 16 (2004) 2259.
- [16] X.D. Xu, M.B. Cortie, M. Stevens, *Mater. Chem. Phys.* 94 (2005) 266.
- [17] T. Ung, L.M. Liz-Marzan, P. Mulvaney, *Colloid Surf. A* 202 (2002) 119.
- [18] G. Gupta, D. Tanaka, Y. Ito, D. Shibata, M. Shimojo, K. Furuya, K. Mitsui, K. Kajikawa, *Nanotechnology* 20 (2009) 25703.
- [19] E. Hutter, J.H. Fendler, *Adv. Mater.* 16 (2004) 1685.
- [20] P. Mulvaney, *Langmuir* 12 (1996) 788.
- [21] T. Karakouz, D. Holder, M. Goomanovsky, A. Vaskevich, I. Rubinstein, *Chem. Mater.* 21 (2009) 5875.
- [22] W.P. Cai, H. Hofmeister, T. Rainer, *Phys. E* 11 (2001) 339.
- [23] C. Worsch, W. Wisniewski, M. Kracker, C. Rüssel, *Appl. Surf. Sci.* 258 (2012) 8506.
- [24] D. Wang, P. Schaaf, *J. Mater. Chem.* 22 (2012) 5344.
- [25] D. Wang, P. Schaaf, *Mater. Lett.* 70 (2012) 30.
- [26] C. Worsch, M. Kracker, W. Wisniewski, C. Rüssel, *Thin Solid Films* 520 (2012) 4941.
- [27] C.M. Müller, R. Spolenak, *Acta Mater.* 58 (2010) 6035.
- [28] E. Jiran, C.V. Thompson, *J. Electron. Mater.* 19 (1990) 1153.
- [29] C. Schrank, C. Eisenmenger-Sittner, E. Neubauer, H. Bangert, A. Bergauer, *Thin Solid Films* 459 (2004) 276.

- [30] R. Seemann, S. Herminghaus, K. Jacobs, *Phys. Rev. Lett.* 86 (2001) 5534.
- [31] M.E. Toimil-Molares, A.G. Balogh, T.W. Cornelius, R. Neumann, C. Trautmann, *Appl. Phys. Lett.* 85 (2004) 5337.
- [32] S. Karim, M.E. Toimil-Molares, A.G. Balogh, W. Ensinger, T.W. Cornelius, E.U. Khan, R. Neumann, *Nanotechnology* 17 (2006) 5954.
- [33] W. Zhou, Z.L. Wang, *Scanning microscopy for nanotechnology*, Springer, New York, 2007.
- [34] R.W. Cohen, G.D. Cody, M.D. Coutts, B. Abeles, *Phys. Rev. B* 8 (1973) 3689.
- [35] J.A. Thornton, *J. Vac. Sci. Technol.* 11 (1974) 666.
- [36] J.A. Thornton, *J. Vac. Sci. Technol.* 12 (1975) 830.
- [37] M. Quinten, *Optical Properties of Nanoparticle Systems*, Wiley-VCH-Verlag, Weinheim, 2011.
- [38] U. Kreibig, M. Vollmer, *Optical Properties of Metal Clusters*, 1st ed. Springer, Berlin, Heidelberg, 1995.
- [39] C.F. Bohren, D.R. Huffman, *Absorption and Scattering of Light by Small Particles*, Wiley, New York, 1983.
- [40] U. Kreibig, L. Genzel, *Surf. Sci.* 156 (1985) 678.
- [41] C.-N. Lok, C.-M. Ho, R. Chen, Q.-Y. He, W.-Y. Yu, H. Sun, P.K.-H. Tam, J.-F. Chiu, C.-M. Che, *J. Biol. Inorg. Chem.* 12 (2007) 527.
- [42] T.L. Slager, B.J. Lindgren, A.J. Mallmann, R.G. Greenler, *J. Phys. Chem.* 76 (1972) 940.
- [43] T.E. Graedel, *J. Electrochem. Soc.* 139 (1992) 1963.
- [44] S.S. Djokic, R.E. Burrell, *J. Electrochem. Soc.* 145 (1998) 1426.
- [45] M.A. Garcia, *J. Phys. D: Appl. Phys.* 44 (2011) 283001.
- [46] P.A. Kilty, W.M. Sachtler, *Catal. Rev. Sci. Eng.* 10 (1974) 1.
- [47] C. Worsch, C. Rüssel, *Thin Solid Films* 518 (2010) 4798.
- [48] M. Pelton, J. Aizpurua, G. Bryant, *Laser Photonics Rev.* 2 (2008) 136.
- [49] J.P. Kottmann, O.J. Martin, *Opt. Express* 6 (2000) 213.
- [50] S. Hornschuh, B. Messerschmidt, T. Possner, U. Possner, C. Rüssel, *J. Non-Cryst. Solids* 347 (2004) 121.

3.4

M. Kracker, C. Worsch, C. Rüssel

Optical properties of palladium nanoparticles under exposure of hydrogen and inert gas prepared by dewetting synthesis of thin-sputtered layers

Journal of Nanoparticle Research, 15 (2013) 1594

DOI: <http://dx.doi.org/10.1007/s11051-013-1594-5>

Optical properties of palladium nanoparticles under exposure of hydrogen and inert gas prepared by dewetting synthesis of thin-sputtered layers				
Beteiligt an				
	Michael Kracker	Dr. Christian Worsch	Prof. Christian Rüssel	
Konzeption des Forschungsansatzes	X		X	
Planung der Untersuchung	X			
Datenerhebung	X			
Datenanalyse und Interpretation	X	X		
Schreiben des Manuskripts	X	X	X	
Vorschlag Anrechnung Publikationsäquivalente	1,0			

Optical properties of palladium nanoparticles under exposure of hydrogen and inert gas prepared by dewetting synthesis of thin-sputtered layers

Michael Kracker · Christian Worsch ·
Christian Rüssel

Received: 11 January 2013 / Accepted: 18 March 2013 / Published online: 28 March 2013
© Springer Science+Business Media Dordrecht 2013

Abstract Thin layers of palladium with a thickness of 5 nm were sputtered on fused silica substrates. Subsequently, the coated glasses were annealed at a temperature of 900 °C for 1 h. This resulted in the formation of small and well-separated palladium nanoparticles with diameters in the range from 20 to 200 nm on the glass surface. The existence of a palladium oxide layer can be detected using optical absorption spectroscopy. Purging with hydrogen leads to an irreversible change in the optical spectra due to the reduction of PdO to metallic palladium. Changing the gas atmosphere from hydrogen to argon leads to significant reversible changes in the optical properties of the particle layer. Based on Mie theory and the respective dielectric functions, the spectra were calculated using the real particle size distribution, weighted dispersions relation to adapt the geometrical conditions and complex dielectric functions of palladium and palladium hydride. A good agreement with measured spectra was found and the dependency of the surrounding media can be explained.

Keywords Dewetting · Palladium · Sputtering · Transmission spectroscopy · Calculation · Palladium oxide

Introduction

The system palladium and hydrogen has frequently been studied in the past (Flanagan and Oates 1991; Manchester et al. 1994; Pundt 2005; Langhammer et al. 2010b, c; Kishore et al. 2005; Ke et al. 2004). Here, especially the interaction with hydrogen has extensively been described and discussed during the past 80 years. Especially, the possibility of using palladium for hydrogen storage was investigated (Kishore et al. 2005; Langhammer et al. 2007b; Hakamada et al. 2010; Bérubé et al. 2007). For this purpose, the properties of solids, layers, and powders (Flanagan and Oates 1991) were investigated. At room temperature, palladium can incorporate huge quantities of hydrogen in its crystal structure. This results in a pressure-dependent phase transition between an alpha and a beta phase (Manchester et al. 1994; Pundt 2005; Flanagan and Oates 1991).

In the past decades, when science discovered the field of nanotechnology, the interest in palladium-based nanoparticles (in the following denoted as PNP) and nanoparticles in generally increased significantly (Shipway et al. 2000; Mulvaney 1996; Katzer et al. 2012; Daniel and Astruc 2004). It was recognized that the interactions of PNPs with hydrogen, in comparison to the bulk material, are fundamentally different and the phase transition between alpha and beta structure on the surface of nanoscaled palladium crystals is suppressed (Pundt 2005; Mütschele and Kirchheim 1987; Kirchheim et al. 1988). Especially, investigations focused on

M. Kracker (✉) · C. Worsch · C. Rüssel
Otto-Schott-Institut, Jena University, Fraunhoferstr. 6,
07743 Jena, Germany
e-mail: Michael.Kracker@uni-jena.de

structural changes during hydrogen exposition and catalytic properties (Schauermann et al. 2002; Edwards et al. 2009) as well as preparation techniques have been published. By contrast, studies on optical properties of palladium-based nanoparticles have scarcely been reported in the literature.

In the beginning of the 20th century, Gustav Mie developed a theory concerning the optical properties of metallic nanoparticles which enabled to describe the red coloration of fluids containing gold nanoparticles (Mie 1908). Mie realized that metallic particles changed their optical properties dramatically, if the size becomes smaller than the wavelength of the incident light. This results in special optical properties, e.g., sharp absorption bands (plasmon resonances) which depend on size and shape of the particles as well as on the distance between the particles, the dielectric properties of the surrounding medium and the type and crystal lattice of the metal. The solution of the Mie equations results in a cross-section C , for the absorption, C_{abs} , and the scattering C_{sca} as well as an extinction cross-section C_{ext} (with: $C_{\text{ext}} = C_{\text{abs}} + C_{\text{sca}}$) of the metallic nanoparticles. This geometrical cross-section is equivalent to the energy loss of the incident light beam after crossing the particle. This cross-section can also be larger than the geometrical cross-section in the case of resonance (plasmon resonance PR). For a better comparison between spectra of different materials, the cross-section can be normalized to the real geometrical cross-section of the particle (Quinten 2011). This normalization is called efficiency Q . For Q , a similar expression as for the cross-section applies: $Q_{\text{ext}} = Q_{\text{abs}} + Q_{\text{sca}}$.

The optical effects associated with nanosized metallic particles were widely studied and are well understood. However, primarily gold, silver, and copper nanoparticles have been used as a model system to investigate the optical properties of the metallic particles. The optical properties of palladium nanoparticles (PNP), especially during contact with hydrogen, are scarcely studied (Langhammer et al. 2007a; Silkin et al. 2012; Creighton and Eadon 1991). These properties, however, are essential for the development of optical sensors based on PNPs. Palladium disks with diameters of a few hundred nm have recently become the focus of research to realize such sensor systems (Langhammer et al. 2007a, b). Even an arrangement comprising palladium disks and gold nanoparticles was reported (Poyli et al. 2012; Langhammer et al. 2010a; Tittel et al. 2012).

In the literature, predominantly wet chemical routes for the preparation of PNPs are described (Cookson 2012; Kishore et al. 2005; Hwang 2000; Wang et al. 2012; Aiken and Finke 1999; Teranishi and Miyake 1998). Furthermore, PVD (Lin et al. 2007; Stevens et al. 2008), CVD (Mekasuwandumrong et al. 2009), and the preparation of nanoscaled palladium bulk material by inert gas condensation followed by a high vacuum sinter procedure has been described in (Gleiter 2000).

Thin metallic layers can be prepared by various approaches; for example by sputtering or thermal evaporation. In this study, a particular route to prepare nanoparticles is used. First, a glass substrate is coated by sputtering a palladium layer with a thickness of a few nm. Then, as a second process step, the sample is thermally annealed which results in a dewetting of the layer. During dewetting, palladium nanoparticles are formed on the surface of the sample. This process is driven by the minimization of surface and interfacial energies and denoted as solid state dewetting. A detailed description of the dewetting procedure of gold and silver layers was presented in previous papers (Worsch et al. 2012a, b).

This paper reports on the optical features of thin-sputtered and subsequently annealed palladium layers and their behavior in contact with hydrogen.

Experimental

Fused silica glass samples with a thickness of 1.35 mm and dimensions of $22 \times 12 \text{ mm}^2$ were used for palladium coatings. Optical windows consisting of fused silica with a diameter of 32.8 mm and a thickness of 1.9 mm were used to measure the optical properties during exposure with hydrogen, inside an optical gas cuvette (Carl Zeiss, Jena, Germany). All the substrates were cleaned using a solution composed of 58.2 vol% deionised water, 29.1 vol% isopropanol, 11.7 vol% ammonia solution (25 vol%) and 1 vol% of an aqueous tenside (15 %) for 10 min at 65 °C in an ultrasonic bath. Afterward the substrates were rinsed with deionised water and treated twice again with deionised water using ultrasonic assistance. Finally, the glass substrates were dried at 110 °C for 1 h in air and stored in vacuum until the layers were sputtered.

Palladium layers were sputtered using a DC-sputter-system (Edwards Auto 306 with high vacuum

system). The target dimensions were $50 \times 50 \text{ mm}^2$; the purity of the target metal was 99.95 % (M&K GmbH Edelmetallrecycling, Kahla, Germany). In all the coating processes, the following parameters were kept constant: substrate-temperature ($21 \text{ }^\circ\text{C}$), target-substrate-distance (100 mm), the pressure in the vacuum-chamber ($<10 \text{ mPa}$), the voltage (4 kV), the argon pressure (10 Pa), and the resulting current (35 mA).

Palladium layers with a thickness of 5 nm were deposited on fused silica sheets. To control the thickness of the sputtered layer, a film thickness monitor (FTM7, BOC Edwards, UK) equipped with a quartz oscillating unit was used. Sample and thickness monitor were covered by a shutter system during the pre-sputtering procedure.

Annealing was carried out in a muffle furnace at a temperature of $900 \text{ }^\circ\text{C}$ using a rate of 10 K/min. The desired temperature was kept for 1 h. Subsequently, the furnace was switched off and allowed to cool to room temperature. This results in a mean cooling rate $<1 \text{ K/min}$ (for a detailed description: see later).

To study the effect of the cooling procedure, after annealing some samples were directly removed from the furnace to allow a rapid cooling to room temperature (cooling rate: $>800 \text{ K/min}$).

UV–Vis–NIR spectra were recorded in the wavelength range from 190 to 1,200 nm using an UV–Vis–NIR spectrometer, Shimadzu 3201 and an optical gas cuvette, shown in Fig. 3. A part of the measurements were made under argon or hydrogen atmosphere. The optical gas cuvette was equipped with two identically prepared palladium coated glasses to double the effect of hydrogen. In order to expose the palladium layers to hydrogen, first the gas cuvette was purged with argon (Argon 4.8, $\geq 99,998$ purity, Linde AG, Pullach, Germany) for 5 min to remove water and air.

Subsequently, the gas cuvette was purged with hydrogen (Hydrogen 3.0, ≥ 99.9 purity, Linde AG, Pullach, Germany) for 5 min.

The electron micrographs were recorded using a scanning electron microscope (SEM JEOL 7001F). For that purpose, most samples had to be coated with a thin carbon layer to avoid charging of the sample surface during scanning.

The particle size distribution was determined by an image analyzing software (AxioVision Ver. 4.8, Carl Zeiss Microscopy GmbH, Jena, Germany).

The calculation of the Q_{Ext} spectra were performed with the software MiePlot 4.3 (supplied by Phillip Laven) (Laven 2003; Sadeghi et al. 2012). For the calculations, the determined dielectric function of palladium reported by Weaver and Benbow (1975) (Haynes and Lide 2010) and the experimental refractive indices (in the wavelength range from 200 to 1,000 nm) of fused silica provided by Maltsion (1965) were used. Furthermore, the particle size distribution determined from the SEM-micrograph was also used for the calculation.

Results and discussion

In Fig. 1, SEM-micrographs at two different observation angles are present. The image Fig. 1a is recorded perpendicular to the surface and shows round particles with diameters in the range from 20 to 200 nm (for a detailed description of the particle sizes see Fig. 2) in a locally non-uniform distribution. Near the largest particles areas without any small particles are found. In Fig. 1b, the same sample tipped by a tilt angle of 70° is shown. It is seen that the large particles are higher than the smaller ones and the dewetting angle is greater than 90° .

Fig. 1 SEM-micrographs of a palladium layer after annealing at $900 \text{ }^\circ\text{C}$ for 1 h, using a heating rate of 10 K/min and after hydrogen treatment. Two different angles for recording were used: **a** the viewing angle perpendicular to the samples surface **b** an angle of 70°

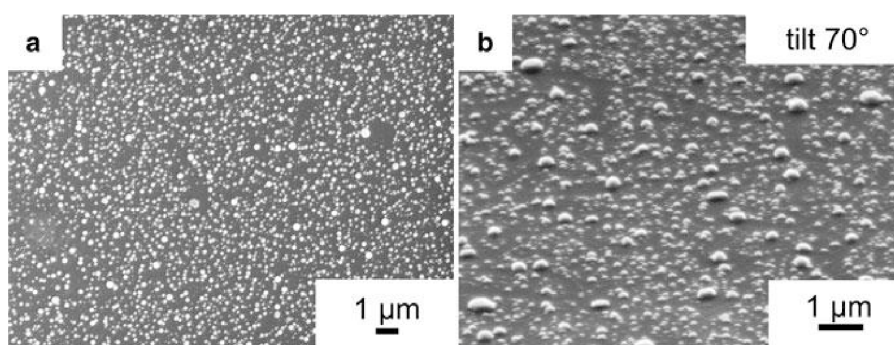


Figure 2 presents the particle size distribution determined from Fig. 1a. The particles at the edges of the image were removed and the binning size is adjusted to 5 nm. In total, 6,440 particles were counted. In the size range from 20 to 25 nm, a significant maximum in the particle size distribution is observed. Exactly 1,053 particles are assigned to this bin, corresponding to 16.4 % of all observed particles. For larger particle diameters, a flat distribution can be seen. The number of particles in each bin is approximately constant (around 200) up to a particle size of 130 nm and then decreases.

In Fig. 3a, a schematic of the optical gas cuvette is shown. To optimize the optical response, two identically palladium coated and annealed windows were used, and mounted at both ends of the tube. The coated layer with the palladium nanoparticles was placed inside. An illustration of the measurement setup for optical transmission spectroscopy is shown in Fig. 3b.

In Fig. 4, optical absorption spectra of dewetted palladium layers before (dashed line) and after (solid line) the hydrogen treatment is shown. Between the two measurements, the cuvettes were flushed with argon. The absorption spectrum of the substrate with the nanoparticle layer after annealing (see dashed curve) shows increasing absorptions with decreasing wavelengths. In this spectrum, some shoulders are observed at 630, 470, and 350 nm. At a wavelength of 270 nm, a local maximum in the absorbance is seen.

Treatment with hydrogen and subsequent purging with argon gives rise to significant changes in the spectrum. In comparison to the spectrum recorded before purging with hydrogen, the absorption

decreases in the wavelength range from 550 to 1,000 nm and below 230 nm. By contrast, at wavelengths between 230 and 550 nm, the absorption is higher in the hydrogen treated sample. The shoulders observed in the spectrum of the untreated sample are no longer visible after hydrogen treatment. The local maximum of the absorption is now located at 242 nm. A new shoulder appears at 270 nm.

In Fig. 5, optical transmission spectra recorded either under hydrogen or argon atmospheres are shown. For this purpose, the gas cuvette was first purged with argon and subsequently filled with hydrogen. This process was repeated several times and after each period of time (time schedule: see “Experimental” section), a separate spectrum was recorded (see also the inset with higher magnification shown in the upper right part of the image). The optical behavior of the particle layers under argon before hydrogen treatment was already shown in Fig. 4. The spectra recorded under a hydrogen atmosphere show increasing absorptions with decreasing wavelengths in the range from 295 to 1,000 nm. At wavelengths below 295 nm, the absorption decreases again, reaches a minimum at around 220 nm but re-increases at further decreasing wavelengths.

The spectra recorded from the samples flushed with argon after hydrogen treatment also show increasing absorptions at decreasing wavelengths. In comparison to the spectra recorded from the hydrogen filled cuvette, the absorptions are smaller at wavelengths larger than 426 nm. At wavelengths smaller than 426 nm, the absorptions are larger than those of the hydrogen purged sample and additionally a shoulder at 270 nm is seen. Also in these spectra, a maximum is observed in the UV-range at 242 nm. The spectra strongly depend on the respective gas atmosphere, however, are almost identical if recorded under the same atmosphere (using the supplied atmosphere/time schedule). As seen in the inset of Fig. 4, the differences in these spectra are within the limits of error.

For a better understanding of the spectra recorded, the spectra were simulated using the software MiePlot 4.3 using the complex dielectric function of metallic palladium. Fig. 6a, b present a comparison of calculated (Q_{EXT}) and measured absorption spectra. The measured spectrum was already shown in Fig. 5. The effect of the substrate was subtracted from the measured spectrum to get the pure optical properties of the nanoparticle layer. The vertical scale of the

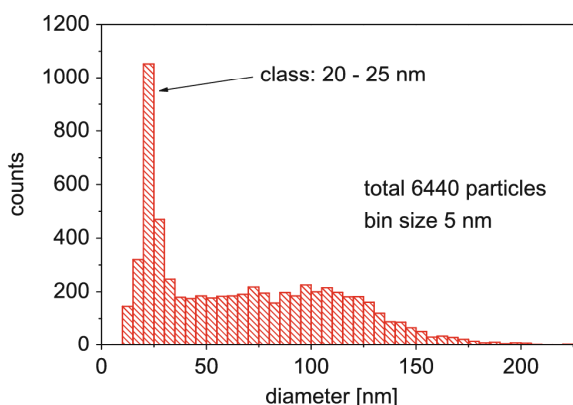


Fig. 2 Absolute particle size distribution determined from SEM-micrograph shown in Fig. 1a

Fig. 3 Schematic illustration of the optical gas cuvette, **a** functional design, **b** measurement setup for optical transmission spectroscopy

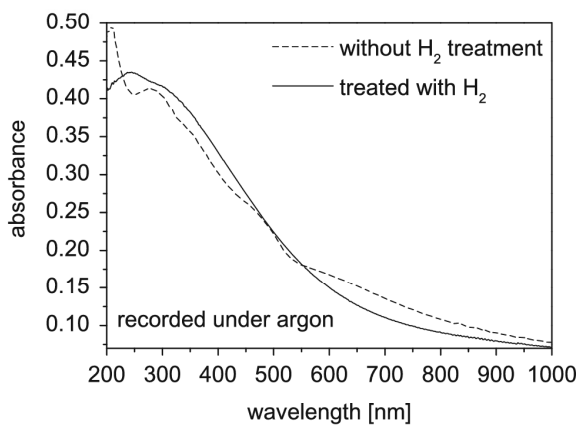
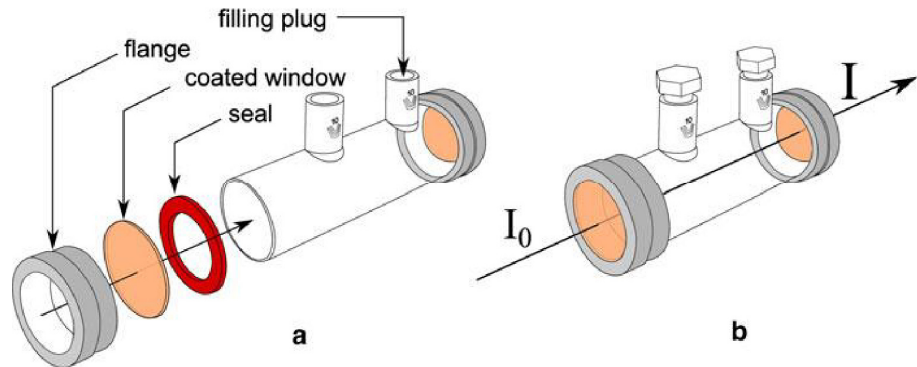


Fig. 4 Optical absorbance spectra of two palladium (one for each optical window) layers inside of an optical gas cuvette filled with Ar, after annealing at 900 °C for 1 h using a heating rate of 10 K/min with and without a hydrogen treatment

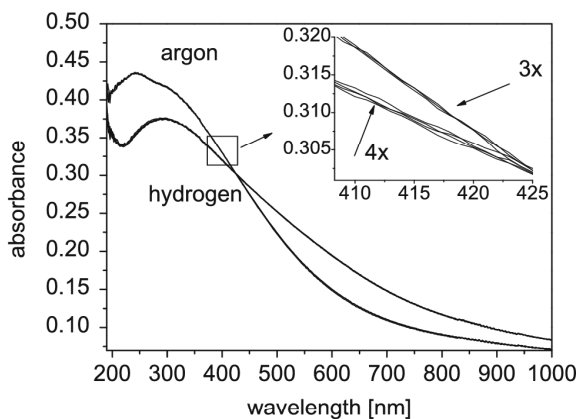


Fig. 5 Optical absorbance spectra of two palladium (one for each optical window) layers inside an optical gas cuvette, after annealing at 900 °C for 1 h using a heating rate of 10 K/min. The gas cuvette was purged alternately with hydrogen and argon

measured graph (solid lines) for better comparison was adjusted to the calculated spectrum.

In Fig. 6a, the effect of the refractive index (n) of the surrounding medium is shown for a particle diameter of 22 nm. For $n = 1.25$, an absorbance peak at 220 nm is shown. While increasing the refractive index to 1.5, the peak is shifted to 247 nm. In addition, a shoulder at wavelengths in the range from 266 to 308 nm is formed. At wavelengths between 350 and 700 nm, the slope of the measured spectrum is smaller than those of the calculated ones (Q_{Ext}).

In addition to the calculated spectra for a unique particle size of 22 nm, in Fig. 6a, a calculated spectrum using the experimentally determined particle size distribution is also shown (see Fig. 2) and a weighted dispersion relation of fused silica. In this model, the particles are located directly at the interface substrate/atmosphere and to improve the adaptation of these geometric conditions, the weighting formula of the interface is defined by

$$n_{\text{eff}}(\lambda) = g \times n_{\text{atmosphere}} + (1 - g) \times n_{\text{fused silica}}(\lambda) \quad (1)$$

For this purpose, the surface (i.e., the interface metal/atmosphere) of the nanoparticle hemisphere in contact with the atmosphere was assumed to be twice as large as the interface glass (substrate)/metal. The refractive index of the atmosphere is equal to unity. Furthermore, for frequencies attributed to UV or visible light, for SiO₂ as optically transparent material, the dielectric function can be calculated in good approximation from the refractive indices:

$$\epsilon_{\text{fused silica}}(\lambda) \approx (n_{\text{fused silica}}(\lambda))^2 \quad (2)$$

A selection of the used refractive indices is given in Table 1. It is seen that the spectrum calculated under

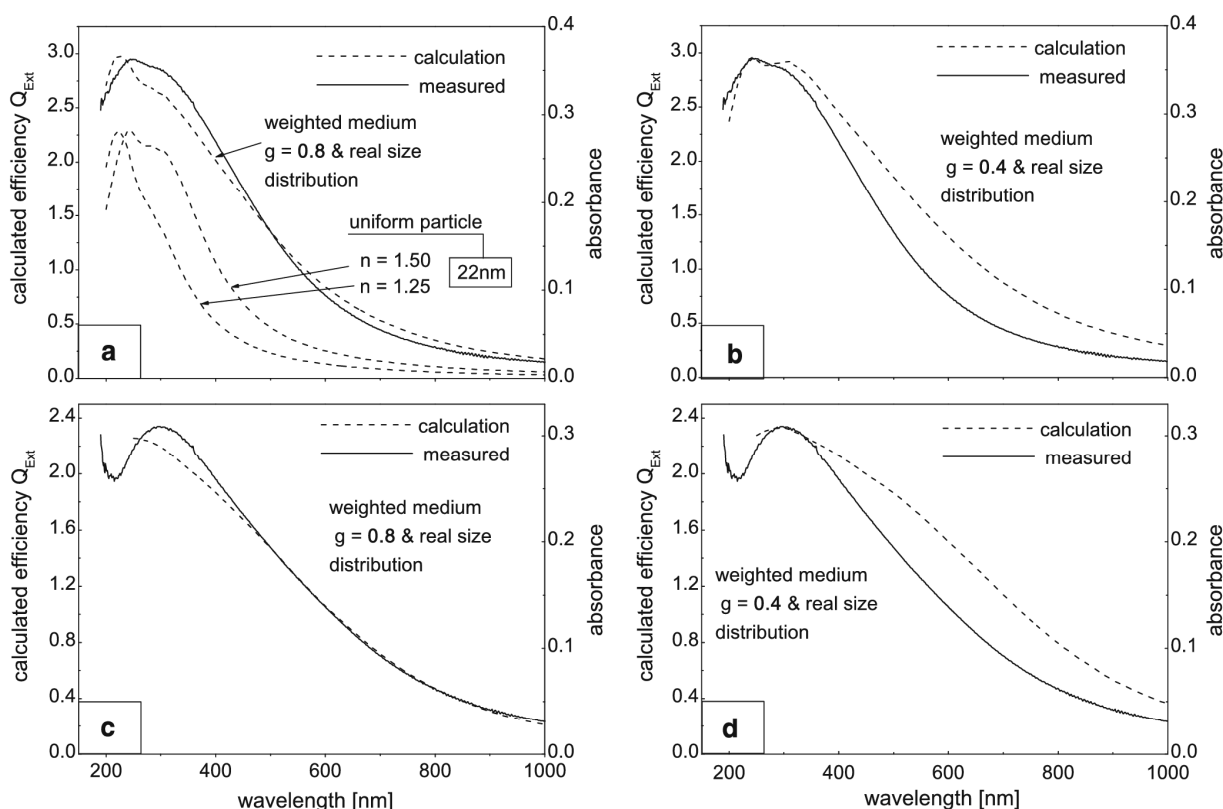


Fig. 6 A comparison of a measured absorption spectrum, and calculated Q_{Ext} spectra. The height of the measured spectrum is also adjusted to clarify. **a** For the calculation of two spectra, fixed refractive indices (n) of 1.25 and 1.5 as well as a constant particle diameter of 22 nm are used. For the calculation of two other spectra, the real particle size distribution (shown in Fig. 2) and the weighted dispersion relation with $g = 0.8$ as a function

of wavelength is used. **b** Calculated Q_{ext} spectra with weighting factor of $g = 0.4$ and real particle size distribution where used to adjusted to the maximum. **c** Calculated Q_{ext} spectra with weighting factor of $g = 0.8$ and real particle size distribution for palladium hydride. **d** Calculated Q_{ext} spectra with weighting factor of $g = 0.4$ and real particle size distribution for palladium hydride where used to adjusted to the maximum

these assumptions fits the experimental absorption spectrum much better than the calculated spectrum for unique particle size shown in Fig. 6b. The shape of the spectrum is fairly similar to the experimental one.

Figure 6b show a measured (corrected) and calculated spectrum. A weighting factor of $g = 0.4$ (see Fig. 1) was chosen, to fit the maximum of the calculated spectra at 242 nm.

Figure 6c, d present a comparison of calculated (Q_{Ext}) for palladium hydride and measured absorption spectra recorded under hydrogen. The measured spectrum was already shown in Fig. 5 and was corrected by subtraction of the absorbance spectrum of the fused silica substrates. The horizontal position was also fitted for a better comparison. The particle size distribution shown in Fig. 2 and the dielectric

Table 1 Refractive indices of fused silica (n) and dispersions relation of surrounding medium calculated by weighting function

Wavelength (nm)	n Fused silica	n Weighted surrounding medium $g = 0.4$	n Weighted surrounding medium $g = 0.8$
190	1.565	1.339	1.113
300	1.488	1.293	1.098
500	1.462	1.277	1.092
700	1.455	1.273	1.091
900	1.452	1.271	1.090

function of palladium hydride for wavelengths >250 nm (thin hydrogen loaded palladium layer) published in (Vargas et al. 2006) were used for the calculation. In Fig. 6c, a weighting factor of $g = 0.8$ was used to get a good comparison in the shape of the spectra. In Fig. 6d, a weighting factor of $g = 0.4$ was used to fit the peak positions.

Optical absorbance spectra of annealed palladium layers prepared using two different cooling rates, are presented in Fig. 7. If the cooling rate is as low as 1 K/min (dashed lines), the spectrum shows a shoulder at 490 nm and a local maximum at 275 nm. The irregularities at 830 and 360 nm are caused by the measurement system itself (switching of the detectors, grating and light source). If a much higher cooling rate was supplied (800 K/min) (the samples was removed from the hot furnace), the absorption is much smaller at wavelengths higher than 230 nm. The shoulder at 490 nm is no longer visible and the local maximum at 275 nm is shifted to 290 nm (with a simultaneous decrease of the absorption difference between the local maximum and minimum).

In Fig. 8, a measured temperature/time graph is presented. At 900 °C, the temperature, the samples were annealed, metallic palladium is thermodynamically stable in contact with air, i.e., PdO which might be formed is decomposed. During cooling, the temperature passes a range ($T < 819$ °C)(Bayer and Wiedemann 1975) in which PdO is the thermodynamically stable phase in equilibrium with air. During slowly cooling, it takes 5 h 43 min until the temperature decreases to 258 °C, the temperature below which palladium does no longer react with oxygen

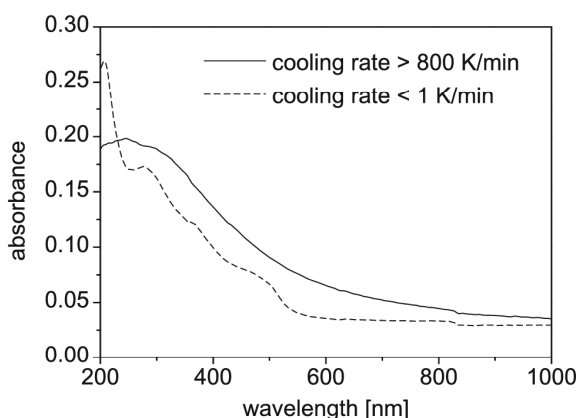


Fig. 7 Optical absorbance spectra of annealed palladium layers prepared using different cooling rates

because the kinetics are frozen. The two samples which spectra are shown in Fig. 7 differ by the cooling rates supplied during the preparation of the samples. The residence time of the respective samples in the temperature range, PdO is formed is sketched for the two samples. First (solid lines), the sample is removed from the furnace directly, and second (dashed lines), the sample is cooled to room temperature (see Fig. 8) inside the furnace, limited by the heat capacity of the furnace. The slowly cooled sample is during a far longer period of time in that temperature range PdO is formed than the rapidly cooled sample. Hence, PdO should occur in a far larger extend in the slowly cooled sample.

Sputtering palladium on fused silica leads to the formation of palladium layers. Subsequent annealing at 900 °C for 1 h results in the formation of well-separated round palladium particles with diameters in the range from 20 to 200 nm with a significant statistical accumulation of particles having diameters in the range from 20 to 25 nm. Fluctuations in the thickness of the layer and in the aging processes such as Ostwald ripening lead to the formation of particles with larger diameters.

The optical properties are studied using a gas cuvette system shown in Fig. 3. After the first contact with hydrogen and subsequent purging with argon,

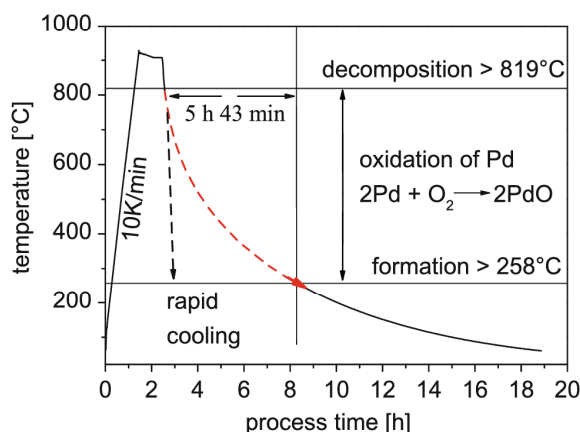


Fig. 8 Temperature/time schedule and stability of PdO. Heating rate: 10 K/min, soaking time: 1 h. Two different cooling procedures were used: *solid line* samples were slowly cooled inside the furnace, supplying a mean cooling rate of 1 K/min, *dashed line* after annealing, the samples were removed from the furnace, the cooling rate is approximately 800 K/min. In addition, the temperature area of stable formation of palladium(II)oxide is shown. The temperatures were taken from (Bayer and Wiedemann 1975)

the optical properties are changed irreversibly (Fig. 4). This can be explained as follows: during annealing of the layer, particles of metallic palladium are formed at a temperature, Pd is thermodynamically stable. During cooling, these particles react with oxygen of the atmosphere and PdO should be formed at least at the surface of the metallic particles. A rapid cooling leads to a lower amount of PdO formed at the particles surface. This is due to the shorter residence time. The spectra presented in Fig. 7 show a significant change in their shape with different cooling rates. The samples cooled to room temperature in few seconds (solid lines) show spectra similar to those of the metallic nanoparticles (see Fig. 5). The total absorbance is lower because only one layer has been measured, in contrast to the experimental set-up of the cuvette with two coated windows. The other sample was cooled to room temperature within more than 18 h and is more than 5 h in the temperature range (258–819 °C) where PdO is formed. These temperatures were taken from Bayer and Wiedemann (1975). We used the onset of the formation of PdO at 258 °C and the offset of the decomposition at 819 °C, because the measured PdO is created during cooling. During purging the cell with hydrogen, palladium(II)oxide should first be reduced to metallic palladium. Furthermore, palladium hydride might be formed. During subsequent purging with argon, notable changes of the spectra are observed. An alternating purging with hydrogen and argon shows a highly reversible change in the spectra. The discrepancies in the individual graphs are marginal and within the error of the measurement. The local maximum in the absorption spectrum shifts to 295 nm and the absorbance is decreased. Also the shape in the local maximum is changed, no shoulder is observed.

The differences in the spectra obtained in the presence of hydrogen and of argon must have their reasons in the electronic structure of the nano particles. It is well-known that palladium incorporates hydrogen and forms palladium hydride. This process is associated with a concentration and temperature dependent structural transformation of the lattice and leads to permanent changes in the crystal structure (Flanagan and Oates 1991).

During the past decade, it turned out that these results obtained from the bulk material cannot directly be applied to nanoscale systems. For nanocrystalline palladium samples, a different behavior with respect to

hydrogen was found (Mütschele and Kirchheim 1987; Kirchheim 1988; Pundt 2005). It was described that the crystal phase transformation from the solid solution (alpha) to the hydride phase (beta) inside particles is hindered near the surface (Pundt 2005). For the optical properties, induced by the movement of electron gas, the electronic structure of palladium and the effect of the hydrogen incorporation hereon is crucial. In this context, also the lattice strain is important, because a change in the interatomic distances also changes the band structure (Pundt 2005; Ruban et al. 1997). This runs parallel to a modification of the dielectric function of palladium. Furthermore, hydrogen will be incorporated into the palladium lattice, which also affects the dielectric function (Kishore et al. 2005; Tittl et al. 2012). Vargas et al. observed that the electron density in the conductive band will be decreased by filling the sp states and screening the conductive d electron. A change in the electronic band structure is also indicated by the disappearance of the shoulder observed in the spectrum of pure palladium. This shoulder results directly from the real and imaginary part of the dielectric function of the pure metal. These functions also have shoulders at the respective wavelengths, which are directly observed in the optical spectrum. This behavior can also be seen in Fig. 6a, b. The changes in the spectra observed during flushing with hydrogen and argon are reversible. It is assumed that also the incorporation of hydrogen into the lattice of palladium nanoparticle and especially the modification of their band structure and hence of their optical properties is a reversible process.

The calculation of the spectra where performed with the software MiePlot 4.3. This software is based on BHMIE-code from Bohren and Huffman (1983). Due to the mathematical conception of the theory behind this algorithm, a sphere as scattering particle is necessary for the simple case. Certainly, recent calculations of optical properties by Sandu (2012a) based on the boundary integral method shows that marginal deviations from the spherical form only induce a negligible influence on the theoretical spectra in case of the quasi-static approximation. However, other local optical properties (e.g., near-field enhancement) are more affected by such a change in shape (Sandu 2012b). The assumption that an ideal spherical shape of the particles is generated by dewetting, is only an approximation. In addition, the particles are located directly at the interface between atmosphere

and substrate, therefore, an (weighted) approximation of the surrounding matrix must be introduced. Furthermore, the interactions of particles with each other are not considered and the particle distribution is normalized to the size of a single scattering particle.

It should be noted that using the particle size distribution experimentally determined from the SEM-micrographs results in a better agreement with the experimental spectra (see Fig. 6a). However, a problem with the adaptation of the system is seen. An adjustment to the maximum of the absorption shows a significant deviation from the shape of the spectrum. Conversely, an adaptation to the shape results in a shift of the calculated absorption maximum to smaller wavelengths. Such a deviation may be explained by the more significant deviation from the spherical shape and hence varying contact to the substrate used for the calculation inside BHMIE-Algorithms.

The preparation method is suited for industrial application very well and devices based on palladium nanoparticles fixed on glass might be utilized as components for gas sensors. Through the preparation by a non-chemical procedure, an application in chemical industry by a high purity catalytic active layer is conceivable.

Conclusion

A non-chemical method for the formation of metallic nanoparticles fixed on a glass surface, offers the advantage of a pure system without the addition of any stabilizing agents. In this paper, a non-chemical route to produce palladium nanoparticles is presented, which provides good conditions to describe the optical properties. A thin layer of metallic palladium is deposited onto fused silica. Subsequent annealing at 900 °C results in the formation of particles with diameters in the range from 20 to 200 nm. A first time purging with hydrogen leads to an irreversible change in the optical spectra due to the reduction of PdO to metallic palladium. The extent of the formation of PdO is strictly dependent on the cooling procedure, because the PdO in contact with air gets thermodynamically stable in the temperature range from 258 to 819 °C. Subsequent hydrogen treatments lead to a significant reversible change in the optical properties of the particle layer by manipulation of the electronic band structure. Simulations of the spectra were performed

using the real particle size distribution, a weighted dispersions relation to adapt to geometrical conditions and complex dielectric functions of palladium and palladium hydride. A good agreement with measured spectra was found and the dependency of the surrounding media can be explained by calculations based on Mie theory and the respective dielectric functions. The measured spectra are due to the Plasmon Resonance of metallic palladium nanoparticles. Also, the change during the contact with hydrogen is due to changes in the dielectric function of the nanoparticles.

Acknowledgments This work is supported by the DFG “Deutsche Forschungsgemeinschaft” under Grant. Nos.: Se 698/10-1 and Se 698/10-2.

References

- Aiken JD, Finke RG (1999) A review of modern transition-metal nanoclusters: their synthesis, characterization, and applications in catalysis. *J Mol Catal A* 145(1–2):1–44
- Bayer G, Wiedemann H (1975) Formation, dissociation and expansion behavior of platinum group metal oxides (PdO, RuO₂, IrO₂). *Thermochim Acta* 11(1):79–88
- Bérubé V, Radtke G, Dresselhaus M, Chen G (2007) Size effects on the hydrogen storage properties of nanostructured metal hydrides: a review. *Int J Energy Res* 31(6–7):637–663
- Bohren CF, Huffman DR (1983) Absorption and scattering of light by small particles. Wiley, New York
- Cookson J (2012) The preparation of palladium nanoparticles. *Platinum Met Rev* 56(2):83–98
- Creighton JA, Eadon DG (1991) Ultraviolet-visible absorption spectra of the colloidal metallic elements. *J Chem Soc Faraday T* 87(24):3881
- Daniel MC, Astruc D (2004) Gold nanoparticles: assembly, supramolecular chemistry, quantum-size-related properties, and applications toward biology, catalysis, and nanotechnology. *Chem Rev* 104(1):293–346
- Edwards JK, Solsona B, Ntainjua EN, Carley AF, Herzing AA, Kiely CJ, Hutchings GJ (2009) Switching off hydrogen peroxide hydrogenation in the direct synthesis process. *Science* 323(5917):1037–1041
- Flanagan TB, Oates WA (1991) The palladium-hydrogen system. *Annu Rev Mater Sci* 21(1):269–304
- Gleiter H (2000) Nanostructured materials: basic concepts and microstructure. *Acta Mater* 48(1):1–29
- Hakamada M, Nakano H, Furukawa T, Takahashi M, Mabuchi M (2010) Hydrogen storage properties of nanoporous palladium fabricated by dealloying. *J Phys Chem C* 114(2):868–873
- Haynes WM, Lide DR (2010) CRC handbook of chemistry and physics. CRC Press, Boca Raton
- Hwang CB, Fu YS, Lu YL, Jang SW, Chou PT, Wang CRC, Yu SJ (2000) Synthesis, characterization, and highly efficient catalytic reactivity of suspended palladium nanoparticles. *J Catal* 195(2):336–341

- Katzer C, Grosse V, Schmidl F, Michalowski P, Schmidl G, Mueller R, Dellith J, Schmidt C, Jatschka J, Fritzsche W (2012) YBa₂Cu₃O₇-delta matrix-induced in situ growth of plasmonic Au nanoparticles for biological sensor devices. *J Nanopart Res* 14(12):1285
- Ke X, Kramer GJ, Løvrvik OM (2004) The influence of electronic structure on hydrogen absorption in palladium alloys. *J Phys Condens Matter* 16(34):6267–6277
- Kirchheim R (1988) Hydrogen solubility and diffusivity in defective and amorphous metals. *Prog Mater Sci* 32(4):261–325
- Kirchheim R, Mütschele T, Kieninger W, Gleiter H, Birringer R, Koblé T (1988) Hydrogen in amorphous and nanocrystalline metals. *Mater Sci Eng* 99(1–2):457–462
- Kishore S, Nelson JA, Adair JH, Eklund PC (2005) Hydrogen storage in spherical and platelet palladium nanoparticles. *J Alloy Compd* 389(1–2):234–242
- Langhammer C, Kasemo B, Zorić I (2007a) Absorption and scattering of light by Pt, Pd, Ag, and Au nanodisks: absolute cross sections and branching ratios. *J Chem Phys* 126(19):194702
- Langhammer C, Zorić I, Kasemo B, Clemens BM (2007b) Hydrogen storage in Pd nanodisks characterized with a novel nanoplasmonic sensing scheme. *Nano Lett* 7(10):3122–3127
- Langhammer C, Larsson EM, Kasemo B, Zorić I (2010a) Indirect nanoplasmonic sensing: ultrasensitive experimental platform for nanomaterials science and optical nanocalorimetry. *Nano Lett* 10(9):3529–3538
- Langhammer C, Zhdanov VP, Zorić I, Kasemo B (2010b) Size-dependent hysteresis in the formation and decomposition of hydride in metal nanoparticles. *Chem Phys Lett* 488(1–3):62–66
- Langhammer C, Zhdanov VP, Zorić I, Kasemo B (2010c) Size-dependent kinetics of hydriding and dehydriding of Pd nanoparticles. *Phys Rev Lett* 104(13):135502
- Laven P (2003) Simulation of rainbows, coronas, and glories by use of Mie theory. *Appl Opt* 42(3):436
- Lin CM, Hung TL, Huang YH, Wu KT, Tang MT, Lee CH, Chen CT, Chen YY (2007) Size-dependent lattice structure of palladium studied by X-ray absorption spectroscopy. *Phys Rev B* 75(12):125426
- Maltsion IH (1965) Interspecimen comparison of the refractive index of fused silica. *J Opt Soc Am* 55(10):1205
- Manchester FD, San-Martin A, Pitre JM (1994) The H–Pd (hydrogen–palladium) system. *J Phase Equilibria* 15(1):62–83
- Mekasuwandumrong O, Somboonthanakij S, Praserttham P, Panpranot J (2009) Preparation of nano-Pd/SiO₂ by one-step flame spray pyrolysis and its hydrogenation activities: comparison to the conventional impregnation method. *Ind Eng Chem Res* 48(6):2819–2825
- Mie G (1908) Beiträge zur optik trüber medien, speziell kolloidaler metallösungen. *Ann Phys Berlin* 330(3):377–445
- Mulvaney P (1996) Surface plasmon spectroscopy of nanosized metal particles. *Langmuir* 12(3):788–800
- Mütschele T, Kirchheim R (1987) Segregation and diffusion of hydrogen in grain boundaries of palladium. *Scripta Metall* 21(2):135–140
- Poyli MA, Silkin VM, Chernov IP, Echenique PM, Muiño RD, Aizpurua J (2012) Multiscale theoretical modeling of plasmonic sensing of hydrogen uptake in palladium nanodisks. *J Phys Chem Lett* 3(18):2556–2561
- Pundt A (2005) *Nanoskalige Metall–Wasserstoff–Systeme*. Universitätsverlag Göttingen, Göttingen
- Quinten M (2011) *Optical properties of nanoparticle systems*. Wiley-VCH-Verlag, Weinheim
- Ruban A, Hammer B, Stoltze P, Skriver HL, Nørskov JK (1997) Surface electronic structure and reactivity of transition and noble metals. *J Mol Catal A* 115(3):421–429
- Sadeghi I, Munoz A, Laven P, Jarosz W, Seron F, Gutierrez D, Jensen HW (2012) Physically-based simulation of rainbows. *ACM T Graphic* 31(1):1–12
- Sandu T (2012a) Shape effects on localized surface plasmon resonances in metallic nanoparticles. *J Nanopart Res* 14(6):905
- Sandu T (2012b) Eigenmode decomposition of the near-field enhancement in localized surface plasmon resonances of metallic nanoparticles. *Plasmonics*. doi:10.1007/s11468-012-9403-z
- Schauermann S, Hoffmann J, Johánek V, Hartmann J, Libuda J, Freund HJ (2002) Catalytic activity and poisoning of specific sites on supported metal nanoparticles. *Angew Chem Int Edit* 41(14):2532–2535
- Shipway AN, Katz E, Willner I (2000) Nanoparticle arrays on surfaces for electronic, optical, and sensor applications. *Chem Phys Chem* 1(1):18–52
- Silkin VM, Díez Muiño R, Chernov IP, Chulkov EV, Echenique PM (2012) Tuning the plasmon energy of palladium–hydrogen systems by varying the hydrogen concentration. *J Phys Condens Matter* 24(10):104021
- Stevens KJ, Ingham B, Toney MF, Brown SA, Lassesson A (2008) Structure of palladium nanoclusters for hydrogen gas sensors. *Curr Appl Phys* 8(3–4):443–446
- Teranishi T, Miyake M (1998) Size control of palladium nanoparticles and their crystal structures. *Chem Mater* 10(2):594–600
- Tittl A, Kremers C, Dorfmueller J, Chigrin DN, Giessen H (2012) Spectral shifts in optical nanoantenna-enhanced hydrogen sensors. *Opt Mater Express* 2(2):111–118
- Vargas WE, Rojas I, Azofeifa DE, Clark N (2006) Optical and electrical properties of hydrided palladium thin films studied by an inversion approach from transmittance measurements. *Thin Solid Films* 496(2):189–196
- Wang W, Yang Q, Zhou R, Fu HY, Li RX, Chen H, Li XJ (2012) Palladium nanoparticles generated from allylpalladium chloride in situ: a simple and highly efficient catalytic system for Mizoroki-Heck reactions. *J Organomet Chem* 697(1):1–5
- Weaver JH, Benbow RL (1975) Low-energy interband absorption in Pd. *Phys Rev B* 12(8):3509–3510
- Worsch C, Kracker M, Wisniewski W, Rüssel C (2012a) Optical properties of self assembled oriented island evolution of ultra-thin gold layers. *Thin Solid Films* 520(15):4941–4946
- Worsch C, Wisniewski W, Kracker M, Rüssel C (2012b) Gold nano-particles fixed on glass. *Appl Surf Sci* 258(22):8506–8513

3.5

M. Kracker C. Worsch, C. Rüssel

The effect of thermal annealing and hydrogen on the morphology and the optical properties of thin palladium layers

Materials Letters 110 (2013) 114–116

DOI: <http://dx.doi.org/10.1016/j.matlet.2013.07.133>

The effect of thermal annealing and hydrogen on the morphology and the optical properties of thin palladium layers				
Beteiligt an				
	Michael Kracker	Dr. Christian Worsch	Prof. Christian Rüssel	
Konzeption des Forschungsansatzes	X		X	
Planung der Untersuchung	X			
Datenerhebung	X			
Datenanalyse und Interpretation	X	X		
Schreiben des Manuskripts	X	X	X	
Vorschlag Anrechnung Publikationsäquivalente	1,0			



The effect of thermal annealing and hydrogen on the morphology and the optical properties of thin palladium layers



Michael Kracker*, Christian Worsch, Christian Rüssel

Otto-Schott-Institut, Jena University, Fraunhoferstraße 6, 07743 Jena, Germany

ARTICLE INFO

Article history:

Received 15 May 2013

Accepted 31 July 2013

Available online 9 August 2013

ABSTRACT

Layers of 12 nm thickness were sputtered on fused silica sheets. Annealing at 720 °C in air results in dense palladium oxide layers with an optical band gap of 1.99 ± 0.01 eV and a surface roughness of 1.95 nm. Subsequent purging with hydrogen leads to the transformation to a metallic Pd layer with increased roughness. It was demonstrated that the oxidation and reduction is responsible for permanent changes of the optical properties and not only the interaction of hydrogen with metallic palladium.

© 2013 Elsevier B.V. All rights reserved.

1. Introduction

In material science and chemistry, palladium has extensively been studied. Nanoparticles, thin layers and foams (Pd-black) were of considerable interest, especially with respect to the interaction with hydrogen [1,2]. In particular, the utilization as a storage material for hydrogen has been discussed. Furthermore, it is frequently used as catalyst, membrane, in sensors, and filters.

However, from materials science perspective not only the palladium-hydrogen system is of particular importance. As previously shown, palladium nanoparticles, formed by dewetting of a 5 nm thin sputtered palladium layer on a glassy substrate at 900 °C have very special optical properties which change significantly if they are oxidized to palladium oxide [3]. It is also well known that PdO is reduced in the presence of hydrogen [4].

Thus, an oxidic layer on palladium nanoparticles can be removed by hydrogen [5]. This leads to a significant change in the optical properties. Nevertheless, studies on the optical properties of PdO films and PdO films in interaction with hydrogen have scarcely been reported. Han et al. [4] demonstrated that the surface morphology is changed after PdO is reduced to metallic Pd and found an increase in the surface area of Pd single crystals after reduction of PdO with hydrogen. Rey et al. [6] reported on the optical properties of PdO layers with thickness in the range from 48 to 218 nm and determined a value of 2.13 eV for the optical band gap.

This article presents a study on the surface morphology and the optical properties of thin oxidized Pd layers and layers subsequently treated with hydrogen.

2. Materials and methods

Fused silica glass samples with 1.25 mm thickness and a dimension of 14×48 mm² were used as substrates. They were cleaned using a 5% commercial cleaning solution Tickopur R36 applied for 10 min at 65 °C in an ultrasonic bath. Subsequently, the substrates were rinsed with deionised water and treated twice again in deionised water with ultrasonic assistance. Finally, the glass substrates were dried at 110 °C for 1 h.

Palladium layers were sputtered using a DC-sputter-system (Edwards Auto 306). The target dimensions were 50×50 mm² (purity 99.95%). During the coating process the following parameters were kept constant: substrate-temperature (21 °C), target-substrate-distance (110 mm), pressure (< 10 mPa), voltage (4 kV) and argon pressure (10 Pa). The supplied conditions resulted in a current of 35 mA.

The thickness of the sputtered palladium layer was 12 nm as controlled using a shutter and a film thickness monitor (FTM7, BOC Edwards).

Annealing was carried out in a muffle furnace at a temperature of 720 °C in air (heating rate 10 K/min). The temperature was kept for 1 h (cool down inside the furnace).

The coated and annealed silica substrates were placed in a special chamber and first purged with argon (purity 99.998) for 5 min in order to remove oxygen from the furnace atmosphere. Subsequently, the sample chamber was purged with hydrogen (purity 99.9) for 5 min. The same procedure was repeated with a not annealed sample.

UV-vis-NIR spectra were recorded at room temperature in the wavelength range from 190 to 1200 nm using an UV-vis-NIR spectrometer, Shimadzu 3201. An uncoated sample was placed in the reference beam. The layer morphology and the arithmetic roughness R_a was determined using an atomic force microscope (Zeiss Ultraobjektiv, SIS).

* Correspondence to: Fraunhoferstraße 6, 07743 Jena, Otto-Schott-Institut, Jena University, Germany. Tel.: +49 3 641 948522; fax: +49 03641 948502.

E-mail address: michael.kracker@uni-jena.de (M. Kracker).

Micrographs were performed using a scanning electron microscope (SEM JEOL 7001F). The samples were coated with a thin carbon layer to avoid charging of the sample surface.

3. Results

In Fig. 1, SEM and AFM micrographs at three different stages are shown. At the left column (Fig. 1a) a 12 nm thick freshly sputtered Pd-layer is presented; the images show a smooth and flat surface morphology (an exact overview is given in Table 1). The SEM micrograph shows the typical structure of a sputtered layer with voids and flaws. The center column (Fig. 1b) shows the layer after annealing at 720 °C for 1 h. A granular structure is seen in the SEM and AFM images.

The structure of the layer after purging with hydrogen is presented at the right column (Fig. 1c). The SEM image reveals a structure with voids, flaws and some additional particle-like fragments similar to that of the sputtered. The AFM image shows a granular structure similar to the treated morphology shown in Fig. 1b.

Fig. 2a presents optical transmission spectra of a freshly sputtered film, an annealed film and a film annealed and subsequently purged with hydrogen. The optical spectrum of the freshly sputtered Pd-layer shows an almost linear curve with a slight increase in the transmission from 36% to 49% for 200 and 1200 nm, respectively. After annealing at 720 °C, the transmission increases rapidly from 31% at 500 nm to 92% at 1200 nm. At wavelengths below 500 nm, shoulders at 450, 350 and 270 nm occur. While increasing the wavelength from 210 to 270 nm, the transmission increases from 20 to 39%. After purging the annealed

layer with hydrogen, the shape of the transmission curve becomes more flat and the transmission decreases from 50% at 200 nm to 32% at 1200 nm with a small additional transmission minimum at 270 nm.

In order to determine the onset of the optical band gap, the absorbance of the annealed layer was plotted against the photon energy (see Fig. 2b). The graphical method for determining the optical band gap energy is indicated by the tangent. The determined band gap is 1.99 ± 0.01 eV.

Fig. 3 presents an optical transmission spectra of a freshly sputtered 12 nm Pd layer before and after purging with hydrogen for 5 min. The two spectra show a nearly identical shape with a slight increase of the transmission from 34% at 200 nm to 47% at 1200 nm. The inset presents a part of the spectra in a higher magnification and shows that the deviation of the two spectra is smaller than 1%.

4. Discussion

Sputtering palladium onto fused silica substrates results in the formation of a smooth ($R_a=0.61$ nm) palladium layer. During annealing in air, the layer is oxidized to PdO [7]. The difference in the densities ($Pd=12$ g/cm³, $PdO=8.3$ g/cm³) [8] of the two phases causes a swelling of the layer. This leads to the granular morphology observed in Fig. 1b which runs parallel with an increase in roughness to $R_a=1.95$ nm. Palladium oxide in contact with hydrogen is reduced to metallic palladium as follows:

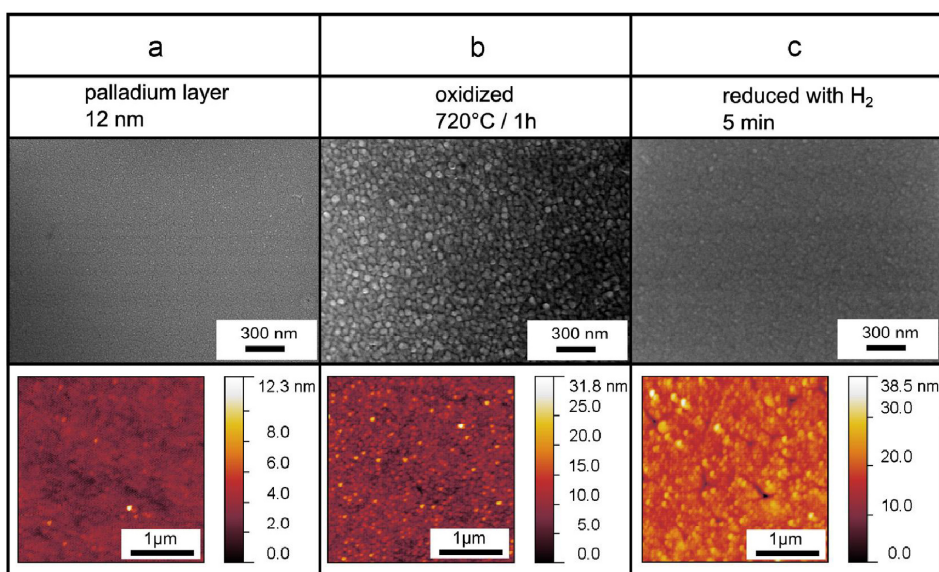
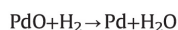


Fig. 1. SEM (top-row) and AFM (bottom-row) micrographs (a) of freshly sputtered Pd layers, (b) annealed at 720 °C for 1 h and (c) annealed at 720 °C and subsequently treated with H₂ for 5 min at room temperature.

Table 1
Treatment of the samples, roughness, optical bandgap and transmittance at selected wavelengths.

Sample	Annealing	Purging	Roughness R_a [nm]	Bandgap [eV]		Transmittance [%]		
				Onset	Offset	300 nm	600 nm	1000 nm
Pd-layer	–	–	0.61	–	–	37	42	47
PdO-layer	720 °C/1 h	–	1.95	1.99 ± 0.01	2.45 ± 0.01	32	60	89
Pd (reduced)	720 °C/1 h	H ₂ for 5 min	1.95	–	–	44	37	35

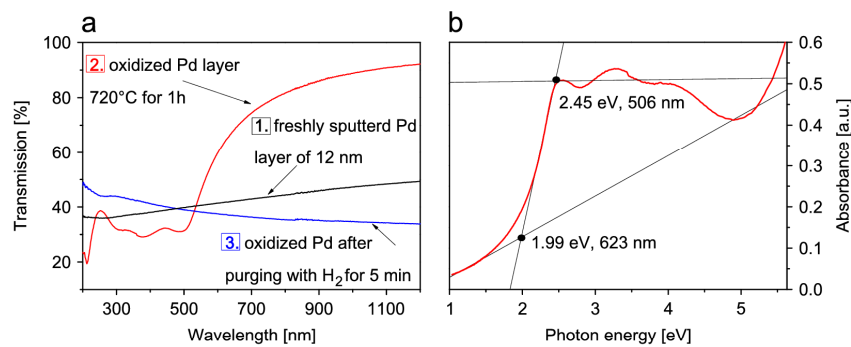


Fig. 2. (a) UV-vis-NIR transmission spectra of freshly sputtered, annealed and reduced Pd-layers and (b) recalculated transmission spectra for the graphical onset and offset determination of the optical band gap.

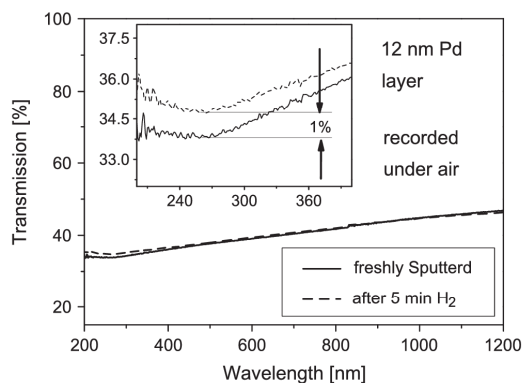


Fig. 3. UV-vis-NIR transmission spectra of a freshly sputtered Pd layer before and after purging with hydrogen without any annealing.

The reduction to the metallic layer with hydrogen does not lead to a structure and roughness similar to that of the initial layer after sputtering, nevertheless, the density increases again. Thus, the surface morphology ($R_a = 1.95$ nm) is retained, however, additionally cracks are formed (Fig. 1c).

Palladium layers show a uniform absorbance over a wide spectral range as presented in Fig. 2a and b. During annealing, a significant change in the shape of the spectra is observed. Palladium oxide is a semiconductor with a small optical band gap (2.13 eV) [6]. This results in a strong increase on absorbance at energies below a characteristic value (see Fig. 2a) which enabled to determine the onset of the optical band gap to 1.99 ± 0.01 eV. This value is smaller than for bulk palladium which is due to the small layer thickness (and the resulting small interaction volume) as well as to impurities and defects which might lead to a “blurring” of the spectral band gap position [9]. The origin of the peaks at higher energies is not completely clarified. However, it can be assumed that they result from the band structure.

The phase transition between the alpha (solid solution Pd+H) and the beta (PdH) phase runs parallel to a change in density, the formation of stress, and an increasing disorder of the crystal structure [1,10]. The reduction of the oxide layer to the metallic layer results in a permanent change of the optical transmission spectra also in comparison to the freshly sputtered Pd layer. However, such a change does not occur in a fresh Pd layer during hydrogen treatment (Fig. 3). Accordingly, the change in optical properties is based on the structural transformation during the

oxidation and reduction procedure. In this case, recrystallization and the effect of the grain boundary are mentioned [11,12]. This is of special importance since grain boundaries give rise to enhanced diffusion.

In addition to morphological changes of the surface, structural changes are also possible. Possibly an amorphous metallic layer on (100) and (111) palladium single crystals occurs after reduction of PdO with hydrogen, as suggested by Han et al. [4,11,13].

5. Conclusion

A sputtered palladium layer with a thickness of only 12 nm was oxidized in air at 720 °C without the formation of particles by dewetting. After the semiconductor PdO is formed, a strong optical absorbance in visible range is observed. An optical band gap of 1.99 ± 0.01 eV (onset) was determined. Subsequent purging with hydrogen gas results in a transformation to a metallic Pd layer with modified optical properties, caused by the structural transformation during oxidation and reduction procedure. This is indicated by an increasing roughness value.

Acknowledgments

This work is supported by the DFG Deutsche Forschungsgemeinschaft (Se 698/10-1 and Se 698/10-2).

References

- [1] Flanagan TB, Oates WA. Annual Review of Materials Science 1991;21:269–304.
- [2] Kishore S, Nelson JA, Adair JH, Eklund PC. Journal of Alloys and Compounds 2005;389:234–42.
- [3] Kracker M, Worsch C, Rüssel C. Journal of Nanoparticle Research 2013;15:1–10.
- [4] Han J. Journal of Catalysis 2004;225:7–15.
- [5] Avila JI, Matelon RJ, Trabol R, Favre M, Lederman D, Volkmann UG, et al. Journal of Applied Physics 2010;107:23504.
- [6] Rey E, Kamal MR, Miles RB, Royce BSH. Journal of Materials Science 1978;13:812–6.
- [7] Bayer G, Wiedemann H. Thermochimica Acta 1975;11:79–88.
- [8] Haynes WM, Lide DR. CRC handbook of chemistry and physics. 91st ed. Boca Raton: CRC Press; 2010.
- [9] Nilsson PO, Shivaraman MS. Journal of Physics C 1979;12:1423–7.
- [10] Manchester FD, San-Martin A, Pitre JM. Journal of Phase Equilibria 1994;15:62–83.
- [11] Sun ZQ, Cao CB, Cao L, Liang P, Huang XF, Song XP. Vacuum 2010;84:828–32.
- [12] Straumal B, Mazilkin A, Protasova S, Myatiev A, Straumal P, Goering E, et al. Physica Status Solidi B 2011;248:1581–6.
- [13] Han J, Zemlyanov DY, Ribeiro FH. Surface Science 2006;600:2730–44.

3.6

M. Kracker C. Worsch, W. Seeber, C. Rüssel

Optical hydrogen sensing with modified Pd-layers: A kinetic study of roughened layers and dewetted nanoparticle films

Sensors and Actuators B: Chemical, 197 (2014) 95–103

DOI: <http://dx.doi.org/10.1016/j.snb.2014.02.063>

Optical hydrogen sensing with modified Pd-layers: A kinetic study of roughened layers and dewetted nanoparticle films				
Beteiligt an				
	Michael Kracker	Dr. Christian Worsch	Dr. Wolfgang Seeber	Prof. Christian Rüssel
Konzeption des Forschungsansatzes	X		X	X
Planung der Untersuchung	X			
Datenerhebung	X			
Datenanalyse und Interpretation	X	X		
Schreiben des Manuskripts	X	X	X	X
Vorschlag Anrechnung Publikationsäquivalente	1,0			
Anmerkung: Weitere Informationen sind in Appendix A aufgeführt.				



Optical hydrogen sensing with modified Pd-layers: A kinetic study of roughened layers and dewetted nanoparticle films



Michael Kracker*, Christian Worsch, Wolfgang Seeber, Christian Rüssel

Otto-Schott-Institut, Jena University, Fraunhoferstr. 6, 07743 Jena, Germany

ARTICLE INFO

Article history:

Received 21 November 2013

Received in revised form 13 February 2014

Accepted 17 February 2014

Available online 25 February 2014

Keywords:

Sputtering

Dewetting

Hydrogen sensing

Optics

Morphologies

ABSTRACT

Thin palladium layers with thickness of 5, 8, 14 or 18 nm were sputtered on fused silica slides. Heat treatment procedures were performed to increase the optical response of palladium layers during purging with hydrogen. First, the layers were oxidized and additionally reduced with hydrogen, to modify the layer roughness. Second, a 5 nm thick layer was dewetted to obtain nanoparticles. This leads to an increase of the optical response by up to the factor of 16. Additionally, the type of the optical response has changed in the case of the nanoparticle layers. The light transmission was determined with simple and inexpensive measuring instrument, described in detail in this article.

© 2014 Elsevier B.V. All rights reserved.

1. Introduction

By the use of hydrogen gas in the technology, science and production, a continuous measurement and control is indispensable. The principles and techniques of hydrogen sensing have been discussed in numerous articles [1–11]. The simple and inexpensive preparation is always a key issue of the sensor development. In this paper, hydrogen sensing by using thermally modified Pd layers and a simple optical measurement is described.

The system palladium and hydrogen has frequently been studied in the past [12–15]. Here, especially the interaction with hydrogen has extensively been described and discussed during the past 80 years. Studies focused on structural investigations during hydrogen exposition and catalytic properties [16–18] as well as preparation techniques [19–24] and palladium as a material for hydrogen storage has been discussed in numerous papers [25–28]. Hydrogen can be incorporated into the palladium crystal structure at room temperature in huge quantities [3,12,29]. This leads to a significant change in the fundamental properties of the material, which otherwise can be utilized to detect hydrogen. Such fundamental properties are electrical (e.g. electron density and internal electric structure), structural (lattice dimension, interstitial gaps) as well as numerous optical properties, such as the complex refractive index.

However, a non-electrical detecting method should be preferred because at least in some cases potentially explosive atmospheres are studied. Hydrogen is incorporated into the palladium host lattice as atomic hydrogen. This is formed by dissociation of molecular hydrogen (H_2) at room temperature on the surface of the palladium metal [12,30–33]. It is hence not surprising, that the surface to volume ratio plays an important part in hydrogen detection systems and has to be optimized depending on the respective purpose.

In case when the detector is based on thin palladium films, the latter must be thick enough to cause detectable changes in the physical properties (e.g. a significant change in light reflection), otherwise it should be thin enough that the incorporation of hydrogen is not delayed by large diffusion paths. Since in the present study a transmission setting is used, a transparent layer is required. In order to achieve a fast detection of atmospheres with changing hydrogen partial pressures, an increase in the surface area should be considered. An increase in surface area in terms of surface roughness caused by oxidation has already been discussed in [34].

By contrast, it has already been demonstrated that the detection of hydrogen using metallic palladium nanoparticles can be realized by the measurement of their optical properties [35]. It was also found that palladium nanoparticles and their interaction with hydrogen can accurately be described by the Mie theory [35–37].

The Mie theory is a general approach to describe optical properties of electron conductive nanoparticles. Mie developed this theory in order to explain the red coloration of fluids containing gold nanoparticles [36,37] based on the dielectric properties of gold and the phase in which the nanoparticles are embedded. The optical

* Corresponding author. Tel.: +49 03641 948522; fax: +49 03641 948502.
E-mail address: Michael.Kracker@uni-jena.de (M. Kracker).

Table 1

Overview of the used Pd layer samples on fused silica (sensor elements) and their preparation parameters. Rapid cooling: the sample was removed from the hot furnace. Slow cooling: the sample was cooled down with the furnace.

Sample	Initial layer thickness (nm)	Heat treatment	Reason for heat treatment	Cooling procedure	References
Freshly sputtered Pd 5	5	–	0	–	[35]
Pd 5	5	900 °C 1 h/air	Dewetting to form particle	Rapid cooling	[35]
Freshly sputtered Pd 8	8	–	–	–	[34]
Pd 8	8	700 °C 1 h/air	Oxidation	Slow cooling	[34]
Freshly sputtered Pd 14	14	–	–	–	[34]
Pd 14	14	700 °C 1 h/air	Oxidation	Slow cooling	[34]
Pd 14 long term	14	700 °C 1 h/air	Oxidation	Slow cooling	[34]
Freshly sputtered Pd 18	18	–	–	–	[34]
Pd 18	18	700 °C 1 h/air	Oxidation	Slow cooling	[34]

properties of metallic particles change, if the size becomes much smaller than the wavelength of the incident light. This results in special optical properties, e.g. sharp absorption bands (plasmon resonance) which depend on size and shape of the particles as well as on the distance between the particles, the dielectric properties of the surrounding medium and the type and crystal lattice of the metal [37–40].

In the literature, the preparation of palladium nanoparticles is predominantly reported by wet chemical routes [18,21,41]. The preparation procedure of stabilizing agents-free nanoparticles (dewetting of Pd-layers) has recently presented in [35]. The driving force of this process is the minimization of the surface and interface energies and, in the literature, denoted as solid state dewetting. It is a fairly versatile route suitable for numerous metals such as gold, silver, platinum and palladium. Further explanations of the dewetting procedure were presented in previous papers [42,43].

This paper reports on a low cost optical transmission hydrogen detection system based on very thin palladium films and palladium nanoparticle layers.

2. Experimental

Fused silica glass samples with a thickness of 1.35 mm and a dimension of 22 mm × 12 mm were used for palladium coatings. All the substrates were cleaned using a commercial solution “Trickopur R36” in an ultrasonic bath at 65 °C. Afterwards the substrates were rinsed with deionised water and treated twice again in deionised water with ultrasonic assistance. Finally the glass substrates were dried at 110 °C for 1 h in air and stored in vacuum until the layers were sputtered.

Palladium layers were sputtered using a DC-sputter-system (Edwards Auto 306 with high vacuum system). The target dimensions were 50 mm × 50 mm; the purity of the target metal was 99.95% (M&K GmbH Edelmetallrecycling, Kahla). In all the coating processes, the following parameters were kept constant: substrate-temperature (21 °C), target-substrate-distance (100 mm), the pressure in the vacuum-chamber (<10 mPa), the voltage (4 kV) and the argon pressure (10 Pa). For these parameters, the resulting current was 35 mA.

Single palladium layers with a thickness of 5, 8, 14 or 18 nm were deposited on fused silica sheets. To control the thickness of the sputtered layer, a film thickness monitor (FTM7, BOC Edwards, UK) equipped with a quartz oscillating unit was used. Sample and thickness monitor were covered by a shutter system during the pre-sputtering procedure.

To prepare oxidized layers, annealing was carried out in a muffle furnace at a temperature of 700 °C in air. The samples were transferred into the furnace and heated using a rate of 10 K/min. The desired temperature was kept for 1 h. Subsequently, the furnace was cooled down to room temperature supplying a cooling rate <1 K/min; then the samples were removed.

In order to dewet the sputtered palladium layer and to transfer it to nanoparticles arranged at the surface of the silica substrate,

annealing was carried out in a muffle furnace at a temperature of 900 °C under ambient conditions. These samples in the following are denoted as “dewetted”. The samples were transferred into the furnace and heated using a rate of 10 K/min. This temperature was kept for 1 h. To minimize the oxidation at the surface of the Pd-nanoparticles, the samples were directly removed from the furnace to allow a rapid cooling to room temperature (cooling rate: >800 K/min). For each sample, an untreated (freshly sputtered) and thermally treated sample (oxidized) was produced. A complete overview of the used preparation conditions and used samples is given in Table 1.

The experimental setup is shown in Fig. 1. The gas flow was controlled by a thermal gas flow meter MC500SCCM-D (Alicat Scientific Inc.) and was kept constant at 250 sccm. The sensor body is a custom build system (excerpt see at the upper right corner at Fig. 1) equipped with a red LED (LED emission spectrum is additionally shown in Fig. 2(A and B)) and a photodiode (Osram SFH 203) to measure the intensity of the transmitted light. The sensor body is equipped with two slices (sensor elements in slot 1 and slot 2) in order to increase the optical response. However, in these studies only one coated slice was used and the opposite sample slot was equipped with an uncoated fused silica slice. The photodiode signal was processed by a current–voltage (TLC271) converter and recorded using a voltmeter (Metrakit 28S) equipped with a data logging unit (Metrakit SI232) to obtain a time resolved measurement. The sampling rate was set at 20 Hz.

3. Results

First the different preparation procedures will be described. Fused silica slides were coated with thin Pd layers, these layers in the following are denoted as “freshly sputtered”. After a heat treatment of 700 °C, films with thickness of 8, 14 and 18 nm are transformed into an oxide layer. These layers will be denoted as “oxidized layers”. In another series of experiments, a 5 nm thick Pd-layer is heat treated at 900 °C which leads to the formation of a nanoparticle film which in the following is denoted as “dewetted layer”. After the first contact to hydrogen, all oxidized layers undergo a significant and irreversible change which leads to highly modified sensing properties. These layers will be denoted as “purged layer”. A complete list of all experimental parameters is given in Table 1.

Fig. 2 shows the optical properties of the different used sensor systems in comparison to the emission spectrum of the light source. In (A) the difference in the optical transmission between a PdO layer (oxidized Pd layer) and its chemically reduced (by hydrogen) metallic Pd layer is shown.

The optical behavior of metallic Pd nanoparticles under different atmospheres (hydrogen and argon) is shown in Fig. 2(B). In this case the optical spectrum under a hydrogen atmosphere was subtracted from the optical spectrum under argon atmosphere. In analogy to Fig. 2(A), the difference in the optical transmission between an

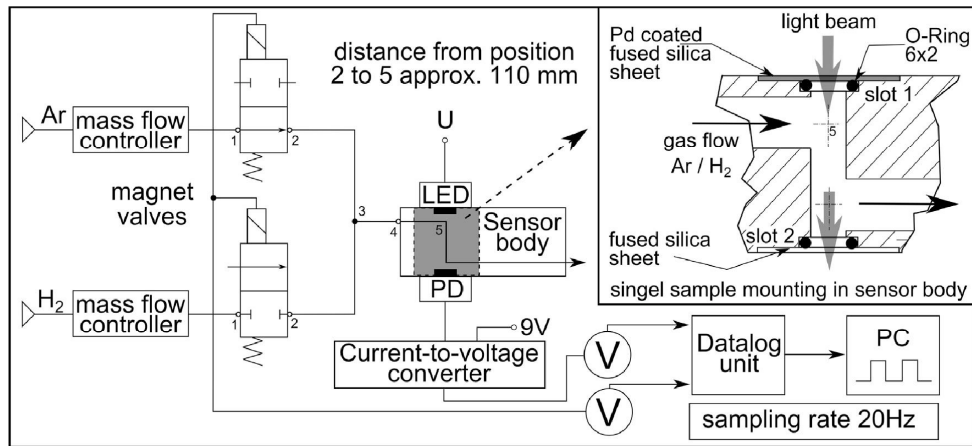


Fig. 1. Schematic drawing of the experimental setup. Upper right corner: enlarged detail of the sensor element and body.

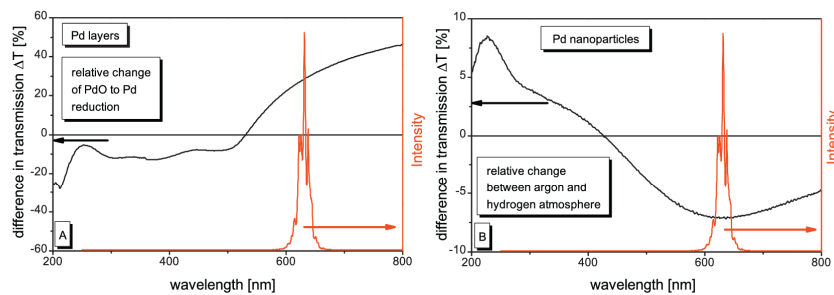


Fig. 2. (A) Difference in optical transmission obtained from UV–vis–NIR spectroscopy of a PdO layers before and after the reduction to Pd with hydrogen (ex situ). See Ref. [34]. Right: emission-spectrum of the LED, which was used as light source for the experiments. (B) Difference in optical transmission obtained from UV–vis–NIR spectroscopy of dewetted Pd nano-particles, recorded under argon and hydrogen atmosphere. Data was taken from [35]. Right: emission-spectrum of the LED, which was used as light source for the experiments.

oxidized and a reduced layer is presented. For this purpose the data were taken from [34].

The emission of the used LED is mainly in the wavelength range from 600 to 660 nm with a sharp maximum at 630 nm. In Fig. 2(A), the above described difference is negative up to a wavelength of

approximately 530 nm, then gets positive and increases steadily in the whole studied wavelength range. At a wavelength the LED emits, the change in the transmission is approximately 28%.

In Fig. 2(B), the difference in the transmission is also negative at short wavelengths and gets positive at wavelengths above 440 nm.

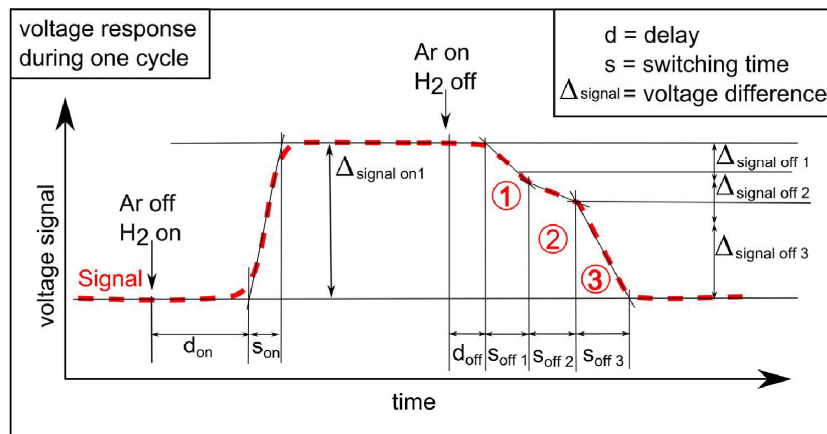


Fig. 3. Schematic drawing of voltage response during one cycle of switching the hydrogen flow on and off. The way of determining the respective characteristic times discussed in the text are also shown in the figure.

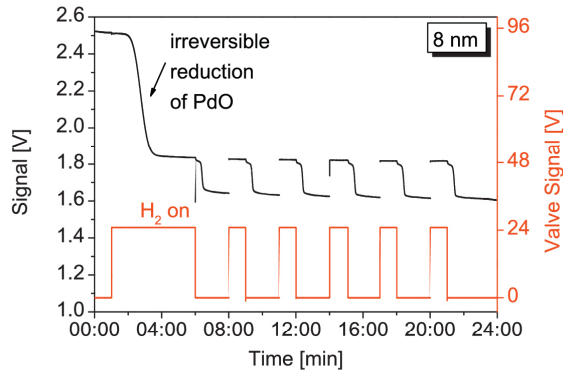


Fig. 4. Voltage response of a single Pd/PdO coated glass sample of 8 nm thickness. The red rectangular graph below shows to the switching state of the H₂ gas magnet valve. (For interpretation of the references to color in this figure legend, the reader is referred to the web version of this article.)

In contrast to Fig. 2(A), a maximum is observed at a wavelength of 630 nm, which is near the emission maximum of the LED. The change of the transmission attributed to this maximum is approximately 7% and hence notably smaller than in Fig. 2(A).

Fig. 3 shows the schematic voltage diagram of a single cycle. The characteristic values were determined by a tangent method. After hydrogen valve is opened, the voltage increases by characteristic value $\Delta\text{signal}_{\text{on}}$ to the hydrated state. The delay is denoted as d_{on} the time to raise the hydrated state is s_{on} . After the hydrogen valve was closed, the voltage drops after a delay time (d_{off}) back to the ground level by passing three different desorbing states (1–3), each with a corresponding switching time (s_{off1} s_{off2} s_{off3}) and characteristic voltage difference ($\Delta\text{signal}_{\text{off1}}$ $\Delta\text{signal}_{\text{off2}}$ $\Delta\text{signal}_{\text{off3}}$).

It should be noted that all values, discussed below and indicated schematically in Fig. 3, are listed in Tables 2 and 3. Fig. 4 shows the voltage response of an oxidized Pd layer with a thickness of 8 nm. The red graph below indicates the switching position of the hydrogen valve (if the hydrogen valve is closed, the argon valve is open). When the layers are first in contact to hydrogen, during 76 s the signal decreases by 0.66 V. After further 64 s, a constant signal of 1.85 V is obtained. After the hydrogen was switched off (valve signal 0 V), the signal decreases to 1.62 V after 26 s of purging with argon. This signal decay occurs in two steps and will be discussed later. In Fig. 5, the signal voltage response and the valve voltage versus time

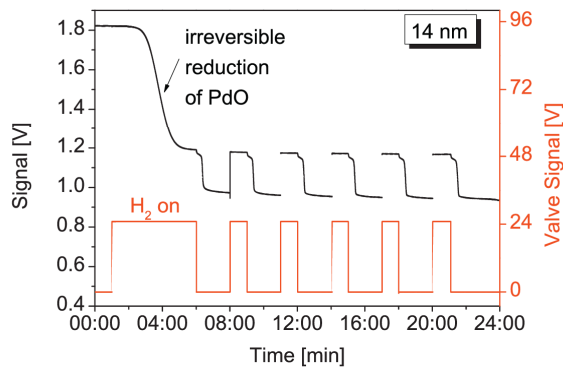


Fig. 5. Voltage response of a single Pd/PdO coated glass sample of 14 nm thickness. The red rectangular graph below shows to the switching state of the H₂ gas magnet valve. (For interpretation of the references to color in this figure legend, the reader is referred to the web version of this article.)

Table 2 Measured time and signal values during cyclic loading with hydrogen. The meaning of the respective values and their description is shown in detail in Fig. 3.

Sample	d_{on} (ms)	s_{on} (ms)	$\Delta\text{signal}_{\text{on}}$ (V)	d_{off} (ms)	$pc_{s_{\text{off1}}}$ (ms)	$pc_{s_{\text{off2}}}$ (ms)	s_{off3} (ms)	$\Delta\text{signal}_{\text{off3}}$ (V)	$\Delta\text{signal}_{\text{off2}}$ (V)	$\Delta\text{signal}_{\text{off1}}$ (V)
Freshly sputtered Pd 5	Hydrogen uptake	<250	0.028	Hydrogen discharge	pc24,142	pcn/a	15.707	0.083	0.009	0.011
Freshly sputtered Pd 8	<250	<200	0.021	19.651	pc19,650	pc	24.777	0.082	0.009	0.011
Freshly sputtered Pd 14	<250	<250	0.021	17.322	pc10,479	pc	7380	-0.014	-0.019	-0.016
Freshly sputtered Pd 18	<250	<250	0.013	22.344	pc8,604	pc	8327	-0.158	-0.015	-0.015
Pd 5 900 °C dewetted and purged	178 (interpolated)	189 (interpolated)	-0.101 (cycle 1)	23.176	pc2,478	pc28,067	15.707	0.083	0.009	0.011
Pd 8 700 °C oxidized and purged	<200	<200	-0.103 (cycle 5)	830	2679	32,300	24.777	0.082	0.009	0.011
Pd 14 700 °C oxidized and purged	<250	<250	0.185 (cycle 1)	<250	2059	17,816	7380	-0.148	-0.019	-0.016
Pd 14 700 °C oxidized and purged, long term	<250	<250	0.207 (cycle 1)	<250	1597	18,388	8347	-0.158	-0.015	-0.015
Pd 18 700 °C oxidized and purged	<200	<200	0.221 (cycle 1)	<250–800	pc16,995	18,388	5986	-0.172	-0.017	-0.015
			0.239 (cycle 5)	<250	pc27,47	18,388	8347	-0.182	-0.018	-0.018
			0.246 (cycle 17)	<250	2433	pc23,743	6577	-0.169	-0.015	-0.015
			0.193 (cycle 1)	<250	2767	24,785	11,036	-0.191	-0.017	-0.017
			207 (cycle 5)	<250	pc22,85	27,150	14,636	-0.200	-0.018	-0.018
					1892	pc17,851	5538	-0.150	-0.016	-0.015
						18,669	7339	-0.165	-0.016	-0.015

Table 3
Measured time and signal values during first contact to hydrogen (purging).

Sample	d_{onset} (min)	s_{onset} (min)	Δ signal (V)
Pd 5 900 °C/1 h	0:15	0:45	0.04
Pd 8 700 °C/1 h	1:16	1:04	0.66
Pd 14 700 °C/1 h	1:13	1:40	0.63
Pd 14 700 °C/1 h, long term	1:56	1:35	0.64
Pd 18 700 °C/1 h	1:21	1:15	0.59

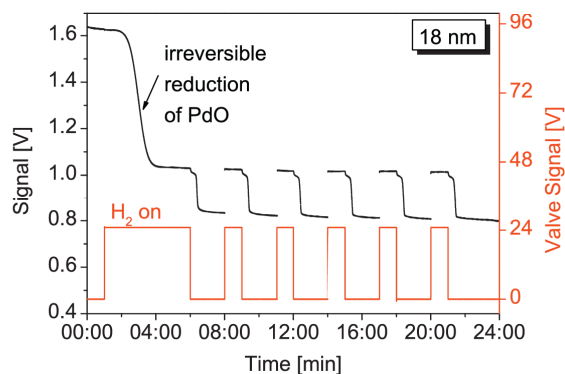


Fig. 6. Voltage response of a single Pd/PdO coated glass sample of 18 nm thickness. The red rectangular graph below shows to the switching state of the H₂ gas magnet valve. (For interpretation of the references to color in this figure legend, the reader is referred to the web version of this article.)

are illustrated for an oxidized palladium layer with a thickness of 14 nm. The signal decreases irreversibly from 1.81 V to 1.2 V after the first contact with hydrogen and subsequently to 0.95 V after the hydrogen was turned off. The total level of the signal is notably lower than at an 8 nm thick layer shown in Fig. 4. Fig. 6 shows the similar result for an 18 nm thick oxidized palladium layer. In comparison to Figs. 4 and 5, the voltage is smaller over the entire studied period of time.

Fig. 7 shows the signal voltage response of the Pd nanoparticle layer, prepared by dewetting of a 5 nm thick freshly sputtered Pd layer at 900 °C. The signal decreases from 2.67 V to 2.625 V after the

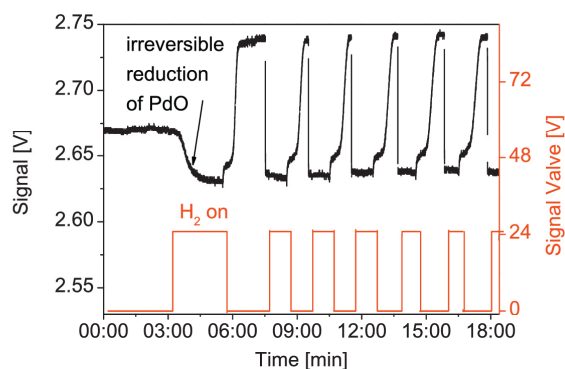


Fig. 7. Voltage response of a single glass coated with Pd-nanoparticles. The red rectangular graph below shows to the switching state of the H₂ gas magnet valve. (For interpretation of the references to color in this figure legend, the reader is referred to the web version of this article.)

first contact with hydrogen. However, after the hydrogen flow was switched off, the signal increased to 2.73 V and decreased rapidly to 2.63 V if the cell was again purged with hydrogen again. This behavior is just the opposite of that shown in Figs. 4–6.

In Fig. 8(A and B), a comparison of as freshly sputtered and oxidized and additionally purged Pd layers as well as nanoparticle Pd layers (after the first contact to hydrogen see Fig. 8(D)) during hydrogen absorption is shown. The graphs are normalized (at the signal axis) and synchronized (at the time axis) and the change in the voltage signal versus time is plotted. After the hydrogen was switched on (at 10 s), as shown in Fig. 8(A), the signal increases by 0.2 V for oxidized and purged Pd-layers and only by 0.028 V in the case of as freshly sputtered Pd-layer. This behavior is almost similar for thicker layers (14 and 18 nm) as shown in Fig. 8(B and C), respectively. However, the behavior changes in the case of a 5 nm thick layer dewetted at 900 °C as illustrated in Fig. 8(D). For a freshly sputtered 5 nm thick layer, the signal change increased by 0.028 V while purging with hydrogen. In the case of a dewetted (900 °C) 5 nm Pd layer, the signal decreased by 0.1 V during hydrogen contact.

In Fig. 9 a similar comparison as in Fig. 8 is shown for the hydrogen discharge behavior. For an freshly sputtered Pd-layer with a thickness of 8 nm (shown in Fig. 9(A)), a signal change of –0.02 V is observed, while in oxidized and purged layers, a signal change (in two steps) of –0.2 V is seen. The values for 14 and 18 nm thick samples show similar signals. In analogy to the behavior shown in Fig. 8, the optical behavior of Pd nanoparticles (dewetted 5 nm thick Pd layer annealed at 900 °C) during hydrogen discharge is notably changed in comparison to as freshly sputtered Pd layers (see Fig. 9(A–C)). The signal is increased by 0.1 V (also in two steps), while the signal of an as freshly sputtered 5 nm layer decreases.

Fig. 10(A) shows the voltage response of an oxidized Pd layer with a thickness of 14 nm with more hydrogen load cycles, to demonstrate the influence of the signal drift observed in Figs. 4–6. During the PdO reduction (first contact to hydrogen) the signal decreased by 0.64 V in 95 s. After the hydrogen is switched off, the signal decreases from 1.42 V to 1.21 V in two steps. After the hydrogen is turned on again, the signal is increased to 1.40 V immediately. In Fig. 10(B) a compilation of the drift properties is shown. Illustrated are the relative voltage changes of all the thermally treated layers in this article. The voltage level was measured while the film is in contact with hydrogen. This value was set in relation to the first hydrated state, just after the PdO reduction.

4. Discussion

A simple, low-priced and highly reproducible method of hydrogen sensor layers based on Pd-coated glass slides is present.

Palladium forms a stable oxide at temperatures above 258 °C (DTA onset) and PdO also decomposes back to metallic Pd above 775 °C (DTA onset) [44]. Caused by recrystallization and an increase in the volume (decrease in density) of the PdO layer, the roughness of the layer is increased. PdO is a semiconductor and in contact with hydrogen it will be reduced to metallic palladium. This causes a sharp change in the optical properties. Furthermore, the surface roughness remains unchanged during reduction. In a further series of samples, thin sputtered layers were prepared and dewetted by thermal treatment which resulted in a layer formed by palladium nanoparticles. An annealing procedure at 900 °C is enough to start the dewetting and is attributed to a temperature range where PdO is not stable. Rapid cooling from 900 °C to RT minimized the quantity of PdO significantly in comparison to slow cooling, since the residence time of the sample is very low in the temperature range of oxide formation. The transmission spectra of layers composed by Pd nanoparticles with diameters of around 20 nm [35] show a well pronounced plasmon resonance. The largest (optical) difference

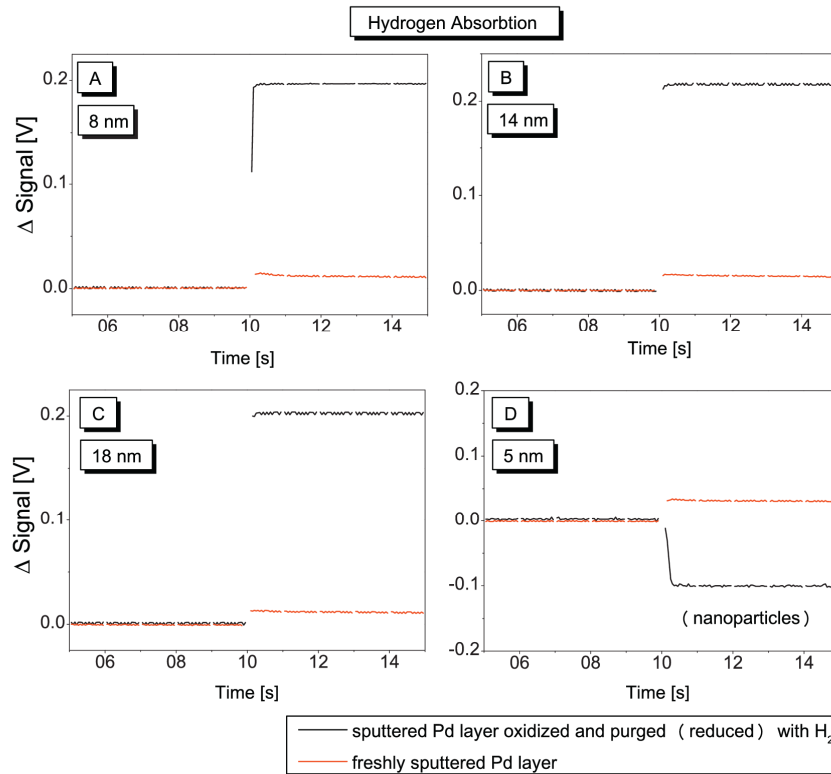


Fig. 8. Voltage response by hydrogen uptake of the coated glass samples, red lines: freshly sputtered Pd and black lines: Pd reduced from PdO. Initial layer thickness: (A) 8 nm, (B) 14 nm and (C) 18 nm. The hydrogen uptake of a 5 nm thick Pd layer (red line) and nanoparticle layer (black line) is illustrated in (D). (For interpretation of the references to color in this figure legend, the reader is referred to the web version of this article.)

between the metallic and the hydrogenated state is observed at a wavelength of 630 nm. For both series of samples, the as sputtered as well as the subsequently dewetted samples, the wavelength attributed to the emission maximum of the LED is close to the maximum change in the transmission. Hence the transmission of light at a wavelength of 630 nm is very sensitive with respect to the interaction with hydrogen.

Fig. 3 presents a simple method of signal processing by a tangent method used for determination of all values listed in Table 2.

4.1. Optical response after the first contact to hydrogen (reduction of PdO to metallic Pd)

After the first interaction of the oxidized Pd layers with hydrogen (shown in Figs. 4–6), the transmission decreased irreversibly. This effect is caused by the reduction of PdO to metallic Pd (compare with the difference transmission spectra shown in Fig. 2A). However, under the experimental conditions supplied the changes in the optical transmission occur only within a narrow time range from 73 to 82 s. First, a certain amount of metallic Pd is necessary, which can provide atomic hydrogen by dissociative adsorption (chemisorption) [12,31,32]. This atomic hydrogen is highly reactive and accelerates the reduction reaction to form metallic palladium, which certainly also accelerates the formation of atomic hydrogen. Su et al. describes such a temperature depend mechanism for the reduction of PdO under CH₄ and H₂ atmospheres [32].

However, the effect of the layer thickness on the resulting voltage difference, the reaction time and offset time is fairly small.

Within the supplied conditions, only the absolute level of the signal depends on the layer thickness.

This behavior is also seen in the case of the dewetted, i.e. the layer composed of palladium nanoparticles (see Fig. 7). In comparison to the oxidized layer, the transmission changes after only 15 s. Also the time to complete the reaction as well as the voltage signal difference is notably shorter than in the case of oxidized continuous layers as discussed above. This is not surprising, because the cooling procedure is the crucial step. The nanoparticle sample was rapidly removed from the furnace in order to decrease the cooling time. Then the temperature range in which oxidation to PdO might occur is short.

It can be concluded, a “pretreatment” with hydrogen is mandatory to remove the irreversible part of the optical response.

4.2. Cyclic loading with hydrogen

Figs. 4–7 (Fig. 8 shows a summarizing representation) show the optical response during cyclic loading with hydrogen and purging with argon. In the case of 8, 14 and 18 nm thick purged Pd layers (after their first contact with hydrogen), the optical transmission increased while hydrogen is incorporated into the palladium matrix [8]. It is found that the layer thickness does neither affect the intensity of the signal nor the response time. Here, the optical response after the hydrogen was switched on is extremely fast. However, due to a magnetic perturbation during the measurement, the reaction time cannot be determined exactly. This perturbation is caused by a switching operation of the magnetic valves, which leads to an electromagnetic pulse coupled into the connection wire and the

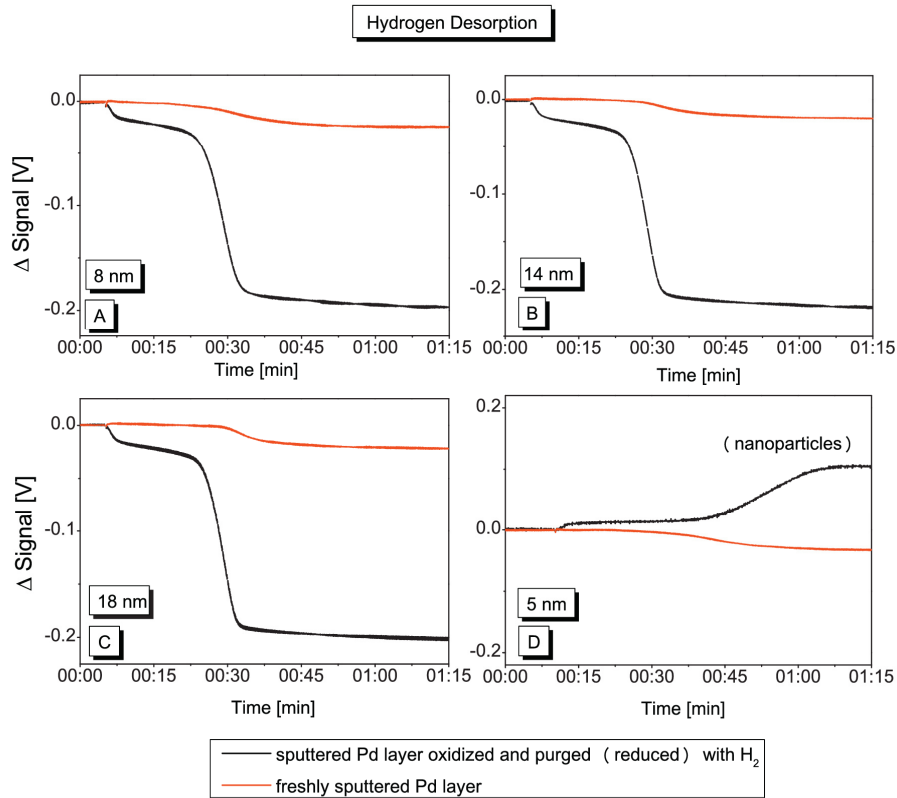


Fig. 9. Voltage response by hydrogen discharge of the coated glass samples, red lines: freshly sputtered Pd and black lines: Pd reduced from PdO. Initial layer thickness: (A) 8 nm, (B) 14 nm and (C) 18 nm. The hydrogen uptake of a 5 nm thick Pd layer (red line) and nanoparticle layer (black line) is illustrated in (D). (For interpretation of the references to color in this figure legend, the reader is referred to the web version of this article.)

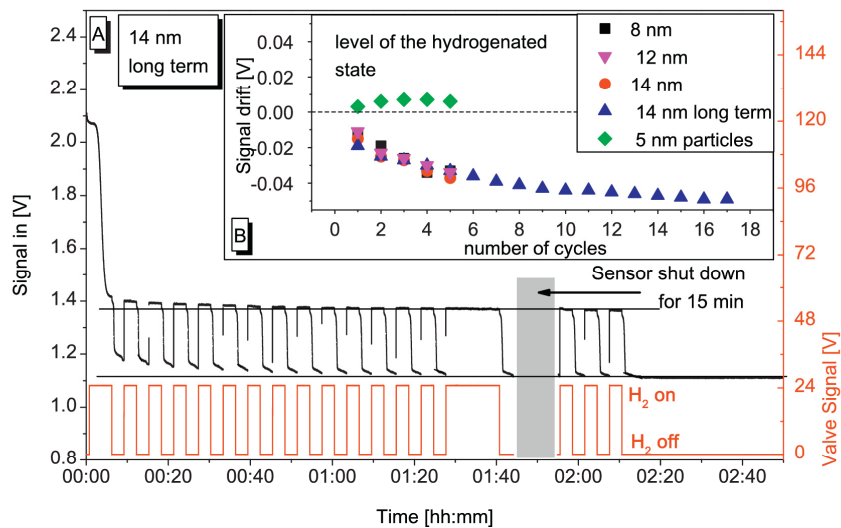


Fig. 10. (A) Voltage response of a single Pd/PdO coated glass sample of 14 nm thickness with an extended number of cycles. The red rectangular graph below illustrates the switching state of the H₂ gas magnet valve. (B) Signal drift, for treated layers: a compilation of all the relative changes in the voltage level of the hydrogen state. (For interpretation of the references to color in this figure legend, the reader is referred to the web version of this article.)

evaluation unit. Nevertheless, it can be stated that the reaction is completed within 250 ms. The only exception is the dewetted nanoparticle layer, because the particles react slightly delayed on hydrogen and the optical response occurs after the perturbation is over. This result in a reaction time of 189 ms with an incubation time of 178 ms. A smaller surface area and an associated reduction to atomic hydrogen, gives a possible explanation for this delay. The surface of the palladium is responsible for the conversion into atomic hydrogen. In addition, the optical response is based on particle plasmons and the absorbance increases which is in contrast to the dense layers.

4.3. Comparison to freshly sputtered layers

Annealed and hydrogen purged layers are most advantageous for sensing which can easily be seen in Fig. 8(A–D). The signal response after heat treatment and subsequent purging with hydrogen (graphs A–C) is between 9 and 16 times higher than that of freshly sputtered layers. The overall 16 times higher response is based on the fact that the freshly sputtered 18 nm thick layer itself has a very low signal value (“ Δ signal” at Table 2). The dewetted layer (graph D) shows a 4 times larger optical response than the freshly sputtered film. Nevertheless, the change in the signal has the opposite direction due to a different mechanism, as explained above.

A further significant change in comparison to freshly sputtered palladium layers occurs during desorption of hydrogen (Fig. 9). The most noticeable difference is the shape of the graph which shows a significant additional plateau. The palladium hydrogen phase diagram possesses three areas, the alpha phase, a miscibility gap, and the beta phase (also called palladium hydride). The alpha phase is a solid solution of hydrogen in palladium. The hydrogen is located inside octahedral interstitial position and is randomly distributed. The lattice parameter of the alpha phase is slightly changed with an increase in the hydrogen concentration (0.3890–0.3894 nm) up to 0.015 H/Pd. For higher concentrations, the H–H interaction leads to the formation of a second fcc phase (palladium hydride) with a notable larger lattice parameter of 0.4025 nm. This corresponds to a volume expansion of 10.4% from alpha to the beta phase. In the phase diagram appears a miscibility gap between 0.015 and 0.58 H/Pd wherein both phases (alpha and beta) exist side by side. Above 0.58 H/Pd and up to 0.7 H/Pd only the beta phase is present; the lattice constant (up to 0.4040 nm for 0.7 H/Pd) is slightly larger [14].

It is assumed that the 3 stages of desorption correspond to the 3 different phases within the system Pd–H (alpha, alpha + beta, beta). The first stage is equal to the beta phase (PdH). The subsequent section, with a smaller slope, corresponds to the compositions containing both the alpha and the beta phase. The last stage corresponds to the alpha phase, i.e. the solid solution of palladium and hydrogen. This is in agreement with the results of Zalvidea et al. [45], which, however, have been obtained at temperatures around -20°C . Another possible explanation is the electron density of thin layers. The electron density for thin Pd films depending of the hydrogen concentration, was published by Vargaz et al. [8] The electron density of the palladium/hydrogen system is a function of the molar hydrogen concentration (molar ratio Pd/H in the metal) and shows a similar dependency as the optical response of all treated layers.

By contrast, all freshly sputtered layers show a single response during desorption. This is certainly in agreement with reports in the literature. However, it should be noted that the transmission of a freshly sputtered layer decreases with a time delay which is nearly the same as the second inflexion of the oxidized and purged layers (at 30 s).

4.4. Long term experiments with an extended number of cycles

The results in Figs. 4–6 provide the indication of a signal drift. Fig. 10(B) (upper diagram) shows the change in the hydrogenated voltage level as a function of cycles for all treated layers performed in this article.

To clarify this behavior, a new layer was prepared and was measured with a higher number of purging cycles. In Fig. 10(A), it can clearly be seen that the ground state and the hydrogen state is decreased up to the 9th cycle. However, the difference in the signal is increased by 12% from the first to the 9th cycle. This effect is found in all treated layers with the exception of the nanoparticle layers.

The basic effect of this work relies on specific destruction (disturbance) of thin Pd-layers. So it is not surprising that repeated purging with hydrogen and a consequent swelling and shrinking of the layer can create additionally faults by a stress relaxations mechanism. However, these faults increase the roughness and also increase the surface area and the response of the layer on the presence of hydrogen. This means that the sensor shows a higher signal intensity due to the aging.

Such stress relaxation mechanisms should not occur in “free-standing” nanoparticles and, by contrast, the signal difference should remain almost constant. As shown in Table 2, the signal difference remains almost constant. The absolute voltage level is slightly increasing with time (7 mV in 18 min) as shown in Fig. 10(B). But it should point out that the difference is positive. This means that the drift has the opposite direction in comparison to that shown in the roughened layer. Since the optical response has also the reverse direction (by the plasmon resonance), this is an indication of the structural reasons of the drifts. However, the statement is speculative, since the magnitude of drifts is very small, so that it is in the measurement error range.

To demonstrate the transient behavior of the sensor, the measurement was interrupted for 15 min (while purging with argon was continued). Subsequently the measurement was started again. In the first cycle, a slight voltage drop is seen. This is attributable to a transient behavior. Especially, the signal difference after the sensor switch on again still remains unchanged.

It should be noted that the absolute voltage level of the 14 nm thick layer in Fig. 10(A) compared to 14 nm thick layer in Fig. 5 is slightly shifted approximately 0.19 V upwards. This should be due to small variations in layer thickness (between coating cycles) due to our chosen preparation process. Nevertheless, all determined relative values of signal difference, signal difference during hydrogen desorption, minimal response time and signal difference during PdO reduction are in an excellent agreement, with the results discussed above.

5. Conclusion

The features of the optical response at Pd coated glass slides with different treatments and thickness have been measured time-resolved under (100%) hydrogen and argon atmosphere. In case of oxidized and subsequently hydrogen purged Pd layers, it could be found that the magnitude of the optical response is up to 16 times larger than that of freshly sputtered layers. In case of a dewetted Pd layer of the optical response is 4 times larger.

In contrast to untreated layers where the optical response occurs in one step, during desorption of hydrogen three subsequent steps are observed. This behavior is not affected by the layer thickness in the studied range from 5 to 18 nm. In a view of a technical application a thinner layer and hence a smaller amount of Pd results in the same sensitivity as a thick layer. In all layers, an irreversible chemical reduction from PdO to metallic Pd was detected at the first contact with hydrogen.

Acknowledgments

This work is supported by the DFG “Deutsche Forschungsgemeinschaft” under Grant nos.: Se 698/10-1 and Se 698/10-2. The authors would like to thank Christian Zeidler, Rainer Weiß and Lutz Preißer for assistance with the circuit design and sensor production.

References

- [1] Y.O. Barmenkov, A. Ortigosa-Blanch, A. Diez, J.L. Cruz, M.V. Andrés, Time-domain fiber laser hydrogen sensor, *Opt. Lett.* 29 (2004) 2461–2463.
- [2] X. Bévenot, A. Trouillet, C. Veillas, H. Gagnaire, M. Clément, Hydrogen leak detection using an optical fibre sensor for aerospace applications, *Sens. Actuators B: Chem.* 67 (2000) 57–67.
- [3] T. Hübert, L. Boon-Brett, G. Black, U. Banach, Hydrogen sensors – a review, *Sens. Actuators B: Chem.* 157 (2011) 329–352.
- [4] C. Hyeonsik, M.J. Jung, Long-term durability of Pd/a-WO₃ and Pd-Pt/a-WO₃ thin films for hydrogen sensors, *J. Korean Phys. Soc.* 57 (2010) 1885–1888.
- [5] E. Maciak, Z. Opilski, Transition metal oxides covered Pd film for optical H₂ gas detection, *Thin Solid Films* 515 (2007) 8351–8355.
- [6] D. Monzón-Hernández, D. Luna-Moreno, D. Martínez-Escobar, Fast response fiber optic hydrogen sensor based on palladium and gold nano-layers, *Sens. Actuators B: Chem.* 136 (2009) 562–566.
- [7] S. Okazaki, H. Nakagawa, S. Asakura, Y. Tomiuchi, N. Tsuji, H. Murayama, M. Washiya, Sensing characteristics of an optical fiber sensor for hydrogen leak, *Sens. Actuators B: Chem.* 93 (2003) 142–147.
- [8] W. Vargas, I. Rojas, D. Azofeifa, N. Clark, Optical and electrical properties of hydrided palladium thin films studied by an inversion approach from transmittance measurements, *Thin Solid Films* 496 (2006) 189–196.
- [9] Z. Zhao, Y. Severyugina, M.A. Carpenter, D. Welch, H. Xia, All-optical hydrogen-sensing materials based on tailored palladium alloy thin films, *Anal. Chem.* 76 (2004) 6321–6326.
- [10] C. Langhammer, E.M. Larsson, B. Kasemo, I. Zorić, Indirect nanoplasmonic sensing: ultrasensitive experimental platform for nanomaterials science and optical nanocalorimetry, *Nano Lett.* 10 (2010) 3529–3538.
- [11] T. Watanabe, S. Okazaki, H. Nakagawa, K. Murata, K. Fukuda, A fiber-optic hydrogen gas sensor with low propagation loss, *Sens. Actuators B: Chem.* 145 (2010) 781–787.
- [12] T.B. Flanagan, W.A. Oates, The palladium–hydrogen system, *Annu. Rev. Mater. Sci.* 21 (1991) 269–304.
- [13] R. Kirchheim, T. Mütschele, W. Kieninger, H. Gleiter, R. Birringer, T. Koblé, Hydrogen in amorphous and nanocrystalline metals, *Mater. Sci. Eng.* 99 (1988) 457–462.
- [14] F.D. Manchester, A. San-Martin, J.M. Pitre, The H–Pd (hydrogen–palladium) system, *J. Phase Equilib.* 15 (1994) 62–83.
- [15] A. Pundt, *Nanoskalige Metall–Wasserstoff–Systeme*, Univ.-Verl. Göttingen, Göttingen, 2005.
- [16] S. Schauer mann, J. Hoffmann, V. Johaneck, J. Hartmann, J. Libuda, H.J. Freund, Catalytic activity and poisoning of specific sites on supported metal nanoparticles, *Angew. Chem. Int. Ed.* 41 (2002) 2532–2535.
- [17] J.K. Edwards, B. Solsona, E.N. N.A.F. Carley, A.A. Herzing, C.J. Kiely, G.J. Hutchings, Switching off hydrogen peroxide hydrogenation in the direct synthesis process, *Science* 323 (2009) 1037–1041.
- [18] C. Hwang, Y.L. Lu, S.W. Jang, P.T. Chou, C.R.C. Wang, S.J. Yu, Synthesis, characterization, and highly efficient catalytic reactivity of suspended palladium nanoparticles, *J. Catal.* 195 (2000) 336–341.
- [19] J.D. Aiken, R.G. Finke, A review of modern transition-metal nanoclusters: their synthesis, characterization, and applications in catalysis, *J. Mol. Catal. A: Chem.* 145 (1999) 1–44.
- [20] K. Stevens, B. Ingham, M. Toney, S. Brown, A. Lassesson, Structure of palladium nanoclusters for hydrogen gas sensors, *Curr. Appl. Phys.* 8 (2008) 443–446.
- [21] J. Cookson, The preparation of palladium nanoparticles, *Platinum Met. Rev.* 56 (2012) 83–98.
- [22] O. Mekasuwandumrong, S. Sombonthanakit, P. Praserttham, J. Panpranot, Preparation of nano-Pd/SiO₂ by one-step flame spray pyrolysis and its hydrogenation activities: comparison to the conventional impregnation method, *Ind. Eng. Chem. Res.* 48 (2009) 2819–2825.
- [23] D. Luna-Moreno, D. Monzon-Hernandez, S. Calixto-Carrera, R. Espinosa-Luna, Tailored Pd–Au layer produced by conventional evaporation process for hydrogen sensing, *Opt. Laser Eng.* 49 (2011) 693–697.
- [24] T. Teranishi, M. Miyake, Size control of palladium nanoparticles and their crystal structures, *Chem. Mater.* 10 (1998) 594–600.
- [25] S. Kishore, J. Nelson, J. Adair, P. Eklund, Hydrogen storage in spherical and platelet palladium nanoparticles, *J. Alloy Compd.* 389 (2005) 234–242.
- [26] C. Langhammer, I. Zorić, B. Kasemo, B.M. Clemens, Hydrogen storage in Pd nanodisks characterized with a novel nanoplasmonic sensing scheme, *Nano Lett.* 7 (2007) 3122–3127.
- [27] V. Bérubé, G. Radtke, M. Dresselhaus, G. Chen, Size effects on the hydrogen storage properties of nanostructured metal hydrides: a review, *Int. J. Energy Res.* 31 (2007) 637–663.
- [28] L. Schlappbach, A. Züttel, Hydrogen-storage materials for mobile applications, *Nature* 414 (2001) 353–358.
- [29] F. Lewis, The palladium–hydrogen system, *Platinum Metals Rev.* 26 (1982) 20–27.
- [30] L. Yi, C. You-ping, S. Han, Z. Gang, Hydrogen gas sensor based on palladium and yttrium alloy ultrathin film, *Rev. Sci. Instrum.* 83 (2012) 125003.
- [31] J. Harris, On the adsorption and desorption of H₂ at metal surfaces, *Appl. Phys.* A 47 (1988) 63–71.
- [32] S.C. Su, J.N. Carstens, A.T. Bell, A study of the dynamics of Pd oxidation and PdO reduction by H₂ and CH₄, *J. Catal.* 176 (1998) 125–135.
- [33] N. Lopez, Z. Łodziana, F. Illas, M. Salmeron, When Langmuir is too simple: H₂ dissociation on Pd(111) at high coverage, *Phys. Rev. Lett.* 93 (2004) 146103.
- [34] M. Kracker, C. Worsch, C. Rüssel, The effect of thermal annealing and hydrogen on the morphology and the optical properties of thin palladium layers, *Mater. Lett.* 110 (2013) 114–116.
- [35] M. Kracker, C. Worsch, C. Rüssel, Optical properties of palladium nanoparticles under exposure of hydrogen and inert gas prepared by dewetting synthesis of thin-sputtered layers, *J. Nanoparticle Res.* 15 (2013) 1–10.
- [36] G. Mie, Beiträge zur Optik trüber Medien, speziell kolloidaler Metallösungen, *Ann. Phys. Berl.* 330 (1908) 377–445.
- [37] M. Quinten, Optical properties of nanoparticle systems, Wiley-VCH-Verlag, Weinheim, 2011.
- [38] K.L. Kelly, E. Coronado, L.L. Zhao, G.C. Schatz, The optical properties of metal nanoparticles: the influence of size, shape, and dielectric environment, *J. Phys. Chem. B* 107 (2003) 668–677.
- [39] U. Kreibitz, L. Genzel, Optical-absorption of small metallic particles, *Surf. Sci.* 156 (1985) 678–700.
- [40] U. Kreibitz, M. Vollmer, Optical Properties of Metal Clusters, 1st ed., Springer, Berlin, Heidelberg, 1995.
- [41] W. Wang, Q. Yang, R. Zhou, H.-Y. Fu, R.-X. Li, H. Chen, X.-J. Li, Palladium nanoparticles generated from allylpalladium chloride in situ: a simple and highly efficient catalytic system for Mizoroki–Heck reactions, *J. Organomet. Chem.* 697 (2012) 1–5.
- [42] C. Worsch, M. Kracker, W. Wisniewski, C. Rüssel, Optical properties of self assembled oriented island evolution of ultra-thin gold layers, *Thin Solid Films* 520 (2012) 4941–4946.
- [43] C. Worsch, W. Wisniewski, M. Kracker, C. Rüssel, Gold nano-particles fixed on glass, *Appl. Surf. Sci.* 258 (2012) 8506–8513.
- [44] G. Bayer, H. Wiedemann, Formation, dissociation and expansion behavior of platinum group metal oxides (PdO, RuO₂, IrO₂), *Thermochim. Acta* 11 (1975) 79–88.
- [45] D. Zalvidea, A. Diez, J. Cruz, M. Andrés, Hydrogen sensor based on a palladium-coated fibre-taper with improved time-response, *Sens. Actuators B: Chem.* 114 (2006) 268–274.

Biographies

Michael Kracker studied materials science at Friedrich-Schiller-University Jena until 2011. He received his diploma degree in 2011. Following he started his Ph.D. thesis at the Otto-Schott-Institut of materials research at Friedrich-Schiller-University Jena. His research interest is focused on the optical properties of thin films and dewetted metallic nanoparticle layers as well as sensing systems.

Christian Worsch studied materials science at Friedrich-Schiller-University Jena from 2001 to 2006. He made his Ph.D. in the field of coating and hot embossing of glass from Friedrich-Schiller-University Jena in 2010. Since 2010 he has been in postdoctoral position at the Otto-Schott-Institut of materials research in section of glass coating and micro-structuring as well as chip-calorimetry. His research interest focuses metallic nanostructures and calorimetric study of ceramic and glassy particles.

Wolfgang Seeber is associate Professor at Friedrich-Schiller-University Jena and works since 2008 for the State Development Corporation of Thuringia as Director Technology Management responsible for the fields New Materials/Photonics/Nanotechnology. He studied chemistry at Friedrich-Schiller-University Jena until 1984 and received his Ph.D. for development and characterization of Nd³⁺ laser materials in 1987. With a Humboldt-Fellowship he worked at Solid-State-Laser-Lab, Technical University of Berlin from 1991 to 1992. In 1994 he worked as visiting scholar at Stanford University/Gintz Lab in the groups of R. Byer, M. Fejer and L. Hesselink in the fields of low-phonon materials, non-linear optics and layers. In 1996 he finished his habilitation and focused the scientific work on application driven multifunctional coatings.

Christian Rüssel is Professor of Glass Chemistry at Friedrich-Schiller-University Jena. He studied Chemistry at University of Erlangen-Nürnberg until 1981 and made his Ph.D. in Physical Chemistry at the same University in 1984. Then he joined the Fraunhofer-Institute for Solar Energy Systems in Freiburg, Germany for one and a half year. He went to the Institute of Materials Science (Glass and Ceramics) to the University of Erlangen-Nürnberg and made his second Ph.D. in Engineering (Dr.-Ing. habil.) in 1991. Since 1992 he has the Chair of Glass Chemistry at Friedrich-Schiller-University Jena. His research field is glass as well as glass-ceramics, from fundamentals to applications.

3.7

C. Worsch, M. Kracker, J. Edelmann, A. Schubert, C. Rüssel

Microfluidic plasmon sensors prepared by dewetting of metal films during hot embossing of glass

Sensors and Actuators B: Chemical 202 (2014) 365–372

DOI: <http://dx.doi.org/10.1016/j.snb.2014.05.092>

Microfluidic plasmon sensors prepared by dewetting of metal films during hot-embossing of glass					
Beteiligt an					
	Dr. Christian Worsch	Michael Kracker	Dr. Jan Edelmann	Prof. Andreas Schubert	Prof. Christian Rüssel
Konzeption des Forschungsansatzes	X	X	X	X	X
Planung der Untersuchung	X				
Datenerhebung	X	X	X		
Datenanalyse und Interpretation	X	X			
Schreiben des Manuskripts	X	X	X	X	X
Vorschlag Anrechnung Publikationsäquivalente		0,75			



Microfluidic plasmon sensors prepared by dewetting of metal films during hot-embossing of glass



Christian Worsch^{a,*}, Michael Kracker^a, Jan Edelmann^b, Andreas Schubert^b,
Christian Rüssel^a

^a Otto-Schott-Institut, Friedrich-Schiller-University Jena, Fraunhoferstr. 6, 07743 Jena, Germany

^b Fraunhofer Institute for Machine Tools and Forming Technology IWU, Reichenhainer Strasse 88, 09126 Chemnitz, Germany

ARTICLE INFO

Article history:

Received 3 February 2014

Received in revised form 11 April 2014

Accepted 9 May 2014

Available online 28 May 2014

Keywords:

Hot embossing

Gold nano particles

Mie theory

Fluidic sensor

ABSTRACT

A method for the preparation of a microfluidic plasmon sensor is proposed. Soda-lime-silica float glass was coated with a 20 nm silica layer and subsequently with a 12 nm gold film. Then these layers were covered with a further 20 nm silica layer. This substrate was structured with microfluidic cavities by isothermal hot-embossing at 660 °C, where the coatings effectively prevented the sticking of the glass on the mold. During the forming process, the formation of gold nanoparticles with a size of 20–150 nm occurs. In the second step, the micro structured substrate was bonded to another equally coated, but unstructured, substrate by annealing at 600 °C for 1 h. The transmission spectra of the resulting microfluidic chip show a local plasmon resonance peak at 551.9 nm (in air). The plasmon resonance responds very sensitive to the refractive index of a surrounded liquid (0.5 nm for $\Delta n = 0.04$), in spite of the covering with a silica layer and the embossing process. For comparison, two simple cuvettes also coated with gold nanoparticles but one with and one without the silica cover layer, both without the hot embossing procedure were prepared. They were filled with the same liquids and transmission spectra were recorded; they show a slightly higher sensitivity. Furthermore, a theoretical model which reflects the measured performance is proposed.

© 2014 Published by Elsevier B.V.

1. Introduction

The special properties of gold nanoparticles (GNP) offer a wide variety of applications. Among them are catalysts [1,2], devices for biological applications [3,4], plasmonic sensors [5–8], sensors based on surface enhanced Raman scattering [9,10], as well as a large variety of applications in non-linear optics [11,12]. Furthermore, gold nanoparticles might increase the efficiency of solar cells [13,14].

Numerous studies on gold nanoparticles were carried out in recent decades and today many optical effects of GNP are well understood [15–23]. A specific property of metal nanoparticles, so called localized surface plasmon resonance (LSPR) results from the collective oscillation of the electrons. These oscillations are stimulated by the incident electromagnetic radiation. Due to the damping forces of the electrons (e.g. restoring force and collision of electrons with atomic nuclei) frequencies exist, where the oscillation

becomes resonant. The resonance frequency of the plasmons of GNP with sizes < 100 nm, is in the visible range of the spectrum [19,24–29]. This LSPR results in absorption and scattering of light at these wavelengths. There are many parameters which affect the LSPR and hence the attributed absorption. For example, the size and shape of the nanoparticles, the dielectric environment and the distance of the particle from each other (if it is small enough to allow electromagnetic coupling) [25–32]. This enables a wide range of variations in the (optical) properties of GNP.

Numerous papers describe the preparation of GNP from (mainly aqueous) solutions using a wide variation of reducing agents and surfactants [27,33]. The precipitation of GNP from glasses by a thermal treatment slightly above the glass transition temperature is known since a long time and is utilized for the fabrication of so called “gold ruby” glasses. Another method which is especially advantageous for the preparation of large areas covered by metallic nanoparticles is the deposition of thin metal layers on flat substrates, such as float glass and subsequent thermal treatment. The thermal treatment of metal films with a typical thickness of 5–29 nm results in a dewetting and the formation of well separated particles of well defined sizes [17,31,34,35].

For many applications, the GNP needs to be applied or embedded on or in solid substrates. Especially for optical and sensor

* Corresponding author at: Otto-Schott-Institut of Materials Research, Jena University, Löbdegraben 32, 07743 Jena, Germany. Tel.: +49 03641 947773; fax: +49 03641 947702.

E-mail address: christian.worsch@posteo.de (C. Worsch).

applications glass as a substrate material offers a number of advantageous properties. In most studies, GNP is precipitated on a substrate; they have usually a poor adhesion to the surface and are not long-term stable. Therefore, it might be required to protect the GNP by an appropriate thin transparent dielectric layer, i.e. embedding them in a matrix [21,36,37]. A further route to prepare strongly adherent and scratch resistant GNP layers is the thermal treatment of soda-lime-silica glasses coated with a thin sputtered gold layer, which was subsequently covered with silica [18].

In this article, a method for the preparation of micro structured glasses functionalized with GNP is presented using the isothermal hot embossing process. If the hot embossing is carried out at high temperatures, which means at low viscosities, it results in strong adherence or a sticking of the glass to the surface of the tool. This will inevitably cause damage to the glass, as well as in most cases of the molds [38]. On the other hand, if hot embossing is carried at lower temperatures, the necessary mechanical load is too large and the embossing time is too long to allow an efficient production process. In addition an increased wear of the tool in the continuous operation of the production process can be observed. It should be noted that this cannot be prevented by coating the tool used for the hot embossing process and which leads to satisfactory results only in the classic glass pressing process [39]. Hence, for structuring, a special coating strategy for the hot embossing of glass is applied [40,41]. In a first step, the substrate glass is coated by a thin silica layer and subsequently sputtered with a thin gold layer. The both layers were covered with a further thin film of silica. The silica layer prevents the sticking of the glass during the subsequent embossing process. Hence, the limitations of the hot embossing process, such as the maximum temperature which can be supplied are significantly less strict [40,41]. Using a thin gold layer as coating on the substrate enables the formation of a stable layer composed by GNP which is spontaneously formed during the hot embossing process. The suitability of an as prepared microfluidic chip as plasmonic sensor is described in the following.

2. Experimental

Two soda-lime-silica glass substrates (glass transition temperature, T_g : 525 °C) with a dimension of 25 mm × 17 mm were cleaned and subsequently coated with a 20 nm thick silica layer using a combustion chemical vapor deposition (CCVD) process. This CCVD procedure has already been described in detail (see e.g. in [42,43]). Second, a 12 nm thick gold layer was deposited using a sputter coater. In a third step, a further 20 nm thick silica layer was applied.

The hot-embossing was realized using an experimental setup consisting of a precision pressing machine with an integrated gas tight process chamber, including mold, substrate, heater as well as sensors for process control. The hot embossing was performed under inert argon gas atmosphere (500 Pa) and isothermal conditions, at 660 °C, i.e. 135 K above the T_g of the glass substrate. The pressing force was 2000 N, corresponding to 8 MPa pressure. In order to prepare a microfluidic structure, a laser-processed silicon carbide mold with a flow analysis system as shown in Fig. 1 was used. The channel width was 500 μm and the depth of the channel was 100 μm.

The gold coated glass sheet covered by silica was hot embossed with the microfluidic structure. The applied pressing impulse has been tailored to achieve an optimum structure replication in the glass. Boundary condition was that the demoulding forces remain small, to avoid damage to the glass or the tool. After the forming process, three holes were drilled in the channels in order to enable injection of the fluids. In a second step, a flat glass substrate coated with the same silica/gold/silica layer was used as a cover

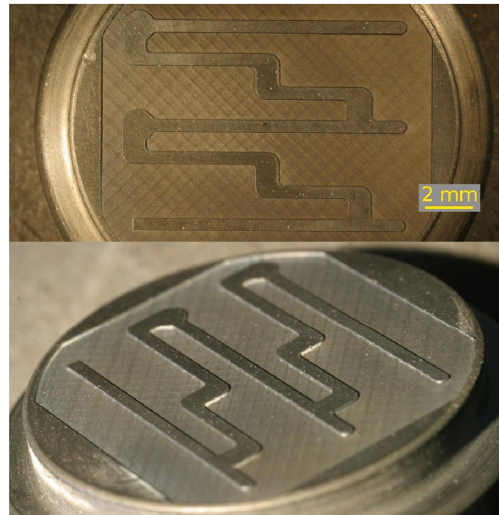


Fig. 1. Laser structured silicon carbide mold with a structure of a microfluidic flow analysis system.

sheet to build the microfluidic structure via bonding at 600 °C, kept for 60 min.

The accuracy of the embossed structure was examined using laser-scanning-microscopy (Zeiss Laser Scanning Mikroskop Axiolmager Z1m PASCAL5). Micrographs of the layers were obtained by scanning electron microscopy (Jeol JSM-7001 F FEG-SEM). Using the complete microfluidic chip, the channels were filled with several different liquids, water, ethanol and xylene. Then UV-vis-NIR spectra were recorded (UV-vis-NIR spectrometer, Shimadzu UV 3101 PC, spot size 7 mm × 16 mm). For comparison UV-vis-NIR spectra were also recorded from respectively two GNP coated glass cuvettes. One was prepared by a simple annealing process which resulted in dewetting of the thin sputtered gold films [17]. In this case, the gold film was not covered with silica. A second cuvette was coated with a thin gold layer sandwiched between two 20 nm silica layers. Both cuvettes were annealed with the same temperature program as the microfluidic chip. Then, the various liquids (deionized water, ethanol, xylene) were given in between the coated glasses and the spectra were recorded. The microfluidic sensor was measured in the same spectrometer, but with a changed spot size of 4 mm in order to minimize the influence of the chip area which is not in contact with the liquid. The measurement procedure where performed in analogy with the cuvettes, described above. All spectra were fitted near the minimum with a Gaussian function in order to determine the center of mass and denoted as "minimum".

The theoretical calculation where performed with the software MiePlot 4.304 based on the BHMIE Mie-code from Bohren and Huffman [26]. The required refractive index data of gold are taken from Johnson and Christy [44]. The simulations were performed by an adjustment of the particle sizes as well as of an effective dielectric medium to adapt the special geometric conditions. A weighting function was applied to calculate an effective medium (see Eq. (1)).

$$n_{\text{eff}} = g * n_{\text{substrate}} + (1 - g) * n_{\text{analyte}} \quad (1)$$

It should be noted that the effective medium is applied only to the dielectric components (silica layer and analyte), in contrast to an effective medium consisting of dielectrics and metallic particles like the Maxwell-Garnett theory.

To determine the minimum of each calculated spectra (extinction cross-section vs. wavelength), the data were fitted with a Gaussian function and the center of mass was taken as the minima. The calculations were performed using the refractive indices of the analyzed liquids with and without the weighting factor in (Eq. (1)). The obtained values of the minima were fitted using a quadratic function across the refractive indices and are plotted in Fig. 7. Additionally, an overview of the used refraction indices and effective refraction indices is given in Table 2.

The real particle size distribution was determined by image processing. The particle diameter is calculated from the circuit area equivalent of the particle projection in Fig. 3c.

3. Results

Fig. 1 shows the mold used for preparation of the microfluidic chip. A schematic drawing of the preparation process (treatment time and temperature), the resulting layer structures and optical transmission set up is presented for the cuvette in Fig. 2a. Here, the analyzed fluid is in direct contact to the GNP. The bonding of the both coated substrates and the dewetting was realized in one single processing step.

By contrast, the microfluidic chip, as well as the second cuvette is schematically shown in Fig. 2b. Both are coated by a layer of GNP plus a silica layer on top. Hence the fluid is in direct contact to the silica layer, but not to the GNP. The microfluidic chip consists of two coated substrates, but only one is structured. The preparation of the chip was performed in two steps. The first step was the hot embossing of the fluidic structure (including dewetting) and the second was the bonding procedure. All sensor types were filled

with water, ethanol or xylene. As reference also spectra from empty sensors (i.e. filled with air) were recorded.

A typical SEM micrograph of a silica layer deposited with CCVD is presented in Fig. 3a. A particle-like structure is observed. Fig. 3b shows an SEM micrograph of a gold layer covered with a CCVD silica layer. The particle-like structure of the silica-layer is observed which is superimposed by the percolated structure of the gold layer. The SEM micrograph of the layer system after the embossing process is shown in Fig. 3c (material contrast) and d (topography contrast). In the material contrast image particles with sizes of 20–150 nm are observed. A detailed analysis (not shown) of the particle derivation exhibits a log-normal distribution with a mean diameter of 64 nm and a consequent asymmetric margin for error of –25 nm and +40 nm (standard deviation). The topography contrast shows a particle-like structure with particle sizes in the range from 50 to 200 nm.

A detail of the topography of the hot embossed microfluidic structure is shown in Fig. 4. The determined edge radius is 15 μm. The obtained structure corresponds to that of the used mold. A photo of the subsequently bonded microfluidic chip is shown in Fig. 5. In order to contact the chip with supplies and drain, three holes were drilled into the cover glass (marked with white arrows in Fig. 5). For the naked eye, the chip shows a gold-ruby color. The structure is completely bonded and without leaks.

The transmission spectra recorded in a wavelength range from 425 to 660 nm from a cuvette deposited only by the GNP layer is shown in Fig. 6a. The spectra show distinct transmission minima, which are observed at different wavelengths in the range from 544 to 557 nm depending on the fluid. The empty sensor shows a minimum at the smallest wavelength of 544 nm, followed by the sensor

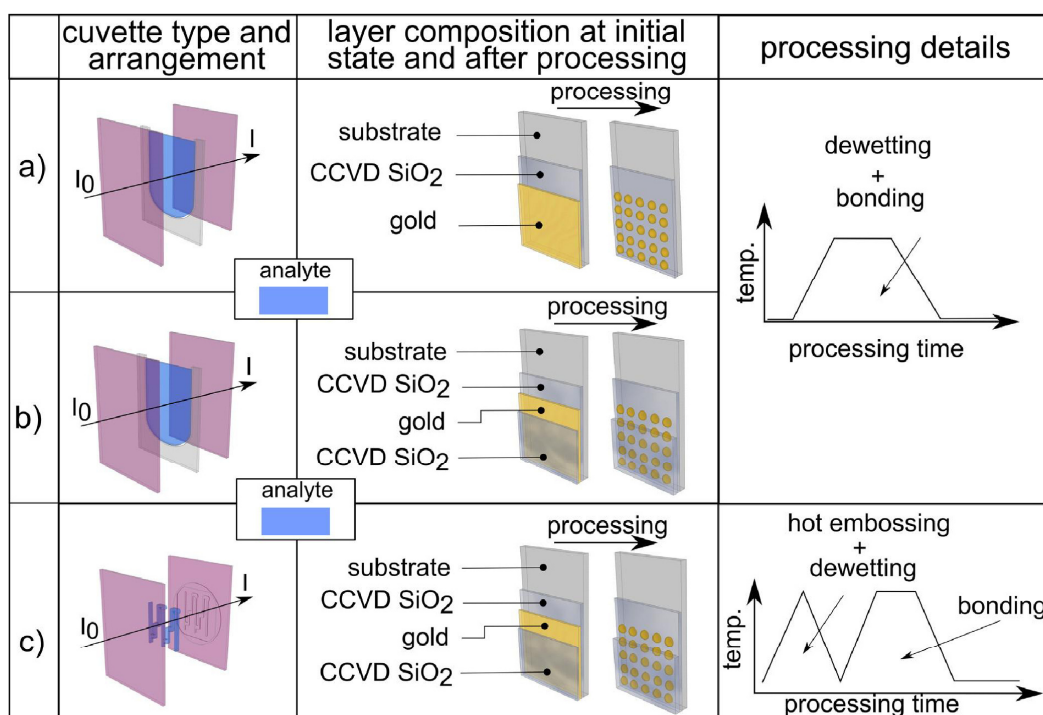


Fig. 2. Schematic drawings of the used sensor systems. (a) A sensor system comparable to the cuvettes, with uncovered GNP, prepared with single step process. (b) A sensor system comparable to the cuvettes, with silica covered GNP, prepared with single step process. (c) A microfluidic sensor embossed directly into the substrate glass and subsequently bonded.

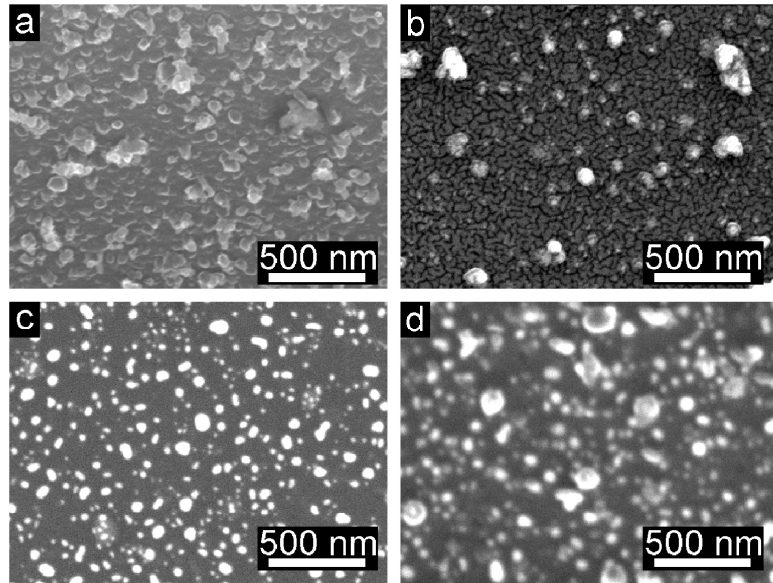


Fig. 3. SEM micrographs of (a) silica layer deposited with CCVD, (b) gold layer covered with a CCVD silica layer, (c) the layer system after the embossing process (material contrast), (d) the layer system after the embossing process (topography contrast).

filled with water (551 nm) and ethanol (552 nm). The largest wavelength (557 nm) was that attributed to the minimum of the xylene filled sensor.

The spectra recorded from the cuvette coated with the silica sandwiched GNP-layer are shown in Fig. 6b. In analogy to Fig. 6a, all spectra exhibit pronounced minima, where the attributed wavelengths depend on the fluid. In comparison to Fig. 6a, the minima occur at somewhat larger wavelengths (approximately 9–12 nm). In analogy to Fig. 6a, the empty coated cuvette exhibits the minimum located at the smallest wavelength (556 nm) and the xylene filled cuvette that at the largest wavelength (568 nm). The minima of the water and ethanol filled cuvette is in between at 562 and 563 nm, respectively.

In Fig. 6c the optical transmission spectra of the hot embossed microfluidic sensor are presented. It should be mentioned that these spectra result from an overlapping of “active” and “non-active” areas of the chip, measured with a spot size of 4 mm. The empty (air filled) chip exhibits a minimum at 551.9 nm, whereas

the minimum of the spectrum recorded from the xylene filling is shifted to 557.6 nm. In analogy to the measurements in the cuvette, the minima of water and ethanol appear between at 554.8 nm and 555.0 nm respectively.

The minima (LSPR) of all recorded spectra are summarized in Table 1.

Fig. 7 shows the resonance wavelengths as a function of the refractive index of the fluid (analyte) for the measured systems points (cuvettes and sensors) as well as the calculated curve (lines) of the cuvettes with and without an effective (dielectric) medium around the particles. All measured and calculated systems show at a refractive index of $n = 1$ the lowest resonance wavelength. While at a refractive index of the xylene ($n = 1.492$), the highest resonance wavelengths are obtained. Within the limits of error, a continuous increase of the wavelengths attributed to the minima is observed with increasing refractive indices. The dashed lines correspond to the calculated LSPR wavelengths based on the Mie theory with a weighed effective dielectric medium surrounding the GNP. The full lines, show the behavior without the weighted effective dielectric

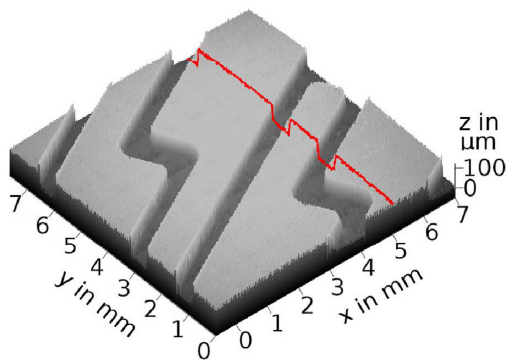


Fig. 4. The topography of the embossed microfluidic structure.

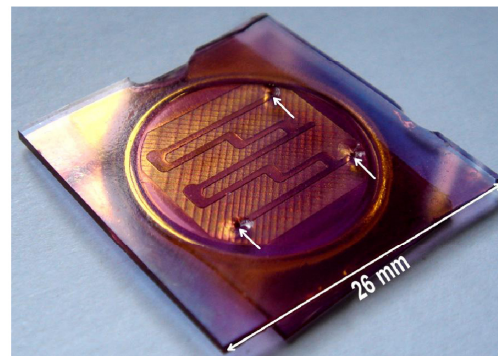


Fig. 5. An image of the bonded microfluidic chip.

Table 1
 Minima of the plasmonic peak of GNP and of silica coated GNP in contact with air and different liquids.

		Air	Water	Ethanol	Xylene
Uncovered gold nanoparticles on a glass cuvette	Plasmon resonance in nm	544	551	552	557
	Δ in nm	0	7	8	13
Silica covered gold nanoparticles on a glass cuvette	Plasmon resonance in nm	556	562	563	568
	Δ in nm	0	6	7	12
Gold/silica layer in the microfluidic chip	Plasmon resonance in nm	551.9	554.8	555	557.9
	Δ in nm	0	2.9	3.1	6

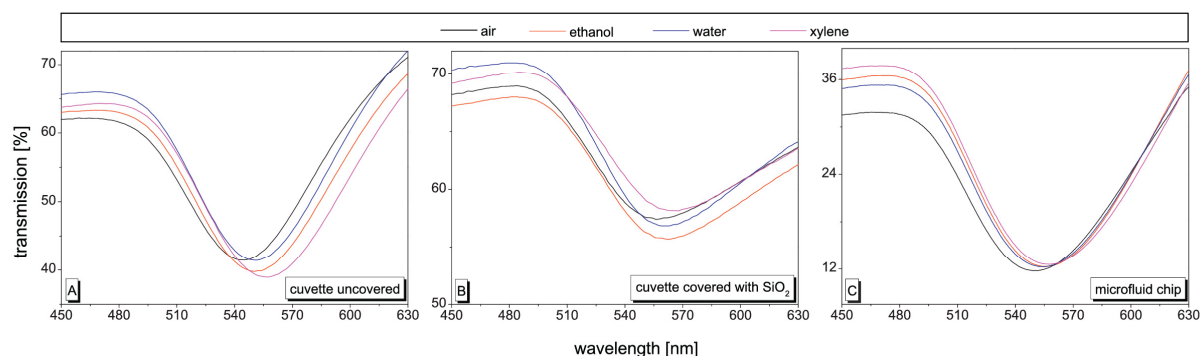

Fig. 6. (a) Transmission spectra in the wavelength range from 460 to 650 nm of the cuvette (only GNP) filled with different liquids. (b) Transmission spectra in the wavelength range from 460 to 650 nm of the cuvette (GNP plus silica layer) filled with different liquids. (c) transmission spectra in the wavelength range from 460 to 650 nm of the microfluidic-chip (GNP plus silica layer) filled with different liquids.

Table 2

 An overview of the used simulation parameters. The refractive index of CCVD silica surface is specified as $n_{\text{substrate}} = 1.460$ [48].

System	Particle diameter (d)	Weighting factor (g)	Analyte	Refractive indices (n_{analyte})	Resulting effective refractive index (n_{eff})
Cuvette, uncovered GNP	64 nm	0.82	Air	1.000 [48]	1.377
			Water	1.332 [48]	1.437
			Ethanol	1.361 [48]	1.442
			Xylene	1.492 [48]	1.466
Cuvette, silica, covered GNP	72 nm	0.85	Air	1.000 [48]	1.391
			Water	1.332 [48]	1.441
			Ethanol	1.361 [48]	1.445
			Xylene	1.492 [48]	1.465

medium, using the experimental particle sizes of 64 and 72 nm determined by the adaption of the cuvettes. All used simulation parameters are summarized in Table 2.

4. Discussion

Hot embossing of glass substrates under isothermal conditions is a serious problem due to a strong adherence of silicate melts with all known tool materials [38]. In the past few years, a technology has been described in the literature according to which not the tool material is coated, but the glass substrate [40,41]. The hot embossing process is carried out while the ductile substrate coating is deformed together with the glass substrate. It has been shown that many coating materials – among these sputtered gold layers – drastically decrease the adhesive forces between the (coated) glass and the tool. As shown in Fig. 4, also high aspect ratios can be achieved using the described technique.

Thin sputtered gold films shows dewetting during thermal treatment and form small islands with sizes in the range from 20 to 150 nm. This effect is well known and has frequently been described in the literature [34,45,46]. The sizes of the GNP depend on the thickness of the sputtered layer, the heating rate and the

temperature where the thermal treatment is carried out [17,35]. The glass forming process occurs at temperatures above T_g of the substrate glass. Hence also the silica covered gold layer can dewet in GNP [18]. Due to the resulting exposed glass surface after dewetting, a thin single gold layer without a silica cover layer is not sufficient to entirely prevent sticking during the hot-embossing process. Hence, the silica layer has three significant functions: first, it should further reduce the sticking of the viscous glass on the mold during the hot-embossing process [41], second the mean free path length for diffusion of the gold atoms will be decreased, which results in smaller particles and third it leads to an increase of the mechanic stability of the GNP [18].

It was shown that two of the coated glass substrates can bond together by a second heating step at a temperature 75 °C above T_g of the glass substrate. It can be assumed that the alkaline ions can diffuse through the silica layer which results in the good bonding [18].

The mold used has tiny structures related to the production process, i.e. small grooves on the surface, and a high roughness, which results from the production process (Fig. 1). These were accurately reproduced into the substrate (see Figs. 4 and 5) which illustrates the high precision of the embossing process. The higher roughness

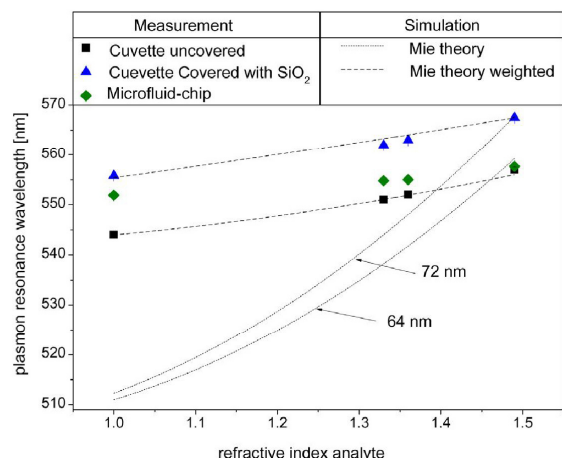


Fig. 7. Minima of the plasmonic peaks shown in Figs. 5 and 6 as a function of the refractive index of the fluid. Circles: cuvette (only GNP), Squares: microfluidic chip (GNP coated with silica). Dashed lines: According to Mie theory taking into account with and without a weighting factor (see text).

provides a higher surface area which facilitates the subsequent bonding process. However, the remaining grooves lead to light scattering and hence the optical properties, especially the transmission will thereby be degraded.

The dewetted films possess red color and the attributed spectra show a well pronounced minimum which is due to the LSPR. The LSPR is affected by a collective oscillation of electrons induced by the incident light and the surrounding medium is, besides the size and shape, one of the crucial points. Since the particles are smaller than the wavelengths of the visible light, the electron can leave the physical boundaries of the particles and thus interact with the surrounding medium. In this case, a higher refractive index shifts the resonance to lower energies. The transmission spectra can be calculated from the geometry (size and shape) and geometric arrangement of the GNP, their distance from each other and the dielectric function of the metal as well as from the refractive index of the surrounding medium using Mie theory. In the following, results of simulations based on Mie theory are described.

As a first approximation, the model of a small spherical and metallic particle within a homogeneous dielectric medium was assumed. The shift of the PR wavelength to higher values with increasing refractive index of the studied liquid is in agreement with Mie theory.

In comparison to simulations using the refractive index (not the weighted effective medium) of the analyzed liquids, the shift in the respective LSPR wavelength of the measured liquids does not quantitatively match the predictions of the model system. Thus, the theoretically resonance wavelengths are significantly (35–45 nm) shifted to smaller values. Whereas the calculated values for xylene, with its refractive index very close to that of SiO₂, corresponds to the predictions very well.

As a medium with a refractive index close to that of the matrix, it can be concluded that the nanoparticles do not interact as strongly as expected on their environment (at lower refractive indices) because their interface to the changeable surrounding matrix is partially blocked by SiO₂. Hence, as mentioned above, the used algorithm is based on the assumption of a free-floating spherical structure within a homogeneous medium and the effect of the (changed) refractive index should be much lower, since the GNP are not entirely surrounded by the analyzed liquid. This was taken into account by introducing a weighting factor into the calculations.

This weighting factor assumes an effective medium consisting of the substrate surface as well as of the surrounding liquid (see Eq. (1)).

Since in this method, the resonance wavelength and slope (LSPR shift vs. refractive index) has been used, an independent determination of the particle size and the weighting factor is possible.

From the chip, spectra of areas which are responsive to a change of the refractive index and areas which are still unchanged, because they do not have a contact to the liquid and cannot be separated due to the comparably large spot size. Hence, a quantitative statement on the system is more difficult. Nevertheless, the determined particle size distribution (from the SEM micrographs in Fig. 3c) of 64 nm is in a very good agreement with the theoretical predictions from the simulation (of the cuvette) discussed above.

A comparison of the measured and calculated data shows that the surrounding liquid has a contribution of only 15–18% to the dielectric function, i.e. to the surrounding medium. This result is not surprising compared to the typical rough surface structure of CCVD silica. However, Okamoto et al. described a sensor system which is based on a single layer of GNP, where the optical properties were determined as a function of a PMMA cover layer thickness [8]. It was shown that the LSPR shifts to higher wavelength, up to a layer PMMA thickness of ca. 20 nm. As also discussed in that article, the narrow range around the GNP can assumed as an effective medium.

Furthermore, the difference in the weighted refractive indices between water and ethanol is only 0.04, but a difference in the PR wavelengths is clearly detected. This is characteristic for the high optical sensitivity of the nanoparticle systems.

The spectral peak shift and the peak broadness result from the dielectric environment, the size and size-distribution of the particles. All samples were annealed above T_g of the glass. In the case of the cuvette, where the gold layer was not covered by a silica layer, the GNP subside in the glass surface. Whereas the silica covered gold layer form GNP, which can lift to the surface and are coated by only a thin silica cover layer. As described in Ref. [18,47] some of the GNP may not be covered by silica and some GNP might be exposed to the atmosphere. The subsidence of the GNP in the uncovered cuvette and the thinning of the silica cover layer of the sandwiched GNP layer results in a comparable high sensitivity to surrounding media.

In comparison to the cuvettes, the transmitted light as well as the sensitivity (i.e. LSPR-shift) of the microfluidic chip is lower. Since the light beam of the used spectrometer is larger than the channel structures, the peak intensity or the transmission of the chips is lower than in the cuvette. Increased peak intensity might be achieved by an adaptation of the beam size (of the spectrometer) to the channel width on the chip, so that the complete fluid-filled area will be transmitted by the beam.

By using other metals, such as silver, palladium, platinum or even alloys, not only the plasmon resonance, but also the reactivity or the catalytic activity of the nanoparticles can be modified. The described preparation method of metal nanoparticle functionalized and structured glass chips will enlarge the list of applications of microfluidics as well as micro electromechanical and micro optic systems.

5. Conclusions

A soda-lime-float glass coated with a layer stack of silica, gold and silica was structured with a microfluidic structure using the isothermal hot-embossing process. The gold film dewets during the forming process and forms a layer of GNP, while the silica layer prevents effectively the sticking of the glass on the mold. The microstructured substrate was bonded together with an identical coated substrate in a second annealing step. The LSPR peak in the

transmission spectra of the GNP in the resulting microfluidic chip shows a detectable sensitivity for the refractive index of filled in liquids. In comparison, two simple cuvettes coated with GNP, with and without a silica cover layer were prepared and the LSPR were theoretically simulated and compared with the measured results. A weighting factor is determinable by a theoretical consideration. This weighting factor is primarily a correction for coverage as well as particle geometry and size distribution. Important is the knowledge about the plasmonic behavior at different refractive indices, thus a particle size and correction factor can be estimated.

Acknowledgments

The research project AIF 245 ZBR of the European Society of Thin Films was promoted by the "Collective Research for SMEs" (IGF), with support from the budget of the Federation of Industrial Research Associations (AiF), Cologne, Germany. The project was financed with funds from the Federal Ministry of Economics and Technology, Berlin, Germany. Parts of this work are supported by the DFG "Deutsche Forschungsgemeinschaft" under Grant. Nos.: Se 698/10-1 and Se 698/10-2. We would like to thank all funding organizations. Further, the authors would like to thank Dr. W. Seeber for support.

References

- [1] M.S. Chen, D.W. Goodman, Catalytically active gold: from nanoparticles to ultrathin films, *Acc. Chem. Res.* 39 (2006) 739–746.
- [2] M.S. Chen, D.W. Goodman, Structure activity relationships in supported Au catalysts, *Catal. Today* 111 (2006) 22–33.
- [3] D. Pissuwan, C.H. Cortie, S.M. Valenzuela, M.B. Cortie, Functionalised gold nanoparticles for controlling pathogenic bacteria, *Trends Biotechnol.* 28 (2010) 207–213.
- [4] L. Olofsson, T. Rindzevicius, I. Pfeiffer, M. Käll, F. Höök, Surface-based gold-nanoparticle sensor for specific and quantitative DNA hybridization detection, *Langmuir* 19 (2003) 10414–10419.
- [5] C. de Julián Fernández, M.G. Manera, J. Spadavecchia, G. Maggioni, A. Quaranta, G. Mattei, M. Bazzan, E. Cattaruzza, M. Bonafini, E. Negro, A. Vomiero, S. Carturan, C. Scian, G. Della Mea, R. Rella, L. Vasanelli, P. Mazzoldi, Study of the gas optical sensing properties of Au-polyimide nanocomposite films prepared by ion implantation, *Sens. Actuators B* 111–112 (2005) 225–229.
- [6] K.-S. Lee, M.A. El-Sayed, Gold and silver nanoparticles in sensing and imaging: sensitivity of plasmon response to size, shape, and metal composition, *J. Phys. Chem. B* 110 (2006) 19220–19225.
- [7] P.K. Jain, X. Huang, L.H. El-Sayed, M.A. El-Sayed, Noble metals on the nanoscale: optical and photothermal properties and some applications in imaging, sensing, biology, and medicine, *Acc. Chem. Res.* 41 (2008) 1578–1586.
- [8] T. Okamoto, I. Yamaguchi, T. Kobayashi, Local plasmon sensor with gold colloid monolayers deposited upon glass substrates, *Opt. Lett.* 25 (2000) 372–374.
- [9] A. Gopinath, S.V. Boriskina, B.M. Reinhard, L. Dal Negro, Deterministic aperiodic arrays of metal nanoparticles for surface-enhanced Raman scattering (SERS), *Opt. Express* 17 (2009) 3741–3753.
- [10] C. Hrelescu, T.K. Sau, A.L. Rogach, F. Jäckel, J. Feldmann, Single gold nanostars enhance Raman scattering, *Appl. Phys. Lett.* 94 (2009) 153113.
- [11] Y. Hosoya, T. Suga, T. Yanagawa, Y. Kurokawa, Linear and nonlinear optical properties of sol-gel-derived Au nanometer-particle-doped alumina, *J. Appl. Phys.* 81 (1997) 1475–1480.
- [12] N. Venkatram, R.S. Kumar, D. Narayana Rao, S.K. Medda, S. De, G. De, Nonlinear optical absorption and switching properties of gold nanoparticle doped SiO₂-TiO₂ sol-gel films, *J. Nanosci. Nanotechnol.* 6 (2006) 1990–1994.
- [13] S. Pillai, K.R. Catchpole, T. Trupke, M.A. Green, Surface plasmon enhanced silicon solar cells, *J. Appl. Phys.* 101 (2007) 93105.
- [14] K.R. Catchpole, A. Polman, Design principles for particle plasmon enhanced solar cells, *Appl. Phys. Lett.* 93 (2008) 191113.
- [15] J. Euler, Ultraoptische Eigenschaften von Metallen und mittlere freie Weglänge der Leitungselektronen, *Z. Phys.* 137 (1954) 318–332.
- [16] U. Kreibitz, L. Genzel, Optical-absorption of small metallic particles, *Surf. Sci.* 156 (1985) 678–700.
- [17] C. Worsch, M. Kracker, W. Wisniewski, C. Rüssel, Optical properties of self assembled oriented island evolution of ultra-thin gold layers, *Thin Solid Films* 520 (2012) 4941–4946.
- [18] C. Worsch, W. Wisniewski, M. Kracker, C. Rüssel, Gold nano-particles fixed on glass, *Appl. Surf. Sci.* 258 (2012) 8506–8513.
- [19] C. Granqvist, O. Hunderi, Optical-properties of ultrafine gold particles, *Phys. Rev. B* 16 (1977) 3513–3534.
- [20] S. Norman, T. Andersson, C.G. Granqvist, O. Hunderi, Optical properties of discontinuous gold films, *Phys. Rev. B* 18 (1978) 674–695.

- [21] T. Ung, L.M. Liz-Marzan, P. Mulvaney, Gold nanoparticle thin films, *Colloid Surf. A* 202 (2002) 119–126.
- [22] T. Karakouz, D. Holder, M. Goomanovsky, A. Vaskevich, I. Rubinstein, Morphology and refractive index sensitivity of Gold Island Films, *Chem. Mater.* 21 (2009) 5875–5885.
- [23] V. Švorčík, J. Siegel, P. Šutta, J. Mistrík, P. Janíček, P. Worsch, Z. Kolská, Annealing of gold nanostructures sputtered on glass substrate, *Appl. Phys. A* 102 (2011) 605–610.
- [24] M. Moskovits, Surface-enhanced spectroscopy, *Rev. Mod. Phys.* 57 (1985) 783–826.
- [25] M. Quinten, *Optical Properties of Nanoparticle Systems*, Wiley-VCH, Weinheim, 2011.
- [26] C.F. Bohren, D.R. Huffman, *Absorption and Scattering of Light by Small Particles*, Wiley, New York, 1983.
- [27] F. Parmigiani, G. Samoggia, G.P. Ferraris, Optical properties of sputtered gold clusters, *J. Appl. Phys.* 57 (1985) 2524–2528.
- [28] U. Kreibitz, M. Vollmer, *Optical Properties of Metal Clusters*, 1st ed., Springer, Berlin/Heidelberg, 1995.
- [29] K.L. Kelly, E. Coronado, L.L. Zhao, G.C. Schatz, The optical properties of metal nanoparticles: the influence of size, shape, and dielectric environment, *J. Phys. Chem. B* 107 (2003) 668–677.
- [30] G. De, S. Bhattacharyya, Au nanoparticles in alumina sols and coatings, *J. Mater. Chem.* 18 (2008) 2816–2824.
- [31] G. Gupta, D. Tanaka, Y. Ito, D. Shibata, M. Shimojo, K. Furuya, K. Mitsui, K. Kajikawa, Absorption spectroscopy of gold nanosized films: optical and structural characterization, *Nanotechnology* 20 (2009) 25703.
- [32] E. Hutter, J.H. Fendler, Exploitation of localized surface plasmon resonance, *Adv. Mater.* 16 (2004) 1685–1706.
- [33] I. Vakarelski, D. Chan, T. Nonoguchi, H. Shinto, K. Higashitani, Assembly of gold nanoparticles into microwave networks induced by drying liquid bridges, *Phys. Rev. Lett.* 102 (2009) 58303.
- [34] C. Schrank, C. Eisenmenger-Sittner, E. Neubauer, H. Bangert, A. Bergauer, Solid state de-wetting observed for vapor deposited copper films on carbon substrates, *Thin Solid Films* 459 (2004) 276–281.
- [35] M. Kracker, C. Worsch, C. Rüssel, Optical properties of palladium nanoparticles under exposure of hydrogen and inert gas prepared by dewetting synthesis of thin-sputtered layers, *J. Nanopart. Res.* 15 (2013) 1–10.
- [36] L.M. Liz-Marzán, M. Giersig, P. Mulvaney, Synthesis of nanosized gold-silica core-shell particles, *Langmuir* 12 (1996) 4329–4335.
- [37] Y. Hu, R.C. Fleming, R.A. Drezek, Optical properties of gold-silica-gold multi-layer nanoshells, *Opt. Express* 16 (2008) 19579–19591.
- [38] F. Klocke, G. Pongs, Precision glass molding of optical components, *Prod. Eng. Ann. WGP* 11 (2004) 21–24.
- [39] D. Rieser, G. Spieß, P. Manns, Investigations on glass-to-mold sticking in the hot forming process, *J. Non-Cryst. Solids* 354 (2008) 1393–1397.
- [40] J. Edelmann, C. Worsch, A. Schubert, C. Rüssel, Micro structuring of inorganic glass by hot embossing of coated glass wafers, *Microsyst. Technol.* 16 (2010) 553–560.
- [41] C. Worsch, J. Edelmann, C. Rüssel, A. Schubert, Determination of adhesive forces and sticking temperature of coated glasses for the hot-embossing-process, *Microsyst. Technol.* 17 (2011) 1401–1406.
- [42] T. Struppert, A. Heft, B. Grüner, Thin functional films by combustion chemical vapour deposition (C-CVD), *Thin Solid Films* 520 (2012) 4106–4109.
- [43] C. Worsch, C. Rüssel, Effect of substrate temperature during combustion chemical vapour deposition on the formation of silica films, *Thin Solid Films* 518 (2010) 4798–4803.
- [44] P.B. Johnson, R.W. Christy, Optical-constants of noble-metals, *Phys. Rev. B* 6 (1972) 4370–4379.
- [45] J. Bischof, D. Scherer, S. Herminghaus, P. Leiderer, Dewetting modes of thin metallic films: nucleation of holes and spinodal dewetting, *Phys. Rev. Lett.* 77 (1996) 1536–1539.
- [46] C.M. Müller, R. Spolenak, Microstructure evolution during dewetting in thin Au films, *Acta Mater.* 58 (2010) 6035–6045.
- [47] S. Christke, C. Katzer, V. Grosse, F. Schmid, G. Schmid, W. Fritzsche, J. Petschulat, T. Pertsch, M. Rettenmayr, Optical resonances of self-organized monocrystalline Au nanoparticles embedded in SrTiO₃ matrix, *Opt. Mater. Express* 1 (2011) 890–897.
- [48] W.M. Haynes, D.R. Lide, *CRC Handbook of Chemistry and Physics*, 91st ed., CRC Press, Boca Raton, London, New York, 2010.

Biographies

Christian Worsch studied materials science at Friedrich-Schiller-University Jena from 2001 to 2006. He made his Ph.D. in the field of coating and hot embossing of glass from Friedrich-Schiller-University Jena in 2010. Since 2010 he has been in postdoctoral position at the Otto-Schott-Institut of materials research in section of glass coating and micro-structuring as well as chip-calorimetry. His research interest focuses metallic nanostructures and calorimetric study of ceramic and glassy particles.

Michael Kracker studied materials science at Friedrich-Schiller-University Jena until 2011. He received his diploma degree in 2011. Following he started his Ph.D. thesis at the Otto-Schott-Institut of materials research at Friedrich-Schiller-University Jena. His research interest is focused on the optical

properties of thin films and dewetted metallic nanoparticle layers as well as sensing systems.

Jan Edelmann has graduated as an engineer in micro technology and mechatronics from the Chemnitz University of Technology in 2004 and attained his doctorate degree in 2012 in the field of micro production technologies. At the Fraunhofer IWU he leads the department Functional Surfaces and Microsystem Manufacturing. Main fields of his activity are replication technologies for structuring the surfaces of metals, plastics and glasses, the influences of miniaturization on the forming process and the application of precise electrochemical machining in mold manufacturing.

Andreas Schubert studied mechanical engineering starting from 1982 at Dresden University of Technology and attained a doctorate degree in 1991 in the field of precision robotics. Afterwards it began to develop the workscope of micro manufacturing technology at the Fraunhofer Institute IWU Chemnitz. Since 2003 he is a professor for Micromanufacturing Technology at the Chemnitz University of Technology beyond that. Main fields of research are cutting and erosion manufacturing

processes as well as micro forming technologies for the production of ultra precise and micro-structured surfaces for optical, fluid and tribological applications. He also supervises the department of Functional Surfaces and Microsystem Manufacturing at the Fraunhofer IWU. He leads several research projects in the areas of the micro and nano manufacturing for applications in mechanical engineering and the automobile industry as well as the optics and electronics manufacturing. Both fundamentally oriented research projects are handled and in co-operation with the industry research results are being converted into application.

Christian Rüssel is Professor of Glass Chemistry at Jena University. He studied Chemistry at University of Erlangen-Nürnberg until 1981 and made his Ph.D. in Physical Chemistry at the same University in 1984. Then he joined the Fraunhofer-Institute for Solar Energy Systems in Freiburg, Germany for one and a half year. He went to the Institute of Materials Science (Glass and Ceramics) to the University of Erlangen-Nürnberg and made his second Ph.D. in Engineering (Dr.-Ing. habil.) in 1991. Since 1992 he has the Chair of Glass Chemistry at Friedrich-Schiller-University Jena. His research field is glass as well as glass-ceramics, from fundamentals to applications.

3.8

M. Kracker, W. Wisniewski, C. Rüssel

Textures of Au, Pt and Pd/PdO Nano Particles Thermally Dewetted from Thin Metal Layers on Fused Silica

Manuscript Submitted To Small, (2014)

Textures of Au, Pt and Pd/PdO Nano Particles Thermally Dewetted from Thin Metal Layers on Fused Silica				
Beteiligt an				
	Michael Kracker	Dr. Wolfgang Wisniewski	Prof. Christian Rüssel	
Konzeption des Forschungsansatzes	X		X	
Planung der Untersuchung	X	X		
Datenerhebung	X	X		
Datenanalyse und Interpretation	X	X		
Schreiben des Manuskripts	X	X	X	
Vorschlag Anrechnung Publikationsäquivalente	1,0			
Anmerkung:				
Weitere Informationen sind in Appendix B aufgeführt.				

Small

Textures of Au, Pt and Pd/PdO Nano Particles Thermally Dewetted from Thin Metal Layers on Fused Silica --Manuscript Draft--

Manuscript Number:	
Full Title:	Textures of Au, Pt and Pd/PdO Nano Particles Thermally Dewetted from Thin Metal Layers on Fused Silica
Article Type:	Full Paper
Section/Category:	
Keywords:	textures; nano particles; dewetting; gold; palladium
Corresponding Author:	Michael Kracker Jena University GERMANY
Additional Information:	
Question	Response
Please submit a plain text version of your cover letter here. If you are submitting a revision of your manuscript, please do not overwrite your original cover letter. There is an opportunity for you to provide your responses to the reviewers later; please do not add them here.	Dear Editor, we would like to submit a manuscript entitled: "Textures of Au, Pt and Pd/PdO Nano Particles Thermally Dewetted from Thin Metal Layers on Fused Silica" for publication in Small. While a large number of articles have been published concerning metal nano particles, the fundamental aspect of the crystallographic relationship between the lattice of the particles and the substrate after dewetting has never been studied in detail. In contrast, the few articles where texture analysis is performed (usually by XRD which is a crude tool for this purpose) only describe the 111 texture which matches the scientific expectation and is therefore readily accepted and promoted. This view is so widely accepted, that no one has questioned its validity for different substrates, temperature or heating rates in the literature to the best of our knowledge. In this article we prove that 001 and 101 textures may coexist next to the 111 texture via fundamental texture analyses of Au, Pt and Pd/PdO NP thermally dewetted on fused silica. Additionally, we prove that texture formation is affected by the annealing temperature as well as the cooling rate of the annealing process. Furthermore, we prove that any crystallographic texture is lost in the case of Au if the metal is annealed above its melting point and rapidly cooled on the amorphous substrate. All in all, this article is aimed at providing a reference for future NP research concerning the systems of Au (optical properties), Pt (catalytic properties) as well as Pd/PdO (catalytic properties and sensor technologies). Additionally, the presented texture information should be of interest to all research where NP are used to induce the growth of nano wires from a surface and a crystallographic relationship between the seeding NP and the growing nano wire is frequently observed. Yours sincerely, Michael Kracker
Corresponding Author Secondary Information:	
Corresponding Author's Institution:	Jena University
Corresponding Author's Secondary Institution:	
First Author:	Michael Kracker
First Author Secondary Information:	

Textures of Au, Pt and Pd/PdO Nano Particles Thermally Dewetted from Thin Metal Layers on Fused Silica

Order of Authors:	Michael Kracker
	Wolfgang Wisniewski
	Christian Rüssel
Order of Authors Secondary Information:	
Abstract:	<p>This article presents results concerning the basic dewetting procedure of thin metal films on an amorphous substrate. Thin layers of gold, platinum and palladium are deposited on fused silica glass sheets by sputtering. The 14 to 18 nm thick layers of Au, Pt and Pd are dewetted into nano particles (NP) at temperatures from 424 to 1600 °C. The morphology of the resulting NP is characterized using scanning electron microscopy (SEM) while crystallographic analyses are performed using electron backscatter diffraction (EBSD).</p> <p>Multiple textures are described to occur and coexist in NP-layers of the respective materials and a temperature dependence of the texture formation in gold NP is proved. The transformation of Pd to PdO and its effects on the texture is also analyzed. It is shown that the cooling rate has an effect on the texture in the case of gold NP as well as on the physical structure of the Pd/PdO NP. Twinning relationships could be described to occur on all samples.</p>

DOI: 10.1002/ ((please add manuscript number))

Article type: Full Paper

Textures of Au, Pt and Pd/PdO Nano Particles Thermally Dewetted from Thin Metal

Layers on Fused Silica

Michael Kracker, Wolfgang Wisniewski and Christian Rüssel*

Otto-Schott-Institut, Jena University, Fraunhoferstr. 6, 07743 Jena, Germany

E-mail: Michael.Kracker@uni-jena.de

Keywords: textures, nano particles, dewetting, gold, palladium

This article presents results concerning the basic dewetting procedure of thin metal films on an amorphous substrate. Thin layers of gold, platinum and palladium are deposited on fused silica glass sheets by sputtering. The 14 to 18 nm thick layers of Au, Pt and Pd are dewetted into nano particles (NP) at temperatures from 424 to 1600 °C. The morphology of the resulting NP is characterized using scanning electron microscopy (SEM) while crystallographic analyses are performed using electron backscatter diffraction (EBSD).

Multiple textures are described to occur and coexist in NP-layers of the respective materials and a temperature dependence of the texture formation in gold NP is proved. The transformation of Pd to PdO and its effects on the texture is also analyzed. It is shown that the cooling rate has an effect on the texture in the case of gold NP as well as on the physical structure of the Pd/PdO NP. Twinning relationships could be described to occur on all samples.

1. Introduction

1
2 Metallic nano particles (NP) have been extensively studied and are most frequently produced
3
4 by chemical methods which include adding organic additives to the system.^[1] By comparison,
5
6 the thermal dewetting of metallic layers with a thickness in the nm-range into NP to achieve
7
8 optically active surfaces is performed less often.
9

10
11 Dewetting allows the production of large, additive free systems and an interaction between
12
13 the dewetting metal layer and its substrate which in turn allows a self assembling orientation
14
15 relationship in the form of a crystallographic texture. Dewetting itself may occur far below the
16
17 melting point of the metal, e.g. as low as 300 °C for gold,^[2,3] and has been performed in a
18
19 number of systems including gold, platinum and palladium. In this article we discuss particle
20
21 formation effects, morphologies and crystallographic orientations as well as textures in
22
23 dependence of the process temperature and the cooling procedure. We also highlight the
24
25 importance of phase transitions during particle formation during heating as well as cooling.
26
27 Because gold does not show any phase transitions during annealing, we use comparably
28
29 produced palladium NP for these experiments which exhibit a pronounced tendency to
30
31 oxidize during sample preparation.
32
33

34
35 The faceting of metallic nano particles has been discussed in detail in Ref. [4] where AFM-
36
37 profiles show a faceted particle to be flat on the upper side. It has also been shown that
38
39 faceted gold NP on sapphire become rounded with increasing temperatures^[2] which was
40
41 reported to be accompanied by a loss of the strong 111 texture observed at lower
42
43 temperatures.^[2] While a large number of publications feature gold NP,^{e.g.[2-7]} the literature
44
45 concerning dewetted NP of Pt and Pd is more manageable.^[8-18]
46
47

48
49 When it comes to literature describing textures and crystallographic orientations, mainly
50
51 information concerning gold NP on substrates such as single crystals,^[2] oxidized Si-wafers^[5]
52
53 or glasses^{[3],[6]} was found by the authors. It has been shown that the gold NP are preferably
54
55 oriented with a {111}-plane parallel to the substrate surface on oxidized Si-wafers^[5] and
56
57
58
59
60
61
62
63
64
65

1 amorphous glasses^{[3],[6]} indicating this is a self organizing process. If the NP are heated above
2 their melting point on a sapphire substrate, the preferred orientation seems to be lost but the
3
4 faceted morphology reoccurs if the NP are held at an appropriate temperature for some
5
6 time.^[7] It was also shown that dewetting is possible on inexpensive materials such as soda-
7
8 lime-silica-glass. Two superimposed textures were described in correlation with the particle
9
10 size in experiments where the gold layers were covered by a layer of silica before the
11
12 dewetting process.^[6]
13
14

15
16 It is generally accepted that the driving force of thermal dewetting is the minimization of the
17
18 surface energy in the three phase system; substrate – metallic NP – furnace atmosphere.
19
20 However, the self-organization into textured layers with defined preferences of certain
21
22 crystallographic orientations is not really understood. While it seems logical that the fcc-
23
24 lattice of gold may prefer orientations where the close-packed {111}-layers arrange
25
26 themselves parallel to the substrate,^[3,5,6] the loss of such a texture at high temperatures^[2] and
27
28 the formation of subtextures where even an obvious relationship to a crystallographic plane is
29
30 lacking^[6] remains an open question which should, however, be of interest for all research
31
32 where dewetted NP are used to induce the growth of nano wires^[19] which frequently show a
33
34 crystallographic relationship to the seeding NP.
35
36

37
38 As a number of parameters such as substrate chemistry, substrate microstructure, cooling rates
39
40 or the atmosphere during annealing may affect this self organization, the current article is
41
42 aimed at providing a reference for future research by presenting texture analysis of a number
43
44 of dewetted metal layers on fused silica glass. Fused silica is a suitable material due to its
45
46 simple chemistry, its high thermal shock resistance and chemical stability as well as its
47
48 excellent optical properties for the analysis of the plasmonic characteristics of metallic NP in
49
50 the near UV range down to 200 nm. Additionally, it is available as a high purity material
51
52 throughout the world. The surface crystallization of fused silica above 1100 °C has recently
53
54 been studied including texture analysis.^[20] In the following we present studies on texture
55
56
57
58
59
60
61
62
63
64
65

1 based on the electron backscatter diffraction (EBSD-) analyses of dewetted layers of Au, Pt
2 and Pd/PdO. In contrast to orientation analyses carried out using X-ray diffraction, EBSD
3 enables to determine the orientation of each individual metallic nano particle from which
4 EBSD-patterns can be obtained and a much more detailed, phase specific texture analysis.
5
6
7
8
9

10 11 12 **2. Results and Discussion**

13
14 In order to visualize the texture information presented in this article, **Figure 1** schematically
15 shows three orientations of a cubic unit cell towards a substrate and the attributed poles these
16 orientations cause in the 001, 101 and 111 pole figures (PFs). The rings in the illustration
17 visualize the result of a random rotation around which ever direction is perpendicular to the
18 substrate. Finally, the superposition of all textures is presented to show that the central dot
19 (see arrows) is characteristic for only one texture while multiple textures may contribute to a
20 ring in some PFs.
21
22
23
24
25
26
27
28
29
30
31
32

33 **2.1. Gold**

34
35 Gold nano particles are by far the most frequently analyzed system of this topic and textures
36 as well as twinning orientations have previously been described in three different
37 experimental setups.^[3,5,6] Gold sputtered on silica at up to 210 °C has been analyzed in ref.
38 [21], however they were not produced by dewetting and information about a crystallographic
39 texture is not presented. The dewetting of Au on fused silica has not been analyzed by EBSD
40 and the result of applying a dewetting temperature high enough to melt the Au layer has not
41 been reported for any substrate to the best of our knowledge. Hence, multiple Au layers with a
42 thickness of 14 ± 1 nm were annealed at temperatures from 424 to 1102 °C to allow
43 comparability to ref. [3], the comparison to the other metal layers featured in this article and
44 finally the self organization of the layer after heating above the melting point of the metal.
45
46
47
48
49
50
51
52
53
54
55
56
57
58
59

60 **Figure 2** presents SEM-micrographs of the dewetted particles after annealing at a) 424 °C and
61
62
63
64
65

1 b) 965 °C. The particles are 159 and 113 nm in size and do not show a bimodal size
2 distribution which is in contrast to the results of Ref. [4] where dewetted Au layers with a
3 thickness of more than 10 nm showed bimodal size distributions. Dewetting at 424 °C
4 (Figure 2 a)) indicates a high degree of faceting which is systematically reduced at the
5 temperature of 965 °C (see Figure 2 b); this is phenomenologically in agreement with ref. [2].
6
7 Hwang and Noh^[2] recently concluded that the surface energy is responsible for the rounding
8 phenomena and additionally proposed a correlation between the crystal structure of their
9 sapphire substrate and the gold NP. However, the NP described in the present paper were all
10 formed on amorphous SiO₂-glass substrates excluding the possibility of a foreign (vaccinating)
11 lattice. The faceting describes a further minimization of the energy and the resulting shape is
12 determined by the Wulff construction and corresponds to a truncated octahedron.^{[4],[22]} In
13 order to describe the morphology, Barnard et al. calculated the equilibrium shape of gold NPs
14 using a thermodynamic model.^[23] They found that significant changes in the particle
15 morphology occur before the melting point of particles is reached. These results were
16 confirmed by Shim et al.^[24] and the rounding was mathematically also confirmed for copper
17 particles by Nielsen et al.^[25] The occurrence of twinning is well known in NP of this system
18 and is also explained by a modified Wulff construction.^[26]

19
20
21
22
23
24
25
26
27
28
29
30
31
32
33
34
35
36
37
38
39
40
41
42
43
44 The articles discussed above describe the fact that the surface fraction of typical crystal facets,
45 e.g. the 111 face, are reduced with increasing temperature. Hence a shape transformation
46 occurs in addition to a premelting mechanism.^{[25],[27]} The preferential 111 orientation of the
47 particles is obtained by the formation (dewetting) of an oriented initial metal layer.^[3] As the
48 temperature increases, the equilibrium shape of the particles is changed, hence the possibility
49 exists, that a particle may tilt by reducing the 111 contact surface,^[22] and a different
50 crystallographic orientation may be adopted. It may be concluded, that slow cooling may
51 cause the optimal surface at low temperatures to be observed after annealing while fast

1 cooling freezes the morphology observed at high temperatures. However, this argumentation
2 must be performed under consideration of the substrate.^[28]
3
4

5
6
7 Figure 2 also shows the 001, 101 and 111 PFs of textures calculated from EBSD-scans
8 performed with a step size of 40 nm covering an area of more than 450 μm^2 . For the
9 temperature of 965 °C, we present textures from two samples prepared simultaneously
10 (sputtering, annealing at 965 °C, slow cooling, and carbon coating) and a rapidly cooled
11 sample to illustrate the differences which may occur despite identical preparation and to test
12 the effect of the cooling rate. Please note that a very weak 111-texture may be shown in the
13 111 PF of the rapidly cooled sample if an even more sensitive scale is chosen.
14
15
16
17
18
19
20
21
22
23

24 The PFs show that only a 111-texture is observed in the annealed samples up to 718 °C. An
25 additional 001 texture occurs after annealing at 815 and 965 °C. At 965 and 1057 °C, a 101
26 texture is additionally detected after annealing. The type of the predominantly occurring
27 texture, i.e. “the strongest texture”, may shift between samples and, as a matter of fact, even
28 between different areas on the surface of one sample, hence we will not state a hierarchy.
29 Surprisingly, annealing at 1102 °C, i.e. above the melting point of Au, does not lead to
30 complete destruction of the particle arrangement. However, a crystallographic texture can no
31 longer be detected after annealing above the melting point, which confirms the previous
32 results obtained for only up to 20 particles^[7] for a statistically representative number of NP.
33
34
35
36
37
38
39
40
41
42
43
44
45

46 In contrast to lower annealing temperatures, substrate modifications in the form of small
47 depressions or holes were detected after annealing at 1102 °C as shown in **Figure 3**. As fused
48 silica is known to crystallize above 1100 °C and the initial crystals have been shown to form
49 depressions in the surface,^[20] it is possible that these small impressions are tiny surface
50 crystals. However, the nucleation rate would be much higher which could point towards the
51 Au layer or the NP functioning as a nucleating agent at the surface. Alternatively, these
52 depressions could also result from a substrate-NP interaction during dewetting and be visible
53
54
55
56
57
58
59
60
61
62
63
64
65

1 if the NP observed after melting are not in the positions of the NP formed during dewetting.
2 Twinning as described in the refs.[3] and [5] may be observed on all the surfaces analyzed
3
4 here.
5
6

7
8
9 These results indicate, that the texture formation is temperature dependent but perhaps not
10 substrate dependent for amorphous substrates, as the sole 111-texture previously described on
11 soda-lime-silica-glass^[3] after annealing at 400 °C corresponds to the data presented here.
12
13 However, only 111-textures were reported in ref. [5] where Au layers were dewetted and
14 annealing was performed at temperatures from 400 to 1000 °C under controlled atmospheres
15
16 on oxidized Si-wafers using polymer microspheres in the setup. Although the dominance of
17 the 111 texture is reduced with an increasing annealing temperature, which was also observed
18
19 using a sapphire substrate,^[2] a clear 111 texture is still observed after annealing at 1057 °C.
20
21 Hence the 111 texture is observed throughout the entire temperature range while the 001
22 texture occurs at 815 and 965 °C and the 101 texture occurs at 965 and 1057 °C.
23
24

25
26 As most samples were cooled slowly, it is impossible that the textures formed solely during
27 cooling because if that were the case all the samples should feature the same textures. At the
28 same time the clear observation of faceted as well as rounded particles clearly shows that the
29 applied “slow” cooling process is still fast enough to freeze the high temperature morphology
30
31 of the particles. The absence of a texture after heating above the melting point may be seen as
32 proof that the NP contributing to the textures measured by EBSD are too large to be
33 significantly affected by the melting point reduction observed in very small NP.^[30]
34
35 Additionally, it clearly proves that texture formation is caused by a self organization during
36 dewetting which does not occur during solidification of a melt.
37
38
39
40
41
42
43
44
45
46
47
48
49
50
51
52
53
54
55
56
57

58 The particle size distributions of the surfaces represented by the SEM-micrographs in the
59 Figures 2 a) and b) are presented in **Figure 4** and are fitted by a Gaussian distribution. The
60
61

area of each particle is determined and a diameter of the corresponding circuit is calculated.

The mean particle diameter is 159 ± 58.5 nm at 426 °C and decreases to 113 ± 38 nm after the heat treatment at 965 °C. This effect can be explained by the Rayleigh instability, where elongated particles disintegrate into several smaller particles at higher temperatures and a decrease in the particle size should occur accompanied by an increase of the particle number and consequently a more narrow size distribution. It should be noted that these micrographs only show a projection of the particles, hence a statement about the three-dimensional shape cannot be made here.

As statistical analyses or the particle size distribution were not given in the refs. [3] and [6] we would like to amend this here: a bimodal size distribution cannot be detected in the SEM-micrographs of the samples featured in both articles.

The circularity of a particle can be mathematically defined by a feret ratio where the maximum and minimum diameter of a particle is determined and the related ratio is calculated.^[3] Hence a value of “1.0” is equivalent to a circle while a value of “0.0” corresponds to an infinitely long string. A detailed analysis of the particle shape in **Figure 5** by ferret ratio exhibits a log-normal distribution. Annealing at 426 °C for 3 h results in a maximum at 0.76 while increasing the temperature to 965 °C shifts the maximum to 0.88 and narrows the distribution.

This confirms the visual impression that the particles become increasingly rounded at higher temperatures which has also been reported for gold NP dewetted on crystalline sapphire.^[2]

The fits shown in Figure 4 are negative skew lognormal distributions. In order to perform a sufficient coverage, the independent variable $x = (x-1)$ is assumed for the equation of the lognormal distribution.

2.2. Platinum

1
2 Platinum nano particles are interesting because they combine the catalytic properties of Pt
3
4 with a relatively large surface. They may also be used as an etch mask. However, Pt and Si
5
6 form alloys of multiple compositions with melting points down to 830 °C and SiO₂ may be
7
8 reduced by H₂^[30] or an electrical current in a glass melt^[31] to provide the alloying component.
9
10 The thermal dewetting of Pt on Si with a natural oxide layer has been studied for layers from
11
12 1.5 to 15 nm deposited by electron beam evaporation and annealed at 400 to 1000 °C for only
13
14 30 to 240 s with a focus on NP morphology.^[8] Increasing the annealing time led to larger
15
16 particles in a narrower size distribution.^{[8],[32]} The formation of PtSi-phases and nano wire
17
18 growth was observed when annealing Pt-layers on Si wafers.^{[8],[9]} In addition, interactions
19
20 with other substrates are not uncommon.^[33]
21
22
23
24
25
26
27

28 Due to the lack of a reducing agent, PtSi alloys should not play a role in the experiments
29
30 performed here. Additionally, all Pt₁Si₁ phases known to the authors are not cubic and hence
31
32 their EBSD-patterns would not be reliably indexable as metallic Pt. Dewetting sputtered Pt
33
34 layers of 14 nm at 965°C for 3 h led to the Pt NP presented in the SEM-micrograph of
35
36 **Figure 6** which show a regular log normal size distribution if the circuit diameter in the SEM-
37
38 micrograph is analyzed as illustrated below. The centre of mass is 84.0 nm -34.1 and + 57.5.
39
40 Some of the large particles show faceting into triangles or irregularly shaped hexagons as well
41
42 as rods. The rods protrude from the surface and hence might also be described as whiskers or
43
44 nano wires, making a statement towards true particles sizes problematic for these samples.
45
46 Figure 6 also presents 001, 101 and 111 PFs of textures calculated from an EBSD-scan
47
48 covering 4,500 μm² with a step size of 100 nm. The PFs show a double texture where crystal
49
50 orientations with either a {101} or a {111} plane parallel to the substrate surface preferably
51
52 occur. A 100 texture is not indicated. Attempting to perform a size-dependent texture analysis
53
54 comparable to that presented in Ref. [6] only showed that reliable data points with a low
55
56
57
58
59
60
61
62
63
64
65

1 image quality (<30%) show the same texture information as the entire scan. 111-twinning in
2 the form of two orientations within one NP sharing a common {111} plane was also detected
3
4 in these samples. Annealing Pt above the melting point of 1772 °C is not possible using fused
5
6 silica substrates because the glass crystallizes to high-cristobalite above 1100 °C which in
7
8 turn melts at 1713 °C.
9
10

14 2.3. Palladium/Palladium Oxide

17 Palladium in the form of NPs, thin layers and foams are of notable interest in materials
18
19 science due to their interaction with hydrogen^[10] and their catalytic activity with respect to
20
21 various redox reactions.^[34] Therefore the material is used as a catalytic agent, in gas
22
23 purification systems and hydrogen sensors.^[35] Pd NP have special optical (plasmonic)
24
25 properties which change significantly if the particles are oxidized to palladium oxide.^[11] Pd is
26
27 not inert during annealing in air but oxidizes to PdO above 258 °C and starts to decompose
28
29 back to metallic Pd at temperatures above 775 °C (both temperatures correspond to DTA
30
31 onset).^[12] The crystal structure changes from cubic to tetragonal during oxidation^[40] which
32
33 enables to identify the individual phases using EBSD. The oxidation of Pd to PdO has been
34
35 studied on a Pd film under a controlled atmosphere.^[36] PdO is also reduced in the presence of
36
37 hydrogen^[13] meaning an oxidized layer may be converted to metallic palladium at room
38
39 temperature.^{[14],[15]} These properties of palladium are of interest for NP research and
40
41 preparation in general. Hence, the effect of the phase transition at higher temperatures can be
42
43 studied at room temperature. In addition, this phase transition can be reversed at room
44
45 temperature by purging with H₂. The size dependent kinetics of Pd-hydration have been
46
47 studied on nano structured materials,^[37] thin films^[38] and nano particles.^[39] Michalak et al.
48
49 described the possibility of thermally induced spinodal dewetting in thin Pd layers.^[16]
50
51 However, those experiments were performed in ultra high vacuum (UHV) which completely
52
53 suppresses the oxide phase. Moreover, Mizsei et al. heated thin Pd layers on glass substrates
54
55
56
57
58
59
60
61
62
63
64
65

1 at atmospheric conditions up to 600 °C and observed no dewetting but the formation of PdO
2 as well as large accumulations of material in the film.^[17] After adding hydrogen at 500 °C, a
3
4 preferred 111 orientation of palladium was described.^[18] While the presented structures
5 resemble those shown in Ref. [15], it would seem the temperature was not high enough to
6
7 produce completely separated particles.
8
9

10
11
12
13
14 In a first step we present results obtained from samples prepared by a non-chemical dewetting
15 procedure at 965 °C and ambient conditions. As the oxidized species of palladium
16 decomposes to metallic Pd between 775 and 800 °C,^{[10],[12]} the use of hydrogen can be omitted
17 during dewetting. Due to the oxidation behavior of Pd, an effect of cooling rates on the PdO
18 formation during cooling may not be neglected and the applicability of texture analysis after
19 flushing with H₂ gas must be analyzed. Hence comparable samples with a Pd layer thickness
20 of 18 nm were annealed at 965 °C for 3 h after which one sample was directly removed from
21 the furnace, causing a high cooling rate of more than 800 °C/min, while the other was left in
22 the furnace to cool slowly. Both samples were then coated with carbon, analyzed by EBSD,
23 flushed with H₂ and reanalyzed by EBSD. The acquired results are presented in **Figure 7**
24 along with EBSD-patterns of Pd and PdO.
25
26
27
28
29
30
31
32
33
34
35
36
37
38
39
40

41 EBSD-pattern acquisition was very difficult from the unpurged, quickly cooled sample so that
42 only ca. 400 data points were of sufficient quality (confidence index CI>0.1) in a scan of
43 almost 200,000 patterns. While this is within the error margin of the indexing procedure, it
44 was possible to locally obtain high quality EBSD-patterns of Pd from this surface. The latter
45 cannot be said for PdO. Hence, the corresponding 111 texture of Pd indicated by the PF is
46 probably real although not representative while the reliability of the PdO texture must be
47 questioned altogether. After flushing with H₂, the NP from the same area provided well
48 indexable EBSD-patterns of Pd indicating clear 001 and 111 textures while the number of
49 patterns attributed to PdO with a CI>0.1 is again within the error margin.
50
51
52
53
54
55
56
57
58
59
60
61
62
63
64
65

1 The increase of the ability to acquire EBSD patterns after flushing may indicate that the NP
2 initially showed a core-shell structure of Pd surrounded by a thin PdO layer despite the high
3 cooling rate. The combination of both crystal lattices (Pd and PdO) within the information
4 volume of EBSD may lead to pattern superposition (e.g. at grain boundaries) or prevent the
5 formation of an EBSD-pattern as may be assumed here.
6
7
8
9

10 The sample cooled slowly showed well indexable EBSD patterns of PdO after annealing
11 while Pd was not detected reliably. After flushing with H₂, the NP on the surface failed to
12 produce a percentage of EBSD-patterns comparable to that obtained from the quickly cooled
13 sample (only 0.03%). However, the 1796 reliably indexed EBSD-patterns of Pd in the scan
14 indicate the same coexistence of a 001 and a 111 texture which was also observed in the
15 quickly cooled sample after flushing with H₂. As the optical properties of this sample indicate
16 a reduction of PdO to Pd and only a negligible amount of patterns is indexed as PdO by
17 EBSD, the question arises why EBSD-patterns cannot be obtained from most particles. This
18 problem was detected on numerous samples cooled slowly after annealing at various
19 temperatures.
20
21
22
23
24
25
26
27
28
29
30
31
32
33
34
35

36 As it is possible to obtain EBSD-patterns of high quality from a few NPs, errors due to sample
37 preparation, i.e. the thickness of the carbon coating, can be neglected. Additionally, the
38 experiments performed on the quickly cooled samples show that flushing with H₂ after carbon
39 coating led to the reduction of PdO in a comparably prepared sample. The detailed SEM-
40 micrographs of Pd NP resulting from slow and rapid cooling after annealing at 965 °C and
41 purging with H₂ presented in **Figure 8** show a pronounced morphological difference between
42 the particles. The particle shape is “rugged” after the particle oxidized completely and formed
43 PdO of higher volume^[15] during the slow cooling process, see Figure 8 a). In contrast, the
44 rapidly cooled NP in Figure 8 b) are rounded, again implying that any oxidation during rapid
45 cooling only forms a thin shell of PdO on a core of Pd as already outlined above. Hence the
46 structure of a quickly cooled Pd/PdO NP is quite different from that of a slowly cooled
47
48
49
50
51
52
53
54
55
56
57
58
59
60
61
62
63
64
65

1 Pd/PdO NP even after being flushed with H₂. However, a more detailed analysis of this aspect
2 is beyond the scope of this article.
3
4

5
6 Hence it must be noted that cooling rates affect the structure of the NPs in this system and
7 possibly the texture formation. It is probable that the phase transformations of Pd to PdO and
8 vice versa have no effect on the texture of quickly cooled NP because they were never fully
9 oxidized (PdO was not reliably detected by EBSD on the quickly cooled sample in contrast to
10 the slowly cooled sample). Please note that none of the PFs of PdO allow any certain
11 conclusion on the possible textures of PdO because the two cubic textures of Pd allow at least
12 six tetragonal PdO textures which in turn would probably not show an elevated probability of
13 any orientation and hence remain unnoticed. A similar cubic-tetragonal transition also occurs
14 during cooling after the surface crystallization of fused silica.^[20]
15
16
17
18
19
20
21
22
23
24
25
26
27
28
29
30

31 A temperature series was performed to allow a comparison with the results of gold presented
32 above. These samples were always rapidly cooled in order to minimize oxidation and flushed
33 with H₂ for at least 15 min to obtain metallic Pd as the results of Figure 7 showed that even
34 rapid cooling cannot prevent the formation of a thin oxide layer. The resulting SEM-
35 micrographs in **Figure 9** show that the palladium has a much smaller temperature window in
36 which dewetting occurs. After 3 h at 767 °C, the layer is not dewetted and contains star
37 shaped cracks which were also observed in Ref. [15]. Well separated particles are observed
38 after annealing at 876 °C for 3 h with an additional substructure between the particles, see
39 arrows, which probably results from the irregularly shaped layer residue. These substructures
40 are no longer visible after annealing at 965 °C. Pd could not be detected by EDX on the
41 surface of the sample annealed at 1256 °C where the SEM-micrograph only shows
42 depressions and a crack. This temperature was chosen to see what happens during the
43 dewetting procedure if the substrate crystallizes during annealing but below the melting point
44
45
46
47
48
49
50
51
52
53
54
55
56
57
58
59
60
61
62
63
64
65

1 of the metal. As the sample is fully crystallized here, these depressions cannot be small
2 cristobalite nuclei as proposed in Figure 3 but probably indicate locations where the Pd NP
3
4 interacted with the substrate after dewetting but before disappearing, probably by evaporation.
5
6 The absence of Pd was also observed for a sample annealed at 1600°C (not shown), i.e. above
7
8 the melting point of Pd, but there was no trace of the depressions shown in Fig. 10. Please
9
10 note that the cracks in crystallized fused silica form due to the phase transformation between
11
12 200 and 275 °C,^[20] i.e. liquid Pd cannot flow into the cracks, again pointing towards an
13
14 evaporation of Pd.
15
16
17
18
19
20
21

22 The particle size distributions corresponding to Figure 9 are presented in **Figure 10** where
23
24 bimodal Gaussian distributions are clearly indicated. At 876 °C, the determined mean particle
25
26 sizes of the respective peaks are 45.6 ± 28.6 and 185 ± 48.0 nm while at 965 °C they are
27
28 88.8 ± 74.4 and 331.0 ± 89.0 nm. A bimodal size distribution was also detected for 5 nm thick
29
30 Pd layers dewetted on fused silica.^[11] It seems logical that the continuously dewetting layer
31
32 residue leads to the smaller particle species in the bimodal size distribution. Coalescence and
33
34 Ostwald ripening shift this bimodal distribution to larger particles sizes as the atomic mobility
35
36 is increased by annealing at the higher temperature. However, the exact reason of the thin
37
38 layer residue is not yet fully understood, because such thin structures should have dewetted
39
40 long before the large particles in the layer were formed. It must be noted, that a statistical
41
42 analysis of the figures presented in ref. [16] where oxidation was prevented during annealing
43
44 does not show a bimodal size distribution.
45
46
47
48
49
50

51 Hence two different dewetting mechanisms may exist: when the layer reaches the dewetting
52
53 temperature, it is heavily disturbed due to the volume expansion during oxidation and the
54
55 subsequent volume decrease due to the thermal reduction. The resulting layer morphology
56
57 containing the star shaped holes (see Figure 9) is not comparable to the hole formation in a
58
59 gold layer.^[41] Please note that dewetting Pd in a vacuum,^[16] i.e. without the phase
60
61
62
63
64
65

transformation, leads to dewetting morphologies similar to the spinodal dewetting of gold.

Hence material accumulations may already exist in the oxidized and reduced system before the actual (spinodal) dewetting begins.^[17]

Figure 10 also presents texture information on the Pd-layers dewetted at 876 and 965 °C, EBSD-patterns could not be obtained from the sample annealed at 767 °C. The PFs of the samples annealed at 876 and 965 °C both show 001 and 111 textures while a 101 texture is not detected. 111-twinning of Pd was observed in all EBSD-scans of H₂-flushed samples featured in this article.

3. Conclusion

The thin films of all studied materials show a dewetting of the metallic film into metal nano particles at high temperatures. The experiments focused on the crystallographic and morphological behavior of the resulting particles as a function of temperatures, cooling rates and chemical phase transitions during preparation. It was shown that the cooling rate may not be neglected in the cases of Au and Pd where temperature dependent particle forming/aging mechanisms were observed. Interactions with the substrate at high temperatures are implied in all cases.

Because Au, Pt, and Pd are all fcc materials, it is of no surprise to find the 111-texture and the 111-twinning in the NP. The 001- and 101-textures, on the other hand, have not been described before and do not occur in the dataset of the previously analyzed Au particles.^[3] For both orientations, a crystallographic axis is oriented parallel to the substrate surface. At 965°C, all three textures were detected in Au NP while only the 111 and 101 textures were detected in Pt NP and only the 111 and 001 textures were detected in Pd NP. Particle size dependent textures were not detected after dewetting on fused silica. 111-twinning was observed in the metallic NP of all metals analyzed here.

In the case of Au, it was shown that any texture is lost if the metal is melted during annealing.

Comparable results could not be obtained for Pd and Pt due to evaporation or the melting of the substrate, respectively.

Gold NP show a rounding in the particle shape with increasing dewetting temperature on the amorphous substrate in agreement to the literature. In contrast to gold, the dewetting of Pd NP leads to a bimodal size distribution caused by a different dewetting mechanism. Pd NP also show faceting and the morphology is affected by the cooling procedure due to the time and temperature dependent phase transition which also affects the ability to acquire EBSD-patterns. The observed structural modification implies a significantly different NP structure.

Nano rods were observed after dewetting Pt on fused silica.

4. Experimental Section

Fused silica glass samples of 8 mm diameter and a thickness of 1.25 mm served as substrates.

They were cleaned in an ultrasonic bath for 10 min at 65 °C using a 5% commercial cleaning solution (Tickopur R36). The substrates were subsequently rinsed with deionised water, followed by another two steps of rinsing in deionised water with ultrasonic assistance and finally dried at 110 °C for 1 h.

A DC-sputter-system (Edwards Auto 306) with target dimensions of 50x50 mm² for gold (purity 99.99%), palladium (99.95%) as well as a round target of 500 mm diameter for platinum (99%) was used to sputter layers of various thicknesses from 14 to 18 nm. The following parameters were kept constant for all metals during the process: substrate-temperature (21 °C), target-substrate-distance (110 mm), pressure (< 10 mPa), voltage (4 kV) and argon pressure (10 Pa). The supplied conditions resulted in a current of 35 mA. The thickness was controlled using a shutter and a film thickness monitor (FTM7, BOC Edwards).

1 Dewetting was achieved by annealing the samples for 3 h in a muffle furnace at temperatures
2 from 424-1600 °C in air (heating rate 10 K/min). For a better control of temperature, all stated
3 annealing temperatures (except 1265 and 1600 °C) were logged during the process using a
4 thermo couple (Ni-CrNi) placed ca. 1 cm vertically above the sample surfaces. After the
5
6
7
8
9
10
11
12
13
14
15
16
17
18
19
20
21
22
23
24
25
26
27
28
29
30
31
32
33
34
35
36
37
38
39
40
41
42
43
44
45
46
47
48
49
50
51
52
53
54
55
56
57
58
59
60
61
62
63
64
65

Dewetting was achieved by annealing the samples for 3 h in a muffle furnace at temperatures from 424-1600 °C in air (heating rate 10 K/min). For a better control of temperature, all stated annealing temperatures (except 1265 and 1600 °C) were logged during the process using a thermo couple (Ni-CrNi) placed ca. 1 cm vertically above the sample surfaces. After the respective annealing time, the furnace was either switched off, enabling slow cooling, or they were directly removed from the furnace (rapid cooling). The exemplary cooling curved of a slow cooling process from 865 °C is presented in **Figure 11**.

The samples were analyzed using a Jeol JSM-7001F equipped with an EDAX Trident analyzing system containing a TSL Digiview 1913 EBSD-camera. EBSD-scans were captured using TSL OIM Data Collection 5.31 and evaluated using TSL OIM Analysis 6.2. The scans were performed using a binning of 4x4, a current of about 2.40 nA (measured with a Faraday cup) and a voltage of 20 kV. Only data points with a confidence index (CI) of at least 0.1 were used for texture calculation. All samples were coated with a thin layer of carbon at about 10⁻³ Pa in order to optimize the surface conductivity for analysis in the SEM. The particle size distribution and particle shape analysis was determined by image processing performed on SEM-micrographs.

Acknowledgements

The authors would like to thank T. Zscheckel for some SEM-micrographs featured in this article and W. Seeber for his support. This work is supported by the DFG “Deutsche Forschungsgemeinschaft” (Se 698/10-1, Se 698/10-2 and Ru 417/14-1).

Received: ((will be filled in by the editorial staff))
Revised: ((will be filled in by the editorial staff))
Published online: ((will be filled in by the editorial staff))

1
2
3
4
5
6
7
8
9
10
11
12
13
14
15
16
17
18
19
20
21
22
23
24
25
26
27
28
29
30
31
32
33
34
35
36
37
38
39
40
41
42
43
44
45
46
47
48
49
50
51
52
53
54
55
56
57
58
59
60
61
62
63
64
65

- [1] a) S. Guo, E. Wang, *Anal. Chim. Act.* **2007**, *598*, 181. b) M. Grzelczak, J. Perez-Juste, P. Mulvaney, L. M. Liz-Marzan, *Chem. Soc. Rev.* **2008**, *37*, 1783. c) R. Sardar, A. M. Funston, P. Mulvaney, R. W. Murray, *Langmuir* **2009**, *25*, 13840. d) K. Na, Q. Zhang, G. A. Somorjai, *J. Clust. Sci.* **2014**, *25*, 83–114.
- [2] J. S. Hwang, D. H. Noh, *J. Korean Phys. Soc.* **2013**, *62*, L6.
- [3] C. Worsch, M. Kracker, W. Wisniewski, C. Rüssel, *Thin Solid Films* **2012**, *520*, 4941.
- [4] C. M. Müller, F. Carlo, F. Mornaghini, R. Spolenak, *Nanotechnol.* **2008**, *19*, 485306.
- [5] M. Bechelany, X. Maeder, J. Riesterer, J. Hankache, D. Leroose, S. Christiansen, J. Michler, L. Philippe, *Cryst. Growth Des.* **2010**, *10*, 587.
- [6] C. Worsch, W. Wisniewski, M. Kracker, C. Rüssel, *Appl. Surf. Sci.* **2012**, *258*, 8506.
- [7] a) H. Sadan, W. D. Kaplan, *J. Mater. Sci.* **2006**, *41*, 5099-5107. b) H. Sadan, W. D. Kaplan, *J. Mater. Sci.* **2006**, *41*, 5371.
- [8] S. Strobel, C. Kirkendall, J.-B. Chang, K.K. Berggren, *Nanotechnol.* **2010**, *21*, 505301.
- [9] P. K. Sekhar, S. N. Sambandam, D. K. Sood, S. Bhansali, *Nanotechnol.* **2006**, *17*, 4606.
- [10] a) T. B. Flanagan, W. A. Oates, *Ann. Rev. Mater. Sci.* **1991**, *21*, 269. b) S. Kishore, J. A. Nelson, J. H. Adair, P. C. Eklund, *J. Alloy. Compd.* **2005**, *389*, 234.
- [11] M. Kracker, C. Worsch, C. Rüssel, *J. Nanopart. Res.* **2013**, *15*, 1.
- [12] G. Bayer, H. G. Wiedemann, *Thermochim. Acta* **1975**, *11*, 79.
- [13] J. Han, G. Zhu, D. Y. Zemlyanov, F. H. Ribeiro, *J. Catal.* **2004**, *225*, 7-15.

- 1
2
3
4
5
6
7
8
9
10
11
12
13
14
15
16
17
18
19
20
21
22
23
24
25
26
27
28
29
30
31
32
33
34
35
36
37
38
39
40
41
42
43
44
45
46
47
48
49
50
51
52
53
54
55
56
57
58
59
60
61
62
63
64
65
- [14] J. I. Avila, R. J. Matelon, R. Trabol, M. Favre, D. Lederman, U. G. Volkmann, A. L. Cabrera, *J. Appl. Phys.* **2010**, *107*, 23504.
- [15] M. Kracker, C. Worsch, C. Rüssel, *Mater. Lett.* **2013**, *110*, 114-146.
- [16] W. D. Michalak, J. B. Miller, C. Yolcu, A. J. Gellman, *Thin Solid Films* **2012**, *522*, 473.
- [17] J. Mizsei, P. Sipilä, V. Lantto, *Sensor. Actuator.* **1998**, *47*, 139.
- [18] J. Mizsei, L. Pirttiaho, M. Karppinen, V. Lantto, *Sensor. Actuator. B* **2000**, *65*, 195.
- [19] a) Y. W. Heo, V. Varadarajan, M. Kaufman, K. Kim, D. P. Norton, F. Ren, P. H. Fleming, *Appl. Phys. Lett.* **2002**, *16*, 3046. b) K. Nagashima, T. Yanagida, H. Tanaka, T. Kawai, *J. Appl. Phys.* **2007**, *101*, 124304. c) A. Vomiero, M. Ferroni, E. Comini, G. Faglia, G. Sberveglieri, *Nano Lett.* **2007**, *7*, 3553-3558.
- [20] W. Wisniewski, S. Berndt, M. Müller, C. Rüssel, *CrystEngCom* **2013**, *15*, 2392.
- [21] L. Armelao, D. Barreca, A. Gasparotto, E. Pierangelo, E. Tondello, S. Polizzi, *J. Nanosci. Nanotechno.* **2005**, *5*, 259.
- [22] L. D. Marks, *Rep. Prog. Phys.* **1994**, *57*, 603.
- [23] A. S. Barnard, X. M. Lin, L. A. Curtiss, *J. Phys. Chem. B* **2005**, *109*, 24465.
- [24] J.-H. Shim, B.-J. Lee, Y. W. Cho, *Surf. Sci.* **2002**, *512*, 262.
- [25] O. H. Nielsen, J. P. Sethna, P. Stoltze, K. W. Jacobsen, J. K. Nørskov, *Europhys. Lett.* **1994**, *26*, 51.
- [26] a) E. Ringe, R. P. Van Duyne, L. D. Marks, *J. Phys. Chem. C* **2013**, *118*, 15859. b) L. D. Marks, *J. Cryst. Growth* **1983**, *61*, 556.
- [27] P. M. Ajayan, L. D. Marks, *Phys. Rev. Lett.* **1989**, *63*, 279.

- 1
2
3
4
5
6
7
8
9
10
11
12
13
14
15
16
17
18
19
20
21
22
23
24
25
26
27
28
29
30
31
32
33
34
35
36
37
38
39
40
41
42
43
44
45
46
47
48
49
50
51
52
53
54
55
56
57
58
59
60
61
62
63
64
65
- [28] a) W. L. Winterbottom, *Acta. Metall.* **1967**, *15*, 303. b) T. Wang, C. Lee, L. D. Schmidt, *Surf. Sci.* **1985**, *163*, 181.
- [29] P. Buffat, J.-P. Borel, *Phys. Rev. A* **1976**, *13*, 2287.
- [30] R. Lamber, N. I. Jaeger, *J. Appl. Phys.* **1991**, *70*, 457.
- [31] W. Wisniewski, M. Nagel, G. Völksch, C. Rüssel, *Cryst. Growth Des.* **2010**, *10*, 1939.
- [32] J. Dufourcq, P. Mur, M. J. Gordon, S. Minoret, R. Coppard, T. Baron, *Mater. Sci. Eng. C* **2007**, *27*, 1496.
- [33] A. Galit, M. Vissarion, E. Gadi, D. K. Wayne, *J. Mater. Sci.* **2014**, *49*, 3863.
- [34] a) C. Hwang, Y. L. Lu, S. W. Jang, P. T. Chou, C. R. C. Wang, S. J. Yu, *J. Catal.*, **2000**, *195*, 336. c) A. F. Littke, G. C. Fu, *Angew. Chem. Int. Ed.* **2002**, *41*, 4176. c) C. T. Campbell, *Surf. Sci. Rep.* **1997**, *27*, 1. d) K. C. Nicolaou, P. G. Bulger, D. Sarlah, *Angew. Chem. Int. Ed.* **2005**, *44*, 4442.
- [35] a) T. Hübert, L. Boon-Brett, G. Black, U. Banach, *Sensor. Actuator. B* **2011**, *157*, 329. b) C. Langhammer, E. M. Larsson, B. Kasemo, I. Zorić, *Nano Lett.* **2010**, *10*, 3529. c) M. Kracker, C. Worsch, W. Seeber, C. Rüssel, *Sensor. Actuator. B* **2014**, *197*, 95.
- [36] H. H. Kan, J. F. Weaver, *Surf. Sci.* **2009**, *603*, 2671.
- [37] H. Gleiter, *Acta. Mater.* **2000**, *48*, 1.
- [38] W. Vargas, I. Rojas, D. Azofeifa and N. Clark, *Thin Solid Films*, **2006**, **496**, 189–196.
- [39] a) C. Langhammer, I. Zorić, B. Kasemo, B. M. Clemens, *Nano Lett.* **2007**, *7*, 3122. b) C. Langhammer, V. P. Zhdanov, I. Zorić, B. Kasemo, *Phys. Rev. Lett.* **2010**, *104*, 135502. c) A. Pundt, *Nanoskalige Metall-Wasserstoff-Systeme*. Univ.-Verl. Göttingen, Göttingen, **2005**.

- [40] W. M. Haynes, D. R. Lide, *CRC handbook of chemistry and physics*. 91st ed. Boca Raton, London, New York: CRC Press; 2010.
- [41] A. B. Tesler, B. M. Maoz, Y. Feldman, A. Vaskevich, I. Rubinstein, *J. Phys. Chem. C*, **2013**, *117*, 11337.

1
2
3
4
5
6
7
8
9
10
11
12
13
14
15
16
17
18
19
20
21
22
23
24
25
26
27
28
29
30
31
32
33
34
35
36
37
38
39
40
41
42
43
44
45
46
47
48
49
50
51
52
53
54
55
56
57
58
59
60
61
62
63
64
65

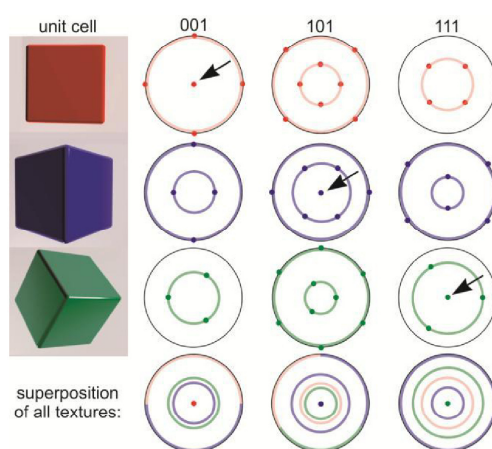


Figure 1. Orientations of a cubic unit cell and their poles in the respective pole figures. The rings indicate the result of a random rotation around the respective direction perpendicular to the image plane.

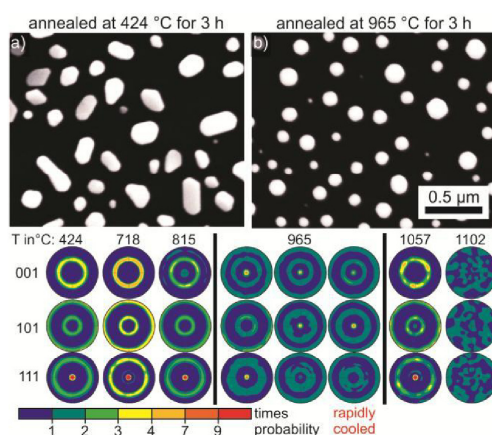


Figure 2. SEM-micrographs of gold NP dewetted on glass at a) 424 °C and b) 965 °C. Pole figures of textures calculated from EBSD-scans performed on layers dewetted at the stated temperatures visualize preferably occurring orientations.

1
2
3
4
5
6
7
8
9
10
11
12
13
14
15
16
17
18
19
20
21
22
23
24
25
26
27
28
29
30
31
32
33
34
35
36
37
38
39
40
41
42
43
44
45
46
47
48
49
50
51
52
53
54
55
56
57
58
59
60
61
62
63
64
65

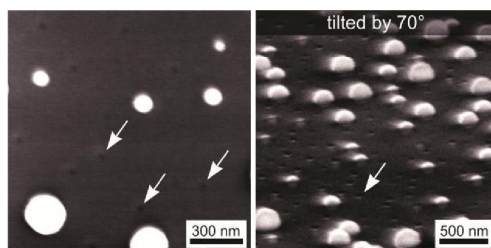


Figure 3. SEM-micrographs Au NP dewetted at 1102 °C for 3h.

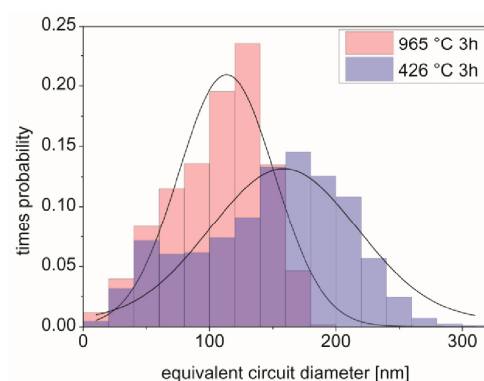


Figure 4. Equivalent circuit diameter of gold NP formed by dewetting at 426 and 965°C.

1
2
3
4
5
6
7
8
9
10
11
12
13
14
15
16
17
18
19
20
21
22
23
24
25
26
27
28
29
30
31
32
33
34
35
36
37
38
39
40
41
42
43
44
45
46
47
48
49
50
51
52
53
54
55
56
57
58
59
60
61
62
63
64
65

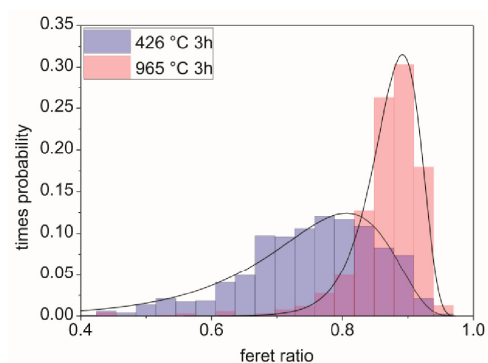


Figure 5. Feret Ratio of gold NP formed by dewetting at 426 and 965 °C.

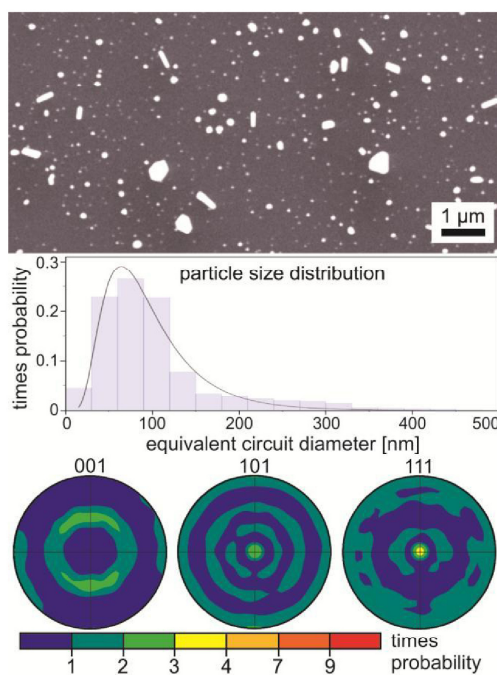


Figure 6. SEM-micrograph of PtNP dewetted at 965 °C and pole figures of a texture calculated from an EBSD-scan performed on the surface. The elongated particles are nano rods protruding from the surface.

1
2
3
4
5
6
7
8
9
10
11
12
13
14
15
16
17
18
19
20
21
22
23
24
25
26
27
28
29
30
31
32
33
34
35
36
37
38
39
40
41
42
43
44
45
46
47
48
49
50
51
52
53
54
55
56
57
58
59
60
61
62
63
64
65

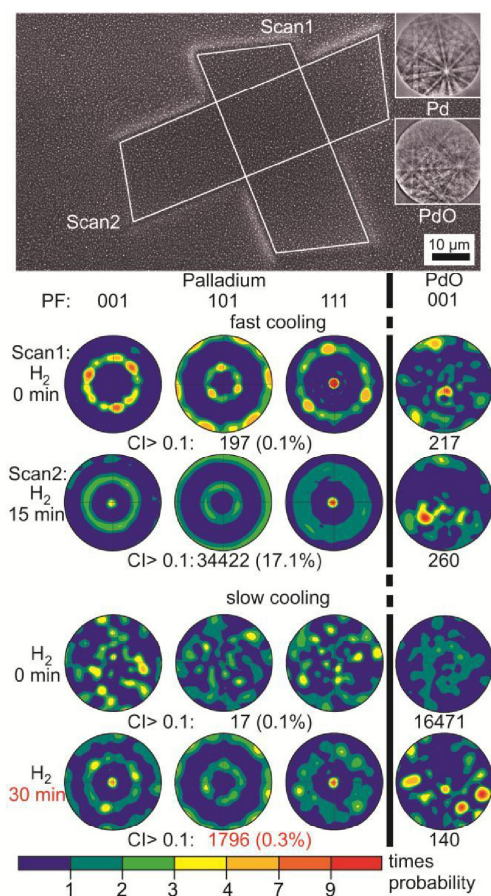


Figure 7. SEM-micrograph of Pd NP dewetted from a 18 nm thick Pd film by annealing for 3 h at 965 °C followed by fast cooling. EBSD-patterns of Pd and PdO are presented in the insets. EBSD-Scan 1 was performed directly after annealing while Scan 2 was performed after the sample was additionally flushed with H₂ gas for 15 min. Textures of Pd and PdO calculated from the Scans 1 and 2 as well as comparable scans obtained from a slowly cooled sample flushed with H₂ for 30 min are presented below along with the number of reliable data points (CI>0.1) contributing to the respective texture.

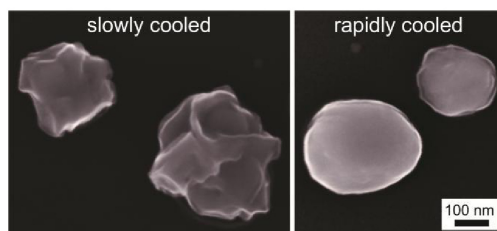


Figure 8. SEM-micrographs of dewetted Pd particles on the glass surface a) cooled slowly and b) cooled rapidly.

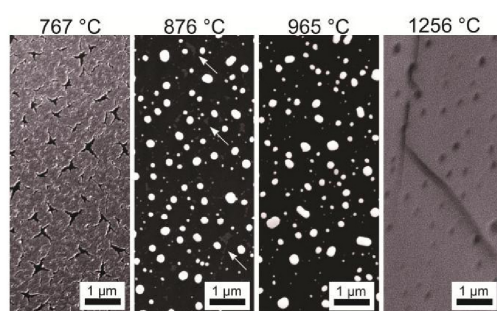


Figure 9. SEM-micrographs of rapidly cooled Pd-films annealed at the stated temperatures for 3 h.

1
2
3
4
5
6
7
8
9
10
11
12
13
14
15
16
17
18
19
20
21
22
23
24
25
26
27
28
29
30
31
32
33
34
35
36
37
38
39
40
41
42
43
44
45
46
47
48
49
50
51
52
53
54
55
56
57
58
59
60
61
62
63
64
65

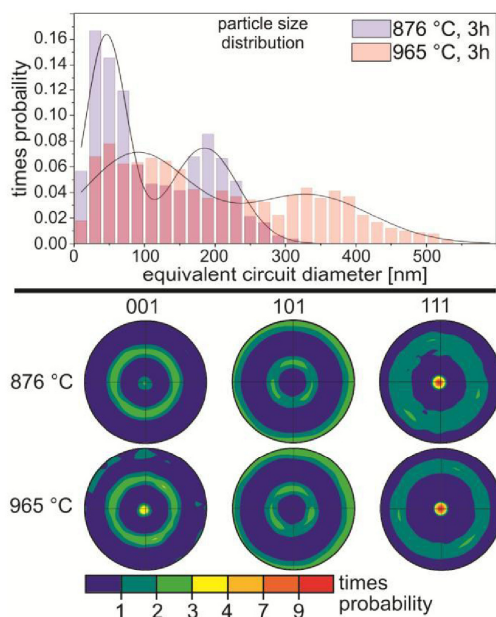


Figure 10. Temperature series of Pd layers annealed at the stated temperatures for 3h. SEM-micrographs feature surfaces from which EBSD-patterns could not be obtained. 001, 101 and 111 PFs of textures calculated from EBSD-scans performed on NPs dewetted from the Pd layers.

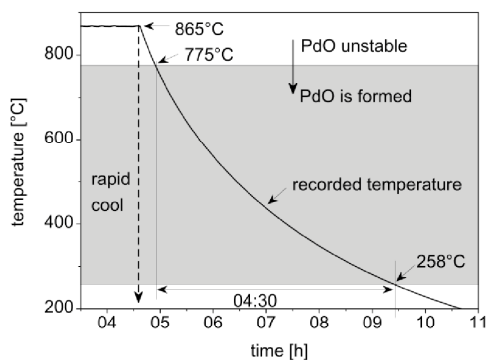


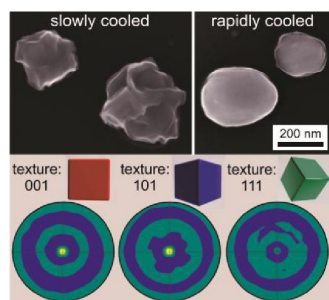
Figure 11. Measured temperature/time correlation of annealing a sample at 865 °C for 3 h followed by the slow cooling process. The rapid cooling procedure is indicated by the dashed line.

This article proves that multiple crystallographic textures coexist in metal nano particles produced by thermal dewetting in contrast to the usually assumed or described 111 texture. It is shown that cooling rates may affect the texture and structure of the nano particles. The texture is lost if annealing is performed above the melting point of the metal.

Keywords: textures, nano particles, dewetting, gold, palladium

M. Kracker*, W. Wisniewski, C. Rüssel

Textures of Au, Pt and Pd/PdO Nano Particles Thermally Dewetted from Thin Metal Layers on Fused Silica



4 Discussion

4.1 Particle preparation

The wording “**dewetting**” is sometimes misleading. The dewetting phenomenon describes basically the rupture of thin films on solid substrates. Spinodal dewetting and heterogeneous hole nucleation represents merely the first step in a sequence of different mechanisms and deals with the first occurrence of fractures inside the layer. The growth of holes, with the formation of rims, networks (by contact of growing holes) and particles, etc. will take place regardless the origin of the initial holes. However the initial condition of the subsequent layer disruption, such as frequencies of the formed holes and time of occurrence, are different. Thus the resulting particle layers are theoretically different.

Furthermore, the structure of deposited metal layers corresponding to the zone 1 in the Thornton model are presented and discussed in [58,59,62]. The layer is not free of irregularities like voids and holes. The discontinuous layer morphology acts as a starting point (heterogeneity) for the heterogeneous hole nucleation. This line of argument does not exclude the spinodal dewetting as a thermodynamically driven process. Rather, it is a superposition of two dewetting (hole nucleation) mechanisms. Hence the layers are thin enough to disrupt by thermal induced surface waves.

Comparable to the spinodal dewetting, the heterogeneous nucleation of holes shows layer thickness-dependent characteristics. According to Lanxner et al. existing or formed holes need a minimum size to enable their growth, otherwise they heal and disappear. Tesler et al. shows the initial states of dewetting, depending on the initial layer thickness [41]. Layers with a thickness of 15 nm, shows the closing of holes in an early stage of dewetting. Such a modification of the initial hole density may lead to larger particles. Hence the frequency of the initial holes decreases, while in thin layers, even the smallest cracks can grow and can initiate a higher frequency of growing holes. As a consequence, a high hole density leads to a higher number of smaller particles. Krishna et al. shows this impressively on the example of silver [68].

Thermal treatment of thin sputtered layers leads to small metal particles. In **article 3.1**, detailed studies are presented which concerned the instability of thin layers, the dewetting phenomena as well as the resulting optical properties. In general, if the layer thickness is increased, the particle size after the dewetting is also increased. However, the temperature range, dewetting occurs is not narrow. As expected, the particle forming procedure shows a transition range. If the required energy is too low and / or the time is too short, the shape becomes irregular (randomly shaped). With longer annealing time such irregular forms are rounded. Elongated particles are separated by the Rayleigh instability

into smaller particles. This can clearly be seen from the constrictions in Figure 1 in **article 3.1** (16 nm, 1 h, 400 °C). Further aging effects can be detected and discussed. Using a longer annealing time and an 8 nm thick initial layer, the particles diameter increases (see Table 1, **article 3.1**). These results from Ostwald ripening, and / or coalescence thereby larger particles grow at the expense of smaller particles. Datye et al. describes a similar evolution of size distribution in case of Pd and Pt particles on alumina also in dependence of the applied atmosphere [96].

Additional morphological changes are also seen at 21 nm thick layers annealed at 400 °C for 1 to 24 h (see Fig. 1 **article 3.1**). The particles show a faceted shape. This is typical for small single crystals [100,103,110,121]. Their occurrence after a long annealing period, suggests that there is a further state of energy minimization. The origin of the facets and their behavior at higher temperatures as well as a detailed EBSD analysis is discussed in more detail in **article 3.8**.

The particle layers prepared according to **article 3.1** are not stable against any physical contact such as touching or scratching. Hence, it was attempted to cover the gold particles with a protecting layer. With respect to the application as anti-adhesive layer for a hot embossing process, an SiO₂ layer prepared by a pyrolytic CCVD (combustion chemical vapor deposition) was applied. However, the dewetting behavior during the thermal annealing described in **article 3.2**, changes totally if the system is covered by an SiO₂ layer. A thin gold layer with a thickness of 12 nm dewet at much higher temperatures in comparison to the uncovered gold film. As reported in the literature and also discussed in **article 3.2**, the minimization of the surface energy during dewetting occurs by surface diffusion. However, since this diffusion pathway is blocked, the material transport is realized by volume diffusion. This results in a higher activation energy and consequently a higher annealing temperature is required. Two different sandwiched layer systems were studied and presented in the micrographs shown as Fig. 2 and Fig. 3 in **article 3.2**. A gold layer directly sputtered onto the soda lime glass substrate and subsequently covered with silica is shown as well as a gold layer embedded in two silica layers (silica-gold-silica). The glass transition temperature (T_g) of the soda lime silicate glass substrate is 525 °C. The dewetting temperature is adjusted in order to enable dewetting of the gold through the interface between glass and SiO₂ layer. Karakouz et al. reported for a borosilicate glass ($T_g = 557$ °C) a sinking of the gold particles into the surface already at 600 °C [40]. In general, annealing at 550 °C for 20 minutes results in irregularly shaped layer fragments since the dewetting procedure is not finished yet. By contrast, an annealing procedure at 600 °C for 20 min leads to well separated and nearly round particles. However, the resulting particle sizes between the two layer systems are quite different. The mobility of the gold atoms is more hindered between the silica layers which should have a very high T_g (1220 °C, [122]). The mobility of the gold atoms is smaller, and therefore smaller structures will be formed. This behavior also affects the optical properties in a clear manner and

provides the basis to realize integrated optical (hot embossed) microfluidic sensors discussed in more detailed in **article 3.7**.

A further possibility to affect the formation of particles by an additional metal layer is presented in **article 3.3**. In contrast to an SiO₂ cover layer, not only the formation is affected, but also the composition of the resulting particles. Thin gold and silver layers were sputtered sequentially onto soda lime glass substrates. During annealing at 400 °C for 1 h nanoparticles are formed. Using different thickness ratios of gold and silver, the composition of the resulting particles may be affected, which leads to a modification in their dielectric function and hence their optical properties. An alloying could be detected under specific conditions but silver tends to oxidation, and an alloying can also be suppressed, if silver is in contact with air. The results illustrated in **article 3.3** are mainly focused on optical properties of the resulting particle layers and will be discussed later.

The previously discussed metals gold and silver feature a model character. First as already mentioned, in optical point of view, they have plasmon resonance frequencies in the visible range of light. Thus, the requirements for the optical measurement technology and particularly the substrate are less than for metals with resonances in the UV range. Certainly these metals (and also copper) play a significant role for decorative applications. Furthermore, the stability against air is advantageous with respect to the application as a sensor. Another advantage, at least for gold, is that the oxidation resistance enables the analysis of dewetting processes at elevated temperatures without the influence of chemical reactions which would distort the results. Nevertheless, in some applications, a chemical reactivity is preferred. Here, especially, the catalytically active metals palladium, platinum and rhodium are to be mentioned. Up to now, a scientific approach of the dewetting process (in the nano meter scale) as well as the optical characteristics is scarcely available. In this thesis, further investigations on palladium were subjected, as it is known to interact at room temperature with hydrogen. Moreover, even studies on platinum are commenced, although in a much lesser extent and reported in **article 3.8**.

In contrast to gold, the preparation of palladium nanoparticles by dewetting is more complex. Concerning its chemical properties, palladium is comparable to silver and thus not inert. Hence, as already shown for silver, a chemical reaction with the surrounding atmosphere during the preparation is not completely ruled out. The reactivity of the palladium is not a disadvantage; on the contrary it will (especially in the nano-particulate appearance) be required in some applications. In **article 3.4**, a new method to obtain palladium nanoparticles by a dewetting procedure at atmospheric conditions was introduced. Michalak et al. also showed recently the dewetting behavior of thin palladium layers under ultra-high vacuum conditions on a sputtered SiN surface of an oxidized Si wafer [79]. In contrast to the previous articles, fused silica glass instead of soda lime silicate glass was used. This

was done taking into account the very high band gap energy of SiO_2 and the associated high optical transmission in the UV range. On the other hand, fused silica possesses excellent thermal properties such as high thermal shock resistance which allows very high cooling rates. A thin palladium layer with a thickness of 5 nm was deposited onto a fused silica surface. A subsequent treatment at 900 °C for 1 h (in air) results in a thermally induced formation of round particles with a diameter up to 200 nm. However, the size distribution diagram shows a significant accumulation in the size range from 15 to 30 nm. Around the largest particles, no smaller particles can be found. This indicates ageing effects such as Ostwald ripening and Kelvin instabilities, Rayleigh instabilities as well as the movement of whole particles, results in coalescent structures. Additionally, the same experiments were also performed on larger fused silica substrates in order to demonstrate the optical properties of palladium nanoparticle layers under different atmospheres. If the palladium nanoparticles are located in a hydrogen atmosphere, the optical properties are changed very significantly by the incorporation of hydrogen into the palladium lattice (see the explanations in **chapter 4.2**). In these experiments, it became also apparent, that probably an oxidation to PdO takes place. By varying the cooling rate, it was observed that there is a clear evidence of the formation of palladium oxide and it was concluded that the oxidation takes place during subsequent cooling. This means that the dewetting at 900 °C takes place in the metallic state, because palladium oxide is not stable in air above 819 °C [123,124]. This assumption was verified by a detailed optical examination in **articles 3.5** and **3.6** as well as a crystallographic EBSD analysis in **article 3.8**.

In order to understand the (optical) oxidation behavior of palladium, oxidation and reduction experiments were carried out on palladium layers with a thickness of 12 nm in **article 3.5**. The oxidation of palladium occurs between 258 and 819 °C. Therefore, the thermal annealing was carried out at 720 °C in order to obtain an oxide layer. From Fig.1 in **article 3.5**, it is seen, that no dewetting has occurred. Hence, the temperature of 720 °C is not high enough for a dewetting procedure. With respect to the oxide phase, however, it is beneficial for the study of optical conditions, since they are more prominent. Although no dewetting occurred, the palladium oxide layer as well as the reduced (by hydrogen) metallic layer shows a significantly changed morphology. This can be explained by the increase in volume during the oxidation. The layer compensates the stress by upraising and in consequence the roughness is notably increased. But surprisingly, this process is not reversible. Because a reduction with hydrogen gas no longer results in a smooth layer. The roughness remains unchanged. Furthermore, this preparations behavior has been used specifically in **article 3.6** in order to develop a highly optically active hydrogen sensing layer.

In **article 3.6**, layers prepared by the procedures in **article 3.4** and **3.5** were investigated in detail, with the aid of a specially developed optical sensor head. This sensor type is used to determine time conditions during the hydrogen absorption and desorption. Freshly sputtered palladium layers with thickness of 12, 14 and 18 nm were deposited onto fused silica. These simple and commonly used hydrogen-sensitive layers, serves as a reference setup for further experiments within the sensor head. The layers were treated at 700 °C for 1 h in air in order to obtain oxidized layers, according to **article 3.5**. This was used to study the reduction behavior as well as the optical response of a roughened layer (after reduction to metallic palladium), compared to a freshly sputtered palladium layer. In order to investigate the optical properties of nanoparticles in contact with hydrogen, a palladium layer with a thickness of 5 nm was prepared and subsequently annealed at 900 °C for 1 h in air. This procedure has been carried out according to **article 3.4**.

The particle formation within and below an SiO₂ layer as presented in **article 3.2** is further described in **article 3.7**. A plasmon based microfluidic sensor made of glass is presented. For this purpose, a microfluidic structure, based on the layer system (SiO₂ / Au / SiO₂) was hot embossed into the soda lime glass surface. Here, during the embossing procedure, *i.e.* at high temperature, also dewetting of the gold layers into nanoparticles occurred. An additional heat treatment was necessary because a back side glass sheet had to be bonded onto the structured glass. The second final SiO₂ layer was necessary in order to prevent the sticking of the mold during the hot embossing process. In order to better show the effect of this top layer, another simple cuvette was prepared without the hot embossing step. It became clear that the double treatment and especially the forming process have a significant influence on the layer structures, and thus the optical properties of the sensor system.

In comparison to **article 3.1**, in which a detailed description of the resulting morphology of the nanoparticles at temperatures up to 400 °C was presented, **article 3.8** deals with the dewetting temperatures > 1300 °C especially for gold and palladium.

For gold, it should be noted that the particles are stable at high temperatures under the applied parameters. Even if the bulk melting point is exceeded (for 1 h), the particles were not completely destroyed, however, the texture is lost in this step. In addition to crystallographic changes, which will be discussed in a later section of this discussion, also significant changes in the resulting shape of the nanoparticles occur. The facets which were described as a result of energy minimization disappear with increasing temperature. This trend of rounding is statistically illustrated by image analysis. Here, the largest (feret) diameter of a single particle was compared with its (feret) smallest diameter. The increase of the coefficient to unity means an approximation to the circular shape.

The layers were annealed in air, and thus the layers oxidize to PdO. Therefore, in contrast to gold, the dewetting mechanism becomes more complex. SEM micrographs (see Fig. 9) show after dewetting at

876 °C residual thin layers between larger particles. However, such structures should be completely dewetted before such large regular particles occur during the course of a normal particle size evolution. An increase in the dewetting temperature to 965 °C leads to the disappearance of the residue and the formation of small particles instead. It can be concluded, that this small particles origin from the residual thin layer and are responsible for the bimodal size distribution shown in Fig. 10. At a temperature of 965 °C, the particles are susceptible to aging effects as discussed in **article 3.1**. Oswald ripening and coalescence leads to a significant shift in the mean particle size.

The oxidation of the layer is maybe responsible for a disturbed dewetting behavior. Thus dewetting performed at 767 °C shows a corrupted layer interpenetrated with star shaped cracks. Mizsei et al. found that thin palladium layers, annealed in air at 600 °C are not dewetted but oxidize and accumulations of material are formed [125]. It can be assumed that these structures may already exist in the oxidized layer and later form the large particles. In a further study he shows comparable granular structure after purging with hydrogen as shown in **article 3.5**. However, in these experiments, the temperature was not high enough to dewet the palladium layer. In contrast, Michalak et al. examined the dewetting behavior of palladium layers under ultra-high vacuum conditions could prove a spinodal dewetting behavior [79]. However, the resulting size distribution is not bimodal as it is also found in **article 3.4** and **3.8**. Furthermore, the bimodal size distribution itself is not an effect of coalescence or Ostwald ripening of particles. This is a hint at another dewetting mechanism which differs significantly from a spinodal dewetting mode.

The oxidization influences the dewetting process, but also affects the particle properties during the cooling down to the room temperature. If the temperature range where PdO is thermodynamic stable is crossed too slowly, a significant deformation of the particles is observed. The shape becomes rugged with sharp edges. This is caused by the same volume expansion, which also destroys the closed palladium layers as reported in the **article 3.5** and **3.8**.

The preparation of platinum nanoparticles by dewetting of sputtered layers was also studied. This topic is only mentioned in this work in order to demonstrate the feasibility. In addition, it is suspected that platinum nanoparticles can affect the crystallization of glasses used as substrate due to their high melting point and high dewetting temperatures. Thermal treatment of a thin sputtered platinum layer at 965 °C leads to the formation of nanoparticles with sizes mainly in the range from 50 to 20 nm, but with a significant occurrence of unusually large particles with sizes in the range from 300 to 500 nm. The largest particles are faceted, similar to the gold particles in **article 3.1** and **3.8** and to the palladium particles in **article 3.8**. Surprisingly, also single crystal platinum whiskers were found which protrude from the glass surface. The particle size distribution shows a log normal size distribution and indicates Ostwald ripening as the predominant mechanism [90].

In the following, reference [126] describes a suitable procedure to analyze surface supported particles by TEM techniques. As already mentioned, the field of nano technology not only deals with the preparation and application of nano structures, also the further development of new analytical methods plays a key role in this research area. The discussions of all articles presented in this work have clearly shown that the surface is certainly essential for the production of nanoparticles by a dewetting procedure. Unfortunately, on top of a glass sheet, the particles are inaccessible for a high resolution TEM analysis. Dissolution of the substrate and a subsequent deposition of the particles on a TEM support destroyed the orientation and distance relationship to the former surface and to the particles to each other. Thus, a fixation of the particles in an additionally applied chemical resistant matrix is necessary. Subsequently, the glass carrier substrate is dissolved in a mixture of hydrofluoric acid and nitric acid. Because the particles and the carbon layer are resistant against the applied acids, the carbon film which contains the particles can now be placed on a TEM chopper grid. This described previously method corresponds to the standard replica technique for the preparation of surface imprints suitable for TEM analyses. However, this simple and fast sample preparation technique allows the detachment of all particles from a glass substrate surface. The inherent nature is now accessible by a TEM analysis. The preparations parameters of the particles are shown in this article and correspond to the specifications in **article 3.8**. The dewetting was performed at 965 °C in air.

4.2 Optical characterization

Light as an electromagnetic alternating field, interacts with the electrons gas of the metallic particles and excites this to oscillate. Damping the restore speed of the electrons (according to the polarization change of the field) is not infinitely fast. The system comes in a resonance state, in mutual dependence of material, particle size and wavelength of the incident light. This resonant state consumes energy, resulting in an increased absorbance at a certain wavelength, in the optical spectrum. The typical resonance wavelengths for gold are in the range of 520 nm to IR range [113].

The fundamental optical properties of gold nanoparticles are described in **article 3.1**. The optical spectra of annealed layers with a different thickness are demonstrated. As described at the beginning of this discussion, an increasing layer thickness leads to an increasing particle size and the optical properties are mainly affected by this particle size. In this specific example, the particle size is increased from 36 to 167 nm and thereby the plasmon resonance peak (absorbance maximum) shifts from 545 to 630 nm. However, it should be noted that with increasing size the particle shape is also changed and this leads to an additional shift of the resonance to longer wavelengths. A shift of the absorbance maximum is also accompanied by a peak broadening which is also due to an increasing scattering power with increasing particle size. From a theoretical point of view, the absorbance of

small metal particles consists of absorption and scattering components. Gustav Mie accurately described this behavior in the theory named after him.

Therefore, an additionally simple but powerful method which deals with these phenomena is also described. The samples are scanned with a flatbed scanner, to capture the color appearance at different backgrounds and optical setups. If the light source is located behind the layer (on transparent substrate), the light passes through the layer. The wavelengths, (back) scattered and absorbed by the nanoparticles are missing and the layer will appear as colored. This setup corresponds to the conditions within an optical spectrometer in transmission arrangement. However, the perception of color of a nanoparticle layer is also affected by the optical properties of the background. If the light source is located *e.g.* behind the observer and if the background (behind the sample) is colored frosted black, it follows that only the back scattered light from the layer is visible to the observer (or the flatbed scanner). However, if the background is white, the light transmitted through the nanoparticle layer is reflected, and passes again the nanoparticle layer on the way back to the eye (sensor). In this case, it superimposes with the back scattered light from the layer which results in a distorted (superimposed) color perception. Accordingly, the color perception of the eye is not fully comparable with the results of a spectrometer. Although calculations allow the determination of the color from an optical spectrum, the optical setup is also crucial for the color impression of the human eye. The presentation and interpretation of these effects succeeds with the aid of optical spectra and Figure 3 and 4 in **article 3.1** illustrate this approach in a significant way. In the first row of Fig. 4, it is demonstrated what the eye sees and the second row (d – q) corresponds to the optical transmission spectra, while the third row illustrates the (diffuse) back scattered light. The change of color in the second row corresponds to a shift of the plasmonic resonance to larger wavelengths. Such a shift results to an increase in transmission in a wavelength range of around 500 nm and also with an increased absorbance at 630 nm. This leads to a higher proportion of blue and a lower red proportion, *i.e.* the appearance of the layer becomes increasingly blue.

A further effect, which has been predicted by the Mie theory, is the appearance and displacement of the scattering maximum with increasing particle sizes and is also responsible for the peak broadening discussed above. The third row in Fig. 4 (r-u) shows the diffuse reflectance of the particles realized by a black background. For the smallest particles, where no scattering phenomena occur, the scanned images remain black. With increasing particle sizes, a diffuse orange layer appears which corresponds to scattering of light by interaction with the oscillating electron gas. It should be noted that with this method, no specular reflection is measured as the optical arrangement of the flatbed scanner is not designed for. Wherefore the closed untreated layers appear also in black.

The **article 3.2** presents the optical properties of gold nanoparticles covered or embedded in an SiO₂ matrix. If nanoparticles coated with a matrix of higher refractive index, their plasmon resonance shifts

toward longer wavelengths [3,113,127] (for more details describing these facts see **article 3.7** and also **3.3**). Since the dewetting occurs in this example inside or within an SiO₂ layer, the structures and the optical properties differ significantly from those dewetted on top of a surface. The most noticeable result of this article is the decolorizing of the sample if it is covered with an SiO₂ layer before dewetting. Figure 4 shows that the plasmon resonance of the gold particles in the visible range is suppressed. Nevertheless, the typical gold inter band absorption in the region below 500 nm is still observed. This suggests that still metallic gold must be present. Furthermore, the range between 600 and 1000 nm shows a consistently low (at least for a transparent and clear sample) transmission of only 60 or even 50 % at lower dewetting temperatures. The optical spectrum of the covered particles corresponds to a thin layer below the percolation threshold [128] and the characteristic spectra of particles and layers are superimposed. Similar structures and their corresponding optical spectra can also be observed in an incompletely dewetted gold layer by time resolved optical spectroscopy [41]. However, even after the dewetting system gold/SiO₂ is completed, no plasmon resonance is observed in the absorption spectrum. The particles with a size up to 750 nm are too large for a strong plasmon resonance in the visible range. Possibly, these large particles are no longer approximately semi spherical, but have the shape of discs. However, such an assertion cannot be derived from the recorded SEM images.

However, the effect of discoloration can be prevented by an additional SiO₂ layer below the gold / SiO₂ system. Then, the resulting gold particles are finally embedded in SiO₂. It has been argued that the increased roughness of the additional first silica layer affects the dewetting and promotes the formation of smaller particles. This is clearly seen in Figs. 2 e and f. Smaller particles exhibit (in agreement with the previous argumentation) a noticeable plasmonic resonance in the visible wavelength range which is also observed in the optical spectra shown in Fig. 4. In analogy to the gold silica system, no clear plasmon resonance is observed at wavelengths up to 1000 nm visible when the dewetting is not yet complete, as it is also seen in [41,129].

The knowledge about this behavior is crucial taking into account the design of sensors in **article 3.7**, which are covered with an SiO₂ layer to prevent sticking during hot embossing. A sensor system, as described above is not possible without a significant plasmon resonance and thus without an additional silica layer.

The effect of an additional metal layer is described in **article 3.3**. In contrast to the dielectric SiO₂ layer, an additional layer formed by another type of metal has, with a suitable choice of the respective metals, the ability to form alloys. In this work, a system consisting of gold and silver was studied which in this sense exhibits a perfect miscibility.

Using a simple mixture of these metals, the plasmon resonance is observed at significantly smaller wavelengths than in the case of pure gold particles. The minimum plasmon resonance of very small gold nanoparticles is located at 510 to 520 nm [3,114,130,131]. An increase in the particle size, in the refractive index of the matrix (or substrate), or if the shape differs significantly from a sphere, leads to a shift of the absorbance maximum to higher wavelengths [3]. For silver, the characteristic transmission minima is located at around 360 to 420 nm [3]. Since the plasmon resonance is defined by the dielectric function of each metal, a mixture performs the tunable optical properties as a function of ratio of the respective metal concentrations. In **article 3.3**, the concentration of each metal was adjusted by the thickness ratio of the initial layers.

With increasing thickness of initial gold layer, the plasmon resonance peak shifts from 488 to 520 nm after the annealing (shown in Fig. 5). This can be explained by an increasing amount of gold in the dielectric function of the resulting nanoparticles. However, the dewetting results also in larger particles, since the initial layer thickness also increases. As already mentioned in **article 3.1**, larger particles leads to an additional shift to longer wavelengths.

If the layer system is deposited in the opposite stacking order, *i.e.* a gold layer with a constant thickness is followed by a silver layer with varied thickness, then the resulting plasmon resonance is also shifted to higher wavelengths. At a first glance, this behavior is surprising; it can, however, be explained taking into account, that silver is oxidized under the applied conditions. Hence, it is due to the oxidation of silver. The effect of alloying is suppressed (or extinguished) by the formation of a matrix around the particles which has a high concentration of silver and hence, a high refractive index. A comparable behavior is shown in **article 3.7**, an increase in the refractive index of the surrounding medium leads to an increase in resonance wavelength.

This behavior can be suppressed in a certain extent by changing the stacking order. An increased silver layer is covered with a gold layer of a constant thickness. Hence, silver is protected against the atmosphere for a longer period of time. This leads to a shift in the plasmon resonance to smaller wavelengths with increasing particle size. An uncovered gold film dewets and forms particles with a resonance wavelength at 527 nm. An additional silver layer with a thickness of 7 nm after dewetting leads to a plasmon resonance at 509 nm, *i.e.* at a smaller wavelength than for pure gold. This means that the long-wavelength shift which should be observed in the case of larger particles is completely compensated and exceeded by the short-wavelength shift caused by the formation of an alloy.

A further important result, taking into account the absence of the plasmon resonance of pure silver, at a temperature above of 400 °C. In Figure 4 in **article 3.3**, a characteristic absorbance peak is not seen in the case of 7 nm thick silver layer according to dewetting. Nanoparticles in general do not show a

Plasmon resonance if they lose their metallic properties, *i.e.* if no longer a free electron gas exists which is necessary for the resonant interaction with a light wave.

In **article 3.4**, the optical properties of palladium nanoparticles prepared by the dewetting method are shown. Dewetting of closed layers to form palladium nanoparticles has the advantage that no chemical substances affect the optical spectrum especially the UV cut off wavelength [12].

Langhammer et al. described the fundamental optical properties of small palladium nano disks [132,133,133] and their application for plasmon resonance based hydrogen sensing [134,135]. As the particles have distorted aspect ratio, the plasmon resonance is shifted into the vis-IR wavelength range. The applied particles were prepared by a hole mask lithography [136].

Since the plasmon resonance depends basically on the intrinsic electronic structure of metals, discontinuities in the dielectric function are directly transferred to the optical properties. The dielectric function of palladium indicates a characteristic shoulder in the range from 200 to 300 nm, which is also observed in the optical spectrum in the form of a significant change in the slope. Simulations, which will be more precisely discussed, confirm this fact and prove the direct relationship of dielectric function and resulting optical spectrum. Hydrogen incorporation into the palladium lattice significantly affects the electrical structure of the host metal, which can also be seen in a clear change in the optical spectrum of the particles in a pure hydrogen atmosphere.

In contrast to gold, the dewetting behavior of palladium is more complex caused by an oxidation process. Palladium reacts (in air) to PdO at a temperature above 258 °C which decomposes to metallic Pd above 819 °C. In order to prevent an oxidation during the formation of the particles, a process temperature of 900 °C was used for dewetting (see **article 3.4**). After the annealing program is completed, the sample was cooled down to room temperature. Below 819 °C, the oxidation to PdO is thermodynamically possible, however, below 258 °C it does not occur for thermodynamically reasons. In order to prove the presence of metallic palladium during dewetting, the cooling rate was increased. This led to a decrease in the amount of oxide formed during the cooling procedure. However, in **article 3.6** it is shown, that a complete suppression is not possible under the conditions applied by this method because the reaction kinetics is too fast. However, PdO at room temperature is not stable against the attack of hydrogen. This enables the preparation of metallic palladium nanoparticles from PdO particles. The optical properties are irreversibly changed by the first interaction with hydrogen, A further contact to hydrogen results only in a reversible change in the optical spectra, caused by the formation of PdH, (see above). This indicates that a chemical reduction of PdO to Pd has expired. Hence, below 258 °C no (significant) PdO is formed and the reaction becomes irreversible at RT.

To get a better insight into the optical and structural behavior of palladium during the oxidation process, palladium layers with a thickness of 12 nm were annealed below the PdO decomposition as

well as below the dewetting temperature. A palladium layer with a thickness of 12 nm still shows optical transparency and an optical transmission analysis as well as an application according to **article 3.6** is even possible. The optical results are basically presented in **article 3.5**, Figs. 2 and 3. After the oxidation, the optical spectrum is changed dramatically caused by the transformation from a metal to a semiconductor (PdO) which results in different effective mechanisms of interacting with light. The optical band gap of the resulting palladium oxide shows a steady transition over a wide wavelength range, which may possibly be due to impurities. Below wavelengths of 500 nm, further optical effects occur upon oxidation and may correspond to the interband transitions or charge transfer bands. Additionally a similar observation in the same wavelength range was also discussed in **article 3.4** after heat treatment which results in the (therein still suspected) oxidation of palladium nanoparticles. However, a continuous layer is much better suited to describe the optical properties of palladium than the oxidized nanoparticles. The exact origin of the optical band is not yet clarified.

In **article 3.5**, a further important fact is exposed. The optical properties of a continuous palladium layer after reduction with hydrogen is not identical to that prior to the oxidation. This is attributed to changes in the surface morphology presented in chapter 4.1. The layer has changed permanently and it cannot be explained only by the interaction (incorporation) of hydrogen and palladium. As explained below, the effect of the interaction of hydrogen with an oxidized layer as well as with palladium nanoparticles is discussed in more detail.

4.3 Sensor application

In some sections of this work it has been discussed that nanoparticles can change the optical properties in dependence of their composition and that of the surrounding matrix. Furthermore, it has been shown, that the metallic particle in a certain way response to the environment and hence, it should also be suitable as a sensor. The next section introduces two basic types of optical sensors which not only enable the detection of substances, but also allows a deep insight into the nature of the nanoparticles and matter in general.

In **article 3.6**, the optical properties of palladium nanoparticles and continuous layers in contact with hydrogen are shown in an application related consideration. The retooling of a spectrometer was too complex and therefore a simple and uncomplicated sensor system which allows time resolved measurements with a suitable sampling rate was developed. The optical setup of the sensor head is equal to a transmission spectrometer. Two windows coated with the target layer are illuminated by a red LED, the light is transmitted through the windows, the layers as well as the chamber. At the opposite side, the light is collected by a photodiode. In contact with hydrogen, the optical properties of the coating will be changed according to **articles 3.4** and **3.5**. The optical analyses given in these **articles**, allow to calculate difference spectra, which provide information about the maximum optical change in the spectrum during and after the contact to hydrogen. It can be concluded: a red LED with the outlined emission spectrum is very suitable as light source for the sensor using palladium coatings. In a home-built system the comparability to other setups is not given sometimes. Hence, the results of this work are discussed in relation to a standard procedure, which consists of untreated freshly sputtered palladium layers of respective thickness.

As expected, the optical transparency at wavelengths which can be generated by LED changes in dependence of the atmosphere applied. If the layers have been oxidized, at the first contact to hydrogen, an irreversible reaction of PdO to PdH takes place which results in an immense decrease in the transparency. With respect to the layers, the change in the transmission is three times as large as that attributed to the conversion from Pd to PdH. The reaction of Pd to PdO is that of a metal to a semiconductor and hence is attributed to a fundamental change of the light absorption mechanism. If, however, particles are used for the measurement, a similar but much smaller (16 times in comparison to the continuously oxidized layers) effect occurs. In this regard, it is also interesting that the particles used for the measurement are rapidly cooled to prevent the oxidation by air as described in **article 3.4**. Therefore it becomes clear that a complete suppression of the oxidation, with the parameters of this cooling method and without replacing air as atmosphere, is not possible.

The reversible effect present in all studied types of coatings corresponds to the formation of palladium hydride. However, all types of coatings also show different optical responses during the contact with hydrogen. The freshly sputtered and oxidized layer differ (beside the signal height) by the desorption behavior. The reduced and roughened layers, shows a three step desorption behavior. However, there are several different lines of argumentation. First, the three steps correspond to the 3 different stages within the Pd-H system. However, the reason why the freshly sputtered layers show only one stage is not yet understood. Possible explanations are the resolution of the measurement is too small, and only the strongest change is visible, or 2 phases (the beta phase and therefore the alpha-beta steady state phase) within the phase diagram are suppressed.

The particles basically show the same behavior (except signal height) as the previously oxidized layers, but the signal has the opposite sign. This is also explained by different absorption mechanisms, but here between two different types of interaction of light with a metal. Firstly, the absorption in a layer, and on the other hand manipulation of a plasmon resonance of small metal nanoparticles. The direction which turns the signal also results from the difference spectra in Fig. 2, in **article 3.6**

Another type of sensor is present in **article 3.7** and deals with a change in the dielectric constant of the surrounding medium. The basics of optics and preparation are described in the **articles 3.1, 3.2** and **3.3** as well as in refs. [137,138].

Gold layers were prepared and subsequently covered by an SiO₂ layer in order to prevent sticking during the hot embossing process. During hot embossing, the particles are formed below or within the silica layer. To investigate the effect of an additionally SiO₂ layer on the sensor properties, cuvettes with and without a silica top layer were prepared and filled with different liquids as well as with air as standard. To illustrate the effect of hot forming, these measurements are compared with an integrated microfluid glass chip. A soda lime glass substrate was coated with an SiO₂/Au/SiO₂ layer system and subsequently hot embossed directly into the coated substrate. As discussed in **article 3.2**, a layer system without silica as the base layer, is not suitable due to discoloration effects.

As expected by numerical calculation and taking into account the relevant literature [3,3,113,119,139], an increase in refractive index of the used liquids, leads to an increase in the plasmon resonance wavelength, illustrated in Fig. 6 (a) in **article 3.7**. The plasmon resonance of an uncovered cuvette shifts from 544 nm (corresponds to air) by 13 nm if xylene is used. A shift of the same magnitude is obtained if the particles are located below a covering SiO₂ layer. Only the absolute plasmon resonance position has shifted towards higher wavelengths.

In contrast, the hot embossing process results in a considerable decrease in the optical sensitivity. This is discussed, by a densification of porous structures by the embossing step. This should also be mentioned that the measurement setup has changed. The spot size is reduced to 7 mm however, some areas of the chips are also transmitted, which are not in contact to the analyte and thus do not show a change in the plasmon resonance position. Superimpositions of sensitive and insensitive areas may result in a distortion of the measured signal. Due to this uncertainty, no simulations were performed for the determination of particle size and coverage.

In a similar way as the sensor based on palladium for the detection of hydrogen, this sensor is suitable for scientific use. The ability to measure the same particle layer in contact with various matrices, allows the estimation of properties, which cannot be derived from static spectra. This fact is discussed in more detail in the following chapter of the discussion, which deals with the simulation.

4.4 Theoretical consideration (Simulation)

To describe or to predict the optical properties of metal nanoparticles and their modification by a couple of parameters, the Mie theory is used. The mathematical algorithm of the software used (BHMIE) was written by Craig F. Bohren and Donald R. Huffman [111]. The graphical implementation (Mie Plot) was realized by Philip Laven and based on the BHMIE code [140]. Regarding the use of the Mie theory, some restrictions have to be applied. The Mie theory, as an analytical solution, is only valid for metal spheres inside a homogeneous medium. However, the nanoparticles described in this work are located in an interface exactly between substrate and atmosphere or liquid and frequently a deviation from the spherical shape occurs (more specifically, the deviation from the circular shape in the projection demonstrated in the **articles 3.1, 3.2, 3.3, 3.4 and 3.8**). This inevitably leads to deviations in the predictions. If a theoretical system no longer applies, then it is possible to adapt it by correction factors. However, this type of adaptation does not always fix the problem itself. In this thesis such factors were used, but it must be noted that the resonance is affected by many parameters, and a single correction includes all influential factors. It also follows that a correction factor is always tailored only to an individual system and is hardly or not transferable at all. Basic statements on the behavior of nanoparticles are still possible and provide an excellent insight into the functional principle of particle based nano optics. It should also be mentioned in passing, that at least some limitations (especially the particle shape) of the system can be described by using numerical methods. In initial experiments, the program DDSCAT of Drain and Flatau [141,142] shows promising results. It is based on the discrete dipole approximation, but requires complicated shaping operations and needs significant more computing power.

The resonance wavelength of small metal nanoparticles is simultaneously influenced by the particle size (distribution), shape, covering degree as well as by the surrounding media. Even if only size and environmental conditions (geometry, refractive index, etc.) are unknown, it is not possible to determine these values based on a single spectrum. This results from the fact that all of these effects lead to a shift of the peak to longer wavelengths. However, if the magnitude of a resonance shifts and the respective refractive index are known, statements about the underlying system are possible by using the Mie theory. An example is already mentioned in **article 3.7** and **chapter 4.3**.

The plasmon resonance wavelength of gold nanoparticles is affected by the dielectric constant and hence the refractive index of the surrounding liquids. The absolute position of the wavelength is basically due to the particle size. Calculation (at a given particle size) performed with the Mie theory pointed out that the slope of the resonance shift versus the change in the refractive index of the liquid, is much too high (see scattered lines in Fig. 7 **article 3.7**). This means that the real system responds much weaker to the presence of a liquid with an associated refractive index, as predicted by Mie theory. The idea is that a particle is not in a complete contact with the surrounding liquid. Introducing an effective medium (consisting of the components of the dielectric matrix) to describe the environment at the interface will solve the problem and allows the description of a mathematical system based on the Mie theory. A suitable choice of this linear weighting variable, accompanied by an appropriate adjustment to the resonance wavelength by the particle size, leads to a model that can describe the real situation in theory very well. For the calculations, a constant dielectric value of fused silica was assumed since within this wavelength range no significant changes in the refractive index are to be expected. This does not apply to the UV range.

Regardless of the selected simulation model (*e.g.* applied weighted and unweighted dielectric environment, Fig. 7, **article 3.7**), nearly the same plasmon resonance is obtained for the refractive index of xylene ($n=1.492$). Hence, the refractive indices of SiO₂ (fused silica) and xylene are very close to each other, thus a comparable dielectric environment is assumed by the simulations.

However, the real implication of the weighting variable, whether it is predominantly due to an incomplete coverage of a particle surface or the plasmon resonance is affected through an SiO₂ closed layer (as seen in [136,139]) cannot be clarified by this way. To the chip itself, no simulations were carried out, since the measurement data can also contain insensitive areas, which may distort the measurement, and thus the results of the simulation.

In **article 3.4** simulations were carried out with the aid of Mie theory in order to identify the absorbance peaks as plasmon resonances and furthermore to explain the change in optical spectra by the incorporation of hydrogen. Hence, an identification and evaluation by literature data was not

possible. For this purpose, the usual assumptions for the Mie theory, a sphere in a homogeneous medium, was adopted. The measured material dielectric functions of palladium, palladium hydride as well as fused silica found in the literature were used to perform the calculations. As already mentioned, a weighted dielectric material as surrounding matrix was used, to adapt the conditions of particles located inside an interface. Since optical induced resonances are expected in the UV range, a wavelength dependent dielectric function must be used in order to describe the SiO₂ substrate. In comparison to **article 3.7**, the particle size distribution is known, and thus the effect of the surrounding matrix and the geometry can be adapted. However, a separation of the effect of the matrix and the geometry is still not possible. On the other hand, in **article 3.4**, different ways of adaptation have been identified. Nevertheless, a theoretical description of the performed measurement taking into account the effect of the geometry is still not possible. Taking into account the above described limitations of the Mie theory, the real system is too complicated.

Important insights are still possible. The shape of the graph provides information on the origin of the optical properties of dewetted palladium layers. The shoulder in the absorption spectrum at wavelengths between 200 and 350 nm is also found in the dielectric function of metallic palladium. The optical spectrum is consequently caused by the electronic structure, and there is an interaction between the electrons and the light. Thus may be argued that there is a plasmon resonance. Furthermore, using the dielectric function of palladium hydride instead of palladium for the calculations leads to a notable change in the simulated absorption spectrum. The same effect can also be observed when the particles are brought in contact with hydrogen. It can be concluded, that the optical spectrum is caused by the formation of palladium hydride.

4.5 Crystallographic, morphological and analytic

Using methods such as a wet chemical route or the preparation of particles from the gas phase and subsequent deposition on a surface can hardly result in an orientation of the particles. By contrast, if a support is used *e.g.* a substrate and thus two degrees of freedom (rotation) are blocked. Additionally an energetically preferred orientation is already a result of the sputtering process. The subsequent dewetting leads to separated particles and all formed particles might have approximately the same orientation with respect to the substrate. The resulting “layer” of oriented particles may hence possess a texture. This texture statistically describes the distribution of crystallographic orientations.

In **article 3.1** the preparation of gold nanoparticles is described. It was found that the dewetting of a sputtered layer which already has a certain orientation leads to the formation of irregularly shaped particles in the first stages of dewetting. However, if annealing time and the temperature is increased, the particle shape becomes more regular and mainly faceted. The faceting is attributed to the crystalline nature of the particles and corresponds to a minimum energy state as described above. The shape follows from the Wulff construction [100,103,143,144] as well as the modified Wulff construction for supported particles [104,121]. The XRD patterns obtained from a 21 nm freshly sputtered and annealed gold layer proved its crystallinity. Mainly, the 111 peak of metallic gold is observed in a freshly sputtered layer. A great number of papers confirmed the orientation of sputtered or evaporated gold layers [60,62,63,145]. After a subsequent annealing solely the 111 and 222 peaks were observed. Thus, it can be concluded, that the particle layer is textured caused by a preferable orientation of the particles with respect to the surface of the substrate. EBSD measurements obtained from the same sample confirmed this result. An orientation with the (111) crystal plane parallel to the substrate is preferred. With respect to the argument of the blocked rotation degrees of freedom, a continuous ring observed at an angle of 70.5 deg in the (111) pole figure indicates a random rotation around the [111]-direction. These results are confirmed by [38]. Similar orientations (partially different measurement methods) are found in numerous references [39,41,145,146,146]. Additionally, Marks [100] and Metois et al. [147] described “kinetic shapes” which occur, during the evaporation at low substrate temperatures. Due to sticking dominated growth processes, a (001) face exhibits a higher “sticking probability” as well as a higher free surface and thus will grow faster than a (111) face. Marks concluded, that a slower growing (111) and (011) faces, will dominate the kinetic shape of small particles. He also reported a possible suppression of the fast growing (001) direction.

The results discussed in **article 3.1** are obtained by thermal annealing at a temperature of 400 °C. At higher temperatures, an interaction with the substrate, a change in morphology as well as in the orientation cannot be ruled out. Hence, the knowledge about the crystallographic shape and orientation at elevated temperatures is very important to the application in catalytic growth processes *e.g.* Au-catalyzed vapor-liquid-solid growth [146,148–157].

Similar to the XRD results in **article 3.1**, the XRD patterns obtained for the layers subsequent annealed at 600 °C in **article 3.2** also show mainly the 111 peak of metallic gold. The preferred 111 orientation is not affected by the changed dewetting mechanism. EBSD analysis, however, shows an 111 pole figure superimposed by another texture. Hence the data points were filter by the confidence index and image quality. A confidence index of 0.1 corresponds to the probability of a correct solution (indexing) of 95%, on a face centered cubic crystal system with 6 activated Kikuchi bands [158]. For a confidence index higher 0.2 and an image quality of more than 20%, strong 111 orientation ([111]-direction perpendicular to the surface)) is indicated. However, if only the acquired patterns with an image quality factor lower than 20 % are used for a statistical analysis, the calculated 111 pole figure totally changed. The middle 111 spot has disappeared, and an true unspecific texture arises. Possibly the smallest particles below an SiO₂ layer (and obtained patterns with the lowest image), exhibit another orientation but the underlying mechanisms is not clarified.

Also the morphology of the particles is further examined at elevated temperatures as well as at high temperatures. In the case of palladium and silver, thermal induced oxidation and reduction as previous discussed in the **articles 3.3, 3.4, 3.5** and **3.6** are also of great interest.

In **article 3.8**, the dewetting temperature for gold was applied at temperatures in the range from 426 to 1102 °C. After tempering at 426 °C, an 111 texture was also found by EBSD and confirmed the results of **article 3.1**. At higher temperatures, additionally 101 and 100 textures are formed. The 111 texture scarcely occurs in a sample dewetted at 965 °C and then rapidly cooled. From this, it can be concluded that the orientation is different if the sample is dewetted at higher temperatures. This texture can be preserved, if cooling is fast enough. By contrast, if a slow cooling process is applied, the particles tilt back and after cooling again an 111 texture is observed. If the melting point of gold (1064 °C) [159] is exceeded, the orientation becomes random and the texture is lost. This indicates that the oriented nature of the particles, caused by manufacturing, is retained up to the melting point. Only a complete destruction of the crystallinity also destroys the orientation.

Statistical analyses of the particles by image processing was used to describe morphological changes with increasing the dewetting temperature. Important parameters are the particles size and feret ratio distribution. Again, the results from **article 3.1** could be confirmed. The particles become faceted by dewetting at 426 °C for 3 h. The particle shape is still irregular, which is reflected also in the aspect

ratio. With increasing dewetting temperature, the particle shape becomes more round and the faceting is less pronounced indicated by a significant increase in the feret ratio. Similar results were obtained by Hwang and Noh [160]. They also describe the rounding of the gold particles on a crystalline sapphire substrate. Due to that, only amorphous substrates were used in the present experiments, an influence of the substrate crystal structure can be neglected. Nevertheless, studies of Sadan and Kaplan show that the morphology is restored after solid-state equilibration of the particles slightly below the melting point [97,110]. Furthermore, it can be concluded that the equilibrium shape of the nanoparticles is temperature dependent. Barnard et al. [103] used a thermodynamic model to determine the shape of a 12 nm gold particle at elevated temperatures. He observed a dramatic decrease in the {111} surface area at temperatures above 800 °C. The morphology of the particle is transferred from “truncated octahedron to a more cuboctahedral morphology”. Thus the area ratio of the individual facets is changes. Hence, it would be conceivable that such a mechanism may influence the orientation of individual particles as discussed above. At the moment, it is not clear, whether a correlation between the change in morphology and the change in orientation exists.

Furthermore, an interaction of the gold particles with the substrate may not be excluded. SEM micrographs in **article 3.8** (Figure 3) show that significant substrate modifications in the form of holes or small depressions have occurred. However, the additionally structures are not in a local relationship to the large gold particles. The dewetting temperature of 1102 °C was higher than the melting point of the gold and the liquid particles (drops) may migrate over the surface and merge. As they wander around, former contact points to the substrate are visible. This would mean that the interaction with the substrate took place already before the particles were melted. One option would be that the interaction takes place with a permeated surface in contact with the substrate. A well-known phenomena occurs in small metal particles, associated with a shape transformation such as rounding or roughening [100, 143,144,161]. It is denoted as “premelting” or “surface melting”. A second option is that the nanoparticles serve as nucleation agents for surface crystallization. The beginning of the surfaces crystallization of SiO₂ is associated with the formation of depressions, which according to [162] may even be larger than the observed impressions.

However, similar modifications are found at crystallized SiO₂ surfaces after annealing at 1256 °C in the presence of palladium nanoparticles on the surface. The resulting crystalline appearance of the surface corresponds to the structure presented in [162]. However additional dark spots occur in which palladium cannot be detected by EDX. The size of the dark spots is comparable in size to the palladium nanoparticles annealed at temperatures of 876 or 965 °C.

The exact nature of the surface modification if there are impressions or the first appearance of surface crystallization has not yet been examined.

Palladium particles were also described in **article 3.8**. In contrast to gold, the temperature range in which dewetting may occur is much smaller. Also multiple orientations (001 and 111) were detected after dewetting at 876 and 965 °C. As already mentioned several times, palladium is oxidized by the atmosphere at higher temperatures and hence shows a phase transition. For this reason, in **article 3.4**, it is proposed to suppress the oxidation by rapid cooling. This has been proved on grounds of the optical properties. However, as noted in **article 3.6**, the applied cooling rate was not fast enough and supposedly some PdO was already formed. To get a better insight, the EBSD investigations were performed on rapidly cooled (take out from the furnace) as well as on slowly cooled samples. For the latter, the sample remains in the furnace during cooling to RT) with and without subsequent hydrogen purging. If the samples were slowly cooled and not purged with hydrogen, the EBSD scan led to a great number (16,471) of 285,566 (5.76 %) of patterns are attributed to PdO. However, no discernible texture is obtained in this case. If the sample was previously purged with hydrogen (30 min) only 0.03 % of the patterns (140 of 542,538 patterns) are attributable to PdO. Nevertheless, (in spite of a larger scan), a large number of patterns attributed to metallic palladium is not found. Only 1,796 of 542,538 patterns are reliable indexed to cubic palladium. These are only 0.33 % of all possible data points. Due to this small amount of statistically reliable points, reliable conclusions can hardly be made.

If the PdO layer is reduced by pure hydrogen at room temperature, a high reaction rate as well as the substantial difference in the density of oxide and metal leads to a highly disturbed crystal lattice where an examination using EBSD is no longer possible.

This assumption is supported by the significant change in the morphology of the particles depending on their cooling rate as demonstrated in Fig. 8 in **article 3.8**. Su et al. proposed a nucleation mechanism on the surface of PdO particles in a methane-helium mixture. However, on the basis of catalytic measurements, they concluded a core-shell structure for the whole particle after contact with hydrogen [163].

A similar effect of difficult EBSD-pattern acquisition is observed using a rapidly cooled sample. However after fast cooling, only 414 of 190,992 data points are reliable. These are 0.22 % of all points but nevertheless, it should be mentioned that a texture calculation reveals a 111 texture, which is statistically not convincing. Furthermore 0.11 % of the patterns (217) can be attributed to PdO. Subsequent purging with hydrogen for 15 minutes shows a completely different behavior during EBSD analysis. Hence, in the same sample section (compare with top of Fig. 7), 34,422 of 200,928 patterns (17.13% of all data points) are attributable to the palladium. And now 001 and 111 textures are established. A similar number of patterns (260) as without hydrogen purging is attributed to PdO, that corresponds to 0.13 % of all possible data points.

During fast cooling, a thin PdO shell is formed and evaluable EBSD patterns cannot be acquired because the respective patterns are superimposed by each other. If the PdO shell is reduced, a large number of patterns can be acquired and be indexed as cubic palladium. It should be mentioned again, the chemical reduction of a slow cooled (completely oxidized) PdO to Pd leads to a very low number of index able patterns.

To ensure the electric conductivity of the surfaces, all samples were coated with a thin carbon layer prior to the electron microscopic analyses. An attempt has been made to treat a carbon coated sample with hydrogen. Surprisingly, this thin carbon layer does not prevent the reduction to metallic palladium initiated by hydrogen and also subsequent investigation with EBSD is still possible. However, even the required hydrogen purge time is probably not comparable to the treatment time obtained in **article 3.6**. Hence, the hydrogen diffusion rate through the carbon layer is decreased, and also the reaction product water has to leave the sample surface. Certainly, it allows studying the reduction behavior for discrete time steps using the same sample.

Additionally, platinum nanoparticles are prepared by dewetting. Also in this sample a preferable orientation is shown. A preferred [101] and [111] orientation perpendicular to the surface is observed.

5. Conclusion

It could be shown that an optical sensor system based on functionalized glass surfaces may provide a large variety of applications.

Thin layers of gold, silver, palladium and platinum were dewetted to small nanoparticles at elevated temperatures. It could be shown that these particles have optical properties which can be attributed to plasmon resonances. The plasmon resonance of gold particles can be tailored towards smaller wavelengths by incorporating silver atoms, provided by an additional sputtered silver layer. An increase in the resonance wavelength is obtained by the prior oxidation of the silver.

The optical properties of gold (and all other nanoparticles) are affected by the surrounding medium. An increase in the refractive index leads to an increase in the resonance wavelength. In addition, it was shown that an embedding in an SiO₂ layer, prepared by a combustion chemical vapour deposition process (CCVD) reduces but does not suppress the sensing properties. Applying the SiO₂ layer allows the hot embossing of fluidic structures in the layer system and the substrate in addition to the fixation of the particles.

Palladium nanoparticles can also be prepared by thermal dewetting of thin sputtered layers. The dewetting behavior is changed by the thermal oxidation and subsequent reduction at higher temperatures and a bimodal size distribution is observed. Palladium nanoparticles respond to the presence of hydrogen by changing the position and shape of the plasmon resonance. The most significant change is obtained in the wavelength range of 550 to 700 nm and is therefore easily detect. Annealing Pd-films at 700 °C, leads to the formation of an oxidized layer. A subsequent reduction with hydrogen results in a roughened surface morphology with improved hydrogen sensing properties.

Most particles layers prepared by dewetting exhibit a strong 111 texture, i.e. the [111] direction preferably occurs perpendicular to the substrate. Additional textures appear at elevated temperatures. An almost absolute suppression of the 111 texture for gold is obtained after annealing at 965 °C and rapid cooled to room temperature. Thermal treatments above the melting point of gold destroy the texture.

6. Abstract

In this work, nanoparticles were deposited on glass surfaces. For this purpose, a dewetting process was used. A closed sputtered metal layer breaks into small particles by a heat treatment. This effect is based on the minimization of the interfacial energy in the system substrate/particle/atmosphere. The size distribution and shape of the particles may be adjusted by the initial layer thickness. If the temperatures are too low (350 and 400 °C) and the layers too thick (15 nm), the dewetting process also produces irregularly shaped particles, since the energy is not sufficient to transform the particles near their state of equilibrium. Based on these studies, ageing effects such as Ostwald ripening and an essential particle-forming mechanism, the Rayleigh-instability were identified. It has been found that the equilibrium shape for larger particles exhibits a clear faceting which is based on the underlying crystal system. In this case, it is assumed that the forming facets correspond to the crystal structure and represent a further stage of the energy minimization. However, the faceting disappears at elevated temperatures (> 800 °C) by the formation of additionally and more favored crystal faces. Using EBSD analyses, it could be shown that the gold nanoparticles are preferably oriented with the densely packed {111}-plane parallel to the amorphous substrate surface. This changes with increasing temperature and {100} as well as {110} planes parallel to surface will also appear. In addition, a correlation with the cooling rate could be expected. Only temperatures above the melting point will destroy the observed texture and the system is transformed in a random orientation.

In order to control the optical properties of metal nanoparticles, several possibilities are offered and in this thesis three different approaches are explained in detail. The first is the adaptation of the particle size, followed by an adjustment of the particle composition, as well as the selective modification of the surrounding media. An increase in the particle size leads to a red shift and to a broadening of the resonance peak. Adding of a metal as component for an alloy, leads to a lower plasmon resonance wavelength. Silver is the ideal material for this purpose because it has a very strong resonance in the visible range (at around 420 nm). Thin gold and silver layers were sequentially sputtered onto the glass surface. A subsequent temperature treatment leads to dewetting and alloying, thus particles with tailored resonance wavelengths are formed. However, the experiments were performed under ambient conditions, so that the silver tended to form an oxide phase. It was found that oxidation of silver suppresses the alloying and leads to an opposite optical effect because the particles are now inside a dielectric matrix with higher refractive index. This effect can be counteracted by a suitable choice of the stacking sequence (silver is always covered by gold) and the process temperature is not too high (< 400 °C). For the application as a sensor element, the incorporated material to manipulate the optical properties does not necessarily have to be a metal. A promising combination is palladium and hydrogen. Hydrogen incorporates into the palladium host lattice at room temperature with almost no

kinetic hindrance, and forms different phases. The amount of dissolved hydrogen in palladium is primarily a function of hydrogen partial pressure. However, the production of palladium nanoparticles concerning the dewetting of a thin layer is mostly unknown. Thus, such a system was characterized for the first time in this work. The possibility, to produce palladium nanoparticles without any chemical stabilizing agents, allows analyzing the optical properties in the UV-range. Then according to mathematical predictions, the plasmon resonance of palladium occurs at around 220 nm. A heat treatment of 5 nm thick palladium layer on a fused silica surface at 900 °C, leads to well separated particles with diameters in the range from 20 to 200 nm. Optical measurements under argon and hydrogen atmospheres show a clear effect of the presents of hydrogen on the dielectric function of palladium and thus the optical properties. This behavior could be mathematically described by using the Mie-theory using optical materials data of Pd and PdH. However, during the first purging cycle with hydrogen, an irreversible change of the optical spectra occurred. This is attributed to the presence of palladium oxide, formed during the cooling procedure between 775 °C down to 258 °C. For this reason, the formation and the chemical, morphological, crystallographic and optical properties of this oxide phase has been studied in more detail. It becomes also apparent that the sensor properties can be significantly improved with such a reduced Pd layer as well as with palladium nanoparticles.

A further way to control the plasmon resonance of metallic nanoparticles is to modify the direct (dielectric) environment. Conversely, this behavior is also very useful for an application as a sensor system. For this reason, an optical sensor chip based on gold nanoparticles with microfluidic structures directly hot embossed into a soda lime glass substrate was designed to demonstrate the ease application of such technologies. It was shown that additional to the necessity of a coating which prevents sticking during the hot embossing procedure, the sensor properties can be used. Furthermore, a mathematical model was adapted to theoretically describe the effect of adjacent chemicals.

7. Zusammenfassung

In dieser Arbeit wurden Nanopartikel auf Glasoberflächen hergestellt. Hierzu wurde ein Entnetzungsprozess genutzt. Eine geschlossene Metallschicht zerfällt unter thermischer Einwirkung zu kleinen Partikeln, basierend auf einer Minimierung der Grenzflächenenergie im System Substrat/Partikel/Atmosphäre. Die Größenverteilung sowie die Form der Partikel kann durch ursprüngliche die Schichtdicke eingestellt werden. Bei einem ungünstigen Verhältnis von relativ niedrigen Temperaturen (350 und 400 °C) und dicken Schichten (15 nm) erzeugt ein solcher Entnetzungsprozess auch unregelmäßig geformte Partikel, da die Energie nicht ausreicht, um die Partikel in ihren Gleichgewichtszustand zu überführen. Anhand dieser Untersuchungen, konnten Alterungseffekte, wie Ostwaldreifung und ein elementarer partikelbildender Mechanismus, die Rayleigh-Instabilität nachgewiesen werden. Es hat sich herausgestellt, dass die Gleichgewichtsgestalt für größere Partikel eine deutliche Facettierung aufweist, welche sich an dem zugrunde liegenden Kristallsystem orientiert. In diesem Fall geht man davon aus, dass die sich ausbildenden Facetten, denen der Kristallstruktur entsprechen und somit eine weitere Stufe die Energieminimierung darstellen. Allerdings zeigt sich dass diese Überlegung für höhere Temperaturen (> 800 °C) durch Auftreten weiterer energetisch begünstigter Kristallflächen keinen Bestand mehr hat und die deutliche Facettierung wieder verloren geht. Mittels weiterer EBSD Analysen konnte gezeigt werden, dass Goldnanopartikel bevorzugt mit ihrer dichtest gepackten {111}-Ebene parallel zur amorphen Substratoberfläche orientiert sind. Dieses erwartungsgemäße Bild ändert sich ebenfalls mit steigender Temperatur und es zeigen sich auch zunehmend {110} und {100} orientierte Ebenen parallel zur Oberfläche. Diesbezüglich konnte auch ein Zusammenhang mit der Abkühlrate der Probe festgestellt werden. Nur ein Überschreiten der Schmelztemperatur zerstört die beobachtete Textur und überführt das System in eine zufällige Orientierung.

Zur Steuerung der optischen Eigenschaften bieten sich grundsätzlich mehrere Möglichkeiten der Manipulation an, was in dieser Arbeit anhand von drei verschiedenen Herangehensweisen erläutert wird. Zum einen die bereits beschriebene Einstellung der Größe sowie die Zusammensetzung oder auch die gezielte Veränderung der direkten umgebenden Matrix des Partikels. Da eine Vergrößerung der Partikel immer eine Rotverschiebung sowie eine Aufweitung des Peaks mit sich bringt, liegt die Überlegung nahe, ein Metall mit einer niedrigeren Plasmonenresonanzwellenlänge hinzu zu mischen, genauer gesagt zu legieren. Hierbei ist Silber die erste Wahl, da es eine sehr starke Resonanz im sichtbaren Bereich bei 420 nm besitzt. Dünne Gold und Silber Schichten wurden nacheinander auf die Glasoberfläche gesputtert. Eine anschließende Wärmebehandlung führt zum Entnetzen und Legieren des Systems und es bilden sich Partikel mit maßgeschneiderten Resonanzwellenlängen. Allerdings wurden die Versuche unter Umgebungsbedingungen durchgeführt, so dass das Silber zum Bilden einer

Oxidphase neigt. Eine Oxidation des Silbers unterdrückt die Legierungsbildung und bewirkt aus optischer Sicht den gegenteiligen Effekt, da sich die Goldpartikel nun in einer dielektrischen Matrix mit höherem Brechungsindex befinden. Diesem Effekt kann in gewisser Weise entgegen gewirkt werden, so dass das anhand der Stapelfolge Silber stets mit Gold bedeckt ist und die Prozesstemperatur nicht zu hoch ($< 400\text{ °C}$) gewählt wird. Zur Anwendung als Sensor, muss der eingebrachte Stoff zur Manipulation optischer Eigenschaften nicht zwangsläufig ein Metall sein. Eine vielversprechende Kombination ist Palladium und Wasserstoff. Wasserstoff löst sich bei Raumtemperatur freiwillig und kinetisch nahezu ohne Hemmung im Wirtsgitter des Palladiums unter Bildung verschiedener Phasen. Die Menge des im Palladium gelösten Wasserstoffs ist in erster Linie abhängig von dessen Partialdruck. Die Herstellung von Palladiumnanopartikeln durch Entnetzung einer dünnen Schicht ist allerdings weitestgehend unbekannt. Somit erfolgte in dieser Arbeit erstmals eine Charakterisierung eines solchen Systems. Die hier gebotene Möglichkeit des Verzichts auf chemische Stabilisationsmaßnahmen erlaubt auch eine Analyse der optischen Eigenschaften im UV-Bereich, wo nach Berechnungen mit Hilfe der Mie Theorie auch die Plasmonenresonanzen von Palladium auftreten. Eine 5 nm dünne Palladiumschicht auf einer Kieselglasoberfläche entnetzt zu Partikeln mit einer Größe von 20 bis 200 nm Durchmesser. Untersuchung der optischen Eigenschaften dieser Partikelschichten unter Argon- und Wasserstoffatmosphäre offenbarten den Einfluss des eingebauten Wasserstoffs auf die dielektrische Funktion der Palladiumnanopartikel. Dieses Verhalten konnte unter Zuhilfenahme der Materialdaten von Pd und PdH mit Hilfe der Mie-Theorie mathematisch beschrieben werden. Jedoch zeigte sich während des ersten Spülzykluses mit Wasserstoff eine nicht reversible Änderung der optischen Eigenschaften. Dies ist auf die Anwesenheit von Palladiumoxid zurückzuführen, welches sich während des Abkühlens der Probe zwischen 775 und 258 °C gebildet hat. Aus diesem Grund wurde die Bildung sowie die chemischen, morphologischen, kristallografischen und optischen Eigenschaften dieser Oxidphase genauer untersucht. Dabei stellt sich heraus, dass die sensorischen Eigenschaften mittels derartig reduzierten Pd-Schichten sowie Palladiumnanopartikeln, deutlich verbessert werden können.

Einen weiteren Weg um die Plasmonenresonanz zu beeinflussen, ergibt sich aus der Änderung der direkten dielektrischen Eigenschaften der Umgebung. In umgekehrter Weise, lässt sich dieses Verhalten auch für sensorische Anwendungen nutzen. Aus diesem Grund wurde ein optischer Sensorchip entwickelt, basierend auf Goldnanopartikeln innerhalb einer Mikrofluidikstruktur, welche direkt in ein Kalk-Natron Glas geprägt wurde. Dies demonstriert auch die einfache Anwendung einer solchen Technologie. Es konnte auch gezeigt werden, dass trotz der Notwendigkeit einer SiO_2 Antihafbeschichtung, die sensorischen Eigenschaften weiterhin vorhanden sind. Weiterhin wurde ein mathematisches Modell so angepasst, dass der Einfluss der veränderten Umgebung auch theoretisch erfasst werden kann.

8. References

- [1] I. Angelini, G. Artioli, P. Bellintani, V. Diella, M. Gemmi, A. Polla, A. Rossi, *Chemical analyses of bronze age glasses from Frattesina di Rovigo, Northern Italy*, *Journal of Archaeological Science*, 31 (2004) 1175–1184.
- [2] P. Colomban, C. Truong, *Non-destructive Raman study of the glazing technique in lustre potteries and faience (9–14th centuries): Silver ions, nanoclusters, microstructure and processing*, *Journal of Raman Spectroscopy*, 35 (2004) 195–207.
- [3] M. Quinten, *Optical properties of nanoparticle systems: Mie and beyond*, Wiley-VCH-Verlag, Weinheim, 2011.
- [4] G. Schmid, B. Corain, *Nanoparticulated gold: Syntheses, structures, electronics, and reactivities*, *European Journal of Inorganic Chemistry*, (2003) 3081–3098.
- [5] E. Hutter, J.H. Fendler, *Exploitation of localized surface plasmon resonance*, *Advanced Materials*, 16 (2004) 1685–1706.
- [6] J.D. Aiken, R.G. Finke, *A review of modern transition-metal nanoclusters: Their synthesis, characterization, and applications in catalysis*, *Journal of Molecular Catalysis A*, 145 (1999) 1–44.
- [7] M. Grzelczak, J. Pérez-Juste, P. Mulvaney, L.M. Liz-Marzán, *Shape control in gold nanoparticle synthesis*, *Chemical Society Reviews*, 37 (2008) 1783–1791.
- [8] T. Ung, L.M. Liz-Marzan, P. Mulvaney, *Gold nanoparticle thin films*, *Colloids And Surfaces A*, 202 (2002) 119–126.
- [9] D.H. Chen, C.J. Chen, *Formation and characterization of Au-Ag bimetallic nanoparticles in water-in-oil microemulsions*, *Journal of Materials Chemistry*, 12 (2002) 1557–1562.
- [10] J. Cookson, *The preparation of palladium nanoparticles*, *Platinum Metals Review*, 56 (2012) 83–98.
- [11] J. Turkevich, P.C. Stevenson, J. Hillier, *A study of the nucleation and growth processes in the synthesis of colloidal gold*, *Discussions Of The Faraday Society* (1951) 55–75.
- [12] C. Hwang, Lu Y.L., Jang S.W., Chou P.T. Wang C.R.C., Yu S.J., *Synthesis, characterization, and highly efficient catalytic reactivity of suspended palladium nanoparticles*, *Journal of Catalysis*, 195 (2000) 336–341.
- [13] C.J. Murphy, T.K. Sau, A.M. Gole, C.J. Orendorff, J. Gao, L. Gou, S.E. Hunyadi, T. Li, *Anisotropic metal nanoparticles: Synthesis, assembly, and optical applications*, *The Journal of Physical Chemistry B*, 109 (2005) 13857–13870.
- [14] A. Henglein, M. Giersig, *Formation of colloidal silver nanoparticles: Capping action of citrate*, *The Journal of Physical Chemistry B*, 103 (1999) 9533–9539.

- [15] F. Porta, L. Prati, M. Rossi, S. Coluccia, G. Martra, *Metal sols as a useful tool for heterogeneous gold catalyst preparation: Reinvestigation of a liquid phase oxidation*, *Catalysis Today*, 61 (2000) 165–172.
- [16] H. Bönemann, G. Braun, W. Brijoux, R. Brinkmann, A. Schulze Tilling, K. Seevogel, K. Siepen, *Nanoscale colloidal metals and alloys stabilized by solvents and surfactants: Preparation and use as catalyst precursors*, *Journal of Organometallic Chemistry*, 520 (1996) 143–162.
- [17] C.S. Hirtzel, R.A. Rajagopalan, *Invited review stability of colloidal dispersions*, *Chemical Engineering Communications*, 33 (1985) 301–324.
- [18] I. Capek, *Preparation of metal nanoparticles in water-in-oil (w/o) microemulsions*, *Advances in Colloid and Interface Science*, 110 (2004) 49–74.
- [19] M. Epifani, C. Giannini, L. Tapfer, L. Vasaneli, *Sol–Gel synthesis and characterization of Ag and Au nanoparticles in SiO₂, TiO₂, and ZrO₂ thin films*, *Journal of the American Ceramic Society*, 83 (2000) 2385–2393.
- [20] M.K. Corbierre, N.S. Cameron, M. Sutton, Mochrie, S. G. J., L.B. Lurio, A. Rühm, R.B. Lennox, *Polymer-stabilized gold nanoparticles and their incorporation into polymer matrices*, *Journal of the American Chemical Society*, 123 (2001) 10411–10412.
- [21] M. Dubiel, J. Haug, H. Kruth, H. Hofmeister, K.-D. Schicke, *Ag/Na ion exchange in soda-lime glasses and the formation of small Ag nanoparticles*, *Materials Science and Engineering: B*, 149 (2008) 146–151.
- [22] S. Hornschuh, B. Messerschmidt, T. Possner, U. Possner, C. Rüssel, *Silver ion exchange in glasses of the system Na₂O/Al₂O₃/B₂O₃/SiO₂*, *Journal of Non-Crystalline Solids*, 347 (2004) 121–127.
- [23] R.H. Magruder, L. Yang, R.F. Haglund, C.W. White, L. Yang, R. Dorsinville, R.R. Alfano, *Optical properties of gold nanocluster composites formed by deep ion implantation in silica*, *Applied Physics Letters*, 62 (1993) 1730–1732.
- [24] C. Li, K.L. Shuford, M. Chen, E.J. Lee, S.O. Cho, *A facile polyol route to uniform gold octahedra with tailorable size and their optical properties*, *ACS Nano*, 2 (2008) 1760–1769.
- [25] H.S. Al-Ghamdi, W.E. Mahmoud, *One pot synthesis of multi-plasmonic shapes of silver nanoparticles*, *Materials Letters*, 105 (2013) 62–64.
- [26] H. Bönemann, R.M. Richards, *Nanosopic metal particles - Synthetic methods and potential applications*, *European Journal of Inorganic Chemistry* (2001) 2455–2480.
- [27] J.A. Creighton, D.G. Eadon, *Ultraviolet-visible absorption spectra of the colloidal metallic elements*, *Journal of the Chemical Society, Faraday Transactions*, 87 (1991) 3881–3891.
- [28] T. Teranishi, M. Miyake, *Size control of palladium nanoparticles and their crystal structures*, *Chemistry of Materials*, 10 (1998) 594–600.

- [29] W. Wang, Q. Yang, R. Zhou, H.-Y. Fu, R.-X. Li, H. Chen, X.-J. Li, *Palladium nanoparticles generated from allylpalladium chloride in situ: A simple and highly efficient catalytic system for Mizoroki-Heck reactions*, *Journal of Organometallic Chemistry*, 697 (2012) 1–5.
- [30] A.N. Shipway, E. Katz, I. Willner, *Nanoparticle arrays on surfaces for electronic, optical, and sensor applications*, *ChemPhysChem*, 1 (2000) 18–52.
- [31] L.L. Henry, Q. Yang, W.C. Chiang, P. Holody, R. Loloee, W.P. Pratt, J. Bass, *Perpendicular interface resistances of sputtered Ag/Cu, Ag/Au, and Au/Cu multilayers*, *Physical Review B*, 54 (1996) 12336–12341.
- [32] C.S. Kealley, M.B. Cortie, A.I. Maarroof, X. Xu, *The versatile colour gamut of coatings of plasmonic metal nanoparticles*, *Physical Chemistry Chemical Physics*, 11 (2009) 5897–5902.
- [33] K.-i. Okazaki, T. Kiyama, K. Hirahara, N. Tanaka, S. Kuwabata, T. Torimoto, *Single-step synthesis of gold-silver alloy nanoparticles in ionic liquids by a sputter deposition technique*, *Chemical Communications* (2008) 691–693.
- [34] P. Sangpour, O. Akhavan, A.Z. Moshfegh, *The effect of Au/Ag ratios on surface composition and optical properties of co-sputtered alloy nanoparticles in Au-Ag:SiO₂ thin films*, *Journal of Alloys and Compounds*, 486 (2009) 22–28.
- [35] J. Siegel, O. Lyutakov, V. Rybka, Z. Kolska, V. Svorcik, *Properties of gold nanostructures sputtered on glass*, *Nanoscale Research Letters*, 6 (2011).
- [36] I. Stokroos, D. Kalicharan, J.J. van der Want, W.L. Jongebloed, *A comparative study of thin coatings of Au/Pd, Pt and Cr produced by magnetron sputtering for FE-SEM*, *Journal of Microscopy*, 189 (1998) 79–89.
- [37] D. Barreca, A. Gasparotto, C. Maragno, E. Tondello, S. Gialanella, *Structure and optical properties of silica-supported Ag-Au nanoparticles*, *Journal of Nanoscience and Nanotechnology*, 7 (2007) 2480–2486.
- [38] C.M. Müller, R. Spolenak, *Microstructure evolution during dewetting in thin Au films*, *Acta Materialia*, 58 (2010) 6035–6045.
- [39] T. Karakouz, D. Holder, M. Goomanovsky, A. Vaskevich, I. Rubinstein, *Morphology and refractive index sensitivity of gold island films*, *Chemistry of Materials*, 21 (2009) 5875–5885.
- [40] T. Karakouz, A.B. Tesler, T. Sannomiya, Y. Feldman, A. Vaskevich, I. Rubinstein, *Mechanism of morphology transformation during annealing of nanostructured gold films on glass*, *Physical Chemistry Chemical Physics*, 15 (2013) 4656–4665.
- [41] A.B. Tesler, B.M. Maoz, Y. Feldman, A. Vaskevich, I. Rubinstein, *Solid-state thermal dewetting of just-percolated gold films evaporated on glass: Development of the morphology and optical properties*, *The Journal of Physical Chemistry C*, 117 (2013) 11337–11346.
- [42] D. Wang, P. Schaaf, *Nanoporous gold nanoparticles*, *Journal of Materials Chemistry*, 22 (2012) 5344–5348.

- [43] D. Wang, P. Schaaf, *Ni–Au bi-metallic nanoparticles formed via dewetting*, *Materials Letters*, 70 (2012) 30–33.
- [44] A.V. Kabashin, M. Meunier, *Synthesis of colloidal nanoparticles during femtosecond laser ablation of gold in water*, *Journal of Applied Physics*, 94 (2003) 7941–7943.
- [45] F. Mafuné, J.-y. Kohno, Y. Takeda, T. Kondow, H. Sawabe, *Formation and size control of silver nanoparticles by laser ablation in aqueous solution*, *The Journal of Physical Chemistry B*, 104 (2000) 9111–9117.
- [46] F. Mafuné, J.-y. Kohno, Y. Takeda, T. Kondow, H. Sawabe, *Formation of gold nanoparticles by laser ablation in aqueous solution of surfactant*, *The Journal of Physical Chemistry B*, 105 (2001) 5114–5120.
- [47] S.I. Dolgaev, A.V. Simakin, V.V. Voronov, G.A. Shafeev, F. Bozon-Verduraz, *Nanoparticles produced by laser ablation of solids in liquid environment*, *Applied Surface Science*, 186 (2002) 546–551.
- [48] T. Tsuji, T. Iryo, N. Watanabe, M. Tsuji, *Preparation of silver nanoparticles by laser ablation in solution: Influence of laser wavelength on particle size*, *Applied Surface Science*, 202 (2002) 80–85.
- [49] W. de Heer, *The physics of simple metal clusters: Experimental aspects and simple models*, *Reviews of Modern Physics*, 65 (1993) 611–676.
- [50] A.-L. Thomann, J.P. Rozenbaum, P. Brault, C. Andreazza-Vignolle, P. Andreazza, *Pd nanoclusters grown by plasma sputtering deposition on amorphous substrates*, *Applied Surface Science*, 158 (2000) 172–183.
- [51] A.L. Thomann, J.P. Salvétat, Y. Breton, C. Andreazza-Vignolle, P. Brault, *Thermal stability of metal nanoclusters formed by low-pressure plasma sputtering*, *Thin Solid Films*, 428 (2003) 242–247.
- [52] P. Brault, A.-L. Thomann, C. Andreazza-Vignolle, *Percolative growth of palladium ultrathin films deposited by plasma sputtering*, *Surface Science*, 406 (1998) L597-L602.
- [53] X. Zhang, X.-H. Song, D.-L. Zhang, *Thickness dependence of grain size and surface roughness for dc magnetron sputtered Au films*, *Chinese Physics B*, 19 (2010) 86802.
- [54] M.W. Thompson, II, *The energy spectrum of ejected atoms during the high energy sputtering of gold*, *Philosophical Magazine*, 18 (1968) 377–414.
- [55] H.-G. Severin, *Sputtern*, *Physik in unserer Zeit*, 17 (1986) 71–79.
- [56] P. Sigmund, *Theory of sputtering. I. Sputtering yield of amorphous and polycrystalline targets*, *Physical Review*, 184 (1969) 383–416.
- [57] K. Wasa, S. Hayakawa, *Handbook of sputter deposition technology: Principles, technology, and applications*, Noyes Publications, Park Ridge, N.J., U.S.A., 1992.

- [58] P.M. Martin (Ed.), *Handbook of deposition technologies for films and coatings: Science, applications and technology*, 3rd ed., Elsevier, Amsterdam, 2010.
- [59] J.A. Thornton, *Influence of substrate temperature and deposition rate on structure of thick sputtered Cu coatings*, *Journal of Vacuum Science and Technology*, 12 (1975) 830–835.
- [60] J.A. Thornton, *The microstructure of sputter-deposited coatings*, *Journal of Vacuum Science and Technology*, 4 (1986) 3059–3065.
- [61] J.A. Thornton, *High rate thick film growth*, *Annual Review of Materials Science*, 7 (1977) 239–260.
- [62] J.A. Thornton, *Influence of apparatus geometry and deposition conditions on the structure and topography of thick sputtered coatings*, *Journal of Vacuum Science and Technology*, 11 (1974) 666–670.
- [63] D.L. Everitt, W.J. Miller, N.L. Abbott, X.D. Zhu, *Evolution of a preferred orientation of polycrystalline grains in obliquely deposited gold films on an amorphous substrate*, *Physical Review B*, 62 (2000) R4833-R4836.
- [64] F. Parmigiani, G. Samoggia, G.P. Ferraris, *Optical properties of sputtered gold clusters*, *Journal of Applied Physics*, 57 (1985) 2524–2528.
- [65] D. Kim, A.L. Giermann, C.V. Thompson, *Solid-state dewetting of patterned thin films*, *Applied Physics Letters*, 95 (2009) 251903.
- [66] D. Wang, P. Schaaf, *Two-dimensional nanoparticle arrays formed by dewetting of thin gold films deposited on pre-patterned substrates*, *Journal of Materials Science: Materials in Electronics*, 22 (2011) 1067–1070.
- [67] S. Henley, J. Carey, S. Silva, *Pulsed-laser-induced nanoscale island formation in thin metal-oxide films*, *Physical Review B*, 72 (2005) 195408.
- [68] H. Krishna, R. Sachan, J. Strader, C. Favazza, M. Khenner, R. Kalyanaraman, *Thickness-dependent spontaneous dewetting morphology of ultrathin Ag films*, *Nanotechnology*, 21 (2010) 155601.
- [69] J. Trice, D. Thomas, C. Favazza, R. Sureshkumar, R. Kalyanaraman, *Pulsed-laser-induced dewetting in nanoscopic metal films: Theory and experiments*, *Physical Review B*, 75 (2007) 235439.
- [70] X. Hu, D.G. Cahill, R.S. Averback, *Burrowing of Pt nanoparticles into SiO₂ during ion-beam irradiation*, *Journal of Applied Physics*, 92 (2002) 3995–4000.
- [71] X. Hu, D.G. Cahill, R.S. Averback, R.C. Birtcher, *In situ transmission electron microscopy study of irradiation induced dewetting of ultra thin Pt films*, *Journal of Applied Physics*, 93 (2003) 165–169.
- [72] Y. Kojima, T. Kato, *Nanoparticle formation in Au thin films by electron-beam-induced dewetting*, *Nanotechnology*, 19 (2008) 255605.

- [73] D. Wang, R. Ji, P. Schaaf, *Formation of precise 2D Au particle arrays via thermally induced dewetting on pre-patterned substrates*, Beilstein Journal of Nanotechnology, 2 (2011) 318–326.
- [74] G. Reiter, *Dewetting of thin polymer films*, Physical Review Letters, 68 (1992) 75–78.
- [75] G. Reiter, *Unstable thin polymer films: Rupture and dewetting processes*, Langmuir, 9 (1993) 1344–1351.
- [76] A. Sharma, G. Reiter, *Instability of thin polymer films on coated substrates: Rupture, dewetting, and drop formation*, Journal of Colloid and Interface Science, 178 (1996) 383–399.
- [77] C. Redon, F. Brochard-Wyart, F. Rondelez, *Dynamics of dewetting*, Physical Review Letters, 66 (1991) 715–718.
- [78] J. Bischof, D. Scherer, S. Herminghaus, P. Leiderer, *Dewetting modes of thin metallic films: Nucleation of holes and spinodal dewetting*, Physical Review Letters, 77 (1996) 1536–1539.
- [79] W.D. Michalak, J.B. Miller, C. Yolcu, A.J. Gellman, *Fabrication of metallic nanoparticles by spinodal dewetting of thin films: A high-throughput approach*, Thin Solid Films, 522 (2012) 473–479.
- [80] R. Xie, A. Karim, J. Douglas, C. Han, R. Weiss, *Spinodal dewetting of thin polymer films*, Physical Review Letters, 81 (1998) 1251–1254.
- [81] S. Herminghaus, K. Jacobs, K. Mecke, J. Bischof, A. Fery, M. Ibn-Elhaj, S. Schlagowski, *Spinodal dewetting in liquid crystal and liquid metal films*, Science, 282 (1998) 916–919.
- [82] E. Ruckenstein, R.K. Jain, *Spontaneous rupture of thin liquid films*, Journal of the Chemical Society, Faraday Transactions 2, 70 (1974) 132–147.
- [83] U. Thiele, M. Velarde, K. Neuffer, *Dewetting: Film rupture by nucleation in the spinodal regime*, Physical Review Letters, 87 (2001) 16104.
- [84] M.E. Toimil-Molaes, A.G. Balogh, T.W. Cornelius, R. Neumann, C. Trautmann, *Fragmentation of nanowires driven by Rayleigh instability*, Applied Physics Letters, 85 (2004) 5337–5339.
- [85] S. Karim, M.E. Toimil-Molaes, A.G. Balogh, W. Ensinger, T.W. Cornelius, E.U. Khan, R. Neumann, *Morphological evolution of Au nanowires controlled by Rayleigh instability*, Nanotechnology, 17 (2006) 5954–5959.
- [86] E. Jiran, C.V. Thompson, *Capillary instabilities in thin-films*, Journal of Electronic Materials, 19 (1990) 1153–1160.
- [87] E. Jiran, C.V. Thompson, *Capillary instabilities in thin, continuous films*, Thin Solid Films, 208 (1992) 23–28.
- [88] J.-Y. Kwon, T.-S. Yoon, K.-B. Kim, S.-H. Min, *Comparison of the agglomeration behavior of Au and Cu films sputter deposited on silicon dioxide*, Journal of Applied Physics, 93 (2003) 3270–3278.
- [89] M. Bowker, *Surface science: The going rate for catalysts*, Nature Materials, 1 (2002) 205–206.

- [90] M. Bechelany, X. Maeder, J. Riesterer, J. Hankache, D. Lerose, S. Christiansen, J. Michler, L. Philippe, *Synthesis Mechanisms of organized gold Nanoparticles: Influence of annealing temperature and atmosphere*, *Crystal Growth & Design*, 10 (2010) 587–596.
- [91] I. Beszeda, E.G. Gontier-Moya, A.W. Imre, *Surface Ostwald-ripening and evaporation of gold beaded films on sapphire*, *Applied Physics A: Materials Science and Processing*, 81 (2005) 673–677.
- [92] A. Howard, C. Mitchell, R. Egdell, *Real time STM observation of Ostwald ripening of Pd nanoparticles on TiO₂(110) at elevated temperature*, *Surface Science*, 515 (2002) L504.
- [93] A. Courty, A.-I. Henry, N. Goubet, M.-P. Pileni, *Large triangular single crystals formed by mild annealing of self-organized silver nanocrystals*, *Nature Materials*, 6 (2007) 900–907.
- [94] M. José-Yacamán, C. Gutierrez-Wing, M. Miki, D.-Q. Yang, K.N. Piyakis, E. Sacher, *Surface diffusion and coalescence of mobile metal nanoparticles*, *The Journal of Physical Chemistry B*, 109 (2005) 9703–9711.
- [95] R. Theissmann, M. Fendrich, R. Zinetullin, G. Guenther, G. Schierning, D. Wolf, *Crystallographic reorientation and nanoparticle coalescence*, *Physical Review B*, 78 (2008) 205413.
- [96] A.K. Datye, Q. Xu, K.C. Kharas, J.M. McCarty, *Particle size distributions in heterogeneous catalysts: What do they tell us about the sintering mechanism?*, *Catalysis Today*, 111 (2006) 59–67.
- [97] O. Malyi, L. Klinger, D.J. Srolovitz, E. Rabkin, *Size and shape evolution of faceted bicrystal nanoparticles of gold on sapphire*, *Acta Materialia*, 59 (2011) 2872–2881.
- [98] C.M. Müller, Mornaghini, Flavio Carlo Filippo, R. Spolenak, *Ordered arrays of faceted gold nanoparticles obtained by dewetting and nanosphere lithography*, *Nanotechnology*, 19 (2008) 485306.
- [99] I.U. Vakarelski, R. Maenosono, J.W. Kwek, K. Higashitani, *Thermal modification of layer-by-layer assembled gold nanoparticle films*, *Colloids And Surfaces A*, 340 (2009) 193–198.
- [100] L.D. Marks, *Experimental studies of small particle structures*, *Reports on Progress in Physics*, 57 (1994) 603–649.
- [101] J.C. Heyraud, J.J. Métois, *Equilibrium shape and temperature; Lead on graphite*, *Surface Science*, 128 (1983) 334–342.
- [102] A.S. Barnard, La Curtiss, *Computational nano-morphology: Modeling shape as well as size*, *Reviews on Advanced Materials Science*, 10 (2005) 105–109.
- [103] A.S. Barnard, X.M. Lin, L.A. Curtiss, *Equilibrium morphology of face-centered cubic gold nanoparticles > 3 nm and the shape changes induced by temperature*, *The Journal of Physical Chemistry B*, 109 (2005) 24465–24472.

- [104] W. Winterbottom, *Equilibrium shape of a small particle in contact with a foreign substrate*, Acta Metallurgica, 15 (1967) 303–310.
- [105] L.D. Marks, P.M. Ajayan, *Equilibrium shape of a buoyant particle*, Journal of Materials Research, 5 (1990) 1496–1501.
- [106] L.D. Marks, *Modified Wulff constructions for twinned particles*, Journal of Crystal Growth, 61 (1983) 556–566.
- [107] E. Ringe, R.P. Van Duyne, L.D. Marks, *Kinetic and thermodynamic modified Wulff constructions for twinned nanoparticles*, The Journal of Physical Chemistry C, 117 (2013) 15859–15870.
- [108] L.D. Marks, *Surface structure and energetics of multiply twinned particles*, Philosophical Magazine A, 49 (1984) 81–93.
- [109] C. Rottman, M. Wortis, *Statistical mechanics of equilibrium crystal shapes: Interfacial phase diagrams and phase transitions*, Physics Reports, 103 (1984) 59–79.
- [110] H. Sadan, W.D. Kaplan, *Au–Sapphire (0001) solid–solid interfacial energy*, Journal of Materials Science, 41 (2006) 5099–5107.
- [111] C.F. Bohren, D.R. Huffman, *Absorption and scattering of light by small particles*, Wiley, New York, 1983.
- [112] M.A. Garcia, *Surface plasmons in metallic nanoparticles: Fundamentals and applications*, Journal of Physics D, 44 (2011) 283001.
- [113] K.L. Kelly, E. Coronado, L.L. Zhao, G.C. Schatz, *The optical properties of metal nanoparticles: The influence of size, shape, and dielectric environment*, Journal of Physical Chemistry B, 107 (2003) 668–677.
- [114] U. Kreibig, M. Vollmer, *Optical properties of metal clusters*, 1st ed., Springer, Berlin, Heidelberg, 1995.
- [115] F. Aussenegg, H. Ditlbacher, *Plasmonen als Lichttransporter: Nanooptik*, Physik in unserer Zeit, 37 (2006) 220–226.
- [116] G. Mie, *Beiträge zur Optik trüber Medien, speziell kolloidaler Metallösungen*, Annalen der Physik (Berlin), 330 (1908) 377–445.
- [117] U. Kreibig, *Hundert Jahre Mie-Theorie. Optische Eigenschaften von Nanopartikeln*, Physik in unserer Zeit, 39 (2008) 281–287.
- [118] U. Kreibig, P. Zacharias, *Surface plasma resonances in small spherical silver and gold particles*, Zeitschrift für Physik, 231 (1970) 128–143.
- [119] M.M. Miller, A.A. Lazarides, *Sensitivity of metal nanoparticle surface plasmon resonance to the dielectric environment*, The Journal of Physical Chemistry B, 109 (2005) 21556–21565.

- [120] Y. Ohko, T. Tatsuma, T. Fujii, K. Naoi, C. Niwa, Y. Kubota, A. Fujishima, *Multicolour photochromism of TiO₂ films loaded with silver nanoparticles*, *Nature Materials*, 2 (2002) 29–31.
- [121] T. Wang, C. Lee, L.D. Schmidt, *Shape and orientation of supported Pt particles*, *Surface Science*, 163 (1985) 181–197.
- [122] J. Matsuoka, M. Sumita, M. Numaguchi, S. Yoshida, N. Soga, *Fracture-induced change in the internal energy of silicate glasses*, *Journal of Non-Crystalline Solids*, 349 (2004) 185–188.
- [123] G. Bayer, H. Wiedemann, *Formation, dissociation and expansion behavior of platinum group metal oxides (PdO, RuO₂, IrO₂)*, *Thermochimica Acta*, 11 (1975) 79–88.
- [124] S. Kishore, J. Nelson, J. Adair, P. Eklund, *Hydrogen storage in spherical and platelet palladium nanoparticles*, *Journal of Alloys and Compounds*, 389 (2005) 234–242.
- [125] J. Mizsei, P. Sipilä, V. Lantto, *Structural studies of sputtered noble metal catalysts on oxide surfaces*, *Sensors and Actuators B: Chemical*, 47 (1998) 139–144.
- [126] C. Bocker, M. Kracker, C. Rüssel, *Replica extraction method on nanostructured gold coatings and orientation determination combining SEM and TEM techniques*, *Microscopy and Microanalysis*, (2014), Article in press, DOI: <http://dx.doi.org/10.1017/S1431927614013336>.
- [127] T. Jensen, L. Kelly, A. Lazarides, G.C. Schatz, *Electrodynamics of noble metal nanoparticles and nanoparticle clusters*, *Journal of Cluster Science*, 10 (1999) 295–317.
- [128] I. Doron-Mor, Z. Barkay, N. Filip-Granit, A. Vaskevich, I. Rubinstein, *Ultrathin gold island films on silanized glass. Morphology and optical properties*, *Chemistry of Materials*, 16 (2004) 3476–3483.
- [129] A.I. Maarouf, M.B. Cortie, G.B. Smith, *Optical properties of mesoporous gold films*, *Journal of Optics A: Pure and Applied Optics*, 7 (2005) 303–309.
- [130] K.J. Major, C. De, S.O. Obare, *Recent advances in the synthesis of plasmonic bimetallic nanoparticles*, *Plasmonics*, 4 (2009) 61–78.
- [131] X.D. Xu, M. Stevens, M.B. Cortie, *In situ precipitation of gold nanoparticles onto glass for potential architectural applications*, *Chemistry of Materials*, 16 (2004) 2259–2266.
- [132] C. Langhammer, Z. Yuan, I. Zorić, B. Kasemo, *Plasmonic properties of supported Pt and Pd nanostructures*, *Nano Letters*, 6 (2006) 833–838.
- [133] C. Langhammer, B. Kasemo, I. Zorić, *Absorption and scattering of light by Pt, Pd, Ag, and Au nanodisks: Absolute cross sections and branching ratios*, *The Journal of Chemical Physics*, 126 (2007) 194702.
- [134] C. Langhammer, I. Zorić, B. Kasemo, B.M. Clemens, *Hydrogen storage in Pd nanodisks characterized with a novel nanoplasmonic sensing scheme*, *Nano Letters*, 7 (2007) 3122–3127.

- [135] M.A. Poyli, V.M. Silkin, I.P. Chernov, P.M. Echenique, R.D. Muiño, J. Aizpurua, *Multiscale theoretical modeling of plasmonic sensing of hydrogen uptake in palladium nanodisks*, The Journal of Physical Chemistry Letters, 3 (2012) 2556–2561.
- [136] H. Fredriksson, Y. Alaverdyan, A. Dmitriev, C. Langhammer, D.S. Sutherland, M. Zäch, B. Kasemo, *Hole–Mask colloidal lithography*, Advanced Materials, 19 (2007) 4297–4302.
- [137] J. Edelmann, C. Worsch, A. Schubert, C. Rüssel, *Micro structuring of inorganic glass by hot embossing of coated glass wafers*, Microsystem Technologies, 16 (2010) 553–560.
- [138] C. Worsch, J. Edelmann, C. Rüssel, A. Schubert, *Determination of adhesive forces and sticking temperature of coated glasses for the hot-embossing-process*, Microsystem Technologies, 17 (2011) 1401–1406.
- [139] T. Okamoto, I. Yamaguchi, T. Kobayashi, *Local plasmon sensor with gold colloid monolayers deposited upon glass substrates*, Optics Letters, 25 (2000) 372–374.
- [140] P. Laven, *Simulation of rainbows, coronas, and glories by use of Mie theory*, Applied Optics, 42 (2003) 436–444.
- [141] B.T. Draine, P.J. Flatau, *Discrete-dipole approximation for scattering calculations*, Journal of the Optical Society of America A, 11 (1994) 1491–1499.
- [142] B.T. Draine, P.J. Flatau, *Discrete-dipole approximation for periodic targets: theory and tests*, Journal of the Optical Society of America A, 25 (2008) 2693–2703.
- [143] P. Ajayan, L.D. Marks, *Experimental evidence for quasimelting in small particles*, Physical Review Letters, 63 (1989) 279–282.
- [144] J.-H. Shim, B.-J. Lee, Y.W. Cho, *Thermal stability of unsupported gold nanoparticle: A molecular dynamics study*, Surface Science, 512 (2002) 262–268.
- [145] A.L. Giermann, C.V. Thompson, *Requirements for graphoepitaxial alignment through solid-state dewetting of Au films*, Journal of Applied Physics, 109 (2011) 83520.
- [146] M. Kirkham, X. Wang, Z.L. Wang, R.L. Snyder, *Solid Au nanoparticles as a catalyst for growing aligned ZnO nanowires: A new understanding of the vapour–liquid–solid process*, Nanotechnology, 18 (2007) 365304.
- [147] J.J. Metois, Spiller, G. D. T., J.A. Venables, *Lead on graphite: Equilibrium shape, crystal growth, melting and the early stages of oxidation*, Philosophical Magazine A, 46 (1982) 1015–1022.
- [148] L.C. Campos, S.H. Dalal, D.L. Baptista, R. Magalhães-Paniago, A.S. Ferlauto, W.I. Milne, L.O. Ladeira, R.G. Lacerda, *Determination of the epitaxial growth of zinc oxide nanowires on sapphire by grazing incidence synchrotron x-ray diffraction*, Applied Physics Letters, 90 (2007) 181929.

- [149] Y.W. Heo, V. Varadarajan, M. Kaufman, K. Kim, D.P. Norton, F. Ren, P.H. Fleming, *Site-specific growth of ZnO nanorods using catalysis-driven molecular-beam epitaxy*, Applied Physics Letters, 81 (2002) 3046–3048.
- [150] B. Kämpken, V. Wulf, N. Auner, M. Winhold, M. Huth, D. Rhinow, A. Terfort, *Directed deposition of silicon nanowires using neopentasilane as precursor and gold as catalyst*, Beilstein Journal of Nanotechnology, 3 (2012) 535–545.
- [151] K. Nagashima, T. Yanagida, H. Tanaka, T. Kawai, *Epitaxial growth of MgO nanowires by pulsed laser deposition*, Journal of Applied Physics, 101 (2007) 124304.
- [152] H.T. Ng, J. Li, M.K. Smith, P. Nguyen, A. Cassell, J. Han, M. Meyyappan, *Growth of epitaxial nanowires at the junctions of nanowalls*, Science, 300 (2003) 1249.
- [153] A. Vomiero, M. Ferroni, E. Comini, G. Faglia, G. Sberveglieri, *Preparation of radial and longitudinal nanosized heterostructures of In_2O_3 and SnO_2* , Nano Letters, 7 (2007) 3553–3558.
- [154] Q. Wan, M. Wei, D. Zhi, J.L. MacManus-Driscoll, M.G. Blamire, *Epitaxial growth of vertically aligned and branched single-crystalline Tin-doped Indium oxide nanowire Arrays*, Advanced Materials, 18 (2006) 234–238.
- [155] Z. Zhu, T.L. Chen, Y. Gu, J. Warren, R.M. Osgood, *Zinc oxide nanowires grown by vapor-phase transport using selected metal catalysts: A comparative study*, Chemistry of Materials, 17 (2005) 4227–4234.
- [156] E. Comini, C. Baratto, G. Faglia, M. Ferroni, A. Vomiero, G. Sberveglieri, *Quasi-one dimensional metal oxide semiconductors: Preparation, characterization and application as chemical sensors*, Progress in Materials Science, 54 (2009) 1–67.
- [157] R.S. Wagner, W.C. Ellis, *Vapor-liquid-solid mechanism of single crystal growth*, Applied Physics Letters, 4 (1964) 89–90.
- [158] D.P. Field, *Recent advances in the application of orientation imaging*, Ultramicroscopy, 67 (1997) 1–9.
- [159] W.M. Haynes, D.R. Lide, *CRC handbook of chemistry and physics: A ready-reference book of chemical and physical data*, 91st ed., CRC Press, Boca Raton, London, New York, 2010.
- [160] J.S. Hwang, D.Y. Noh, *Rounding of Au nano-crystals supported on sapphire at high temperatures*, Journal of the Korean Physical Society, 62 (2013) 6–9.
- [161] O.H. Nielsen, J.P. Sethna, P. Stoltze, K.W. Jacobsen, J.K. Nørskov, *Melting a copper cluster: Critical-droplet theory*, Europhysics Letters, 26 (1994) 51–56.
- [162] W. Wisniewski, S. Berndt, M. Müller, C. Rüssel, *Stress induced texture formation in surface crystallized SiO_2 glass*, CrystEngComm, 15 (2013) 2392–2400.
- [163] S.C. Su, J.N. Carstens, A.T. Bell, *A Study of the dynamics of Pd oxidation and PdO reduction by H_2 and CH_4* , Journal of Catalysis, 176 (1998) 125–135.

9. Figures

Figure 1 Wulff – construction, to determine the equilibrium shape of small single crystal [109] 11

Figure 2 Modified Wulff – construction for supported nanoparticles [110] 11

Figure 3 Illustration of small metal particle by light irradiation induced electron movement (plasmon oscillation) 13

Figure 4 Resulting polarization of the metal particle by accumulation of electrons (negative pole) and the remaining lattice of ionic cores (positive pole)..... 13

10. Poster

C. Worsch, M. Kracker, C. Rüssel, „**Temperaturinduzierte Entnetzung dünner Goldschichten zur Herstellung nanoskaliger Partikel**“, Thüringer Werkstofftag, Jena (2011)

M. Kracker, C. Worsch, F. Döhler C. Rüssel, „**Optische Eigenschaften metallischer Nanopartikel auf Gläsern**“, Thüringer Werkstofftag, Weimar (2012)

M. Kracker, C. Worsch, W. Seeber, C. Rüssel, „**Palladiumnanopartikel – Herstellung und optische Eigenschaften unter Wasserstoffatmosphäre**“, Thüringer Werkstofftag, (Ilmenau 2013)

M. Kracker, C. Worsch, W. Seeber, C. Rüssel, „**Optische Wasserstoffsensoren aus modifizierten Palladiumschichten und Palladium-Nanopartikeln**“, Thüringer Werkstofftag, (Jena 2014)

M. Kracker, C. Worsch, W. Seeber, C. Rüssel, „**Plasmonic resonance of dewetted metallic films on glass: applicability as sensors based on glass Substrates**“, 88th Annual Meeting of German Society of Glass Technology (DGG) and the Glass & Optical Materials Division Annual Meeting (ACerS GOMD) Aachen (2014)

11. Presentations

M. Kracker, C. Worsch, C. Rüssel, **„Optische Eigenschaften Legierter Nanopartikel“**
Otto-Schott-Institut, Jena University (2011)

M. Kracker, C. Worsch, C. Rüssel, **„Funktionelle Sensorschichten aus Palladium“**,
Otto-Schott-Institut, Jena University (2012)

M. Kracker, C. Worsch, W. Seeber, C. Rüssel, **„Funktionalisierung von Glasoberflächen mittels metallischer Nanopartikel“**, Technical Committee 1 “Physics and Chemistry of Glasses” of the German Glass Society (DGG), Clausthal University (2012)

M. Kracker, C. Worsch, C. Rüssel, **„Optische Charakterisierung von Palladium Nanopartikeln“**
Otto-Schott-Institut, Jena University (2012)

M. Kracker, C. Rüssel, **„Einfluss der Oberflächenmorphologie von Palladiumschichten auf die optische Wasserstoffsensitivität“**
Otto-Schott-Institut, Jena University (2013)

M. Kracker, C. Rüssel, **„Beeinflussung der Plasmonenresonanz durch Legierungsbildung in Nanopartikeln“**
Otto-Schott-Institut, Jena University (2013)

M. Kracker, C. Worsch, W. Seeber, C. Rüssel, **„Metallische Nanopartikel auf Glasoberflächen für sensorische Anwendungen“** Technical Committee 1 “Physics and Chemistry of Glasses” of the German Glass Society (DGG), Halle University (2014)

M. Kracker, C. Worsch, W. Seeber, C. Rüssel, **„Dewetting of Metallic Films on Glass for Optical Sensing“** Materials Science Engineering Congress (MSE), Darmstadt (2014)

12. Danksagung

Eine wissenschaftliche Arbeit ist nie das Werk einer einzelnen Person. Somit ist es an der Zeit mich bei denjenigen gebührend zu bedanken, die mich auf dem Weg zu dieser Arbeit begleitet haben. Zu besonderem Dank bin ich meinem Professor verpflichtet. Ohne Herrn Professor Rüssels wertvollen akademischen Rat, die stetige Betreuung und die gegebenen Denkanstöße wäre diese Arbeit nicht möglich gewesen. Weiter bin ich Herrn Dr. Wolfgang Seeber zu großem Dank verpflichtet für die Ermöglichung dieser Arbeit und das diesbezüglich mir entgegengebrachte Vertrauen sowie für die Übernahme des Zweitgutachtens.

Dank gebührt weiterhin Thomas Kittel für die AFM-Untersuchungen und der stetigen Hilfestellung in Ofen, Steuer- und Temperaturmesstechnik sowie Dr. Matthias Müller für die XRD-Messungen und die Einführungen in die optische Spektroskopie, Dr. Wolfgang Wisniewski für EBSD-Untersuchungen und die vielen fruchtbaren Diskussionen, Dr. Christian Bocker und Claudia Siedler für zahlreichen Elektronenmikroskopischen Analysen, Christian Zeidler und Dietmar Güttler für alle Belange rund um das Thema Elektrotechnik, Gabriele Möller für die zahlreichen glastechnischen Probenpräparationen, Dr. Matthias Carl und Corinna Seelheim für die andauernde Unterstützung bei der Projektverwaltung und Bettina Hartmann für die unzähligen optischen Spektren. Weiter bedanke ich mich bei Steffi Ebbinghaus und Angelika Hacker.

Spezieller Dank gebührt auch Lutz Preißer und Rainer Weiß für die Herstellung vielfältigster Probenhalter und Sonderbauteilen für die mannigfaltigsten Anwendungen sowie die stetige Unterstützung in allen technologischen Belangen. Ich danke Frau Prof. Stachel für die stetige Unterstützung während der Studienzeit. Natürlich gebührt den Koautoren Dr. Jan Edelmann und Prof. Andreas Schubert Dank für die anregenden Diskussionen und die Herstellung der optischen Mikrofluidikstrukturen. Besonderen Dank verdient Dr. Christian Worsch für die Betreuung meiner Diplomarbeit und die darauf folgende wichtige Unterstützung und die kreativen Diskussionen in weiten Teilen der Promotion. Auch danke ich Stefan Kuhn für die so vielen hilfreichen Diskussionen. Ich danke der Deutschen Forschungsgemeinschaft (DFG) für die finanzielle Unterstützung in den letzten Jahren. Ich danke herzlich allen Freunden sowie Kollegen und Kolleginnen des Otto-Schott-Institutes für die angenehme Zusammenarbeit.

Ein liebevoller Dank richtet sich an meine Partnerin Susanne für die moralisch Unterstützung und die herzliche Fürsorge in dieser so spannenden Lebensphase. Zum Schluss danke ich meinen Eltern und meiner ganzen Familie für die unglaubliche Unterstützung die mir während des Studiums und der Promotion zuteil wurde und dafür, dass sie den Glauben an mich nie verloren haben.

Danke

Michael Kracker

13. Lebenslauf / Curriculum Vitae

Dipl.-Ing. Michael Kracker
Laasener Str. 18
07545 Gera

E-Mail: Kracker.Michael@googlemail.com
Geboren am 14. April 1984 in Sonneberg

Ausbildung und Studium:

Seit April 2011	Doktorand am Otto-Schott-Institut der Friedrich-Schiller-Universität Jena
April 2011	Diplom-Ingenieur an der Friedrich-Schiller-Universität Jena
Juli 2007	Weiterbildung „Zerstörungsfreie Prüfung, Grundlagenkenntnisse zur Stufe 3“ Modul 1 nach DIN EN 473 der Deutsche Gesellschaft für Zerstörungsfreie Werkstoffprüfung e.V. (Berlin-Adlershof)
2004 bis 2011	Studium der Werkstoffwissenschaft an der Friedrich-Schiller-Universität Jena
März 2011	Diplomarbeit: „Temperaturinduzierte Entnetzung dünner Goldschichten zur Herstellung nanoskaliger Partikel“ Prof. Christian Rüssel Dr. Christian Worsch
April 2009	Studienarbeit: „Untersuchung zum Beizverhalten der Magnesiumlegierung AZ91 in Schwefel und Phosphorsäurehaltigen Beizen“ Prof. Markus Rettenmayr (Friedrich-Schiller-Universität Jena) Dipl.-Ing. Jürgen Schmidt (Innovent – Technologieentwicklung Jena)
2003 bis 2004	Berufsausbildung zum Elektrotechnischen Assistenten an der Höheren Berufsfachschule der Staatlichen Berufsbildende Schule Sonneberg
2000 bis 2003	Abitur am Staatlichen berufsbildenden Gymnasium der Staatlichen Berufsbildende Schule Sonneberg
1994 bis 2000	Mittlere Reife an der Staatlichen Regelschule Sonneberg-West
1990 bis 1994	Grundschule Mürschnitz

Berufliche Tätigkeiten:

Seit April 2011

Wissenschaftlicher Mitarbeiter am Otto-Schott-Institut der Friedrich-Schiller-Universität Jena

September 2010 bis September 2012

Kurierfahrer für die Saale Apotheke e.K. Jena

März bis April 2007

Praktikant bei Innovent Technologie-Entwicklung Jena

Juli bis September 2008

Zusteller der Deutschen Post AG am Zustellstützpunkt Sonneberg

September 2007

März 2004

Juli bis August 2003

Juli 2002

August bis September 2006

Wehrdienst, geleistet in Abschnitten

August bis September 2005

April bis September 2004

Sprachkenntnisse

Deutsch, Englisch

EDV Kenntnisse

Origin Ver. 6 bis 9, Sigma Plot, Image J, Corel, Inkscape, Literaturdatenbanken Citavi und Endnote, Photoshop, div. Simulations Software DDSCAT, Mie-Plot, sicherer Umgang mit Office-Paket und Windows von Microsoft, sowie diverse gerätespezifische Software

Selbstständigkeitserklärung

Ich erkläre, dass ich die vorliegende Arbeit selbständig und unter Verwendung der angegebenen Hilfsmittel, persönlichen Mitteilungen und Quellen angefertigt habe.

Jena, 3. Juli 2014

Michael Kracker

14. Appendix A:

M. Kracker C. Worsch, W. Seeber, C. Rüssel

Corrigendum to

“Optical hydrogen sensing with modified Pd-layers: A kinetic study of roughened layers and dewetted nanoparticle films”

[Sensors and Actuators B: Chemical, 197 (2014) 95–103]

DOI: <http://dx.doi.org/10.1016/j.snb.2014.06.039>

Optical hydrogen sensing with modified Pd-layers: A kinetic study of roughened layers and dewetted nanoparticle films				
Beteiligt an				
	Michael Kracker	Dr. Christian Worsch	Dr. Wolfgang Seeber	Prof. Christian Rüssel
Konzeption des Forschungsansatzes	X		X	X
Planung der Untersuchung	X			
Datenerhebung	X			
Datenanalyse und Interpretation	X	X		
Schreiben des Manuskripts	X	X	X	X
Vorschlag Anrechnung Publikationsäquivalente	1,0			
Erklärung:				
Bedingt durch Formatierungsfehler wurde zur Verbesserung der Lesbarkeit sowie Verhinderung von Missverständnissen, eine korrigierte Version von Tabelle 2 als „Corrigendum“ veröffentlicht.				



Corrigendum

Corrigendum to “Optical hydrogen sensing with modified Pd-layers:
A kinetic study of roughened layers and dewetted nanoparticle films”
[Sens. Actuators B: Chem. 197 (2014) 95–103]



Michael Kracker*, Christian Worsch, Wolfgang Seeber, Christian Rüssel

Otto-Schott-Institute, Jena University, Fraunhoferstr. 6, 07743 Jena, Germany

The authors regret that Table 2 contains some minor errors. This corrigendum is meant to improve the understanding and reduce the probability of misleading interpretations. Please find the correct table below.

Table 2

Sample	d_{on} (ms)	s_{on} (ms)	$\Delta signal_{on}$ (V)	d_{off} (ms)	$s_{off 1}$ (ms)	$s_{off 2}$ (ms)	$s_{off 3}$ (ms)	$\Delta signal_{off 1}$ (V)	$\Delta signal_{off 2}$ (V)	$\Delta signal_{off 3}$ (V)
	Hydrogen uptake			Hydrogen discharge						
Pd 5 Freshly sputtered	<250	<250	0.028	19,651	24,142					
Pd 8 Freshly sputtered	<200	<200	0.021	17,322	19,650			n/a		
Pd 14 Freshly sputtered	<250	<250	0.021	22,344	10,479					
Pd 18 Freshly sputtered	<250	<250	0.013	23,176	8604					
Pd 5 900 °C Dewetted and purged	178 (interpolated)	189 (interpolated)	−0.101 (cycle 1) −0.103 (cycle 5)	830	2478 2679	28,067 32,300	15,707 24,777	0.011 0.011	0.009 0.009	0.083 0.082
Pd 8 700 °C Oxidized and purged	<200	<200	0.185 (cycle 1) 0.200 (cycle 5)	<250	2350 2059	17,066 17,816	7380 8327	−0.019 −0.016	−0.014 −0.015	−0.148 −0.158
Pd 14 700 °C Oxidized and purged	<250	<250	0.207 (cycle 1) 0.222 (cycle 5)	<250	1864 1597	16,995 18,388	5986 8347	−0.017 −0.016	−0.015 −0.018	−0.172 −0.182
Pd 14 700 °C Oxidized and purged, long term	<250	<250	0.221 (cycle 1) 0.239 (cycle 5) 0.246 (cycle 17)	<250–800	2747 2433 2767	23,743 24,785 27,150	6577 11,036 14,636	−0.015 −0.017 −0.018	−0.020 −0.014 −0.018	−0.169 −0.191 −0.200
Pd 18 700 °C Oxidized and purged	<200	<200	0.193 (cycle 1) 0.207 (cycle 5)	<250	2285 1892	17,851 18,669	5538 7339	−0.015 −0.015	−0.016 −0.016	−0.150 −0.165

DOI of original article: <http://dx.doi.org/10.1016/j.snb.2014.02.063>.

* Corresponding author. Tel.: +49 03641 948522; fax: +49 03641 948502.

E-mail address: Michael.Kracker@uni-jena.de (M. Kracker).

<http://dx.doi.org/10.1016/j.snb.2014.06.039>

0925-4005/© 2014 Elsevier B.V. All rights reserved.

15. Appendix B:

M. Kracker, W. Wisniewski, C. Rüssel

Textures of Au, Pt and Pd/PdO Nanoparticles Thermally Dewetted from Thin Metal Layers on Fused Silica

Finally published in

RSC Advances, 4 (2014) 48135 – 48143

DOI: <http://dx.doi.org/10.1039/C4RA07296K>

Textures of Au, Pt and Pd/PdO Nano Particles Thermally Dewetted from Thin Metal Layers on Fused Silica				
Beteiligt an				
	Michael Kracker	Dr. Wolfgang Wisniewski	Prof. Christian Rüssel	
Konzeption des Forschungsansatzes	X		X	
Planung der Untersuchung	X	X		
Datenerhebung	X	X		
Datenanalyse und Interpretation	X	X		
Schreiben des Manuskripts	X	X	X	
Vorschlag Anrechnung Publikationsäquivalente	1,0			
Erklärung:				
Dieser Artikel wurde während des Promotionsverfahrens nach Ablehnung durch das Journal „Small“ zu erneuten Begutachtung bei „RSC Advances“ eingereicht und anschließend Publiziert.				



Cite this: *RSC Adv.*, 2014, 4, 48135

Textures of Au, Pt and Pd/PdO nanoparticles thermally dewetted from thin metal layers on fused silica

Michael Kracker,* Wolfgang Wisniewski and Christian Rüssel

This article presents results concerning the basic dewetting procedure of thin metal films on an amorphous substrate. Thin layers of gold, platinum and palladium are deposited on fused silica glass sheets by sputtering. The 14 to 18 nm thick layers of Au, Pt and Pd are dewetted into nanoparticles (NP) at temperatures from 424 to 1600 °C. The morphology of the resulting NP is characterized using scanning electron microscopy (SEM) while crystallographic analyses are performed using electron backscatter diffraction (EBSD). Multiple textures are described to occur and coexist in NP-layers of the respective materials and a temperature dependence of the texture formation in gold NP is proved. The transformation of Pd to PdO and its effects on the texture is also analyzed. It is shown that the cooling rate has an effect on the texture in the case of gold NP as well as on the physical structure of the Pd/PdO NP. Twinning relationships could be described to occur on all samples.

Received 18th July 2014
Accepted 22nd September 2014

DOI: 10.1039/c4ra07296k

www.rsc.org/advances

Introduction

Metallic nanoparticles (NP) have been extensively studied and are most frequently produced by chemical methods which include adding organic additives to the system.¹⁻⁴ In comparison, the thermal dewetting of metallic layers with a thickness in the nm-range into NP to achieve optically active surfaces is performed less often.

Dewetting allows the production of large, additive free systems and an interaction between the dewetting metal layer and its substrate which in turn allows a self assembling orientation relationship in the form of a crystallographic texture. Dewetting itself may occur far below the melting point of the metal, e.g. as low as 300 °C for gold,^{5,6} and has been performed in a number of systems including gold, platinum and palladium. In this article we discuss particle formation effects, morphologies and crystallographic orientations as well as textures independent of the process temperature and the cooling procedure. We also highlight the importance of phase transitions during particle formation while heating as well as cooling. Because gold does not show any phase transitions during annealing, we use comparably produced palladium NP for these experiments which exhibit a pronounced tendency to oxidize during sample preparation.

The faceting of metallic nano particles has been discussed in detail in ref. 7 where AFM-profiles show a faceted particle to be flat on the upper side. It has also been shown that faceted gold NP on sapphire become rounded with increasing temperatures⁵

which was reported to be accompanied by a loss of the strong 111 texture observed at lower temperatures.⁵ While a large number of publications feature gold NP e.g.⁵⁻¹¹ the literature concerning dewetted NP of Pt and Pd is more manageable.¹²⁻²³

When it comes to literature describing textures and crystallographic orientations, mainly information concerning gold NP on substrates such as single crystals,⁵ oxidized Si-wafers⁸ or glasses^{6,9} was found by the authors. It has been shown that the gold NP are preferably oriented with a {111}-plane parallel to the substrate surface on oxidized Si-wafers⁸ and amorphous glasses^{6,9} indicating this is a self organizing process. If the NP are heated above their melting point on a sapphire substrate, the preferred orientation seems to be lost but the faceted morphology reoccurs if the NP are held at an appropriate temperature for some time.^{10,11} It was also shown that dewetting is possible on inexpensive materials such as soda-lime-silica-glass. Two superimposed textures were described in correlation with the particle size in experiments where the gold layers were covered by a layer of silica before the dewetting process.⁹

It is generally accepted that the driving force of thermal dewetting is the minimization of the surface energy in the three phase system; substrate – metallic NP – furnace atmosphere. However, the self-organization into textured layers with defined preferences of certain crystallographic orientations is not really understood. While it seems logical that the fcc-lattice of gold may prefer orientations where the close-packed {111}-layers arrange themselves parallel to the substrate,^{6,8,9} the loss of such a texture at high temperatures⁵ and the formation of sub-textures where even an obvious relationship to a crystallographic plane is lacking⁹ remains an open question. These effects, however, should be of interest for all research where

Otto-Schott-Institut, Jena University, Fraunhoferstr. 6, 07743 Jena, Germany. E-mail: Michael.Kracker@uni-jena.de; Fax: +49 03641 948502; Tel: +49 03641 948516



dewetted NP are used to induce the growth of layers and nano wires^{24–26} which possibly show a crystallographic relationship to the seeding NP.

As a number of parameters such as substrate chemistry, substrate microstructure, cooling rates or the atmosphere during annealing may affect this self organization, the current article is aimed at providing a reference for future research by presenting texture analysis of a number of dewetted metal layers on fused silica glass. Fused silica is a suitable material due to its simple chemistry, its high thermal shock resistance and chemical stability as well as its excellent optical properties for the analysis of the plasmonic characteristics of metallic NP in the near UV range down to 200 nm. Additionally, it is available as a high purity material throughout the world. The surface crystallization of fused silica above 1100 °C has recently been studied including texture analysis.²⁷ In the following, we present studies on texture using electron backscatter diffraction (EBSD-) analyses of dewetted layers of Au, Pt and Pd/PdO. In contrast to orientation analyses carried out using X-ray diffraction, EBSD enables to determine the orientation of each individual metallic nano particle from which EBSD-patterns can be obtained and a much more detailed, phase specific texture analysis.

Experimental section

Fused silica glass samples of 8 mm diameter and a thickness of 1.25 mm served as substrates. They were cleaned in an ultrasonic bath for 10 min at 65 °C using a 5% commercial cleaning solution (Tickopur R36). The substrates were subsequently rinsed with deionised water, followed by another two steps of rinsing in deionised water with ultrasonic assistance and finally dried at 110 °C for 1 h.

A DC-sputter-system (Edwards Auto 306) with target dimensions of 50 × 50 mm² for gold (purity 99.99%), palladium (99.95%) as well as a round target of 50 mm diameter for platinum (99%) was used to sputter layers of various thicknesses from 14 to 18 nm. The following parameters were kept constant for all metals during the process: substrate-temperature (21 °C), target-substrate-distance (110 mm), pressure (<10 mPa), voltage (4 kV) and argon pressure (10 Pa). The supplied conditions resulted in a current of 35 mA. The thickness was controlled using a shutter and a film thickness monitor (FTM7, BOC Edwards).

Dewetting was achieved by annealing the samples for 3 h in a muffle furnace at temperatures from 424–1600 °C in air (heating rate 10 K min⁻¹). For a better control of the temperature, all stated annealing temperatures (except 1265 and 1600 °C) were logged during the process using a thermo couple (Ni-CrNi) placed ca. 1 cm vertically above the sample surfaces. After the respective annealing time, the furnace was either switched off, enabling slow cooling, or they were directly removed from the furnace (rapid cooling). The exemplary cooling curve of a slow cooling process from 865 °C is presented in Fig. 1.

The samples were analyzed using a Jeol JSM-7001F equipped with an EDAX Trident analyzing system containing a TSL Digi-view 1913 EBSD-camera. EBSD-scans were captured using TSL

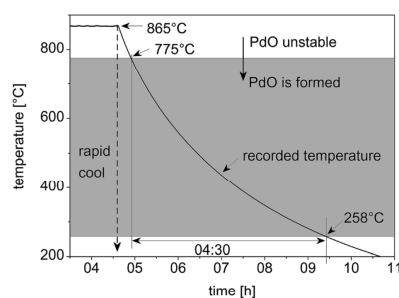


Fig. 1 Measured temperature/time correlation of annealing a sample at 865 °C for 3 h followed by the slow cooling process. The rapid cooling procedure is indicated by the dashed line.

OIM Data Collection 5.31 and evaluated using TSL OIM Analysis 6.2. The scans were performed using a binning of 4 × 4, a current of about 2.40 nA (measured with a Faraday cup) and a voltage of 20 kV. Only data points with a confidence index (CI) of at least 0.1 were used for texture calculation. All samples were coated with a thin layer of carbon at about 10⁻³ Pa in order to optimize the surface conductivity for analysis in the SEM. The particle size distribution and particle shape analyses were determined by image processing performed on SEM-micrographs.

Results and discussion

In order to visualize the texture information presented in this article, Fig. 2 schematically shows three orientations of a cubic unit cell towards a substrate and the attributed poles these orientations cause in the 001, 101 and 111 pole figures (PFs).

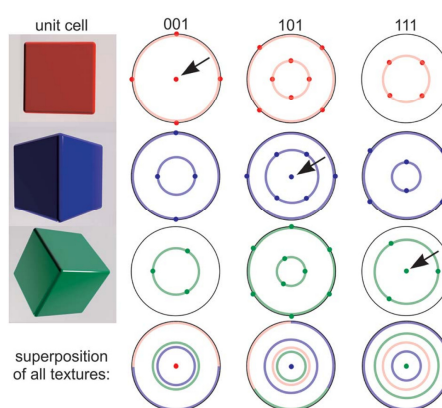


Fig. 2 Orientations of a cubic unit cell and their poles in the respective pole figures. The rings indicate the result of a random rotation around the respective direction perpendicular to the image plane.



The rings in the illustration visualize the result of a random rotation around which ever direction is perpendicular to the substrate. Finally, the superposition of all textures is presented to show that the central dot (see arrows) is characteristic for only one texture while multiple textures may contribute to a ring in some PFs.

Gold

Gold nano particles are by far the most frequently analyzed system of this topic and textures as well as twinning orientations have previously been described in three different experimental setups.^{6,8,9} Gold sputtered at a deposition temperature up to 210 °C onto silica has been analyzed in ref. 28, however the NP were not produced by dewetting and information about a crystallographic texture is not presented. The dewetting of Au on fused silica has not been analyzed by EBSD and the result of applying a dewetting temperature high enough to melt the Au layer has not been reported for a sufficiently representative number of particles on any substrate to the best of our knowledge. Hence, multiple Au layers with a thickness of 14 ± 1 nm were annealed at temperatures from 424 to 1102 °C to allow comparability to ref. 6, the comparison to the other metal layers featured in this article and finally the self organization of the layer after heating above the melting point of the metal. Fig. 3 presents SEM-micrographs of the dewetted particles after annealing at (a) 424 °C and (b) 965 °C. The particles are 159 and 113 nm in size and do not show a bimodal size distribution which is in contrast to the results of ref. 7 where dewetted Au layers with a thickness of more than 10 nm showed bimodal size distributions. Dewetting at 424 °C (Fig. 3a) indicates a high degree of faceting which is systematically reduced at the temperature of 965 °C (see Fig. 3b); this is phenomenologically in agreement with ref. 5.

Hwang and Noh⁵ recently concluded that the surface energy is responsible for the rounding phenomena and additionally proposed a correlation between the crystal structure of their sapphire substrate and the gold NP. However, the NP described in the present paper were all formed on amorphous SiO₂-glass substrates excluding the possibility of a foreign (vaccinating) lattice. The faceting describes a further minimization of the energy and the resulting shape is determined by the Wulff construction and corresponds to a truncated octahedron.^{7,29} In order to describe the morphology, Barnard *et al.* calculated the equilibrium shape of gold NPs using a thermodynamic model.³⁰ They found that significant changes in the particle morphology occur before the melting point of the particles is reached. These results were confirmed by Shim *et al.*³¹ and the rounding was mathematically also confirmed for copper particles by Nielsen *et al.*³² The occurrence of twinning is well known in NP of this system and is also explained by a modified Wulff construction.³³

The articles discussed above describe the fact that the surface fraction of typical crystal facets, *e.g.* the 111 face, are reduced with increasing temperature. Hence a shape transformation occurs in addition to a premelting mechanism.^{32,34} The preferential 111 orientation of the particles is obtained by the formation (dewetting) of an oriented initial metal layer.⁶ As the temperature increases, the equilibrium shape of the particles is changed, hence the possibility exists, that a particle may tilt by reducing the 111 contact surface,²⁹ and a different crystallographic orientation may be adopted. It may be concluded, that slow cooling may cause the optimal surface at low temperatures to be observed after annealing while fast cooling freezes the morphology observed at high temperatures. However, this argumentation must be performed under consideration of the substrate.^{35,36}

Fig. 3 also shows the 001, 101 and 111 PFs of textures calculated from EBSD-scans performed with a step size of 40 nm covering an area of more than 450 μm². For the temperature of 965 °C, we present textures from two samples prepared simultaneously (sputtering, annealing at 965 °C, slow cooling, and carbon coating) and a rapidly cooled sample to illustrate the differences which may occur despite identical preparation and to test the effect of the cooling rate. Please note that a very weak 111-texture may be shown in the 111 PF of the rapidly cooled sample if an even more sensitive scale is chosen.

The PFs show that only a 111-texture is observed in the annealed samples up to 718 °C. An additional 001 texture occurs after annealing at 815 and 965 °C. At 965 and 1057 °C, a 101 texture is additionally detected after annealing. The type of the predominantly occurring texture, *i.e.* "the strongest texture", may shift between samples and, as a matter of fact, even between different areas on the surface of one sample, hence we will not state a hierarchy. Surprisingly, annealing at 1102 °C, *i.e.* above the melting point of Au, does not lead to complete destruction of the particle arrangement. However, a crystallographic texture can no longer be detected after annealing above the melting point, which confirms the previous results obtained from only up to 20 particles^{10,11} for a statistically representative number of NP.

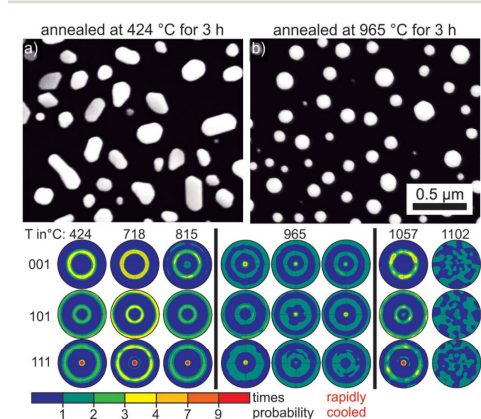


Fig. 3 SEM-micrographs of gold NP dewetted on glass at (a) 424 °C and (b) 965 °C. Pole figures of textures calculated from EBSD-scans performed on layers dewetted at the stated temperatures visualize preferably occurring orientations.



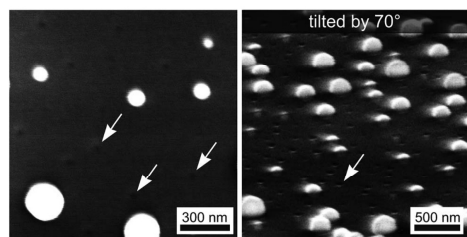


Fig. 4 SEM-micrographs of Au NP dewetted at 1102 °C for 3 h.

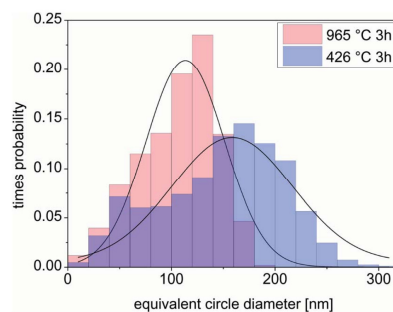


Fig. 5 Equivalent circle diameter of gold NP formed by dewetting at 426 and 965 °C for 3 h.

In contrast to lower annealing temperatures, substrate modifications in the form of small depressions or holes were detected after annealing at 1102 °C as shown in Fig. 4. As fused silica is known to crystallize above 1100 °C and the initial crystals have been shown to form depressions in the surface,²⁷ it is possible that these small impressions are tiny surface crystals. However, the nucleation rate would be much higher which could point towards the Au layer or the NP functioning as a nucleating agent at the surface. Alternatively, these depressions could also result from a substrate–NP interaction during dewetting and be visible if the NP observed after melting are not in the positions of the NP formed during dewetting. Twinning as described in ref. 6 and 8 may be observed on all the surfaces analyzed here.

These results indicate that the texture formation is temperature dependent but perhaps not substrate dependent for amorphous substrates, as the sole 111-texture previously described on soda-lime-silica-glass⁶ after annealing at 400 °C corresponds to the data presented here. However, only 111-textures were reported in ref. 8 where Au layers were dewetted and annealing was performed at temperatures from 400 to 1000 °C under controlled atmospheres on oxidized Si-wafers using polymer microspheres in the setup. Although the dominance of the 111 texture is reduced with an increasing annealing temperature, which was also observed using a sapphire substrate,⁵ a clear 111 texture is still observed after annealing at 1057 °C. Hence the 111 texture is observed throughout the entire temperature range while the 001 texture occurs at 815 and 965 °C and the 101 texture occurs at 965 and 1057 °C.

As most samples were cooled slowly, it is impossible that the textures formed solely during cooling because if that were the case all the samples should feature the same textures. At the same time the observation of faceted as well as rounded particles clearly shows that the applied "slow" cooling process is still fast enough to freeze the high temperature morphology of the particles. The absence of a texture after heating above the melting point may be seen as proof that the NP contributing to the textures measured by EBSD are too large to be significantly affected by the melting point reduction observed in very small NP.³⁷ Additionally, it clearly proves that texture formation is caused by a self organization during dewetting which does not occur during the solidification of a melt.

The particle size distributions of the surfaces represented by the SEM-micrographs in Fig. 3a and b are presented in Fig. 5 and are fitted by a Gaussian distribution. The (SEM projection) area of each particle was determined and the diameter of the corresponding area equivalent circle is calculated. The mean particle diameter is 159 ± 58.5 nm at 426 °C and decreases to 113 ± 38 nm after the heat treatment at 965 °C. This effect can be explained by the Rayleigh instability, where elongated particles disintegrate into several smaller particles at higher temperatures and a decrease of the particle size should occur accompanied by an increase of the particle number and consequently a more narrow size distribution. It should be noted that these micrographs only show a projection of the particles, hence a statement about the three-dimensional shape cannot be made here.

As statistical analyses of the particle size distribution were not given in ref. 6 and 9 we would like to amend this here: a bimodal size distribution cannot be detected in the SEM-micrographs of the samples featured in both articles.

The circularity of a particle can be mathematically defined by a feret ratio where the maximum and minimum diameter of a particle is determined and the related ratio is calculated.⁶ Hence a value of "1.0" is equivalent to a circle while a value of "0.0" corresponds to an infinitely long string. A detailed analysis of the particle shape in Fig. 6 using the feret ratio exhibits a lognormal distribution. Annealing at 426 °C for 3 h results in a maximum at 0.76 while increasing the temperature to 965 °C shifts the maximum to 0.88 and narrows the distribution.

This confirms the visual impression that the particles become increasingly rounded at higher temperatures which has also been reported for gold NP dewetted on crystalline sapphire.⁵ The fits shown in Fig. 5 are negative skew lognormal distributions. In order to perform a sufficient coverage, the independent variable $x = (x - 1)$ is assumed for the equation of the lognormal distribution.

Platinum

Platinum nano particles are interesting because they combine the catalytic properties of Pt with a relatively large surface.



Paper

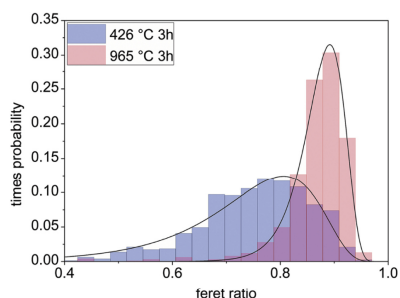


Fig. 6 Feret ratio of gold NP formed by dewetting at 426 and 965 °C.

They may also be used as an etch mask. However, Pt and Si form alloys of multiple compositions with melting points down to 830 °C and SiO₂ may be reduced by H₂ (ref. 38) or an electrical current in a glass melt³⁹ to provide the alloying component. The thermal dewetting of Pt on Si with a natural oxide layer has been studied for layers from 1.5 to 15 nm deposited by electron beam evaporation and annealed at 400 to 1000 °C for only 30 to 240 s with a focus on NP morphology.¹² Increasing the annealing time led to larger particles in a narrower size distribution.^{12,40} The formation of PtSi-phases and nano wire growth was observed when annealing Pt-layers on Si wafers.^{12,13} In addition, interactions with other substrates are not uncommon.⁴¹

Due to the lack of a reducing agent, PtSi alloys should not play a role in the experiments performed here. Additionally, all Pt₁Si₁ phases known to the authors are not cubic and hence their EBSD-patterns would not be reliably indexable as metallic Pt. Dewetting sputtered Pt layers of 14 nm at 965 °C for 3 h led to the Pt NP presented in the SEM-micrograph of Fig. 7 which show a regular log normal size distribution if the circle diameter in the SEM-micrograph is analyzed as illustrated below. The centre of mass is 84.0 nm – 34.1 and + 57.5. Some of the large particles show faceting into triangles or irregularly shaped hexagons as well as rods. The rods protrude from the surface and hence might also be described as whiskers or nano wires, making a statement towards true particles sizes problematic for these samples. Fig. 7 also presents 001, 101 and 111 PFs of textures calculated from an EBSD-scan covering 4500 μm² with a step size of 100 nm. The PFs show a double texture where crystal orientations with either a {101} or a {111} plane parallel to the substrate surface preferably occur. A 100 texture is not indicated. Attempting to perform a size-dependent texture analysis comparable to that presented in ref. 9 only showed that reliable data points with a low image quality (<30%) show the same texture information as the entire scan. 111-twinning in the form of two orientations within one NP sharing a common {111} plane was also detected in these samples. Annealing Pt above the melting point of 1772 °C is not possible using fused silica substrates because the glass crystallizes to high-cristobalite above 1100 °C which in turn melts at 1713 °C.

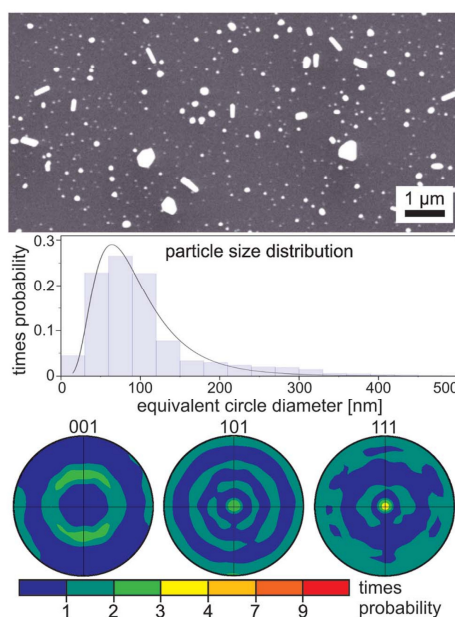


Fig. 7 SEM-micrograph of Pt NP dewetted at 965 °C and pole figures of a texture calculated from an EBSD-scan performed on the surface. The elongated particles are nano rods protruding from the surface.

Palladium/palladium oxide

Palladium in the form of NPs, thin layers and foams are of notable interest in materials science due to their interaction with hydrogen^{14,15} and their catalytic activity with respect to various chemical reactions.^{42–45} Therefore the material is used as a catalytic agent, in gas purification systems and hydrogen sensors.^{46–48} Pd NP have special optical (plasmonic) properties which change significantly if the particles are oxidized to palladium oxide.¹⁶ Pd is not inert during annealing in air but oxidizes to PdO above 258 °C and starts to decompose back to metallic Pd at temperatures above 775 °C (both temperatures correspond to the DTA onset).¹⁶ The crystal structure changes from cubic to tetragonal during oxidation⁴⁹ which enables to identify the individual phases using EBSD. The oxidation of Pd to PdO has been studied on a Pd film under a controlled atmosphere.⁵⁰ PdO is also reduced in the presence of hydrogen¹⁸ meaning an oxidized layer may be converted to metallic palladium at room temperature.^{19,20} These properties of palladium are of interest for NP research and preparation in general. Hence, the effect of the phase transition at higher temperatures can be studied at room temperature. In addition, this phase transition can be reversed at room temperature by purging with H₂. The size dependent kinetics of Pd-hydration have been studied on nano structured materials,⁵¹ thin films⁵² and nano particles.^{53–55} Michalak *et al.* described the possibility of



thermally induced spinodal dewetting in thin Pd layers.²¹ However, those experiments were performed in ultra high vacuum (UHV) which completely suppresses the oxide phase. Moreover, Mizsei *et al.* heated thin Pd layers on glass substrates at atmospheric conditions up to 600 °C and observed no dewetting but the formation of PdO as well as large accumulations of material in the film.²² After adding hydrogen at 500 °C, a preferred 111 orientation of palladium was described.²³ While the presented structures resemble those shown in ref. 20, it would seem the temperature was not high enough to produce completely separated particles.

In a first step we present results obtained from samples prepared by a non-chemical dewetting procedure at 965 °C and ambient conditions. As the oxidized species of palladium decomposes to metallic Pd between 775 and 800 °C,^{15,17} the use of hydrogen can be omitted during dewetting. Due to the oxidation behavior of Pd, an effect of cooling rates on the PdO formation during cooling may not be neglected and the applicability of texture analysis after flushing with H₂ gas must be analyzed. Hence comparable samples with a Pd layer thickness of 18 nm were annealed at 965 °C for 3 h after which one sample was directly removed from the furnace, causing a high cooling rate of more than 800 K min⁻¹, while the other was left in the furnace to cool slowly. Both samples were then coated with carbon, analyzed by EBSD, flushed with H₂ and reanalyzed by EBSD. The acquired results are presented in Fig. 8 along with EBSD-patterns of Pd and PdO.

EBSD-pattern acquisition was very difficult from the unpurged, quickly cooled sample so that only *ca.* 400 data points were of sufficient quality (confidence index CI > 0.1) in a scan of almost 200 000 patterns. While this is within the error margin of the indexing procedure, it was possible to locally obtain high quality EBSD-patterns of Pd from this surface. The latter cannot be said for PdO. Hence, the corresponding 111 texture of Pd indicated by the PF is probably real although not representative while the reliability of the PdO texture must be questioned altogether. After flushing with H₂, the NP from the same area provided well indexable EBSD-patterns of Pd indicating clear 001 and 111 textures while the number of patterns attributed to PdO with a CI > 0.1 is again within the error margin.

The increase of the ability to acquire EBSD patterns after flushing may indicate that the NP initially showed a core-shell structure of Pd surrounded by a thin PdO layer despite the high cooling rate. The combination of both crystal lattices (Pd and PdO) within the information volume of EBSD may lead to pattern superposition (*e.g.* at grain boundaries) or prevent the formation of an EBSD-pattern as may be assumed here.

The presence of PdO despite rapid cooling and its influence on the optical properties of the nanoparticles was already shown in ref. 48.

The sample cooled slowly showed well indexable EBSD patterns of PdO after annealing while Pd was not detected reliably. After flushing with H₂, the NP on the surface failed to produce a percentage of EBSD-patterns comparable to that obtained from the quickly cooled sample (only 0.03%). However, the 1796 reliably indexed EBSD-patterns of Pd in the

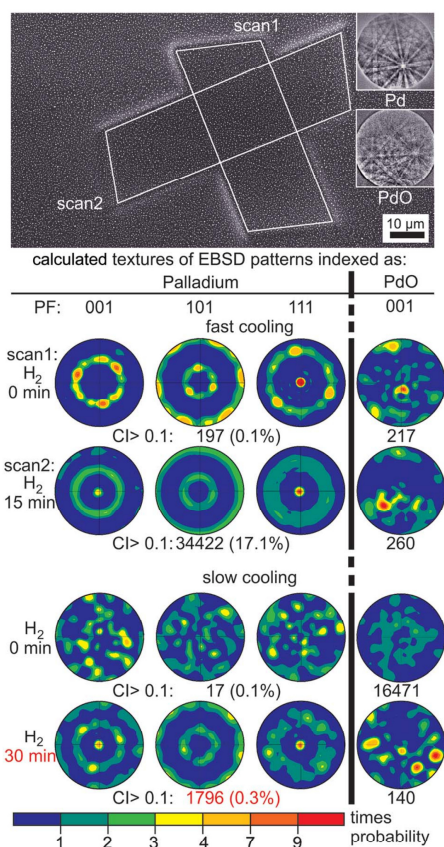


Fig. 8 SEM-micrograph of Pd NP dewetted from a 18 nm thick Pd film by annealing for 3 h at 965 °C followed by fast cooling. EBSD-patterns of Pd and PdO are presented in the insets. EBSD-scan 1 was performed directly after annealing while scan 2 was performed after the sample was additionally flushed with H₂ gas for 15 min. Textures of Pd and PdO calculated from the scans 1 and 2 as well as comparable scans obtained from a slowly cooled sample flushed with H₂ for 30 min are presented below along with the number of reliable data points (CI > 0.1) contributing to the respective texture.

scan indicate the same coexistence of a 001 and a 111 texture which was also observed in the quickly cooled sample after flushing with H₂. As the optical properties of this sample indicate a reduction of PdO to Pd and only a negligible amount of patterns is indexed as PdO by EBSD, the question arises why EBSD-patterns cannot be obtained from most particles. This problem was detected on numerous samples cooled slowly after annealing at various temperatures.

As it is possible to obtain EBSD-patterns of high quality from a few NPs, errors due to sample preparation, *i.e.* the thickness of



the carbon coating, can be neglected. Additionally, the experiments performed on the quickly cooled samples show that flushing with H₂ after carbon coating led to the reduction of PdO in a comparably prepared sample. The detailed SEM-micrographs of Pd NP resulting from slow and rapid cooling after annealing at 965 °C and purging with H₂ presented in Fig. 9 show a pronounced morphological difference between the particles. The particle shape is "rugged" after the particle oxidized completely and formed PdO of higher volume²⁰ during the slow cooling process, see Fig. 9a. In contrast, the rapidly cooled NP in Fig. 9b are rounded, again implying that any oxidation during rapid cooling only forms a thin shell of PdO on a core of Pd as already outlined above. Hence the structure of a quickly cooled Pd/PdO NP is quite different from that of a slowly cooled Pd/PdO NP even after being flushed with H₂. However, a more detailed analysis of this aspect is beyond the scope of this article.

Hence it must be noted that cooling rates affect the structure of the NPs in this system and possibly the texture formation. It is probable that the phase transformations of Pd to PdO and *vice versa* have no effect on the texture of quickly cooled NP because they were never fully oxidized (PdO was not reliably detected by EBSD on the quickly cooled sample in contrast to the slowly cooled sample). Please note that none of the PFs of PdO allow any certain conclusion on the possible textures of PdO because the two cubic textures of Pd allow at least six tetragonal PdO textures which in turn would probably not show an elevated probability of any orientation and hence remain unnoticed. A similar cubic-tetragonal transition also occurs during cooling after the surface crystallization of fused silica.²⁷

A temperature series was performed to allow a comparison with the results of gold presented above. These samples were always rapidly cooled in order to minimize oxidation and flushed with H₂ for at least 15 min to obtain metallic Pd as the results of Fig. 8 showed that even rapid cooling cannot prevent the formation of a thin oxide layer. The resulting SEM-micrographs in Fig. 10 show that the palladium has a much smaller temperature window in which dewetting occurs. After 3 h at 767 °C, the layer is not dewetted and contains star shaped cracks which were also observed in ref. 20. Well separated particles are observed after annealing at 876 °C for 3 h with an additional substructure between the particles, see arrows, which probably results from the irregularly shaped layer

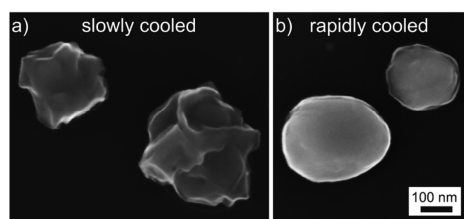


Fig. 9 SEM-micrographs of dewetted Pd particles on the glass surface (a) cooled slowly and (b) cooled rapidly.

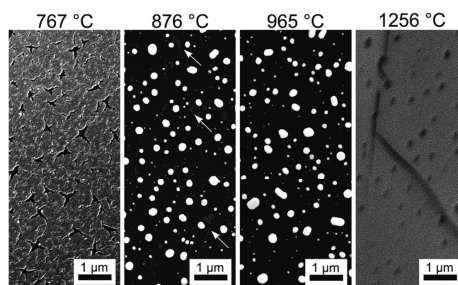


Fig. 10 SEM-micrographs of rapidly cooled Pd-films annealed at the stated temperatures for 3 h.

residue. These substructures are no longer visible after annealing at 965 °C. Pd could not be detected by EDX on the surface of the sample annealed at 1256 °C where the SEM-micrograph only shows depressions and a crack. This temperature was chosen to see what happens during the dewetting procedure if the substrate crystallizes during annealing but below the melting point of the metal. As the sample is fully crystallized here, these depressions cannot be small cristobalite nuclei as proposed in Fig. 4 but probably indicate locations where the Pd NP interacted with the substrate after dewetting but before disappearing, probably by evaporation. The absence of Pd was also observed for a sample annealed at 1600 °C (not shown), *i.e.* above the melting point of Pd, but there was no trace of the depressions shown in Fig. 11. Please note that the cracks in crystallized fused silica form due to the phase transformation between 200 and 275 °C,²⁷ *i.e.* liquid Pd cannot flow into the cracks, again pointing towards an evaporation of Pd.

The particle size distributions corresponding to Fig. 10 are presented in Fig. 11 where bimodal Gaussian distributions are clearly indicated. At 876 °C, the determined mean particle sizes of the respective peaks are 45.6 ± 28.6 and 185 ± 48.0 nm while at 965 °C they are 88.8 ± 74.4 and 331.0 ± 89.0 nm. A bimodal size distribution was also detected for 5 nm thick Pd layers dewetted on fused silica.¹⁶ It seems logical that the continuously dewetting layer residue leads to the smaller particle species in the bimodal size distribution. Coalescence and Ostwald ripening shift this bimodal distribution to larger particle sizes as the atomic mobility is increased by annealing at the higher temperature. However, the exact reason of the thin layer residue is not yet fully understood because such thin structures should have dewetted long before the large particles in the layer were formed. It must be noted, that a statistical analysis of the figures presented in ref. 21 where oxidation was prevented during annealing does not show a bimodal size distribution.

Hence two different dewetting mechanisms may exist: when the layer reaches the dewetting temperature, it is heavily disturbed due to the volume expansion during oxidation and the subsequent volume decrease due to the thermal reduction. The resulting layer morphology containing the star shaped holes (see Fig. 10) is not comparable to the hole formation in a



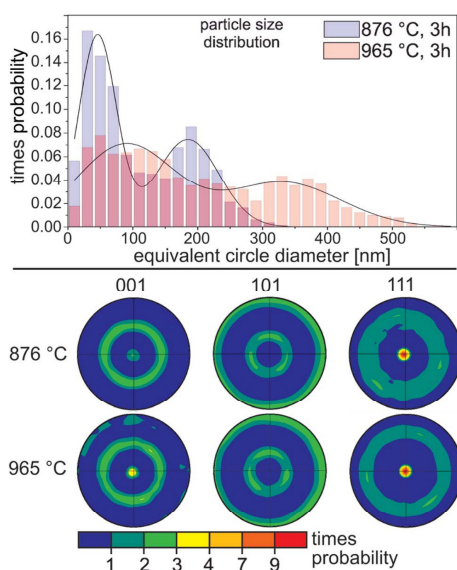


Fig. 11 Temperature series of Pd layers annealed at the stated temperatures for 3 h. SEM-micrographs feature surfaces from which EBSD-patterns could not be obtained. 001, 101 and 111 PFs of textures calculated from EBSD-scans performed on NPs dewetted from the Pd layers.

gold layer.⁵⁶ Please note that dewetting Pd in a vacuum,²¹ *i.e.* without the phase transformation, leads to dewetting morphologies similar to the spinodal dewetting of gold. Hence material accumulations may already exist in the oxidized and reduced system before the actual (spinodal) dewetting begins.²²

Fig. 11 also presents texture information on the Pd-layers dewetted at 876 and 965 °C, EBSD-patterns could not be obtained from the sample annealed at 767 °C. The PFs of the samples annealed at 876 and 965 °C both show 001 and 111 textures while a 101 texture is not detected. 111-twinning of Pd was observed in all EBSD-scans of H₂-flushed samples featured in this article.

Conclusion

The thin films of all studied materials show a dewetting of the metallic film into metal nano particles at high temperatures. The experiments focused on the crystallographic and morphological behavior of the resulting particles as a function of temperatures, cooling rates and chemical phase transitions during preparation. It was shown that the cooling rate may not be neglected in the cases of Au and Pd where temperature dependent particle forming/aging mechanisms were observed. Interactions with the substrate at high temperatures are implied in all cases.

Because Au, Pt, and Pd are all fcc materials, it is of no surprise to find the 111-texture and the 111-twinning in the NP. The 001- and 101-textures, on the other hand, have not been described before and do not occur in the dataset of the previously analyzed Au particles.⁶ For both orientations, a crystallographic axis is oriented parallel to the substrate surface. At 965 °C, all three textures were detected in Au NP while only the 111 and 101 textures were detected in Pt NP and only the 111 and 001 textures were detected in Pd NP. Particle size dependent textures were not detected after dewetting on fused silica. 111-twinning was observed in the metallic NP of all metals analyzed here.

In the case of Au, it was shown that any texture is lost if the metal is melted during annealing. Comparable results could not be obtained for Pd and Pt due to evaporation or the melting of the substrate, respectively.

Gold NP show a rounding in the particle shape with increasing dewetting temperature on the amorphous substrate in agreement to the literature. In contrast to gold, the dewetting of Pd NP leads to a bimodal size distribution caused by a different dewetting mechanism. Pd NP also show faceting and the morphology is affected by the cooling procedure due to the time and temperature dependent phase transition which also affects the ability to acquire EBSD-patterns. The observed structural modification implies a significantly different NP structure.

Nano rods were observed after dewetting Pt on fused silica.

Acknowledgements

The authors would like to thank T. Zscheckel for a number of SEM-micrographs featured in this article and W. Seeber for his support. This work is supported by the DFG "Deutsche Forschungsgemeinschaft" (Se 698/10-1, Se 698/10-2 and Ru 417/14-1).

References

- 1 S. Guo and E. Wang, *Anal. Chim. Acta*, 2007, **598**(2), 181.
- 2 M. Grzelczak, J. Pérez-Juste, P. Mulvaney and L. M. Liz-Marzán, *Chem. Soc. Rev.*, 2008, **37**(9), 1783.
- 3 R. Sardar, A. M. Funston, P. Mulvaney and R. W. Murray, *Langmuir*, 2009, **25**(24), 13840.
- 4 K. Na, Q. Zhang and G. A. Somorjai, *J. Cluster Sci.*, 2014, **25**(1), 83.
- 5 J. S. Hwang and D. Y. Noh, *J. Korean Phys. Soc.*, 2013, **62**(1), 6.
- 6 C. Worsch, M. Kracker, W. Wisniewski and C. Rüssel, *Thin Solid Films*, 2012, **520**(15), 4941.
- 7 C. M. Müller, F. C. F. Mornaghini and R. Spolenak, *Nanotechnology*, 2008, **19**(48), 485306.
- 8 M. Bechelany, X. Maeder, J. Riesterer, J. Hankache, D. Lerose, S. Christiansen, J. Michler and L. Philippe, *Cryst. Growth Des.*, 2010, **10**(2), 587.
- 9 C. Worsch, W. Wisniewski, M. Kracker and C. Rüssel, *Appl. Surf. Sci.*, 2012, **258**(22), 8506.
- 10 H. Sadan and W. D. Kaplan, *J. Mater. Sci.*, 2006, **41**(16), 5099.
- 11 H. Sadan and W. D. Kaplan, *J. Mater. Sci.*, 2006, **41**(16), 5371.



Paper

- 12 S. Strobel, C. Kirkendall, J.-B. Chang and K. K. Berggren, *Nanotechnology*, 2010, **21**, 505301.
- 13 P. K. Sekhar, S. N. Sambandam, D. K. Sood and S. Bhansali, *Nanotechnology*, 2006, **17**(18), 4606.
- 14 T. B. Flanagan and W. A. Oates, *Annu. Rev. Mater. Sci.*, 1991, **21**(1), 269.
- 15 S. Kishore, J. Nelson, J. Adair and P. Eklund, *J. Alloys Compd.*, 2005, **389**(1–2), 234.
- 16 M. Kracker, C. Worsch and C. Rüssel, *J. Nanopart. Res.*, 2013, **15**(4), 1594.
- 17 G. Bayer and H. Wiedemann, *Thermochim. Acta*, 1975, **11**(1), 79.
- 18 J. Han, G. Zhu, D. Y. Zemlyanov and F. H. Ribeiro, *J. Catal.*, 2004, **225**(1), 7.
- 19 J. I. Avila, R. J. Matelon, R. Trabol, M. Favre, D. Lederman, U. G. Volkmann and A. L. Cabrera, *J. Appl. Phys.*, 2010, **107**(2), 23504.
- 20 M. Kracker, C. Worsch and C. Rüssel, *Mater. Lett.*, 2013, **110**, 114.
- 21 W. D. Michalak, J. B. Miller, C. Yolcu and A. J. Gellman, *Thin Solid Films*, 2012, **522**, 473.
- 22 J. Mizsei, P. Sipilä and V. Lantto, *Sens. Actuators, B*, 1998, **47**(1–3), 139.
- 23 J. Mizsei, L. Pirttiaho, M. Karppinen and V. Lantto, *Sens. Actuators, B*, 2000, **65**(1–3), 195.
- 24 C. Katzer, V. Grosse, F. Schmidl, P. Michalowski, G. Schmidl, R. Mueller, J. Dellith, C. Schmidt, J. Jatschka and W. Fritzsche, *J. Nanopart. Res.*, 2012, **14**(12), 1285.
- 25 K. Nagashima, T. Yanagida, H. Tanaka and T. Kawai, *J. Appl. Phys.*, 2007, **101**(12), 124304.
- 26 A. Vomiero, M. Ferroni, E. Comini, G. Faglia and G. Sberveglieri, *Nano Lett.*, 2007, **7**(12), 3553.
- 27 W. Wisniewski, S. Berndt, M. Müller and C. Rüssel, *CrystEngComm*, 2013, **15**(13), 2392.
- 28 L. Armelao, D. Barreca, A. Gasparotto, E. Pierangelo, E. Tondello and S. Polizzi, *J. Nanosci. Nanotechnol.*, 2005, **5**(2), 259.
- 29 L. D. Marks, *Rep. Prog. Phys.*, 1994, **57**(6), 603.
- 30 A. S. Barnard, X. M. Lin and L. A. Curtiss, *J. Phys. Chem. B*, 2005, **109**(51), 24465.
- 31 J.-H. Shim, B.-J. Lee and Y. W. Cho, *Surf. Sci.*, 2002, **512**(3), 262.
- 32 O. H. Nielsen, J. P. Sethna, P. Stoltze, K. W. Jacobsen and J. K. Nørskov, *Europhys. Lett.*, 1994, **26**(1), 51.
- 33 E. Ringe, R. P. van Duyne and L. D. Marks, *J. Phys. Chem. C*, 2013, **117**(31), 15859.
- 34 P. Ajayan and L. D. Marks, *Phys. Rev. Lett.*, 1989, **63**(3), 279.
- 35 W. Winterbottom, *Acta Metall.*, 1967, **15**(2), 303.
- 36 T. Wang, C. Lee and L. D. Schmidt, *Surf. Sci.*, 1985, **163**(1), 181.
- 37 P. Buffat and J. P. Borel, *Phys. Rev. A*, 1976, **13**(6), 2287.
- 38 R. Lamber and N. I. Jaeger, *J. Appl. Phys.*, 1991, **70**(1), 457.
- 39 W. Wisniewski, M. Nagel, G. Völksch and C. Rüssel, *Cryst. Growth Des.*, 2010, **10**(4), 1939.
- 40 J. Dufourcq, P. Mur, M. J. Gordon, S. Minoret, R. Coppard and T. Baron, *Mater. Sci. Eng., C*, 2007, **27**(5–8), 1496.
- 41 A. Galit, M. Vissarion, G. Eisenstein and W. D. Kaplan, *J. Mater. Sci.*, 2014, **49**(11), 3863.
- 42 C. Hwang, Y. L. Lu, S. W. Jang, P. T. Chou, C. R. C. Wang and S. J. Yu, *J. Catal.*, 2000, **195**(2), 336.
- 43 A. F. Littke and G. C. Fu, *Angew. Chem., Int. Ed.*, 2002, **41**(22), 4176.
- 44 C. T. Campbell, *Surf. Sci. Rep.*, 1997, **27**(1–3), 1.
- 45 K. C. Nicolaou, P. G. Bulger and D. Sarlah, *Angew. Chem., Int. Ed.*, 2005, **44**(29), 4442.
- 46 T. Hübert, L. Boon-Brett, G. Black and U. Banach, *Sens. Actuators, B*, 2011, **157**(2), 329.
- 47 C. Langhammer, E. M. Larsson, B. Kasemo and I. Zorić, *Nano Lett.*, 2010, **10**(9), 3529.
- 48 M. Kracker, C. Worsch, W. Seeber and C. Rüssel, *Sens. Actuators, B*, 2014, **197**, 95.
- 49 W. M. Haynes and D. R. Lide, *CRC handbook of chemistry and physics: A ready-reference book of chemical and physical data*, CRC Press, Boca Raton, London, New York, 2010.
- 50 H. H. Kan and J. F. Weaver, *Surf. Sci.*, 2009, **603**(17), 2671.
- 51 H. Gleiter, *Acta Mater.*, 2000, **48**(1), 1.
- 52 W. Vargas, I. Rojas, D. Azofeifa and N. Clark, *Thin Solid Films*, 2006, **496**(2), 189.
- 53 C. Langhammer, I. Zorić, B. Kasemo and B. M. Clemens, *Nano Lett.*, 2007, **7**(10), 3122.
- 54 C. Langhammer, V. P. Zhdanov, I. Zorić and B. Kasemo, *Phys. Rev. Lett.*, 2010, **104**(13), 135502.
- 55 A. Pundt, *Nanoskalige Metall-Wasserstoff-Systeme*, Univ.-Verl. Göttingen, Göttingen, 2005.
- 56 A. B. Tesler, B. M. Maoz, Y. Feldman, A. Vaskevich and I. Rubinstein, *J. Phys. Chem. C*, 2013, **117**(21), 11337.

